



Albina Mikhralieva

Synthesis and characterization of hybrid silica-based nanostructures with immobilized carbogenic materials having enriched π -electron system and their analytical applications

Tese de Doutorado

Thesis presented to the Programa de Pós-graduação em Química of PUC-Rio in partial fulfillment of the requirements for the degree of Doutor em Química.

Advisor: Prof. Volodymyr Zaitsev

Rio de Janeiro

May 2020



Albina Mikhralieva

Synthesis and characterization of hybrid silica-based nanostructures with immobilized carbogenic materials having enriched π -electron system and their analytical applications

Thesis presented to the Programa de Pós-graduação em Química of PUC-Rio in partial fulfillment of the requirements for the degree of Doutor em Química. Approved by the Examination Committee.

Prof. Volodymyr Zaitsev

Advisor

Departamento de Química - PUC-Rio

Prof. Ricardo Queiroz Aucélio

Departamento de Química - PUC-Rio

Prof. Pierre Mothé Esteves

UFRJ

Prof. Emerson Schwingel Ribeiro

UFRJ

Prof. Fernando Henrique Cincotto

UFRJ

Prof. Célia Machado Ronconi

UFF

Rio de Janeiro, May 27th, 2020

All rights reserved.

Albina Mikhralieva

Doctorate candidate in Chemistry of the Pontifical Catholic University of Rio de Janeiro (PUC-Rio). She holds both Bachelor's degree and Master's degree in Chemistry from the V. N. Karazin Kharkiv National University in 2013 and 2014, respectively. In addition, she obtained her Master's degree in Administrative Management from the V. N. Karazin Kharkiv National University in 2015. She has experience in Chemistry, focusing on the preparation of new materials and their application in chemical analysis.

Ficha Catalográfica

Mikhralieva, Albina

Synthesis and characterization of hybrid silica-based nanostructures with immobilized carbogenic materials having enriched π -electron system and their analytical applications / Albina Mikhralieva ; advisor: Volodymyr Zaitsev. – 2020.

260 f. : il. color. ; 30 cm

Tese (doutorado)–Pontifícia Universidade Católica do Rio de Janeiro, Departamento de Química, 2020.

Inclui bibliografia

1. Química – Teses. 2. Nanorreator. 3. Material híbrido. 4. Extração em fase sólida. 5. Antraceno. 6. Análise eletroquímica. I. Zaitsev, Volodymyr. II. Pontifícia Universidade Católica do Rio de Janeiro. Departamento de Química. III. Título.

CDD: 540

I would like to dedicate this work to my family. A special feeling of gratitude to my loving parents, Akhmedullakh and Oleksandra Mikhraliiev's, and to my brother Rustam for their love and support throughout my life, effort and immense dedication.

Acknowledgements

First of all, I would like to thank my family, namely, to my father and mother Akhmedullakh and Oleksandra, and brother Rustam, for driving force in the achievement of PhD degree and supporting in this period of my life.

I wish to express my sincere appreciation to my advisor in Ukraine, Prof. Yuriy Kholin, who believed in me as a researcher. He was the principal person who had opened to me the world of hybrid silica-based materials and door forward Brazil, in particular Pontifical Catholic University of Rio de Janeiro.

I would like to pay my special regards to the current scientific advisor, Prof. Volodymyr Zaitsev, who confided in me from the first days in the laboratory. Thanks to him, I learned a lot of things during carrying out this thesis. He is the person that guided and encouraged me to be professional and find another alternative way when the road got tough. Without his persistent help, as advisor and friend, the goal of this project would not have been realized.

Special thanks to the PUC-Rio, Brazilian Agencies CNPq, CAPES, and FAPERJ for grants, doctoral scholarship.

I am grateful to the Department of Chemistry at PUC-Rio for the warm welcome, great opportunity, the new knowledge and the support of the research, professional and friendly collectives. Fátima Almeida, thank you for professional, personal support that I received from my first day at PUC-Rio until now. I was very happy to be part of our research group at LAQAPAB laboratory. Henrique B. da Motta, thank you for working with the development of our CDs synthesis approach. Thank you, Michael Nazarkovsky, for your support, friendship, help with analysis of the textural properties by Nguyen-Do approach and technical support in SEM analyses.

I am extremely grateful to Prof. Ricardo Queiroz Aucélio for giving me confidence and opportunity to work with facilities in his laboratory, especially with a fluorescent spectrophotometer. Besides, I thanks to support and fruitful help during the research.

I wish to acknowledge Prof. Omar Pandoli due to his responsiveness, technical support and fruitful help in Raman and AFM analyses.

Prof, Jiang Kai, thank you very much for professional and friendly support, and opportunity to see and work at Brazilian Synchrotron Light Laboratory (LNLS) to obtain 3D photoluminescence spectra at UV range.

I am appreciating the generous help received from Prof. Edilson V. Benvenutti in BET measurements and for using the electrochemical facility. I wish to express my deepest gratitude to my friend, colleague and Ukrainian co-advisor, Prof. Oleg Tkachenko for your support until now, collaboration, fruitful discussion and technical assistance in the electrochemical study.

I am extremely grateful to technician staff of the Department of Chemistry represented by Rodrigo Gonçalves, Álvaro J. Pereira, Maurício O. Dupim, Beatriz M. Souza e Silva for friendship, support and constantly willing to help me in the laboratory. In addition, I am grateful to secretary staff of the Department of Chemistry represented by Carlos Roberto da Silva, Marlene de Paula, Didimo Esperidião for technical and organizational support during the study.

I would like to thank Prof. Marco Cremona and his laboratory staff for advice and using fluorescent facilities to analyzed sold sample. Profa. Maria Isabel Pais da Silva, thank you for the opportunity to work with FTIR facilities. Thanks to Profa. Camilla Djenne Buarque and her laboratory for friendly support and the possibility of using some reagents. In addition, I am grateful to Prof. Nicolás A. Rey for technical support in the realization of TGA analysis. I wish to express my deepest gratitude to the staff and technical support of TGM beamline at LNLS, Laboratory for Surface Science (in AFM analyses) and Nanostructured Soft Materials Laboratory (in XPS analyses) at Brazilian National Nanotechnology Laboratory (LNNano) at Brazilian Center for Research in Energy and Materials (CNPEM); LABNANO of The Brazilian Center for Research in Physics (CBPF), in particular Dr. Horácio Coelho-Júnior, and Prof. Rubem Luis Sommer, for using of electron microscopy facilities; Nuclear Magnetic Resonance Laboratory of IQ- UFRGS and IQ-UFRJ for technical support in solid ^{13}C NMR analyses. Thank you very much, Prof. Yutao Xing from LaMAR, for responsiveness, flexibility in realization TEM analyses. In addition, I thank Dr. Sergei A. Khainakov for XRD measurements.

I would like to recognize the invaluable assistance that you all provided during my study. I also thank all my friends and other people that influenced me in some way but were not mentioned here.

This study was financed in part by the Coordenação de Aperfeiçoamento de Pessoal de Nível Superior - Brasil (CAPES) - Finance Code 001.

Abstract

Mikhraliieva, Albina; Zaitsev, Volodymyr (Advisor). **Synthesis and characterization of hybrid silica-based nanostructures with immobilized carbogenic materials having enriched π -electron system and their analytical applications.** Rio de Janeiro, 2020. 260p. Tese de Doutorado – Departamento de Química, Pontifícia Universidade Católica do Rio de Janeiro.

The objective of the present research was devoted to the preparation of new silica-based hybrid materials having covalently immobilized carbon-containing molecular and nanometric systems with delocalized π -electrons that can be used as adsorbents and electrodes for preconcentration and determination of aromatic compounds. For this purpose, methodologies for covalent immobilization of anthracene (Ant), graphene oxide quantum dots (GOQDs) and carbon nanodots (CDs) on silica surface (SiO_2) have been developed. These compounds have a conjugated system of π -electrons and thus can form intramolecular π - π stacking interaction with aromatic compounds. The nanocomposite with immobilized GOQDs was prepared by covalent immobilization of nanoscale graphene oxide (GO) fragments. Three sets of SiO_2 -Ant were obtained using reaction surface assembling reactions by alkylation and condensation of silica with immobilized primary amines. These materials can have different arrangements of anthracene ligands on silica surface and so π -donor properties. Silica gel nanocomposites with immobilized CDs were prepared by two different approaches. For the first one, the CDs were obtained from the molecular precursor and then immobilized on silica. For the second method, CDs were prepared by nanoreactor approach directly in silica gel pores. The second method is facile and robust and also allows better control of the particle size and composition. The effects of silica gel modification, pore size, synthesis time, hydrolytic stability, carbon nanoparticle size and quantum yield of the fluorescence were studied. It was demonstrated that the carbonization of aminosilica gel with embedded citric acid resulted in the formation of unbound CDs and immobilized CDs. Due to firm attachment to the surface CDs can be easily separated from low-molecular-weight impurities and CDs by simple rinsing of the nanocomposite with water. As prepared

CDs demonstrate excitation-independent photoluminescence at 445 nm with quantum yield up to 80% that makes them attractive for bioanalytical application. The composition of the surface layer of the adsorbents was determined from elemental and thermogravimetric analysis, X-ray photoelectron, solid nuclear magnetic resonance, Raman, FTIR, and fluorescent spectroscopy. The textural properties of the adsorbents were determined as well as ligand immobilization kinetics, the degree of surface transformation and hydrolytic stability of the grafted groups, the effect of silica porosity on ligand conversion degree. The adsorption properties of the materials were studied in dynamic and static solid-phase extraction (SPE) modes for the model compounds methylene blue and anthracene in various aqueous-organic and organic mobile phases, in the presence of interfering components. It was demonstrated that studied materials have a higher affinity towards aromatic compounds than commercial C18 SPE cartridges in organic mobile phases that allow one-step separation of polycyclic aromatic hydrocarbons in the matrix with a high concentration of fatty acids. Also, silica-immobilized GOQDs was used for electrochemical analysis of selected antibiotics and hormones. The electrode demonstrated electrocatalytic activity towards estriol (ET), diethylstilbestrol (DES), sulfamethoxazole (SMZ), and trimethoprim (TMP) that made it possible to determine these analytes with up to 9 nmol L⁻¹ (ET).

Keywords

Nanoreactor; Hybrid material; Solid-phase extraction; Anthracene; Electrochemical analysis.

Resumo

Mikhraliieva, Albina; Zaitsev, Volodymyr (Advisor). **Síntese e caracterização de nanoestruturas híbridas baseadas em sílica com materiais carbogênicos imobilizados tendo sistemas ricos em elétrons π e suas aplicações na química analítica.** Rio de Janeiro, 2020. 260p. Tese de Doutorado – Departamento de Química, Pontifícia Universidade Católica do Rio de Janeiro.

O objetivo da pesquisa foi dedicado à preparação de novos materiais híbridos à base de sílica contendo sistemas moleculares ou nanométricos de carbono com sistema de elétrons π conjugados, imobilizados covalentemente para posterior aplicações como adsorventes e eletrodos para pré-concentração e determinação de compostos aromáticos. Deste modo, propôs-se o desenvolvimento das metodologias para as imobilizações covalentes de antraceno (Ant), pontos quânticos de óxido de grafeno (GOQDs) e nanopontos de carbono (CDs) na superfície da sílica (SiO_2). Estes compostos são constituídos de sistemas conjugados de elétrons π e, portanto, podem formar interação intramolecular de empilhamento π - π com compostos aromáticos. Nanocompósito de GOQDs imobilizados foi preparado através da interação covalente de fragmentos nanométricos de óxido de grafeno (GO). Três tipos de SiO_2 -Ant foram obtidos através de abordagem de montagem da superfície pela reação de alquilação e condensação de sílica modificada com grupos aminopropila. Estes materiais podem ter diferentes arranjos de ligantes de antraceno na superfície da sílica e, portanto, podem apresentar diferentes propriedades doadoras de elétrons- π . Nanocompósitos de sílica gel com CDs imobilizados foram preparados por duas abordagens diferentes. Na primeira, os CDs foram obtidos a partir do ácido cítrico como material de partida e posteriormente imobilizados em sílica. O segundo método consistiu no uso de sílica gel porosa como nanorreator para a preparação de CDs. Este método é simples e robusto, o qual permite um maior controle do tamanho e da composição do nanomaterial. Além disso, os efeitos da modificação da sílica, tamanho dos poros, tempo de síntese, estabilidade hidrolítica, tamanho das nanopartículas de carbono e rendimento quântico da fluorescência foram avaliados. Foi demonstrado que a carbonização do gel aminosilica com ácido cítrico incorporado resultou na formação

de CDs não imobilizados e CDs imobilizados. Devido à forte fixação na superfície, os CDs podem ser facilmente purificados através de simples lavagem do nanocompósito com água. Os C-pontos preparados apresentaram fotoluminescência independente de excitação a 445 nm com rendimento quântico até 80%, o que os tornam atraentes para aplicação bioanalítica. O nanocompósito imobilizado com GOQDs foi preparado por ligações covalentes dos fragmentos de GO em nanoescala. A composição da camada superficial de todos adsorventes foi determinada a partir de análises elementares e termogravimétricas, fotoelétrons de raios X, ressonância magnética nuclear no estado sólido, Raman, FTIR e espectroscopia de fluorescência. As propriedades texturais dos adsorventes foram determinadas, bem como a cinética de imobilização do ligante, o grau de transformação da superfície e a estabilidade hidrolítica dos grupos enxertados, o efeito da porosidade da sílica no grau de conversão do ligante. As propriedades de adsorção dos materiais foram avaliados pela extração em fase sólida nos modos dinâmico e estático para os compostos modelos azul de metileno e antraceno em várias fases móveis aquosas-orgânicas e orgânicas, na presença de componentes interferentes. Os nanomateriais obtidos apresentaram maior afinidade para compostos aromáticos do que os cartuchos comerciais C18 para extração em fase sólida (SPE) de fases orgânicas móveis que permitem a separação em uma etapa dos hidrocarbonetos aromáticos policíclicos (PAHs) na matriz com alta concentração de ácidos graxos. Ademais, sílica gel com GOQDs imobilizados foi usado para análise eletroquímica de antibióticos e hormônios selecionados. O eletrodo demonstrou atividade eletrocatalítica em relação ao estriol (ET), dietilestilbestrol (DES), sulfametoxazol (SMZ) e trimetoprim (TMP) que possibilitaram determinar esses analitos com até $0.009 \mu\text{mol L}^{-1}$ (ET).

Keywords

Nanorreator; Material híbrido; Extração em fase sólida; Antraceno; Análise eletroquímica.

Table of contents

1.	Introduction	25
1.1.	Thesis proposal	25
1.2.	Thesis structure	27
1.3.	Objective of the thesis	29
1.3.1.	General objective	29
1.3.2.	Specific objectives	29
2.	Theoretical Part	32
2.1.	Polyaromatic hydrocarbons and their derivatives	32
2.1.1.	Sources of PAHs, environmental risk	32
2.1.2.	Sample pre-treatment in PAHs determination	36
2.1.3.	Analytical methods for PAHs determination.	39
2.2.	Adsorbent for solid-phase extraction of aromatic compounds	40
2.3.	Interaction between aromatic compounds	47
2.4.	SPE adsorbents based on carbogen nanoparticles	49
2.5.	PAH-anchored materials	50
2.5.1.	Adsorption properties of PAHs anchored materials	51
2.5.2.	Luminescent properties of immobilized PAHs	52
2.6.	Graphene-based materials	55
2.6.1.	Fabrication of graphene	56
2.6.2.	Functionalization of graphene oxide	65
2.6.3.	Characterization of Graphene	68
2.7.	Carbon Dots materials	69
2.7.1.	Properties of CDs	70
2.7.2.	Synthesis approaches	71
2.7.3.	Mechanism of PL origin	81
2.7.4.	Applications	82
2.8.	Conclusion for the theory review	85
3.	Experimental section	86
3.1.	Materials and methods	86
3.1.1.	Chemicals and reagents	86
3.1.2.	Characterization techniques	87
3.2.	Preparation of materials	89
3.2.1.	Activation of silica gel	89
3.2.2.	Synthesis of modified supports	89
3.2.3.	Synthesis of anthracene-functional silica gel	90
3.2.4.	Synthesis of GO and modification of silica gel with GOQDs	93
3.2.5.	Synthesis of Carbon Dots samples	94
3.3.	The simulation of H ⁺ adsorption process	96
3.4.	Determination of the concentration of grafted groups	97
3.5.	Kinetic studies during synthesis	100
3.6.	Calculation of defect distance in graphene	100
3.7.	Non-specific adsorption of anthracene	101
3.8.	Adsorption studies in static mode	101

3.9.	Adsorption studies in dynamic mode	102
3.10.	Calculation of $\text{SiO}_2\text{-NH}_2\text{@CA}$ mass loss	104
3.11.	Calculation of quantum yield of CDs	104
3.12.	Preparation of electrode for electrochemical study	105
4.	Preparation and characterization of silica	106
4.1.	Silica gel with immobilized aminogroups	106
4.1.1.	Functional analysis of amine-groups on the surface	106
4.1.2.	Textural properties	107
4.1.3.	Morphological properties	110
4.1.4.	NMR study	111
4.1.5.	Structure of the grafted layer	111
4.1.6.	XPS characterization	112
4.1.7.	Acid-base equilibria at the silica interface	114
4.1.8.	Quantification of functional group loading	116
4.2.	Silica gel with immobilized mercapto-groups	120
4.2.1.	Synthesis and analysis of mercaptopropyl silica	120
4.2.2.	Textural properties	121
4.2.3.	FTIR characterization	122
4.2.4.	Quantification of immobilized groups	123
4.3.	Conclusions of the chapter 4	126
5.	Anthracene-immobilized silicas	127
5.1.	Synthesis of silica with immobilized anthracene derivatives	127
5.2.	Textural characterization	133
5.3.	Solid state ^{13}C NMR	136
5.4.	FTIR characterization	138
5.5.	XPS characterization	138
5.6.	Thermogravimetric analysis	140
5.7.	Element analysis	142
5.8.	Surface functionality	143
5.9.	Solid-state photoluminescence of anthracene-containing materials	145
5.9.1.	Photoluminescence study of anthracene adsorbed on SiO_2	145
5.9.2.	Photoluminescence study of silicas with immobilized anthracene	148
5.9.3.	3D UV spectra of anthracene-based silicas	150
5.10.	Conclusions of the chapter 5	153
6.	Graphene-based materials	154
6.1.	Synthesis approach	154
6.2.	Nitrogen adsorption-desorption measurements	155
6.3.	SEM	156
6.4.	Fluorescence spectroscopy	157
6.5.	Raman spectroscopy	158
6.6.	FTIR characterization	159
6.7.	MAS ^{13}C NMR spectroscopy of $\text{SiO}_2(4)\text{-GOQDs}$.	160
6.8.	XPS spectroscopy	161
6.9.	Electrochemical application of $\text{SiO}_2(4)\text{-GOQDs}$	163
6.9.1.	Critical information about analytes	163
6.9.2.	Electrochemical properties of the carbon paste electrode modified with $\text{SiO}_2(4)\text{-GOQDs}$	164

6.10. Conclusions of the chapter 6	167
7. Carbon Dots based materials	168
7.1. CDs prepared without nanoreactor approach	168
7.2. Synthesis and optical properties of CDs	168
7.3. XRD of CDs, TEM and AFM microscopy	173
7.4. FTIR characterization	174
7.5. Raman	175
7.6. Adsorption study of CDs on silica-based support	176
7.7. Effect of adsorbent dose	178
7.8. Adsorption isotherms	179
7.9. Isothermal adsorption equilibrium study	180
7.10. Desorption assay	182
7.11. Preparation of adsorbent	183
7.12. Adsorption study of organic dye onto silica-based materials	184
7.13. Carbon Dots obtained from nanoreactor approach	187
7.14. Morphological properties of host silicas	187
7.15. Preparation of silica-based@ nanocomposite	188
7.16. Thermochemical treatment of $\text{SiO}_2\text{-NH}_2\text{@CA}$	191
7.17. Synthesis of $\text{SiO}_2\text{@CDs}$, $\text{SiO}_2\text{-NH}_2\text{@CDs}$ and $\text{SiO}_2\text{-EDA@CDs}$	192
7.18. Characterization of silica-based@CDs composites	192
7.19. FTIR spectroscopy	192
7.20. XPS spectroscopy	195
7.21. Photoluminescence of solid composites $\text{SiO}_2\text{@CDs-T}$.	198
7.22. Elution of CDs from the host	201
7.23. Characterization of CDs	204
7.24. Microscopy	204
7.25. Photoluminescence of CDs obtained in nanoreactors	208
7.26. Quantum Yield	211
7.27. Conclusions for Chapter 7	213
8. Application of nanocomposites for SPE preconcentration of anthracene	215
8.1. Adsorption of anthracene on SPE cartridges from the organic mobile phase	215
8.2. Anthracene adsorption from mixed-solvent systems	219
8.3. Adsorption of anthracene from solution with interfering compounds	221
8.4. Conclusion for Chapter 8	227
9. General conclusions	229
10. Future work	232
11. References	233
12. Attachment	257
A Published papers	257
B Participation in Congress	259
Oral presentation	259
Poster presentation	259

List of figures

Figure 1 - Structure of the solid phases	51
Figure 2 - Reaction of 1-pyrenecarboxylic acid on aminosilicas representing π - π stacking (excimer) and monomeric emission, adapted from [200]	54
Figure 3 - A piece of a honeycomb lattice of graphene displaying both zigzag and armchair edges and AA (a), AB (b) and ABC (c) stacking of graphene layers ..	56
Figure 4 - The chart of graphene synthesis	57
Figure 5 - The earliest structural models of GO	62
Figure 6 - Lerf – Klinowski model of GO (Adatped to [145])	63
Figure 7 - CDs evolution based on a bottom-up approach	70
Figure 8 - General scheme of the nanoreactor approach	74
Figure 9 - Scheme of synthesis of CDs using a nanoreactor approach	96
Figure 10 - Schematic diagram of SPE adsorption study	103
Figure 11 - Schematic illustration of reaction ninhydrin and salicylaldehyde with aminated silica gel	106
Figure 12 - Digital photographs of aminosilica gel (a), after reaction with ninhydrin (b) and salicylic aldehyde (c)	107
Figure 13 - Formation Ruheman's complex on aminated silica gel	107
Figure 14 - N_2 adsorption-desorption isotherms of pristine silica gels (a, b) and modified with amino-groups (c, d)	108
Figure 15 - The incremental pore size distribution of silica and aminopropyl silica gels	110
Figure 16 - SEM images of pristine silica gel $SiO_2(4)$ (a), $SiO_2(11)$ (b) and Asil (c)	110
Figure 17 - Solid-state ^{13}C NMR spectrum of SiO_2 -EDA	111
Figure 18 - FTIR spectra of aerosil and aminated silica gel	112
Figure 19 - Survey (a, d) and fitted XPS spectra of the C1s (b, e) and N1s (c, f) regions corresponding to $SiO_2(4)-NH_2$ (a, b, c) and $SiO_2(11)-EDA$ (d, e, f)	113
Figure 20 - Protonation of aminopropyl groups fixed on silica surface	114
Figure 21 - The formation degrees of different amine-species on the surface at different pH of solutions	115
Figure 22 - TGA thermograms of aminosilicas	117
Figure 23 - Schematic illustration of reaction ninhydrin and salicylaldehyde with aminated silica gel	120
Figure 24 - Digital photo of $SiO_2(4)$ (A) and $SiO_2(4)-SH$ (B) after reaction with sodium nitroprusside in alkaline medium	121
Figure 25 - N_2 adsorption-desorption isotherms of pristine silica gels and modified with mercaptopropyl-groups	122
Figure 26 - FTIR spectra of aerosil and silica gel with mercaptopropyl groups	123
Figure 27 - Plots of electrical conductivity of suspensions of $SiO_2(4)-SH(n)$ versus added sodium chloride	124
Figure 28 - TGA thermograms of aminosilicas	125
Figure 29 - The summarized scheme of synthesis of the anthracene-based silica gels	128
Figure 30 - Plot of consumed quantity of 9CMA by aminated silicas at different synthesis time (points – experiment; lines-model of pseudo-second-order)....	131
Figure 31 - N_2 adsorption-desorption isotherms of $SiO_2(6)$ -Ant-1-t (a), $SiO_2(9)$ -Ant-1-t (b), $SiO_2(11)$ -Ant-1-t (c), aerosil-based materials (d)	134

Figure 32 - N ₂ adsorption–desorption isotherms of SiO ₂ (11)-Ant-3b, SiO ₂ (11)-Ant-4b, SiO ₂ (11)-Ant-5b	134
Figure 33 - Plots of relative changes of S _{BET} during synthesis.....	135
Figure 34 - ¹³ C CP/MAS NMR solid state spectrum of SiO ₂ (11)-EDA derivatives; (*) - Spinning sidebands.....	137
Figure 35 - FTIR spectra on Asil-Ant-1-t.....	138
Figure 36 - High-resolution C1s spectra of aminopropyl and anthracene-based silica gel (a) and N1s spectrum of anthracene-based silica gel (b).....	139
Figure 37 - High resolution C1s spectra of SiO ₂ -EDA and reduced imine anthracene silica gels	140
Figure 38 - TGA thermograms of pristine aminopropyls and anthracene-based silica gels	141
Figure 39 - Photoluminescence spectra of anthracene solution before and after adsorption, exc 360 nm (solvent=ethanol, V=5 mL, m=300 mg, time=120 min)	146
Figure 40 - Normalized PL spectra of solid bulk samples of SiO ₂ (6)@Ant, exc=340 nm, T=298K, m=100 mg	147
Figure 41 - PL intensity of solid sample of silica gels with introduced anthracene at different concentrations without heating (T=298K) and after heating at 323K, exc=340 nm	148
Figure 42 - Scheme of silica gel surface modified with anthracene groups	148
Figure 43 - Normalized PL spectra of solid Asil-Ant-1-t (a) and SiO ₂ (11)-Ant-1-t (b), exc=340 nm	149
Figure 44 - Solid 3D Photoluminescence spectra of Asil-1-Ant-15 (a), Asil-1-Ant-360 (b), Asil-1-Ant-1440 (c) and normalized spectra of Asil-1-Ant-t (d)	151
Figure 45 - Solid 3D Photoluminescence spectra of SiO ₂ (11)-1-Ant-15 (a), SiO ₂ (11)-1-Ant-240 (b), SiO ₂ (11)-1-Ant-1440 (c) and normalized spectra of SiO ₂ (11)-1-Ant-t (d).....	152
Figure 46 - Solid 3D Photoluminescence spectra of SiO ₂ (9)-Ant-1-15 (a), SiO ₂ (9)-Ant-1-1440 (b), normalized spectra of SiO ₂ (9)-1-Ant-t (c) and absolute spectra of SiO ₂ (9)-1-Ant-t (d) excited at 5eV.....	152
Figure 47 - Effect of washing on c(Mn) in supernatants (a) and monitoring of electrical conductivity with water washing (b)	155
Figure 48 - N ₂ adsorption/desorption isotherms of SiO ₂ (4)-NH ₂ (blue curve) and SiO ₂ (4)-GOQDs (red curve)	156
Figure 49 - SEM images of GO(a) and SiO ₂ -GOQDs (b).....	157
Figure 50 - Photoluminescent spectra of solid samples SiO ₂ (4)-NH ₂ (black line) and SiO ₂ (4)-GOQDs (red line) under excitation light at 340 nm	157
Figure 51 - Raman spectra of GOQDs (—) and SiO ₂ -GOQDs (- -).....	158
Figure 52 - FTIR spectra of GOQDs, SiO ₂ -NH ₂ , SiO ₂ -GOQDs	159
Figure 53 - CP/MAS ¹³ C NMR spectrum of SiO ₂ -GOQDs	160
Figure 54 - Survey (a) and fitted XPS spectra of the C1s (b) and N1s (c) of SiO ₂ -GOQDs and pristine SiO ₂ -NH ₂ with deconvoluted data regions corresponding to SiO ₂ -NH ₂ and SiO ₂ -GOQDs	161
Figure 55 - Schematic structure of surface layer in SiO ₂ -GOQDs	162
Figure 56 - Chemical structure of the tested analytes	164
Figure 57 - DPV analysis of sulfamethoxazole (SMZ) and trimethoprim (TMP) on modified with SiO ₂ -GOQDs (black line) and bulk (red line) carbon paste electrodes. The analytes were presented in a mixture (5:1) with next concentration of SMZ: 4.0, 8.0 and 20 µmol L ⁻¹ of SMZ and bulk test at 4.0 µmol L ⁻¹ of SMZ	165

Figure 58 - DPV analysis of DES (a) and ET (c) on modified with SiO ₂ -GOQDs (black line) and bulk (red line) carbon paste electrodes. Concentration of the analytes: DES - 0.15, 0.30 and 0.52 $\mu\text{mol L}^{-1}$ (black lines) and 0.15 $\mu\text{mol L}^{-1}$ (red line), ET - 0.014, 0.027, 0.062 $\mu\text{mol L}^{-1}$ (black lines) and 0.014 $\mu\text{mol L}^{-1}$ (red line). Supporting electrolyte: 0.04 mol L ⁻¹ of BRbs (pH 5.8), 0.5 mol L ⁻¹ of NaNO ₃ .	166
Figure 59 - UV-vis spectra of the neutralized solution of melted CA.....	169
Figure 60 - UV-Vis spectra of CDs-170 and CDs-200 at pH 5.....	170
Figure 61 - Normalized PL spectra of CDs-170 (a) and CDs-200 (b) with different excitation wavelengths; the relationship between excitation and an emission wavelength of PL spectra (inset a,b)	171
Figure 62 - PL spectra of CDs-170 (a) and them absorbance dependence (b) at different pH and influence of concentration of CDs on absorbance (c) and PL (d)	172
Figure 63 - PL spectra of CDs-200 in NaCl aqueous solution and effect of NaCl content on PL intensity of peak maximum (insets)	173
Figure 64 - TEM (a) with HRTEM (a,inset), AFM image (b) with length profiles (c) of CDs-170 and XRD pattern of CDs-200 (d)	174
Figure 65 - FTIR spectrum of CDs-170	175
Figure 66 - Raman spectrum of solid CDs-200	175
Figure 67 - Effect of pH on percentage removal of CDs-170 (a) and CDs-200 (b) by SiO ₂ (6)-NH ₂ , SiO ₂ (6), SiO ₂ (6)-SH(2) (initial concentration = 80 dilution, adsorbent dosage: 5 g L ⁻¹ , contact time: 120 min).....	177
Figure 68 - Effect of NaCl concentration on percentage removal of CDs-170 (a) and CDs-200 (b) by SiO ₂ (6)-NH ₂ (adsorbent dosage: 5 g L ⁻¹ , contact time: 120 min, pH 5).....	177
Figure 69 - Solid-state 3D PL spectra and its excitation-emission-intensity spectra of CDs-170 adsorbed on SiO ₂ (6)-NH ₂ at pH=1 (a), pH=4 (b), pH (7).....	178
Figure 70 - Effect of adsorbent mass on percentage removal of CDs-170 in (C ₀ =5.0 mmol L ⁻¹ , total volume: 10 ml, pH =5, contact time: 120 min)	179
Figure 71 - Evaluation of adsorption CDs-170 (a) and CDs (b) depends on adsorbent	180
Figure 72 - Adsorption isotherms of CDs-170 (a) and CDs-200(b) by silica-based adsorbents (adsorbent dosage: 5 g L ⁻¹ , contact time: 120 min, pH 5). The solid lines are Langmuir model simulation; the dashed lines are Freundlich model simulation; the dotted lines are Temkin model simulation.....	181
Figure 73 - CDs-170 loading on aminosilica before and after desorption (a) and desorption degree after heating (b)	183
Figure 74 - FTIR spectra of pristine aminosilica gel and with CDs loading	183
Figure 75 - Chemical structures of MB and its UV-Vis spectrum	184
Figure 76 - Effect of pH on the equilibrium adsorption capacity of MB onto SiO ₂ (9), SiO ₂ (9)-NH ₂ and SiO ₂ (9)-NH ₂ /CDs-170 (C ₀ =1.56 mmol L ⁻¹ , m=50 mg, V=10 mL)	185
Figure 77 - Adsorption isotherms of MB by silica-based adsorbents (m=50 mg, V=10 mL, contact time: 120 min, pH 7). The solid lines are Langmuir model simulation; the dashed lines are Freundlich model simulation.....	186
Figure 78 - SEM images of rSiO ₂ @CA (a), SiO ₂ (11)@CA (b), pristine SiO ₂ (11) (c) and CA content on SiO ₂ (9)-NH ₂ @CA after 0-4 of washing cycles with ether (bottom axis) and further thermal treatment (upper axis) (d)	190
Figure 79 - EDS elemental mapping of silicon (a) and carbon (b) on SiO ₂ -NH ₂ @CA	191

Figure 80 - FTIR spectra of $\text{SiO}_2(6)@\text{CDs-180}$, $\text{SiO}_2(6)\text{-NH}_2@\text{CDs-180}$ and $\text{SiO}_2(6)\text{-NH}_2$	193
Figure 81 - FTIR spectra of CDs-150-10h and composites $\text{SiO}_2(11)\text{-EDA}@\text{CDs-150-600}$, $\text{SiO}_2(11)\text{-EDA}@\text{CDs-180-600}$	194
Figure 82 - Survey (a) and high resolution fitted XPS spectra (b, c) of $\text{SiO}_2(6)@\text{CDs-180}$ in O1s (b) and C1s (c) regions	195
Figure 83 - Survey (a, d) and fitted XPS spectra of the C1s (b, e) and N1s (c, f) regions corresponding to $\text{SiO}_2(4)\text{-NH}_2$ (a, b, c) and $\text{SiO}_2(4)\text{-NH}_2@\text{CDs-720}$ (d, e, f).	197
Figure 84 - Atomic percentage from the survey (a) and fitted XPS spectra of the C1s corresponding to CDs-150-600 , $\text{SiO}_2(11)\text{-EDA}@\text{CDs-150-600}$, $\text{SiO}_2(11)\text{-EDA}@\text{CDs-180-600}$, $\text{SiO}_2(11)\text{-EDA}$	198
Figure 85 - Normalized PL spectra of $\text{SiO}_2(d)@\text{CDs-t}$	198
Figure 86 - Photoluminescence spectra of $\text{SiO}_2(9)@\text{CDs-t}$ for different time of the thermal treatments (a), and changes of photoluminescent intensity versus time (b)	199
Figure 87 - 3D photoluminescent spectra and excitation-emission map of $\text{SiO}_2(6)@\text{CDs-180}$ (a, b)	200
Figure 88 - Normalized PL spectra of $\text{SiO}_2(4)\text{-NH}_2@\text{CDs-t}$ (a) and $\text{SiO}_2(9)\text{-NH}_2@\text{CDs-t}$ (b) obtained after the different time (t, min) of the thermal treatment of $\text{SiO}_2(d)\text{-NH}_2@\text{CA}$	200
Figure 89 - Normalized PL spectra of $\text{SiO}_2(11)\text{-EDA}@\text{CDs-T-t}$ obtained after the different time (t, min) and the thermal treatment (T, °C) of $\text{SiO}_2(11)\text{-EDA}@\text{CA}$	201
Figure 90 - (a) Electroconductivity of the supernatant solution obtained after immersing of $\text{SiO}_2(4)@\text{CDs-60}$ (0.5 g) to 10 ml of water with further filtration and cycling the procedure; (b-d) UV-VIS spectra of the supernatant solutions, obtained by successive treatment of $\text{SiO}_2(4)@\text{CDs-60}$ with water (b), $0.1 \text{ mol L}^{-1} \text{ NaHCO}_3$ (c), $3 \text{ mol L}^{-1} \text{ NaOH}$ (d) after different time of the thermal treatment.	202
Figure 91 - Scheme of C-dots formation form CA encapsulated in $\text{SiO}_2\text{-NH}_2$ pores.	204
Figure 92 - TEM and HRTEM (in insets) images with the size distribution profiles of water extracted CDs (a, b) and CDs obtained by dissolution of $\text{SiO}_2(4)\text{-NH}@\text{CDs-240}$ (c, d) and $\text{SiO}_2(11)\text{-NH}@\text{CDs-600}$ (e, f)	206
Figure 93 - AFM images (left), height distribution (upper right) and profile (lower right) of the CDs obtained from $\text{rSiO}_2@\text{CDs}$ (a) and $\text{SiO}_2(4)@\text{CDs-180}$ (b) after their elution with water	207
Figure 94 - AFM images and height profiles of CDs eluted from $\text{SiO}_2(11)\text{-NH}_2@\text{CDs-600}$	208
Figure 95 - Photoluminescence emission spectra of the first supernatant obtained by the washing of $\text{SiO}_2(d)@\text{CDs-t}$ with water (a-c), and normalized PL spectra of $\text{SiO}_2(d)@\text{CDs-60}$ for d= 4, 9, and 11 (d)	209
Figure 96 - PL spectra of water extracted CDs(a) and CDs (b) obtained after removing of solid support in $\text{SiO}_2(d)\text{-NH}_2@\text{CDs}$ and $\text{SiO}_2(11)@\text{CDs}$ (inset). The excitation wavelength of 340 nm	210
Figure 97 - Normalized PL spectra of CDs-200(a) and CDs after etching of $\text{SiO}_2(4)\text{-NH}_2@\text{CDs-240}$ (b)	210
Figure 98 - PL spectra of CDs after etching of $\text{SiO}_2(11)\text{-EDA}@\text{CDs-180-600}$	211
Figure 99 - Integrated PL intensity (black line) and QY (red line) of extracted CDs-150 (sphere) and CDs-180 (square) at different pH.	213

Figure 100 – Adsorption of anthracene from MeCN in dynamic conditions on various SPE cartridges: a) the breakthrough curves, b) dynamic adsorption capacity of SPE the cartridges, c) adsorption rate (R, %). The adsorbent mass 200 mg, anthracene concentration $1 \cdot 10^{-5} \text{ mol L}^{-1}$	216
Figure 101 - Adsorption of anthracene from acetone in dynamic conditions on various SPE cartridges: a) the breakthrough curves, b) dynamic adsorption capacity of SPE the cartridges, c) adsorption rate (R, %). The adsorbent mass 200 mg, anthracene concentration $1 \cdot 10^{-5} \text{ mol L}^{-1}$	217
Figure 102 - Adsorption of anthracene from MeCN:H ₂ O=50:50 with pH=3.0 in dynamic conditions on various SPE cartridges: a) the breakthrough curves, b) dynamic adsorption capacity of SPE the cartridges, c) adsorption rate (R, %). The adsorbent mass 200 mg, anthracene concentration $1 \cdot 10^{-5} \text{ mol L}^{-1}$	219
Figure 103 - Adsorption of anthracene from MeCN:H ₂ O=50:50 with pH=6.0 in dynamic conditions on various SPE cartridges: a) the breakthrough curves, b) dynamic adsorption capacity of SPE the cartridges, c) adsorption rate (R, %). The adsorbent mass 200 mg, anthracene concentration $1 \cdot 10^{-5} \text{ mol L}^{-1}$	221
Figure 104 - Dynamic adsorption of anthracene from $2 \cdot 10^{-5} \text{ mol L}^{-1}$ MY solution in MeCN:H ₂ O=50:50 with pH=3.0, contaminated with $1 \cdot 10^{-5} \text{ mol L}^{-1}$ of anthracene: a) the breakthrough curves, b) dynamic adsorption capacity of SPE the cartridges, c) adsorption rate (R, %). The adsorbent mass 200 mg, anthracene concentration $1 \cdot 10^{-5} \text{ mol L}^{-1}$	222
Figure 105 - Dynamic adsorption of anthracene from 1% solution of sunflower oil in acetone, contaminated with $1 \cdot 10^{-5} \text{ mol L}^{-1}$ of anthracene: a) the breakthrough curves, b) dynamic adsorption capacity of SPE the cartridges, c) adsorption rate (R, %). The adsorbent mass 200 mg, anthracene concentration $1 \cdot 10^{-5} \text{ mol L}^{-1}$	224
Figure 106 – Composition of the immobilized layer on SiO ₂ -Ant adsorbents	226
Figure 107 - Dynamic adsorption of anthracene from 1% solution of sunflower oil in heptane, contaminated with $1 \cdot 10^{-5} \text{ mol L}^{-1}$ of anthracene: a) the breakthrough curves, b) dynamic adsorption capacity of SPE the cartridges, c) adsorption rate (R, %). The adsorbent mass 200 mg, anthracene concentration $1 \cdot 10^{-5} \text{ mol L}^{-1}$	227

List of tables

Table 1 - Physical characteristics of 16 EPA Priority PAHs	33
Table 2 - Extraction and chromatographic conditions during PAHs analysis of samples with high lipid content.....	41
Table 3 - SPE adsorbent for organic compounds from different matrices	46
Table 4 - Applications of some carbon-based adsorbent in SPE	50
Table 5 - Peculiarities of CDs synthesis in mesoporous organo-mineral materials..	78
Table 6 - Summary of representative acids and green synthetic precursors for CDs preparation.....	79
Table 7 - Important characteristics of N-containing CDs	81
Table 8 - Commercial information about silica gel.....	89
Table 9 - The textural characteristics of the obtained materials.....	109
Table 10 - The results of C1s and N1s XPS spectra for SiO ₂ (4)-NH ₂ and SiO ₂ (11)- EDA	114
Table 11 - The results of modeling by polydentate binding	115
Table 12 - The results of elemental analysis	116
Table 13 - The estimated concentrations of selected samples by TGA	118
Table 14 - Concentrations of immobilized aminogropus.....	119
Table 15 - The density of binding sites and average intermolecular distance between neighboring groups in hybrid nanoparticles.....	119
Table 16 - The textural characteristics of the obtained materials.....	122
Table 17 - The results of elemental analysis	124
Table 18 - The estimated concentrations of selected samples by TGA	125
Table 19 - Concentrations and density of immobilized groups	126
Table 20 - Identification of the anthracene-containing silicas and their descriptions	127
Table 21 - The parameters of kinetic modeling for anthracene modified silica gel.	132
Table 22 - The textural characteristics of the obtained materials.....	136
Table 23 - The estimated concentrations of selected samples by TGA	142
Table 24 - The results of elemental analysis	142
Table 25 - Matrix model to calculate the concentration of SiO ₂ (6)-NH-Ant-1440 ...	143
Table 26 - Summarized information about concentrations of grafted Ant and density of immobilized groups	144
Table 27 - The textural characteristics of the obtained materials.....	156
Table 28 - XPS results of SiO ₂ (4)-NH ₂ and SiO ₂ (4)-GOQDs	162
Table 29 - The isotherm parameters for the adsorption of CDs onto silica gel modified with aminopropyl groups.....	182
Table 30 - Linear partition coefficient of CDs on aminated silicas	182
Table 31 - The isotherm parameters for the adsorption of MB onto silica-based materials	186
Table 32 - Morphological characteristics of silica templates and the concentration of immobilized amines.	188
Table 33 - Overview of the host samples used for the preparation of CDs from citric acid precursor	192
Table 34 - QY of CDs obtained from SiO ₂ (4)@CDs-720, SiO ₂ (d)-NH ₂ @CDs-t by single-point method.....	212
Table 35 - QY at 350 nm of water extracted CDs from SiO ₂ (11)-EDA@CDs-T-t...	212

Table 36 - Parameters of SPE cartridges used for dynamic adsorption of anthracene.	218
Table 37 - Dynamic adsorption parameters from the breakthrough curves	220
Table 38 - Dynamic adsorption parameters from the breakthrough curves	223
Table 39 - Dynamic adsorption parameters from the breakthrough curves	225

List of abbreviations

9CMA	9-(chloromethyl)anthracene
9ACA	9-Anthracenecarboxaldehyde
AIEE	Aggregation induced emission enhancement
AIEQ	Aggregation induced emission quenching
Ant	Anthracene
APTES	(3-aminopropyl)triethoxysilane
ATRP	Atom transfer radical polymerization
AFM	Atomic force spectroscopy
ASE	Accelerated solvent extraction
Asil	Aerosil
BAs	Biogenic amines
BaP	Benzo[a]pyrene
BSSE	Basis set superposition error
CA	Citric acid
CDs	Carbon Dots
CDs-170	CDs prepared at 170 °C
CDs-200	CDs prepared at 200 °C
CH	Cyclohexane
CHN	Elemental analysis
CMG	Chemically modified graphene
CNTs	Carbon nanotubes
CPE	Carbon paste electrode
CTAB	Cetyltrimethylammonium bromide
CVD	Chemical vapor deposition
Cys	L-cysteine
DAD	Diode-array detector
DCC	N,N'-dicyclohexylcarbodiimide
DES	Dietilestilbestrol
DFT	Density functional theory
DIPEA	N,N-Diisopropylethylamine
DVP	Differential pulse voltammetry
DXR	Doxorubicin hydrochloride
EA	Ethanolamine
ED	endocrine disruptor
EDA	Ethylenediamine
EDAS	N-[3-(Trimethoxysilyl)propyl]ethylenediamine
EDC	1-ethyl-3-(3-dimethylaminopropyl)-carbodiimide
EDS	Energy-Dispersive Spectroscopy

EELS	Electron Energy Loss Spectroscopy
EIT	Electron transfer
EPA	The US Environmental Protection Agency
ER	Eley-Rideal process
ET	Estriol
FLD	Fluorescence detector
FLG	Few-layer graphene
FID	Flame ionization detection
FRET	Fluorescence resonance energy transfer
FTIR	Fourier transform infrared
G	Graphene
GC	Gas chromatography
GO	Graphene oxide
GTO	Graphite oxide
GOQDs	Graphene oxide quantum dots
HATU	2-(7-aza-1H-benzotriazole-1-yl)-1,1,3,3-tetramethyluronium hexafluorophosphate
HMTA	Hexamethylenetetramine
HILIC	hydrophilic interaction liquid chromatography
HMW	High molecular weight
HPLC	High-performance liquid chromatography
HRTEM	High-resolution TEM
IFE	Inner filter effect
IGO	Improved graphene oxide
LAH	Lithium aluminium hydride
LH	Langmuir- Hinshelwood process
LD50	The median lethal dose
LLE	Liquid-liquid extraction
LMG	Leucomalachite green
LMW	Light molecular weight
LOD	Limit of detection
LOQ	Limit of quantification
MA	Myristic acid
MB	Methylene blue
MG	Malachite green
MS	Mass spectrometry
MIP	Molecularly imprinted polymer
MNPs	Magnetic nanoparticles
MLG	Multilayer graphene
MP	Mobile phase
MProP	Metalloprotoporphyrins

MPTMS	(3-Mercaptopropyl)trimethoxysilane
MWCNT	Multiwall carbon nanotubes
MOFs	Mesoporous metal-organic frameworks
NMR	Nuclear magnetic resonance
Oasis HLB	Copolymer of N-vinylpyrrolidone and divinylbenzene
ODS	Octadecylsilane
PAHs	Polycyclic aromatic hydrocarbons
PC	Paper chromatography
PCDD	Polychlorodibenzo-p-dioxin
PDMS	Polydimethylsiloxane
PEA	Phenylethylamine
PhDA	Phenylenediamines
PL	Photoluminescent
PMMA	Poly(methyl methacrylate)
PNIPAAm	Poly(N-isopropylacrylamide)
PVA	Poly (vinyl alcohol)
PLE	Pressurized liquid extraction PLE
PNIPAAm	Poly(N-isopropylacrylamide)
PPT	Photo-induced proton transfer
PUFAs	Polyunsaturated essential fatty acids
rGO	Reduced graphene oxide
SDD	Silicon drift detector
SEM	Scanning electron microscope
SFE	Supercritical fluid extraction
SMZ	Sulfametoxazol
STM	Scanning tunnelling microscope
SIM	Selected ion monitoring
SiO ₂	Silica gel
SiO ₂ (d)- Ant-1-t*	Organosilica with nominal pore size d = 6, 9 and 11 nm), having immobilized anthracene fragments obtained by N-alkylation of SiO ₂ -NH ₂
Asil-Ant-1-t	Non-porous silica having immobilized anthracene fragments obtained by N-alkylation of Asil-NH ₂
SiO ₂ (11)- Ant-2a	Organosilica with nominal pore size 11 nm, having immobilized anthracene fragments obtained by condensation of SiO ₂ -NH ₂ with 9-aldehyde derivatives of anthracene
SiO ₂ (11)- Ant-2b	The same as SiO ₂ (11)-Ant-2a after reduction with NaBH ₄
SiO ₂ (11)- Ant-3a	The same as SiO ₂ (11)-Ant-2a but SiO ₂ -EDA have been used instead of SiO ₂ -NH ₂
SiO ₂ (11)- Ant-3b	The same as SiO ₂ (11)-Ant-3a after reduction with NaBH ₄

SiO ₂ (11)-Ant-4a	Anthracene-containing silane was obtained from EDAS by condensation with 9-aldehyde derivatives of anthracene and further silane immobilization on silica
SiO ₂ (11)-Ant-4b	The same as SiO ₂ (11)-Ant-4a after reduction with NaBH ₄
SiO ₂ (11)-Ant-5b	The same as SiO ₂ (11)-Ant-4a but silane synthesis was performed in diglyme with a further reduction of the product by NaBH ₄
TEM	Transmission electron microscopy
TGA	Thermogravimetric analysis
TLC	Thin-layer chromatography
TMP	Trimetoprim
TOF	Time of flight mass spectrometer
TEOA	Triethanolamine
TPCA	5-Oxo-3,5-dihydro-2H-thiazolo[3,2-a] pyridine-7-carboxylic acid
TPP	Tetraphenylporphyrin
USAE	Ultrasound-assisted solvent extraction
USAEME	Ultrasound-assisted emulsification–microextraction
RP	Reversed-phase
QY	Quantum yield
XAD-2	Styrene-divinylbenzene adsorbent
XRD	X-ray diffraction
XPS	X-ray photoelectron

1. Introduction

1.1. Thesis proposal

Many biologically active as well as ecologically hazardous compounds contain aromatic or heterocyclic fragments in their molecules. They can be highly toxic, such as pesticides and polycyclic aromatic hydrocarbons (PAHs), or demonstrate highly attractive properties such as polyphenolic antioxidants, antibiotics, hormones. In both cases, the identification and quantification of such types of compounds in complex multicomponent matrices is a challenge for modern analytical chemistry. Sample preparation with subsequent determination of the target compounds by gas chromatography, high-performance liquid chromatography, electrophoresis or voltammetry is a modern approach in chemical analysis of traces of organic compounds and contaminants.

The identification of the aromatic content is based mainly on real environmental samples. The extremely low concentrations in the environment and the complexity of their matrices make a determination as challenging tasks. The sample cannot be applied to the chromatograph in its original form. Because of this complex the trace analysis in body fluids is more complicated than trace analysis in surface water in environmental chemistry. Isolation of PAHs from biological matrices is necessarily needed. Sample preparation often involves complicated and laborious extraction and clean up procedures to provide extracts ready for accurate analytical determination [1–7]. Unfortunately, PAH extracts are not pure and inevitably contain substantial amounts of other compounds that may hinder the subsequent determination. Solid-phase extraction (SPE) helps to avoid such interferences. This approach allows us to pre-concentrate and to separate the analytes from the matrix. It is less time-consuming and solvent-consuming than traditional extraction methods. The selectivity of SPE cartridge provided by the corresponding adsorbent with a specific affinity to the target group of compounds. For sample pretreatment in environmental analysis, the commercial adsorbents (C8, C18 or Oasis HLB etc.) have been widely used [8–12]. To date, the selection of the adsorbents suitable for selective preconcentration of aromatic compounds is very limited. Existing SPE cartridges adsorb the target analytes due to dispersion (hydrophobic), ion-exchange or dipole-dipole interactions, which does not

allow them to be used for selective preconcentration of aromatic and heterocyclic compounds. For that reason, the search for new extraction solid materials for SPE is still highly relevant.

A significant difference between aromatic and other hydrophobic compounds is a system of π -bonds. It is known that conjugated polycyclic compounds demonstrate a tendency to form π - π molecular complexes with aromatic compounds. Thus, covalent immobilization of such compounds on the carrier surface can result in the adsorbent having increased affinity to aromatic compounds. Matrix of oil and fat samples has triacylglycerols and fatty acids. These components have polarities similar to that of PAHs, but aromatic (or unsaturated) moieties are different. Taking it into account, separation of PAHs from lipid medium can be implemented using a separation principle based on π -interactions. The main role in this process is assigned to the specific adsorbent capability of making π - π interactions with PAHs molecules. Modified silica gel is key to successful problem-solving. Silica gel is ideal support for SPE. It provides considerable properties such as high chemical and thermal stability and most importantly its easy modification by a wide range of functional groups. In this case, the functional group must contain electron-rich rings. The derivatives of graphene perfectly fit this condition. An enormous specific surface area (theoretical value is $2630 \text{ m}^2 \text{ g}^{-1}$) and the large delocalized π -electron system of graphene can provide a strong affinity for ring structures in PAHs [13, 14]. Another approach is adsorbent with excimer-forming functional groups [15, 16]. Complex formation between the immobilized fluorophore and PAH molecule is a way of monitoring the PAHs binding.

In the present work three types of solid materials were developed and can be used as adsorbents for SPE of aromatic compounds in the presence of other types of hydrophobic components in the matrix.

In the thesis, anthracene having three conjugated aromatic cycles was used as a π -donor ligand for immobilization on mesoporous silica gel. Also, recently discovered carbogenic nanodots have a large number of conjugated aromatic cycles and thus they can also form molecular π - π complexes with aromatic analytes. Hence graphene oxide quantum dots (GOQDs) and carbon dots (CDs) were also selected for immobilization

on the silica surface. In contrast to anthracene, GOQDs and CDs are not PAH and contain different amounts of carboxyl and carbonyl groups, which can significantly reduce the density of delocalized π -electrons, and thus results in changing of the macromolecule properties from π -donor to π -acceptor. Three sets of adsorbents with different arrangements of anthracene derivatives were obtained using surface assembling reactions and their properties were compared with that one obtained in one step silanization reaction. Silica gel nanocomposites with immobilized CDs were obtained by two different approaches. For the first one, the CDs were obtained from the molecular precursor and then immobilized on silica. For the second method, CDs were prepared “in situ” directly in silica gel pores. This method was developed by us for the first time and allows better control of the particle size and composition. The effects of silica gel modification, pore size, synthesis time, hydrolytic stability, carbon nanoparticle size and quantum yield of the luminescence were studied. The nanocomposite with immobilized GOQDs was obtained by covalent immobilization of nanoscale GO fragments obtained by ultrasonic decomposition of GO in silica pores.

The adsorption properties of the materials were studied in dynamic and static SPE modes for the model compounds: methylene blue, and anthracene in various aqueous-organic and organic mobile phases, in the presence of interfering components.

Also, silica-immobilized GOQDs was used for electrochemical analysis of selected antibiotics and hormones such as estriol, diethylstilbestrol, sulfamethoxazole, and trimethoprim.

1.2. Thesis structure

This thesis is structured in nine chapters. In Chapter 2, a bibliographical review is made to present the theoretical basis on PAHs-derivatives, carbon nanomaterials namely graphene-derivative and carbon nanodots. This part divided into three sections according to nature of the materials and focusing on the aromatic properties, analysis of aromatic compounds, synthesis, characterization, and application of PAHs-derivatives, graphene-derivatives and carbon dots in analytical chemistry as adsorbent and sensors.

Chapter 3 contains detailed information on materials and instrumentation used in this work, preparation of modified silica gel materials and carbon dots. Extraction

procedure, the equation for different calculations as the concentration of grafted functional groups, modelling of surface protonation process, isotherm and kinetic adsorption.

The results are presented in the next four chapters (4, 5, 6 and 7) each referring to one of the synthesized materials with their characterization. A partial conclusion regarding each chapter is also presented. Chapter 4 is referred to the overall studies of modified silica support such with different organosilanes such as aminopropyl, ethylenediamine and mercaptopropyl. Characterization of interface silica surface mainly was carried out by FTIR, NMR, XPS, N₂ adsorption desorption isotherms, SEM, CHN, TGA analyses, especially to confirm modification of silica gel and estimate number of functional groups.

Chapter 5 is referred to as the overall studies of silica gel modified with anthracene groups. Different synthetic approaches were presented. Results of the kinetic study, textural and morphological properties, NMR, FTIR, XPS, CHN analyses were presented. In addition, the photoluminescence properties of solid materials modified with anthracene moieties were carried out.

Chapter 6 is related to results of characterization and application in the electrochemical analysis of silica gel modified with graphene oxide quantum dots. Data used in this chapter was used to prepare the manuscript for submission to the journal. Information about analytes and differential pulse voltammogram for detection of selected antibiotics and hormones.

The results are presented in Chapter 7 referred to materials published in two articles [17, 18], Attachment A, related to the development of photoluminescent CDs from silica-based nanoreactor. In addition, information about CDs prepared by pyrolysis CA at two selected temperatures and their adsorption onto silica-based support was presented. Adsorption study of aromatic dye as methylene blue by silica gel with adsorbed CDs was demonstrated.

Chapter 8 contains the results of the dynamic adsorption study of anthracene onto SPE tubes packed with synthesized our samples.

Finally, in chapter 9 the overall conclusion of the thesis.

1.3. Objective of the thesis

1.3.1. General objective

The objective of the current research is preparation of new silica-based hybrid materials having covalently immobilized carbon-containing molecular and nanoscale systems with delocalized π -electrons that can be used as adsorbents and electrodes for preconcentration and determination of aromatic compounds. The idea is based on the fact that organic compounds with aromatic fragments have a tendency to form supramolecular complexes with other conjugated polycyclic compounds. Thus, covalent immobilization of conjugated polycyclic compounds on the carrier surface can result in the adsorbents having specific selectivity to aromatic compounds in solution. To verify this idea, we developed several methodologies for covalent immobilization of polycyclic aromatic compounds on the silica surface. Three different objects having different sizes of enriched π -electron systems were selected: 1) anthracene – polycyclic aromatic molecule with three conjugated benzene rings, having size about 0.75 nm; 2) carbon nanodots – carbogenic nanoparticles presumably with sp^2 planar polycyclic system and average size 5 nm; and 3) graphene oxide quantum dots (GOQDs), carbogenic nanoparticles similar to CDs but with average size up to 100 nm. It was expected that by changing the immobilized object size we can control the affinity of the analyte to the adsorbent. Availability and orientation of π -donor systems on the carrier surface are also important for the analytical properties of the adsorbent. Therefore, three sets of anthracene-containing organo-silicas were obtained using the reaction of surface assembling. Silica gel nanocomposites with immobilized CDs were prepared by two different approaches.

The adsorption properties of the materials were studied in dynamic and static modes for the model compounds: methylene blue and anthracene in various aqueous-organic and organic mobile phases, in the presence of interfering components and in real object – vegetable oil. Also, electrochemical properties of graphite paste electrode modified with silica with immobilized GOQDs have been studied for voltammetric analysis of selected antibiotics and hormones having aromatic rings.

1.3.2. Specific objectives

In order to fulfil the project objectives, the next task should be elaborated:

1. Implement covalent immobilization of organic silanes on silica gel surface for a further anchoring of π -conjugated fragments, and particularly:
 - a. Immobilization of aminopropyl silane,
 - b. Immobilization of ethylenediamine silane,
 - c. Immobilization of mercaptopropyl silane;
2. To develop the methodology for surface-assembling preparation of anthracene-immobilized silicas from the organo-silicas listed in § 1a-c, having different pore size and next precursors:
 - a. 9-aldehyde anthracene,
 - b. 9-chloromethyl anthracene;
 - c. Develop synthesis of anthracene-containing silane for its further immobilization on silica gel surface;
 - d. Study anthracene-immobilized silicas by various methods in order to characterize their composition, porous structure, fluorescence properties, evaluate excimer formation between two neighboring anchoring anthracene group;
3. Develop a procedure for preparation and immobilization of GOQDs on silica surface and particularly:
 - a. Preparation of graphene oxide from graphite,
 - b. Preparation of graphene oxide quantum dots (GOQDs),
 - c. Immobilization of GOQDs on aminosilica gel;
 - d. Characterize surface functionality and composition of the materials, their morphological and textural properties, the concentration of functional groups;
4. Study the process of CDs synthesis in nanoreactors and particularly:
 - a. Functionality of silica nanoreactor;
 - b. Nanoreactor size;
 - c. Conditions of synthesis;
 - d. Releasing of as-prepared CDs,
 - e. Study of optical properties of obtained silica composites and CDs;
5. Develop procedures for preparation and immobilization of CDs on silica surface and particularly:

- a. Study of CDs formation in a “bottom-up” approach from citric acid;
- b. Study adsorption of CDs on silica-based materials, listed in § 1a-c;
6. Investigate the adsorption properties of the prepared adsorbents for model contaminants:
 - a. In static mode, in adsorption of methylene-blue dye and anthracene;
 - b. In dynamic mode, in adsorption of anthracene from acetonitrile, acetone and heptane solutions as well as from acetonitrile-water media;
 - c. Study of anthracene removal from the model solution of myristic acid in acetonitrile-water media;
 - d. Study of anthracene removal from a sample of vegetable oil;
7. Investigate electroanalytical properties of carbon paste electrode modified with GOQDs immobilized on silica surface in differential pulse voltammetric determination of:
 - a. Antibiotics such as sulfamethoxazole and trimethoprim
 - b. Endocrine disruptors, such as diethylstilbestrol (DES) and estriol (ET).

2. Theoretical Part

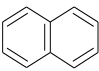
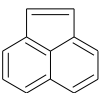
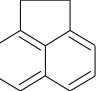
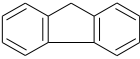
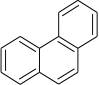
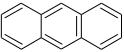
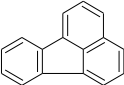
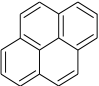
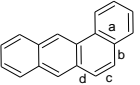
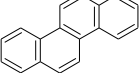
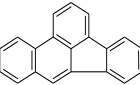
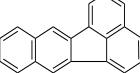
In this part, we will discuss recent achievements in adsorbents preparation investigation and their application for pre-concentration of various organic compounds and particularly about endocrine disruptors such polyaromatic hydrocarbons, environment antibiotics and hormones. Composition, the origin of production, toxicity and environmental impact of the pollutions was also discussed together with an overview of modern methods of their analysis.

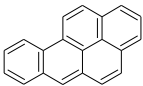
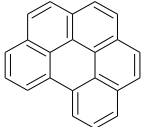
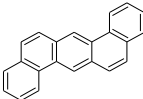
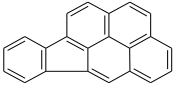
2.1. Polyaromatic hydrocarbons and their derivatives

2.1.1. Sources of PAHs, environmental risk

PAHs are environmental pollutants group containing two or more fused aromatic rings. These pollutants are highly stable and widely spread in various matrices, such as water, soil or dust particles. Presence PAHs in the environment is an important risk factor for various health aspects not only for marine animals but also for human. It has been proved that some PAHs can cause carcinogenic and mutagenic effects. In 1984, The US Environmental Protection Agency (EPA) has declared 16 unsubstituted PAHs as priority pollutants [19]. The list of priority PAHs varies in different countries. In the United States, the EPA has listed 16 priority PAHs (Table 1) [20]. Benzo[e]pyrene and the four benzo[a]fluoranthene isomers all have a molecular weight (MW, g mol⁻¹) of 252.3, but are much less potent carcinogens than benzo[a]pyrene (BaP).

Table 1 - Physical characteristics of 16 EPA Priority PAHs

Compound	Abbr. ¹	Structure	MW, g mol ⁻¹	Log K _{OW} ²	Log K _{OC} ²	TEF ³	LD ₅₀ ³ , mg kg ⁻¹
Naphthalene	Nap		128.1	3.37	2.97	0.001	Rat 1250 Mice 580 Guinea pig 1200
Acenaphthylene	Ace		152.1	4.00	3.40	0.001	Rat 1700 Mice 3000
Acenaphthene	Acp		154.2	3.92	3.65	0.001	Rat 600 Mice 2100
Fluorene	Fl		166.2	4.18	3.86	0.001	Mice 2000
Phenanthrene	Phe		178.2	4.57	4.15	0.001	Rat 1800
Anthracene	Ant		178.2	4.54	4.15	0.01	Rat 430
<u>Fluoranthene</u>	Flu		202.3	5.22	4.58	0.001	Rat 2000
Pyrene	Pyr		202.3	5.18	4.58	0.001	Rat 2700 Mice 800
<u>Benzo(a)anthracene</u>	BaA		228.3	5.91	6.14	0.1	Rat 200
<u>Chrysene</u>	Chr		228.3	5.65	5.30	0.01	Rat 320
<u>Benzo(b)fluoranthene</u>	BbF		252.3	5.80	5.74	0.1	Mice 72
<u>Benzo(k)fluoranthene</u>	BkF		252.3	6.00	5.74	0.1	Mice 2820

<u>Benzo(a)pyrene</u>	BaP		252.3	6.04	6.74	1	Mice 10
Benzo(ghi)perylene	BghiP		276.3	6.50	6.52	0.01	n. r.
<u>Dibenzo(ah)anthracene</u>	DbA		278.4	6.75	6.20	5	n. r.
<u>Indeno (1,2,3-cd)pyrene</u>	InP		276.3	7.66	6.20	0.1	n. r.

¹ abbreviation;

² Kow and Koc from [14];

³TEF – toxicity equivalent factors from [17, 30];

⁴LD50 – the median lethal dose from [31];

n.r. – non-reported.

Alkylated PAHs may have greater toxicity than the parent compound [21]. The general characteristics of PAHs are high melting and boiling points (therefore they are solid), low vapor pressure (tends to decrease with increasing molecular mass), and very low aqueous solubility, which both tend to decrease with increasing molecular weight (Table 1).

The circulation of PAHs in the environment depends on their properties. In the atmosphere, PAHs can undergo photo-degradation and react with other pollutants, such as sulfur dioxide, nitrogen oxides, and ozone [22]. The pollutants can be formed during biological processes and as products of incomplete from either natural combustion sources (forest and brush fires) or man-made sources (automobile emissions and cigarette smoke) [22].

Sources of PAHs include emissions from industrial activities, such as primary aluminium and coke production, petrochemical industries, rubber tire and cement manufacturing, bitumen and asphalt industries, wood preservation, commercial heat and power generation, and waste incineration. Water-courses can be chronically contaminated through industrial discharges, wastewater treatment plants, marine oil spills and that's why filter-feeding organisms, such as bivalve molluscs, can accumulate high concentrations of PAHs [2]. Therefore, PAHs are typically more concentrated near urban centers. Atmospheric deposition is the main reason for finding them in soil. PAHs are capable to stick tightly to particles and move through the soil to

contaminate underground water [23]. The organic pollutants entering the marine ecosystem become bioavailable to native organisms via the food chain as waterborne compounds and from contaminated sediments. Due to accumulation and lipophilic nature, PAHs contents of fish tissue may be much higher than PAHs contents of the water in which they live [24]. The residue levels of PAHs in aquatic organisms also depend on the ability of these organisms to metabolize the contaminants.

PAHs are introduced into the human body through the gastrointestinal tract, respiratory tract and skin [8]. But it has been confirmed that the main source of exposure for a human is through food. Fish constitutes an important source of proteins, minerals, vitamins and unsaturated essential fatty acids (PUFAs), especially omega-3 PUFAs. However, light molecular weight PAHs (LMW, up to five rings) PAHs are able to taint fish and shellfish and render them unfit for sale. Due to the low metabolization capability of fish, fish oils could contain elevated levels of these lipophilic pollutants [25]. PAHs are transported into all tissues of the human body containing fat. They can accumulate by repeated and long-term exposures. The main quantity is stored in fat, liver and kidneys, while smaller amounts in the spleen, adrenal glands, and ovaries [22]. The concentration of PAHs varies greatly from raw to processed foodstuffs [26]. Raw foods should usually not contain high levels of PAH. After cooking of foods (drying, smoking, grilling, roasting, frying) concentration of pollutants is increased ($200 \mu\text{g kg}^{-1}$ in smoked fish and meat, when $3 \mu\text{g kg}^{-1}$ in uncooked shellfish from an unindustrialized area of Japan) [1].

Fats and oils are most contaminated with these substances due to the lipophilic nature [27]. Contamination of vegetable oils usually occurs during technological processes like direct fire drying. On the other hand, decolourization with carbon or clay and bleaching reduce PAH content during the production of refined oils.

Fish are exposed to PAHs both via uptake across gill surfaces and from their diet [1, 23, 26, 28]. Shellfish are preferred for monitoring because PAHs concentrations are generally higher in their tissues [2]. The blue mussel (*Mytilus edulis*) occurs in shallow waters along almost all coasts of the Northeast Atlantic. It is, therefore, suitable for monitoring in nearshore waters. Levels of BaP in mussels from the Campanian Sea ($1.5 \mu\text{g kg}^{-1}$) were higher than the Ionian Sea (Italy) [29], but it was under the established

limit [30]. There are advantages in the use of molluscs for this purpose because they are sessile. They, therefore, reflect contamination in the local area to a greater degree than fish, which are mobile. LMW PAH ($0.1 \mu\text{g kg}^{-1}$) concentrations in bream of the river Elbe was determined [28]. These results are similar to observation for fish from Lake Ontario [28]. It has been shown that vertebrate fish rapidly metabolize PAH to intermediates that either bind to liver DNA or form conjugates for ultimate transfer to bile. The experiment with BaP has shown that the concentrations of this compound in the liver are approximately 100 times higher than that in muscle [24]. Because fish metabolize PAHs rapidly, measurement of tissue PAH concentrations by standard analytical techniques is generally not a useful method for assessing exposure that's why alternative chemical and biological methods have been developed including the study of bile metabolites, DNA adducts and CYP1A (cytochrome P450-associated enzymes (CYP) in the liver) that have been applied to Puget Sound fishes [31].

2.1.2. Sample pre-treatment in PAHs determination

Because of their mutagenic and carcinogenic nature, determination PAHs in a variety of matrices has become an important task. Nowadays accurate quantification and removal of polyaromatics from objects with predominant lipid composition is a challenge for researchers. The obstacles are the low concentration of an analyte in a complex matrix and time-consuming sample preparation before chromatographic determination. The main limit of known analysis is sample preparation. Commonly, it consists of an extraction, a clean-up and an enrichment step prior to chromatographic determination [28, 32, 33]. Extraction and cleanup are often exhausting, long and solvent-consuming procedures. Aim of these multi-steps procedures is to separate PAHs from the rest of lipids. Unfortunately, in complex matrix each step can be led to insufficient recovery and/or contamination, so to improve the result of extraction, a combination of different methods is admissible. Most extraction methods for PAHs are based on the release of compounds due to interaction with a selected solvent.

Less visible stages, and often neglected, are sampling and storage. Plastic materials must not be used for sampling and storage because of possible adsorption of the PAHs onto the container material [2]. As mentioned earlier, PAHs are sensitive to photodegradation. Direct sunlight or other strong light must be avoided during the

storage of the samples and sample preparation. The practice of drying the raw material, before oil extraction, by direct contact with combustion gases can greatly increase the PAHs content [34].

Classical ways to remove lipid matrix before injection into chromatographic equipment are divided into Soxhlet extraction, caffeine complexation [28], alkaline hydrolysis (saponification), followed by liquid-liquid extraction (LLE) with an organic solvent [35]. Nowadays, pressurized liquid extraction (PLE) [27, 36], ultrasonic-assisted extraction [37] accelerated solvent extraction (ASE) [5] and subcritical water extraction [38], supercritical fluid extraction (SFE) [39] have been developed as alternative techniques to replace classical extraction methods.

During liquid-liquid partitioning, oil samples are dissolved in an organic solvent (cyclohexane, *n*-hexane) and PAHs extracted with dimethylsulphoxide [28], dichloromethane (DCM) [40] or a 9:1 mixture of dimethylformamide (DMF) and water [41], while the fat matter remains in the organic layer [7]. Separation is performed by dilution with water in order to alter their coefficients of partition between the two phases.

A relatively rapid method for determining PAHs in lipid medium based on the phenomenon of caffeine-PAH complex was described [28]. PAHs can be selectively extracted by vigorous shaking in a caffeine-formic acid solution. Subsequently, the caffeine-PAH complexes are decomposed with 2% aqueous NaCl and then PAHs are extracted with cyclohexane (CH).

The extract obtained with one of the methods above described usually contains substantial amounts of material other than PAH. They may interfere with the following analytical determination. Different clean-up procedures, such as thin-layer chromatography (TLC) and column chromatography on different adsorbent materials are traditionally applied [23]. Generally, silica gel, alumina, Florisil and Sephadex LH-20 are used as classical adsorbent materials in columns packed. The column with the sample is eluted with CH, and then a first fraction containing more alkanes is discharged while the PAH fraction is collected, leaving the coloured substances and more polar compounds in the column. Unfortunately, these columns give not always reproducible results.

Welling and Kaandorp compared an LLE procedure in combination with column chromatography on Amberlite XAD-2 adsorbent and the caffeine-formic acid complexation method [33]. XAD-2 is a styrene-divinylbenzene adsorbent that usually uses to extract hydrophobic compounds. The XAD-2 method showed better repeatability and simplicity and was selected for the determination of PAHs in 14 different vegetable oils. Total PAH in salad oils varied from 5.7 to 44.5 $\mu\text{g kg}^{-1}$; two corn-oil samples appeared to be heavily contaminated with PAHs (240 and 81.7 $\mu\text{g kg}^{-1}$).

Moret and co-workers [37, 42] compared the extraction procedures (saponification and LLE with CH and DMF–water) on an olive oil sample. Sample purification was performed by modern SPE and PAHs have been determined by high-performance liquid chromatography (HPLC) with spectrofluorometric detection. The degree of purification for each approach was not equivalent. The single saponification method was not effective because of the appreciable residue of unsaponifiable matter. The liquid-liquid partition method showed a higher purification power. Combination with SPE clean-up step resulted to be the best method with recoveries ranged between 42.5 and 92.2%, depending on molecular masses of PAHs.

Another type of extraction is SFE. It is a fast preparation technique which facilitates automation of the preliminary operations of the analytical process [39]. The ability to adjust the solvent power of the supercritical fluid (usually CO_2) simply by changing the pressure and temperature makes SFE extremely selective and suitable for selective extraction. In [7] successfully SFE system coupled on-line with a fluorimetric detector to determine PAHs was applied. PAHs were selectively extracted by silica gel in the thimble and cleaned up by passage through a C18 column. Interferences were retained by the silica gel during the SFE process, while PAHs were adsorbed in the C18 column and the remainder of the matrix is sent to waste. In this work, the limit of detection (LOD) ranged from 12 to 16 $\mu\text{g kg}^{-1}$.

Yebra-Pimentel proposed ultrasound-assisted solvent extraction (USAE) and ultrasound-assisted emulsification–microextraction (USAEME) for determining 11 PAHs in fish oil. The recoveries ranged from 70% to 100% by USAE and from 70%

to 108% by USAEME with estimated quantification limits (LOQ) between 0.020 and 2.6 $\mu\text{g kg}^{-1}$ were achieved.

2.1.3. Analytical methods for PAHs determination.

Analytical determination of PAH after sample preparation step has usually been carried out by HPLC coupled to fluorometric or ultraviolet light detection, or through high-resolution capillary gas chromatography (GC) coupled to flame ionization detection (FID) or mass spectrometry (MS) [43].

Progenitors of modern GC and HPLC techniques were semi-quantitative procedures based on paper chromatography (PC) and TLC, followed by ultraviolet (UV) detection or fluorescence spectroscopy. TLC is commonly used only for identifying individual compounds, such as BaP, during screening. PAHs possess very characteristic UV absorbance spectra. This is especially useful in the identification of PAHs. Most PAHs are also fluorescent, emitting characteristic wavelengths of light when they are excited. These features help to perform quantification in solution by spectrophotometric or spectrofluorimetric methods. The scrubbed substance spot from the TLC plate can be extracted or *in situ* analyzed by scanning spectrofluorimetry [44].

Capillary GC with MS allows detection of known and unknown PAHs at the same time and low concentration. Weak polar stationary phase such as OV-1701 (50% Diphenyl, 50% Dimethylpolysiloxane) provided better separation than the traditionally recommended SE-54 (5% Phenyl, 1% Vinyl, 94% Methyl Polysiloxane). Among injection techniques, the ones most often utilized are splitless and cold on-column injection, the latter being the most precise for PAHs quantification [45]. GC-MS cannot be used for identifying the thousands of unresolved components, and FID represents, in this case, the only way of quantitating hydrocarbons of unknown identity [37].

When parent non-substitute PAHs are predominated, HPLC is the preferable technique. The availability of special column materials for the HPLC-PAHs analysis eliminated its most important disadvantage, namely poor resolution. HPLC offers lower resolution efficiency in separating low-molecular-mass PAHs, reversed-phase (RP) columns can readily separate a number of PAHs isomers that are difficult to make by GC [46]. The most widely used columns with C18, polystyrene divinylbenzene

groups employing acetonitrile-water or methanol-water mobile phase and gradient elution. Like a lot of PAHs exhibit strong fluorescence, wavelength-programmed fluorescence detection in combination with HPLC now provides a rapid and less cumbersome way of analysis and represents the most powerful technique for what concerns sensitivity and selectivity (comparable only to that obtained with gas GC-MS in selected ion monitoring (SIM)) [33]. HPLC technique has also the advantage to allow detection of HMW PAHs which cannot be detected by GC methods because of the thermal decomposition occurring at high temperatures [47].

The PAHs analysis is time-consuming and unsuitable for routine work, as they do not permit analysis of a large number of samples per day. HPLC silica column is able to retain a large number of triglycerides (at least 100 mg) [9]. The highly purified PAH fraction eluting from the silica column can be collected, concentrated, and injected off-line into the second HPLC unit [9] or transferred on-line to the second HPLC column via a solvent evaporator is able to reconcentrate the large fraction coming from the first column [10]. In [1] was proposed more simple procedure without an additional HPLC pump for sample preparation and used large silica cartridges (5 g) that retains large amounts of an extra virgin olive oil sample (300 mg) by an eluent mixture of n-hexane-DCM 70:30 v/v. The PAH fraction was eluted in a smaller volume by increasing the percentage of dichloromethane in the eluent mixture.

The sample preparation approaches for PAHs analysis with some quantitative results are reported in Table 2.

2.2. Adsorbent for solid-phase extraction of aromatic compounds

The basic dynamic SPE procedure consists of loading a solution onto a solid phase (usually a cartridge containing the sorbent) capable of retaining the target analytes, washing away undesired components, and washing off/eluting the desired analytes with another solvent into a collection tube [59]. Previously, conditioning the solid-phase materials is needed to increase the effective surface area and reduce interferences.

Table 2 - Extraction and chromatographic conditions during PAHs analysis of samples with high lipid content

Sample	Extraction	Purification	Determination	Chromatographic column	LOD/LOQ	Ref
Vegetable oil (olive)	SFE	silica gel + C18 column	LC-FLD	Ultrabase C18, (250mm x 4.6mm i.d., 5 µm particle size)	12–16 µg kg ⁻¹	[7]
Virgin olive oils	LLE with DMSO-water and CH	SPE on silica gel cartridge (500mg)	HPLC-SFE	n. r.	0.012-1.4 µg kg ⁻¹	[48]
Olive oils	LLE with DMF-water and CH	Silica gel column + GPC on S-X3 column	GC-MS	A DB-5 50-m fused silica column	Total PAH 54.4–110.8 µg kg ⁻¹	[28]
Smoked oysters in oil					BaP 75.8 µg kg ⁻¹ (in oil), 12.2 µg kg ⁻¹ (in meat)	[28]
Fish	Ultrasonication	Teflon syringe filters; PSA, C18 and magnesium sulfate mixture; diatomite	LC-UV	non-polar column YMC PAH (250 mm x 3.0 mm; 5 mm)	BaP, µg kg ⁻¹ 0.225 (cormorant); 0.0752 (herring); 0.063 (cod)	[8]
Olive oil	SPE (silica5g)		HLPC-UV	C18 column 250x3mm i.d., 5 µm particle size;	BaP 0.1 µg kg ⁻¹	[34]
Coconut oil (from Sri Lanka)	SPE		HPLC-FLD	Chromosphere PAH column 20 cm*3 mm i. d.	Total PAH 399 µg kg ⁻¹ (coconut oil); 60 µg kg ⁻¹ (sun-dried copra)	[42]
Vegetable oils	LLE with DMF-water and CH	XAD-2 column	HPLC-FLD	Column: 25 cm x 4.6 mm, Vydac 201 TP PAH, Chrompack,	Total PAH - 5.7-44.5 µg kg ⁻¹ (salad oils); 8.3-243.7 µg kg ⁻¹ (corn-oil)	[33]
	Caffeine complexation and extraction with CH	SPE				[33]
Vegetable oils	GPC (Bio-Beads S-X3, 200–400 mesh)	SPE	GC-MS	DB-5MS 50-m column, 0.25mm i.d., 0.25 mm film thickness	0.2-1.5 µg kg ⁻¹	[43]
Edible oil	Saponification+LLE with DCM and n-hexane	SPE	GC-FID	ZB-5MS column 30 m x 0.25 mm i.d. x 0.25 µm film thickness	0.1 µg kg ⁻¹ (Phe) 0.4 µg kg ⁻¹ (BkF)	[40]

Coconut kernel	Soxhlet extraction with CH	SPE	HPLC-FLD	Chromospher PAH column 20 cmx3 mm i.d.	Coconut oil BaP - 12 $\mu\text{g kg}^{-1}$, total PAH - 102 $\mu\text{g kg}^{-1}$ (in copra)	[49]
Fish	Accelerated solvent extraction	GPC and silica gel-alumina (2:1) column	HPLC-DAD-FLD	Supelcosil LC-PAHs column, 3.0mm i.d.x250mm, 5 μm particle size	Total LMW PAHs 70.4-281 $\mu\text{g kg}^{-1}$ (bighead carp), 27.1-191 $\mu\text{g kg}^{-1}$ (silver carp), HMW PAHs 23.6-232 $\mu\text{g kg}^{-1}$ (bighead carp), 14.4-210 $\mu\text{g kg}^{-1}$ (silver carp)	[37]
Mussel (from Campania, Italy)	Saponification (KOH/EtOH)	SPE	HPLC-FLD	C18 column 2.1mmx50mm, 1.8 μm particle size	BaP-0.3- 9.3 $\mu\text{g kg}^{-1}$	[29]
Oyster (from Urdaibai estuary, Spain)	Static AUE		HPLC-FLD	Hypersil Green PAH column 200 mmx4.6 mm; 5 μm particle size	BaP-0.96 $\mu\text{g kg}^{-1}$, total PAHs 306.6 $\mu\text{g kg}^{-1}$	[5]
Soybean oils (from Campinas, Brazil)	LLE with DMSO-water and CH	SPE	HPLC-FLD	A C18 Vydac 201 TP column 250x4.6 mm; 5 μm particle size	BaP - 1-15.8 $\mu\text{g kg}^{-1}$; the mean levels individual PAHs ranged 0.2 - 26.1 $\mu\text{g kg}^{-1}$	[50]
Fish liver (from European lakes)	Soxhlet extraction	Al ₂ O ₃ chromatographic column	GC-MS	HP-5MS capillary 50 m x 0.25 mm i.d. 0.25 mm film thickness	Total PAH 2.1 - 65.4 $\mu\text{g kg}^{-1}$	[24]
Vegetable oils		SPE	HPLC-2xFLD-UV	C18 column Supelcosil LC-PAH 250x3mm i.d, 5 μm particle size	BaP 1.2-2.4 $\mu\text{g kg}^{-1}$	[51]
Smoked fish	PLE		GC-MS	40m ZB-5 capillary column 0.18mm i.d x 0.25 μm film)	n.r.	[27]
Liquid smoke	ASE	GPS SPE and	GC-MS	DB5-ms cross-linked 5%-phenyl-methyl-siloxane capillary column 60 m x 0.25 mm i.d., 0.25 μm film thickness	Mean BaP 120 $\mu\text{g kg}^{-1}$	[52]
Fish oil	USAE	SPE	LC-FLD	Supelcosil LC-PAH, 25 cm x 4.6 mm, 5.0 μm	Total PAHs 35 $\mu\text{g kg}^{-1}$	[25]
	USAEME				Total PAHs 28 $\mu\text{g kg}^{-1}$	

SPE has two important functions. The first is that the analytes can be concentrated by elution in a small amount of solvent. The second is the clean up of the sample. The advantages of using the method are that small volumes of the solvent are needed, and operation time is short. The main limitation associated with this approach is usually the low selectivity of the generic SPE sorbents. The lack of selectivity has important consequences.

The choice of the sorbent is a crucial step in SPE. The adsorbent is the core of extraction procedure and it controls parameters such as selectivity, affinity and adsorption capacity. The most common and classic material used as sorbent media in SPE is chemically bonded silica, usually with a C8 or C18 [53] organic group, carbon or ion-exchange materials, the polymeric materials based on styrene-divinylbenzene.

Wide progress of SPE has been achieved due to the introduction of numerous new types of packings. These materials consist mainly of chemically bonded phases, prepared on the base of silica gel. Selection of a suitable ligand is important as each ligand contains different functional groups, and hence has a different affinity for the target analytes, especially if the analyte is aromatic compounds.

Polymers with low to a modest degree of crosslinking swell in many non-polar solvents and then cease functioning as adsorbents. The Russian research group have focused the study on hyper-crosslinked polystyrene-type ($S_{BET} > 1000 \text{ m}^2 \text{ g}^{-1}$) adsorbent that allows selective extraction and pre-concentration of the aromatic compounds from non-polar media and fatty matrices [12, 54]. The extraction of 4-6-rings PAHs from vegetable oil was practically quantitative with recoveries varied from 70 to 102 % and for smoked fish samples 50-95 %. A practically zero baseline in the "blank test" was achieved by the replacement of polypropylene cartridge to glass cartridge [54].

As a rule, polar materials can be used to remove polar analytes from hexane extracts, but they cannot be employed if the analytes are non-polar. Hence, most of the classical adsorbents for SPE are unsuitable for pre-concentration of aromatic contaminants in these circumstances. Alkyl-silica (C1–C18) does not adsorb non-polar compounds from non-polar solvents. It is possible to overcome the problems with non-aqueous matrix if the analytes and contaminating compounds with similar polarities have different aromatic (or unsaturated) moieties it may be possible to separate them

from each other using a separation principle based on π -interactions. The leading role of π -interactions in retention and separation of various aromatic compounds in the charge-transfer mode of hypercrosslinked neutral polystyrene SPE adsorbent in combination with hexane-based eluents was demonstrated [55].

Introduction of a very stable molecule with an aromatic character such as porphyrin was a successful approach to the preparation of selective adsorbent for PAHs. It was achieved by modification of the commercially Amberlite XAD-2 and XAD-4 resins [56]. Recoveries were determined to be 90.8% to 104.9%.

Various metaloporphyrins (MProP) covalently linked to silica are examined as stationary phases for reversed-phase HPLC separation of PAHs [57]. The MProP-silicas is shown to exhibit extraordinary shape selectivity for planar over non-planar PAHs, with the selectivity factors for the triphenylene/o-terphenyl solute pair approaching 30 on Cu^{II} ProP-silica phases using 100% acetonitrile as the mobile phase. Shape selectivity and solute retention are highly dependent on the metal ion within the center of the immobilized protoporphyrin (ProP) structure in accordance with the following sequence: $\text{Cu(II)} > \text{Fe(III)} > \text{Ni(II)} > \text{Zn(II)} \approx \text{Cd(II)}$. The capacity factor of chrysene on a column packed with tetraphenylporphyrin (TPP)-silica (surface coverage $0.35 \mu\text{mol m}^{-2}$) using acetonitrile:water (60:40 v/v) as mobile phase is ~ 2.6 , while the value is ~ 3.4 on ProP-silica (surface coverage $0.61 \mu\text{mol m}^{-2}$) using 100% acetonitrile as mobile phase.

Extraction based on magnetic sorbent received some attention in recent years. Magnetite (Fe_3O_4) and magnetite ($\gamma\text{-Fe}_2\text{O}_3$) are usually represented as the core of a magnetic material. The magnetic adsorbent is dispersed in a sample solution containing the target analytes instead of loading into a cartridge [58]. This avoids limited mass transfer and/or blocking cartridges that sometimes can occur in traditional SPE. In general, magnetic NPs (MNPs) are easily separated by using an external magnet without additional centrifugation or filtration of the sample solution. This makes the sample treatment procedure easier and faster. However, pure iron-oxide NPs can easily form large aggregates [59]. The coating can help to avoid this limitation. Surface modification stabilizes the NPs and prevents their oxidation. The modifying ways applied to MNPs can be divided into two major groups by coating with inorganic

components (silica) or organic molecules (octadecylsilane (ODS), polymer or surfactant). The second route is more effective in adsorption and separation of hydrophobic substances than the first one. Alkyl (C10–C18) carboxylates chemisorbed on the MNPs were used to extract carcinogenic PAHs from environmental water samples prior to analysis by HPLC-FLD [60]. Mechanism of binding organic compounds achieved via hydrophobic and π -cation interactions.

The new nanosize SPE methods and sorbent were applied to pre-concentrate PAHs [60]. The structure of the proposed sorbent was presented as cetyltrimethylammonium bromide (CTAB) coated titanate (0.2 mm thick, 20×20 mm size) nanotube array. Surfactant-coated TiO₂ nanotube surface became hydrophobic, which played an important role in the adsorption of nonionic organic compounds onto the sorbents. The highest retention for all analytes was obtained when the sample pH was near to pH 7.

A miniature version of SPE is called solid-phase microextraction (SPME). SPME fibre, namely, Carboxen Z/polydimethylsiloxane (PDMS), is suitable for PAHs extraction from vegetable oils and lipid extracts due to a high affinity for planar compounds [61]. The mechanism of extraction of this fibre is related to the π - π interaction between the carbon surface and the planar compounds. The best absorption results of PAHs were given by diluting 200 μ L of oil with hexane volume of 1.5 mL. In the sample of oil extracted from olive pomace concentration BaP (0.5 μ g kg⁻¹) was less than in the oil extracted from olive pomace after being dried (16.1 μ g kg⁻¹).

Eight hydrazone-based silica sol-gel adsorbents were prepared for selective extraction of biogenic amines (BAs) from orange juice using SPME [62]. The most hydrophobic ligand (with symmetrical benzene rings) achieved the highest extraction capability due to an enhancement of π - π interaction with the analytes. Additional polar hydroxyl group allows increasing of electrostatic force but did not achieve sufficient extraction efficiency.

According to review [63], Oasis HLB sorbent (copolymer of N-vinylpyrrolidone and divinylbenzene) was applied independently for purification of wide classes of aromatic compounds (pesticides, antibiotics, PAHs, Illicit drugs) because of

hydrophobic and hydrophilic properties simultaneously. Due to the variety of compounds being retained, Oasis HLB and some SPE sorbents are not expected to be selective for a unique type of molecule.

Nevertheless, till today silica-based adsorbents suitable for selective pre-concentration of PAHs from organic media have not yet developed, Table 3. Particularly essential problem is to extract PAHs in the large excess of fatty acids and from the matrix with high lipid content.

Table 3 - SPE adsorbent for organic compounds from different matrices

Adsorbent	Analyte	Sample	Method	Sample volume, ml	Extraction time, min	Massa of adsorbent, mg	Ref
ProElut C18+ProElut PSA (Ethylenediamino-N-propyl)	PAHs	flowers, fruits, and seeds	SPE-GC-MS/MS	20	30	1000	[64]
ProElut C18+ProElut Florisil (Magnesium-silica gel)+ProElut PSA (Ethylenediamino-N-propyl)	PAHs	leaves and barks		20	30	1000	
ProElut PSA (Ethylenediamino-N-propyl)	PAHs	roots and stems		20	30	500	
Carbopack Z/PDMS (graphitized carbon black)	PAHs	vegetable oils	SPME-GC×GC-TOF-MS	1.5	30	n. r.	[65]
Strata C18-E	PAHs	Smoked salmon, frankfurter, steak, and pork chop fish oil	SPE-UHPLC-MS/MS	1.2	2	n. r.	[56]
PSA+SAX	PAHs	coffe	dSPE/LL E-GC-SIM-MS	6	3	150	[66]
molecularly imprinted polymer (MIP)+graphitized carbon black (GCB)	PAHs	vegetable oils	SPE-GC/MS/MS	6	30	500	[54]
MTMOS-TEOS	OPPs	water/fruit	SPE-GC/MS	10	30	100	[67]
hydrazone-based silica	BAs	orange juice	μ-SPE-HPLC-UV	10	20	20	[68]

Fe ₃ O ₄ -ODS	fat-soluble vitamins (Ergocalciferol, tocopherol, phytonadione)	Fruit juice-milk beverage	SPE-CLC-UV-Vis	2	30	20	[168]
Fe ₃ O ₄ -hemimicelle of alkyl (C10-C18) carboxylates	PAHs	Surface and Ground Waters	SPE-HPLC-FLD	350	15	200	[69]
C30 silica	PAHs	airborne particulates	SPE-GC-MS	n. r.	20	500	[70]
Oasis HLB	Drugs	Fish tissues	SPE-UHPLC-UV	350	30	500	[71]
Hypercrosslinked polystyrene	PAHs	Sunflower oil and smoked fish	SPE-HPLC-FLD	10	10	500	[72]
Amberlite XAD-2 - Protoporphyrin IX	PAHs	Soil	SPE	50	50	10	[73]
TiO ₂ nanotube-CTAB	PAHs	Environmental water	μ -SPE-HPLC-UV	10	60	200	[74]

2.3. Interaction between aromatic compounds

Aromatic components can offer a variety of binding interactions, including the formation of hydrogen bonds via their π -system, π - π interactions and cation- π interactions [75]. Polyaromatic groups are capable of forming T-shaped arrangements allowing edge-to-face interactions as well as parallel-displaced arrangements allowing π - π stacking interactions. Aromatic partners may also form charge-transfer complexes under parallel alignments. These π - π stacking interactions are affected by the electrostatics of component atoms in addition to the geometric alignment of molecular dipoles. These contributing factors determine how the π -systems interact and thus affect the strength of the π - π interaction based on the stacking geometry. Perhaps the strongest interaction arising from aromatics occurs between cation- π conjunction with the aromatic face of the π system [76].

The nature of the aromatic components is important in determining the strength of the interaction. Strong cation- π binding occurs with presence of electron-donating groups [77]. Additionally, hydrophobic complementarity has the tendency of non-polar groups to associate in an aqueous medium. In general, this phenomenon results in the minimization of contact between non-polar and polar regions.

It was described below that graphene sheets can be stacked into bilayers and multilayers by virtue of π - π interactions between the neighbouring sheets. The stacked graphene segments can be held together in different orientations by π - π interactions.

PAHs with only benzenoid hexagonal rings can be viewed as fragments of a graphene sheet with the peripheral atoms saturated with hydrogen. The binding energy between PAHs and graphene materials is strongly dependent on the size of the PAH, stacking order and on the number of stacked layers [78].

According to computer calculation, the binding energies of PAH molecules adsorbed in the interior and at the edge of graphene electrodes get larger as the number of carbon and hydrogen atoms contained in the PAH molecule increases. The adsorption geometry and the binding energy of several typical PAH molecules on the graphene which made up of linearly fused benzene rings were investigated [68].

When these polyacenes adsorb on the surface of an infinite graphene layer, the AB stacking is always the most stable structure. The binding energies (E_{bind} , eV (kcal mole⁻¹)) have been computed by taking into account basis set superposition error (BSSE) corrections are 0.45 (10.38) (benzene), 0.73 (16.83) (Nap), 0.98 (22.60) (Ant), 1.23 (28.36) (tetracene) and 1.48 (34.13) (pentacene). Thus, the binding energies of polyacenes on the graphene surface increase linearly following the increase of the number of fused benzene rings and illustrated by plotting the binding energies per carbon atom as a function of the ratio of hydrogen to carbon in these polyacenes [79]. The resulting equation is

$$E_{\text{bind}} = N_C \cdot E_{\text{CC}} + N_H \cdot (E_{\text{CH}} - E_{\text{CC}})$$

with parameters $E_{\text{CC}} = 51.8 \text{ meV}$ and $E_{\text{CH}} = 76.4 \text{ meV}$, in which N_C and N_H are, respectively, the number of carbon atoms and the number of hydrogen atoms in each PAHs.

When angular PAH molecules adsorb on the graphene surface in AB stacking manner, E_{bind} , eV (kcal mole⁻¹), obtained by including BSSE corrections are 0.97 (22.37) (Phe), 1.22 (28.13) (Chr), 1.23 (28.36) (benz[a]anthrene), and 1.32 (30.44) (BaP). Comparing with linear molecules, the molecular configuration has only a minor influence on the binding energies of linear and angular PAH molecules. For example, chrysene, benz[a]anthrene, and tetracene are isomers, and the difference of their

calculated E_{bind} is less than 0.01 eV (0.23 kcal mole⁻¹), but as the number of carbon and hydrogen atoms in PAHs increases, E_{bind} in the AB stacking manner always increase.

2.4. SPE adsorbents based on carbogen nanoparticles

Graphene (G) became used as sorbent material in the separation process most recently, due to the large surface area and rich π -electron system that promote high adsorption capacity for aromatic analytes [80]. The combination of simple separation of MNPs (Fe_3O_4) and high adsorption capacity of graphene oxide (GO) can lead to producing the adsorbents with excellent separation properties. After the decoration of MNPs on the surface of GO (or G), the unprotected particles can easily be oxidized under harsh extraction conditions and lose their magnetism at long-term use. These problems can be avoided with coating the magnetic core with suitable materials, for example, silica. $\text{Fe}_3\text{O}_4@\text{SiO}_2@\text{GO}$ -PEA was synthesized via covalent bonding of the GO nanosheets with silica-coated Fe_3O_4 microparticles, and after that, the GO surfaces were chemically modified phenylethylamine (PEA) [58]. The existence of oxygen-functional groups on the surfaces of GO is responsible for hydrophilicity, but the oxygen-functional groups interrupt the sp^2 -hybridized structure of GO, resulting in weaker π interactions with organic molecules. Fortunately, modification of GO with PEA promotes π interactions of the adsorbent with analytes. Analysis in environmental water sample showed the recoveries in the range between 71.7% to 106.7%.

Reduced GO was investigated as SPE sorbents for determination of Malachite green (MG) and leucomalachite green (LMG) in fish samples [69]. The result shows the robustness of graphene-packed SPE cartridges during thoroughly washing with water and selected organic solvents. Only 10-mg of rGO was used. It was smaller than in classical SPE clean-up procedures, for example, C18 with 500 mg cartridge.

The stability in acid, alkali, organic solutions and under high temperature of the as-prepared GO/SPME fibre was also shown in [79]. The adsorbent was prepared via modification of the hydroxylated part of the fibre with APTES solution and after that, it was covalently bonded with GO.

Carbon nanotubes (CNTs) can be divided into single-walled carbon nanotubes (SWCNTs) and multiwalled carbon nanotubes (MWCNTs) depending on the number of carbon atom layers. Due to their extremely large surface area and the special tubular

structure, CNTs have been used as a sorbent for organic compounds only ten years. It was firstly reported in 2001 that SWCNTs possess excellent adsorption of dioxin [81], then bisphenol A (2003) [82], pesticides (2008) [83] and PAHs (2007) [81, 84].

Good recoveries of PAHs from environmental water samples (78.7 to 118.1%) were observed for SPE from MWCNTs [71].

A new CNTs modified sorbent was prepared by combining the high adsorption ability of MWCNTs (average diameter of 60–100 nm; a length of 2–5 μm) and the high porosity of poly (vinyl alcohol) cryogel (MWCNTs/PVA) [81]. BaA, BbF and BaP in real water sample were found in the range of 7 to 22 ng L^{-1} . The major advantages of MWCNTs/PVA over the commercial C18 is that it can be operated at a higher loading flow rate without sorbent clogging.

Generally, carbon-based materials were applied for adsorption aromatic compounds from water media, thus further developed of carbon-containing adsorbents suitable for lipid matrix is needed, Table 4.

Table 4 - Applications of some carbon-based adsorbent in SPE

Sorbent	Analyte	Sample	Method	LODs	Ref
MWCNTs/PVA	PAHs	Water sample (Thailand)	SPE-HPLC-FLD	BaP - 5ng/L	[85]
MWCNTs	PAHs	River water	SPE-HPLC-UV	0.005–0.058 $\mu\text{g/L}$	[71]
Fe ₃ O ₄ @SiO ₂ @GO-PEA	PAHs	River water (Iran)	SPE-CG-FID	0.005-0.1 $\mu\text{g/L}$	[58]
rGO	MG and LMG	Fish tissue	SPE-UHPLC-MS/MS	MG - 0.09 $\mu\text{g/kg}$; LMG - 0.12 $\mu\text{g/kg}$	[69]
GO-SiO ₂	PAHs	River water, milk	SPE-HPLC-UV	0.0029–0.052 mg/L	[14]
GO@SiO ₂ , G@SiO ₂	Chlorophenols, proteins	Water, biosamples	MALDI-TOF-MS	n. r.	[86]

2.5. PAH-anchored materials

In recent years, the design and development of new aromatic stationary phases for the separation of highly aromatic compounds have been increased. Phenyl-type phases have a greater specificity towards PAHs, indicating additional selectivity, presumably due to π - π interactions. Previously studies showed [87, 88] that the dominant factors affecting retention on phenyl-types of phases were the size and shape of the PAHs, and that retention was mainly due to a combination of both π - π - and shape interactions.

2.5.1. Adsorption properties of PAHs anchored materials

The PAH-anchored materials as sorbents which allow more complete separation based on the planarity of solutes were developed [11, 15, 89]. Non-polar organic solvents show better solubility for hydrophobic aromatic compounds and high structural selectivity for chlorinated aromatic compounds can be provided by stationary phases having electron-donor or acceptor groups in non-polar solvents. Pyell showed the application of different silica modified solid phases for separation tetrachlorodibenzo-p-dioxin (TCDD) isomers [90]. The highest selectivities were obtained for TNF-, TCP- and TCP5-SG in the normal-phase mode. Structures of these sorbents are presented in Figure 1. Due to the high capacity factors, PE-SG with methanol as the mobile phase can be used to adsorption of polychlorodibenzo-p-dioxin (PCDD), congeners with more than four chlorine substituents [88, 91].

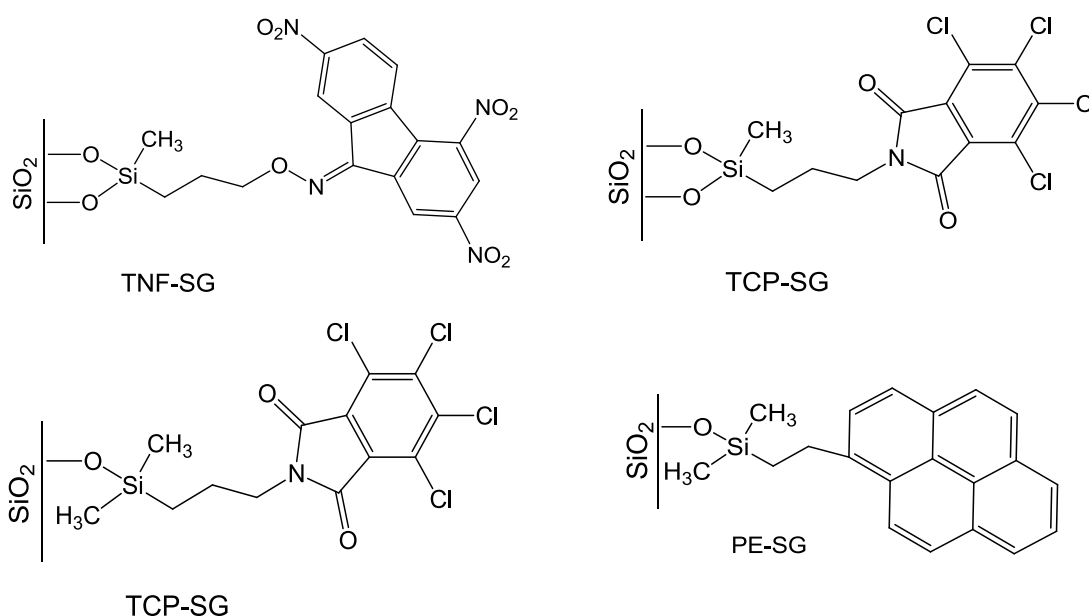


Figure 1 - Structure of the solid phases

In the study [87] the retention behavior of PAHs on both the Synergi polar RP (propyl-ethoxy phenyl bonded silica) phase and the Cosmosil 5PBB phase (pentabromo-benzyl-oxypropyl bonded silica) in a variety of solvent systems was compared. The molecular interactions between the solute and the stationary phase were greater in the methanol systems than in the acetonitrile systems. The Synergi polar-RP column was very similar to C18 with respect to PAH retention and selectivity in

methanol-water mobile phases. It was demonstrated that the π - π interactions with the stationary phase were affected by competing for π - π interactions from the acetonitrile mobile phases. Addition of the π -electron competitors (benzene) in mobile phase essentially resulted in the surface mimicking a more densely packed stationary phase surface. Acetonitrile did not significantly decrease selectivity when using the Cosmosil 5PBB column, as was observed with the Synergi polar-RP stationary phase. This organic modifier was suitable to reduce retention and keep resolution, however, selectivity was lost between structural isomers.

2.5.2. Luminescent properties of immobilized PAHs

For selecting a surface-confined sensing element, two factors are concerned. One is the fluorescent quantum yield, and the other is the molecular size. This is because the surface reaction always bears low reaction efficiency as a result of steric hindrance [92]. Therefore, among various fluorescent species, PAHs such as pyrene, anthracene, and dansyl are an important class of small fluorophores because they consist of π -conjugated ring structures, have a high fluorescent quantum yield, and more importantly, are highly sensitive to their microenvironments.

Surface modification by highly fluorescent aromatic polycyclic hydrocarbon such as anthracene opens the opportunity to bring it in π -stacking interactions and the possibility of detecting the coordination medium through modulation of the fluorescence emission. Commonly, similar materials are used as a fluorescence sensor [93].

Modification of silica gel with fluorescent probes for pH sensing was first reported by Ayadim and co-workers [73]. They prepared a pH-sensitive silica gel by the covalent attachment of an anthracene fluorophore to the surface of silica. The response time of sensor with a low concentration of anthracene suspended in the water solution is very short (less than half a second) when for high loading is longer (more than 15 minutes), rendering this grafted silica unable to function as a pH probe.

The fluorescence of the material changed essentially from environmental. For example, in dry acetonitrile or methanol, an emission between 480 and 600 nm shows up, corresponding to excimer fluorescence. Completely and rapidly (response time of less than 1 s) disappeared off the excimer-like emission when a small amount of water

was added to these solvents (1 μ l of water in 3 ml of solvent) [72, 94]. The excimer like emission arises from ground state associations and, additionally, the adsorbed water molecules on the silica surface have been reported to create a well-defined structure made of regular layers of adsorbed water molecules. The mobility of the grained anthracene molecule may be strongly reduced if the covalently attached probes are maintained by the hydrophobic interactions like in holes drilled in the water layers. This may be an explanation for the excimer like emission disappearance.

According to the continuum model of diffusion theory, the value of the distance in solution between anthracene in the excited state and that in the ground state was estimated to be 8 ± 2 Å (in chloroform) [95]. The appearance of a new band at 500 nm is a characteristic feature of excimer. The amine fragments could also give charge-transfer interactions with photo-excited anthracene to form complexes that are known as exciplexes [96]. The possibility of observing exciplexes between anthracene and primary or secondary amines was discarded by authors from Poland [97]. They reported that instead of the exciplex formation a photo-induced proton transfer (PPT) occurs. Fluorescence measurements the solid functionalized with a small amount of anthracene in an organic aprotic solvent (acetonitrile) showed no unstructured band that's why the band at 500 nm must be attributable to the formation of anthracene–anthracene excimers rather than to the amine–anthracene exciplexes. It was noted that Ant excimer appears when an anthracene molecule in the excited state is *lined up* with another anthracene molecule in the ground state and forms a dimer through π -*interaction*. The detection of excimers in anthracene-anchored solid would indicate that the anthracene molecules can freely move in the solid then they are well-solvated with acetonitrile and their interaction with the silica surface is not very strong.

Pyrene luminescence has been found useful as a probe of surface, solvent and interfacial properties. The spectrum structure of pyrene is dependent on the solvating environment, and it has a relatively long decay time. At high solution concentration or when forced into close proximity, excited-state dimers (excimers) of pyrene are observed in Figure 2. The distance between two fluorescing pyrene molecules in crystal form yielding an excimer has been calculated to be approximately in the range 3–10 Å [98]. Thus, pyrene molecules must be 1 nm or closer to form excimers, and the presence

or lack of excimer formation can be used as a sensitive probe of pyrene separation. In [99] were reported the effects of changing the silica pore size on the formation of excimers from pyrene molecules confined in the mesopores, which indicated that pore sizes of 20-40 Å produce fewer excimers than mesoporous materials synthesized with >40 Å pores.

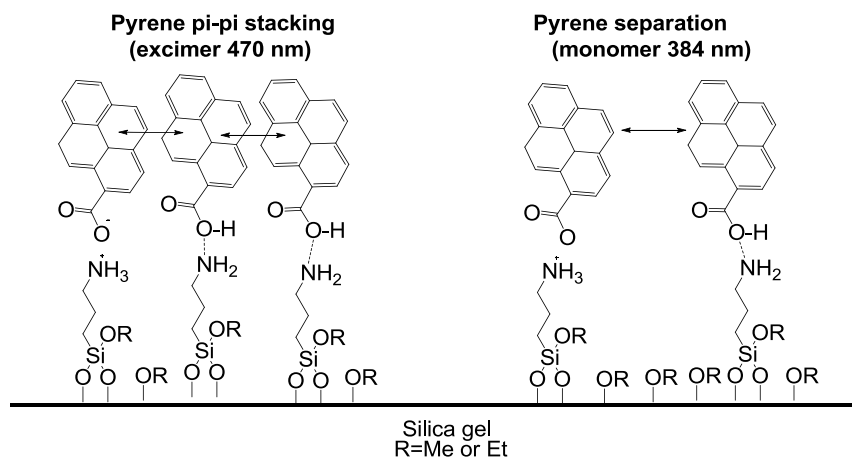


Figure 2 - Reaction of 1-pyrenecarboxylic acid on aminosilicas representing π - π stacking (excimer) and monomeric emission, adapted from [200]

The ratio of excimer to monomer intensity obtained from emission spectra is often utilized as a measure of pyrene mobility and proximity [100]. An interesting aspect was observed in studies of pyrene molecules covalently bound to and adsorbed on silica gel. Lochmuller [101] found that at low concentrations of bound pyrene, which are achieved by either low surface coverages or dilution of pyrene-derivative silica with underivative silica, the excimer and monomer excitation spectra are identical (cause of excimer emission was a dynamic process). However, for pyrene adsorbed on silica gel [102], excimer excitation spectrum was red-shifted relative to that of the monomer at all concentrations examined. It was concluded that the “excimer-like” species for pyrene adsorbed on silica gel was a ground-state dimer. The difference between adsorbed and bound pyrene may be the result of distinction manner in which the experiments are performed. Studies of bound pyrene were performed with the silica in contact with the solvent, whereas studies of adsorbed pyrene were implemented with the silica gel in contact with the gas phase.

In review, Ding raised the phenomenon of “spacer layer screening effect”, considering a major role of surrounding chemical microenvironment in mediating the

photophysical properties of the surface-confined fluorophores as well as their accessibility to analytes [92]. Longer, flexible, hydrophobic spacers tend to form a more compact layer (termed as “spacer layer”) in aqueous solution than shorter spacers and incorporate fluorophores deeper inside the “spacer layer”. As a result, it generates a significant hindrance effect on target molecules (especially large molecules) accessing fluorophores. In less polar solvents, the bent spacer was expected to stretch out and thereby the fluorophore moieties became more exposed to the solvent phase.

2.6. Graphene-based materials

Carbon is one of the most abundant elements in the Earth. It is the basis of all organic chemistry. Among systems with only carbon atoms, graphene shows unique properties include extremely high intrinsic mobility of charge carriers, zero bandgaps, large surface area and high chemical stability. A single graphene sheet is a planar monolayer of sp^2 bonded carbon atoms arranged on a two-dimensional honeycomb lattice made of hexagons [103]. Its extended honeycomb network is the basic building block for carbon allotropes of any dimensionality [104]. It can be stacked to form 3D graphite, rolled to form 1D nanotubes [105] and wrapped to form 0D fullerenes (1985) [89] (Figure 3). Interestingly, graphene has been discovered much later than the mentioned carbon materials. Experimental isolation of graphene was implemented in 2004 by the Novoselov and co-workers [106].

The chemical nature of carbon in these materials comes from its hybridization states, which also determines the features of the variety of organic compounds. The sp^2 hybridization between one s orbital and two p orbitals lead to a trigonal planar structure with a formation of σ bond between carbon atoms that are separated by 1.42 Å and the lattice constant is 2.46 Å [104]. The σ band is responsible for the robustness of the lattice structure in all allotropes. The unaffected p orbital can bind covalently with neighbouring carbon atoms, leading to the formation of a π half-filled band [107]. While the strong σ bonds work as the rigid backbone of the hexagonal structure, the out-of-plane π bonds control the interaction between different graphene layers [108].

Single-layer graphene (SLG) is well known as one graphitic layer. Two and three graphitic layers are known as bilayer and trilayer graphene, respectively. More than 5

layers up to 10 layers graphene are generally called few-layer graphene (FLG), and 20–30 layers graphene is referred to as multilayer graphene (MLG), thick graphene, or nanocrystalline thin graphite [108]. In bi- and few-layer graphene, carbon atoms can be stacked in different ways, generating hexagonal or AA stacking (Figure 3a), Bernal or AB stacking (Figure 3b) and rhombohedral or ABC stacking (Figure 3c) [109]. It has been recently found that bilayer graphene often exhibits AA stacking [110].

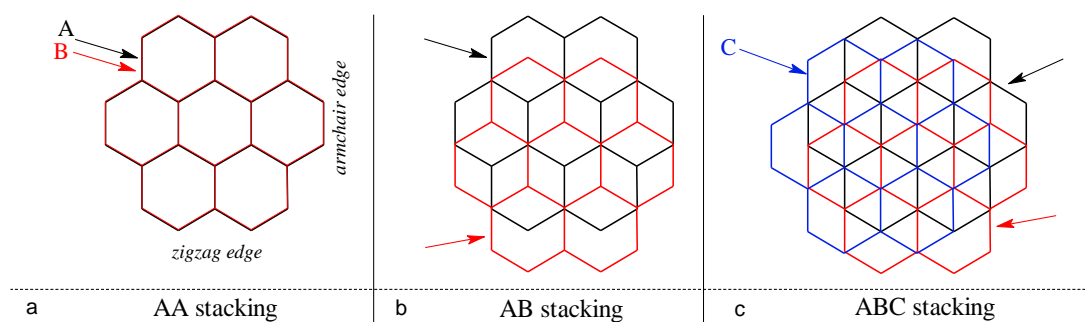


Figure 3 - A piece of a honeycomb lattice of graphene displaying both zigzag and armchair edges and AA (a), AB (b) and ABC (c) stacking of graphene layers

2.6.1. Fabrication of graphene

A method for graphene synthesis is crucial to realize the optimum potentiality of graphene in a broad range of its applications. The next sub-sections are devoted to some of the commonly used methods based on the next literature data [45, 106, 108, 111–115] The size and quality of the graphene depends on the techniques used, Figure 4. The resulting graphene probes have similar, but not always equal, physical properties.

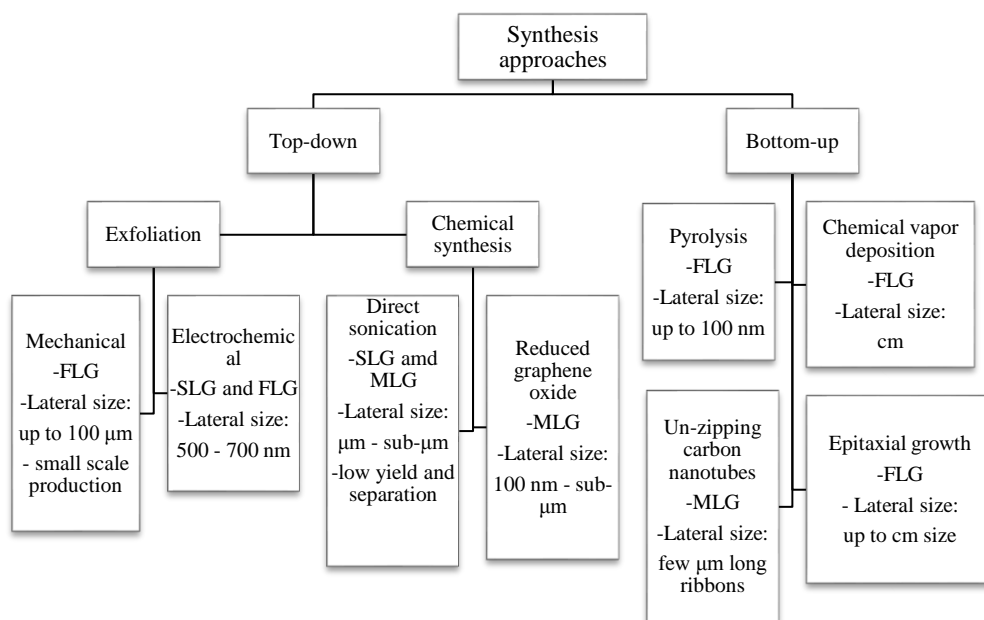


Figure 4 - The chart of graphene synthesis

Mechanical exfoliation

One of the simplest methods of graphene preparation is mechanical exfoliation (repeated peeling) or cleavage of highly ordered graphite [106, 116]. The technique now provides high-quality graphene up to 100 μm in size, which is sufficient for most research purposes. In nanotechnology mechanical exfoliation refers to a top-down method [117]. Generally, the peeling/exfoliation can be done using a variety of instruments like scotch tape [106], ultrasonication [118] and even by transfer printing technique [119].

Thermal decomposition of SiC

Epitaxial growth by SiC thermal graphitization is a substrate-based method, where isolated monolayer of graphene is grown on single-crystal silicon carbide by vacuum graphitization [114, 120]. Since the thermal treatment of silicon carbide at $\sim 1300^\circ\text{C}$ under vacuum results in the sublimation of the silicon atoms while the carbon-enriched surface undergoes reorganization and graphitization. As a result, graphene islands over the entire surface of SiC wafers were obtained through careful control of the sublimation [121]. The thickness of the graphene layers was controlled mainly by annealing temperature and time. Due to the influence of interfacial effects in epitaxial

graphene, the physical properties of graphene varied significantly between those grown epitaxial and exfoliated mechanically. However, controlling the thickness of graphene in routine production is very hard. Due to the different epitaxial growth patterns on different SiC polar faces, unusual rotational graphene stacking was observed in multilayer graphene [122].

The most commonly used SiC polytype structures for thermal decomposition is 6H-SiC [123]. Graphene sheets were found to be formed when H₂-etched surface of 6H-SiC was heated to temperatures of 1250 to 1450 °C for a short time (1 to 20 minutes). Graphene, epitaxially grown on this surface, typically had 1 to 3 graphene layers. The number of layers depends on the decomposition temperature. In a similar process, Rollings [114] has produced atomically thin graphene films of thicknesses down to 1–2 graphene layers.

Machac [124] have utilized a Ni/SiC structure. The method is very promising for stripping of graphene layers from the substrate and their transfer to other substrates. Graphene films were prepared by synthesis on a SiC substrate via Ni-silicidation reaction. Through optimization of the technological process, three-layer graphene was prepared. The best results were provided with the optimal annealing temperature at 1050 °C and the best annealing time was 120 s. In addition, continuous films (mm scale) of graphene were synthesized on a Ni thin film coated SiC substrate, at a quite lower temperature (750 °C) [125].

This process has the added advantage in preparing continuity of graphene film over the entire Ni-coated surface. Large area production of graphene makes this route favourable for industrial application [109].

Chemical Vapor Deposition

In CVD methods, graphene is grown directly on a transition metal substrate via saturation of carbon upon exposure to a hydrocarbon gas at a high temperature. It is a recent method for the preparation of graphene and it was introduced in 2008 [115, 126–128]. Graphene achieved from the CVD process has demonstrated large area, high quality, controllable number of layers and low defects.

The synthesis process typically involves a thin layer of a transition metal (usually a few hundred nanometers thick) deposited on a substrate (SiO₂). Then the substrate is

put into a furnace at 1000° C in a hydrocarbon gas (methane and hydrogen) environment. The transition metallic layer catalyzes the decomposition of hydrocarbon gas. As a result, the dissociated carbon atoms gradually absorb into the metal layer or diffuses/remains on the metal surface depending on the metal.

Graphene islands were also grown on Pd (111) [120]. The size of the graphene islands largely varied between 200 and 2000 Å (from images of the scanning tunnelling microscope (STM)). Due to the superposition of the honeycomb lattice of graphene and the hexagonal lattice of Pd (111), these superstructures are of Moiré patterns [129].

The epitaxial and CVD growth techniques have been found to be by far the most effective technique to produce high quality, large scale graphene that can be compatibly integrated into the Si device flows. An important disadvantage is a need for expensive substrate materials for graphene growth, considerably limiting its applications for large-scale production.

Un-zipping carbon nanotubes

Recently, MWNT as the starting material have been used for graphene synthesis and this process is known as “un-zipping of CNTs” [45]. MWNTs can be opened up longitudinally by using intercalation of Li and ammonia, followed by exfoliation in acid and abrupt heating [130]. The product, among nanoribbons and partially opened MWNTs, also contained graphene flakes. Jiao [131] produced graphene nanoribbons by plasma etching of MWNTs, partially embedded in a polymer film. The etching treatment basically opened up the MWNTs to form graphene with narrow width distribution (10–20 nm). MWNTs were un-zipped by multi-step chemical treatment, including exfoliation by concentrated H₂SO₄, KMnO₄ and H₂O₂, stepwise oxidation using KMnO₄ and finally reduction in NH₄OH and hydrazine monohydrate (N₂H₄·H₂O) solution [132].

This new process route of unzipping MWNTs to produce graphene creates possibilities of synthesizing graphene in a substrate-free manner.

Chemical exfoliation

Chemical method is the favourable method for the synthesis of graphene in solution. The purpose is to separate the layers of graphite or graphite intercalation

compound [108]. GO is a product which can be obtained by chemically oxidizing of graphite to graphite oxide (GTO) with strong oxidants and following ultrasonic cleavage. It has attracted much attention as a possible intermediate for the manufacture of graphene in large volume [133]. The graphene sheet consists of only trigonal bonded sp^2 carbon atoms, while the heavily decorated GO sheets consist partly of tetrahedral bonded sp^3 carbon atoms. They are displaced slightly above or below the graphene plane. Sonication or rapid heating of GTO results in its expansion and delamination, forming GO. It is caused by rapid evaporation of the intercalated water and evolution of gases from pyrolysis of the oxygen-containing functional groups. Interlayer distance in graphite is about 3.4 Å and after the oxidation step, it is increasing to 7-10 Å [134]. The next step is the reduction of GO. In the literature, the product of this reaction has been given a variety of names such as rGO, chemically-reduced graphene oxide (CrGO) and graphene. To avoid uncertainty, we will refer to the product as “reduced graphene oxide,” because distinction such as structural differences with pristine graphene exists.

Oxidation. GTO has a decades-long history. Nowadays, it is produced by the oxidative treatment of graphite through one of three principal methods developed by Brodie (1859) [135], who added a single portion of potassium chlorate $KClO_3$ to a slurry of graphite in fuming nitric acid HNO_3 , Staudenmaier (1898) and Hummers (1958) [136]. In two of the last-mentioned method were used more convenient oxidizing reagents, but all three of these procedures involve generation of the toxic gases NO_2 , N_2O_4 , chlorine dioxide ClO_2 .

Brodie found the resulted material to be dispersible in pure or basic water, but not in acidic media, which prompted him to term the material “graphic acid”[137]. Staudenmaier improved Brodie’s protocol by multiple adding the chlorate over the course of the reaction with the addition of concentrated sulfuric acid H_2SO_4 to increase the acidity of the mixture. The Hummers used oxidation method by reacting graphite with a mixture of sulfuric acid, sodium nitrate $NaNO_3$ and potassium permanganate $KMnO_4$. Now, this method is the most popular and widely used with some modifications. Importantly, it has been demonstrated that the products of these reactions show strong variance which depends on oxidants, the graphite source and

reaction conditions. In 2010 the new “improved method” was highlighted by Marcano and co-workers [138]. They excluded the NaNO_3 , increased amount of KMnO_4 and used a mixture of concentrated $\text{H}_2\text{SO}_4/\text{H}_3\text{PO}_4$ (9:1). The method did not generate toxic gas and temperature is easily controlled. The mechanism for producing GO refers to the formation of five-membered cyclic phosphate groups between the phosphoric acid and two vicinal diols formed on the graphite basal plane.

The most common source of graphite used for chemical reactions is flake graphite. It contains numerous localized defects in its π -structure that may serve as seed points for the oxidation process [139]. In [140] was observed that graphite can be exfoliated into individual sheets via mild oxidation followed by intercalation. However, the exfoliation of partially oxidized and intercalated graphite was less efficient compared to GTO prepared through the modified Hummers method.

GO and GTO are very similar chemically, but structurally they are very different. The main difference is the interplanar spacing between individual atomic layers of the compounds, which is caused by water intercalation [141]. The exfoliation of GTO depends on strength between layers and force of the reaction between the layers and the solvent. Rather than retaining a stacked structure, the material is exfoliated into monolayers or few-layered stacks [137]. The surface functionality (particularly in basic media) greatly weakens the platelet–platelet interactions, owing to its hydrophilicity. Sonication in water or polar organic media has a great disadvantage in that it causes substantial damage to the graphene oxide platelets. The dimensions are diminished to several hundred nanometers per side and the product contains a considerably larger distribution of sizes [142].

The correct chemical structure of GO (after oxidative step) has been discussed for many years and even to this day no explicit model exists. Some of the reasons for this are the complexity of the material, including sample-to-sample variability, due to its amorphous, nonstoichiometric atomic composition and the lack of precise analytical techniques for characterizing such materials. The older structural models of GO proposed regular lattices composed of discrete repeat units Figure 5. Hofmann proposed a structure of GO with only epoxy groups on the basal planes of graphite, with a net molecular formula of C_2O [137]. Ruess has complemented the structure with

a hydrogen content of GO and presence hydroxyl groups into the basal plane [143]. Another difference from the Hofmann's model is the basal plane structure changed to a sp^3 hybridized system.

Scholz and Boehm suggested a model without the epoxide groups but consisted of ribbons of the conjugated carbon backbone and regular quinoidal species [143]. Nakajima and Matsuo proposed a lattice framework similar to poly(dicarbonmonofluoride) (C_2F)_n model. In this model, two carbon layers link to each other by sp^3 C–C bonds perpendicular to the layers, where carbonyl and hydroxyl groups are present in relative amounts depending on the level of hydration [144].

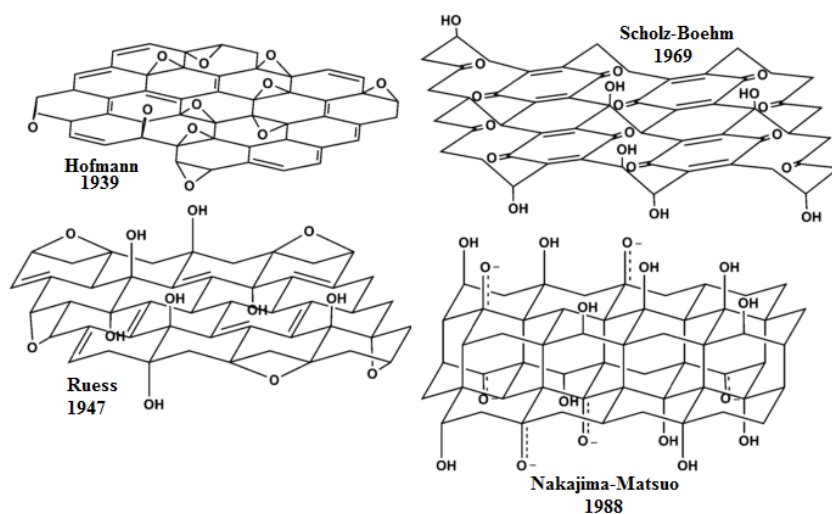


Figure 5 - The earliest structural models of GO

Nowadays the most well-known model is introduced by Lerf and Klinowski (1998) Figure 6 [145]. It was based on expert solid-state nuclear magnetic resonance (NMR) studies. In the Lerf model, epoxy and hydroxyl groups on the GO surface are the main structural feature, and they contribute the ^{13}C NMR peaks at 60 and 70 ppm, respectively [134]. Isolated double bonds are unlikely to exist in the strong oxidizing conditions. Carboxylic acid groups are present at the edge of the graphitic platelets. These oxygen functionalities render the graphene oxide layers of GTO hydrophilic and water molecules can readily intercalate into the interlayer galleries. GTO can, therefore, be also thought of as a graphite-type intercalation compound with both covalently bound oxygen and non-covalently bound water between the carbon layers.

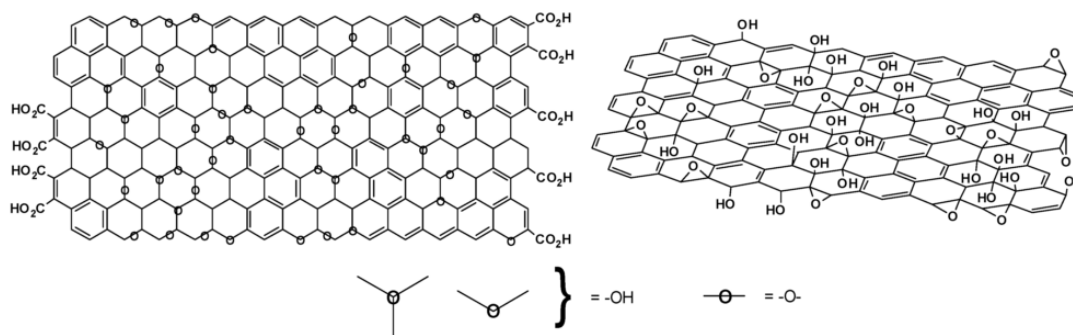


Figure 6 - Lerf – Klinowski model of GO (Adapted to [145])

As a result, due to presence of hydroxyl and epoxy groups on the interior of the plane and carboxyl groups at the edges of layers, GO has negatively charged surface. GO can be electrostatically stabilized to form a colloidal suspension in water, alcohols and certain organic solvents without surfactants, making it easier to handle and functionalize than native graphene [133]. However, the oxidation mechanism and the structure of GTO are still elusive due to its nonstoichiometric structure and strongly hygroscopic property.

Reduction. The next step of proximity to graphene is the reduction of GO. However, usually, a significant amount of residual oxidation functionality and defects still exist in rGO [13]. The problem is to make a clean and complete reduction of all the oxygen functionalities. The reduction process is among the most important reactions of graphene oxide, because of the similarities between rGO and pristine graphene. The reduction methods can be achieved through thermal [146], chemical [13] or electrochemical reduction pathways [137].

Bagri has directly studied the thermal annealing of GO with randomly distributed hydroxyl and epoxy groups [146]. It was observed a large number of holes formed during the breaking of C–C bonds in the basal plane. As a result, these holes are decorated by either a pair of carbonyl groups or carbonyl and hydroxyl group. Formation of these holes can be induced by interactions between neighbouring hydroxyl and epoxy groups. Their studies suggest the possibility of the existence of C=O in the basal plane of GO.

Variety of chemical means may be used to reduce graphene oxide. Hydrazine monohydrate (the highly toxic reagent) is widely used in chemical reduction of GO

[13]. At the same time most strong reductants have strong reactivity with water, hydrazine monohydrate does not have. This feature making it an attractive agent for reducing aqueous dispersions of GO. The reduction process of GO with extremely strong reducing agents, such as lithium aluminium hydride (LAH), remains a challenge due to side reactions with solvents (i.e. water) commonly used for dispersing graphene oxide.

Kim and co-workers examined two possible mechanisms of the hydrazine reduction reaction: direct Eley-Rideal (ER) process and the intermediate anchored Langmuir- Hinshelwood (LH) process [147]. It has been found that the ER mechanism with the epoxide ring-opened via H abstraction from hydrazine $\text{NH}_2\text{-NH}_2$ is likely to be more kinetically facile. After H transfer, the newly formed OH group can easily obtain another H from NH-NH_2 and desorb from the surface.

The reactions of oxygen functionalities of GO were systematically investigated under hydrazine and heat treatment conditions, using the density functional theory (DFT) method [148]. For hydrazine reduction, three possible mechanisms for epoxide reduction have been identified. No reduction route has been determined for hydroxyl, carbonyl or carboxyl groups. However, increasing of annealing temperature improves the efficiency of thermal reduction considerably. Thermal annealing of GOs at 500, 700, and 900 °C respectively yielded chemically modified graphene with C:O ratios of 8.9, 13.2, and 14.1, respectively [149]. During an annealing thermal process at temperatures higher than approximately 700°C, hydroxyl groups, including those in carboxylic groups at the edges of aromatic domains, were eliminated from GO. The epoxide groups of GO were classified into two types: epoxides that are located at the interior of an aromatic domain of GO and epoxides located at the edges of an aromatic domain. The hydrazine reductions of epoxide groups attached to the interior of an aromatic domain of GO was thermodynamically spontaneous. On the other hand, the hydrazine reduction of an epoxide located at the edges of an aromatic domain is blocked by the formation of hydrazino alcohol that thermodynamically is more stable than the corresponding de-epoxidation products at room temperature [150].

One of the disadvantages of using hydrazine is the introduction of heteroatomic impurities. Nitrogen tends to remain covalently bound to the surface of graphene oxide,

likely in the form of hydrazones, amines, aziridines or other similar structures [13]. Sodium borohydride NaBH_4 is more effective reducing agent for carbonyl groups than hydrazine, although hydrazine commonly used for reduction of epoxide groups. NaBH_4 is slowly hydrolyzed by water. This process is kinetically slow enough that freshly prepared solutions, having a large excess of reducing agent, still function effectively as reductants of GO. Additional alcohols are the principal impurities that are generated during this reductive process (as a result of the hydrolysis of the boronic ester).

Sulfuric acid or other strong acids can also be used to facilitate dehydration of the graphene surface [151]. Acid treatment leads to dehydrate the remaining tertiary alcohols to form alkenes that are part of a graphitic sp^2 carbon network with protons and carboxylic acid groups on the periphery. For graphene structures that are contaminated with large amounts of alcohols (obtained after borohydride reduction), this is a particularly useful workup procedure. The main disadvantages of chemical methods are partial reduction of GO to graphene and fragile stability of the colloidal dispersion [141].

2.6.2. Functionalization of graphene oxide

The hydrophobic property of graphene limits functionalization or study in most liquids, due to its difficult formation of dispersion. As previously indicated, GTO has a layered structure similar to that of graphite, but the plane of carbon atoms in GTO is heavily decorated by oxygen-containing groups, which not only expand the interlayer distance but also make the atomic-thick layers hydrophilic. After exfoliation of these oxidized layers in water under ultrasonication GO can be obtained. GO shows excellent hydrophilicity and relatively easy it can be dispersed in water. The next sub-sections are devoted to some types of functional groups on GO using various chemical reactions that provide for either covalent or non-covalent attachment. Modified GO is a more versatile precursor for a wide range of applications.

Via the carboxylic acid and hydroxyl groups of graphene oxide

The coupling reactions often need activation of the acid group using thionyl chloride (SOCl_2) [127], 1-ethyl-3-(3-dimethylaminopropyl)-carbodiimide (EDC) [152], N,N'-dicyclohexylcarbodiimide (DCC) [76] or 2-(7-aza-1H-benzotriazole-1-

yl)-1,1,3,3-tetramethyluronium hexafluorophosphate (HATU) [153]. Subsequent addition of nucleophilic species, such as amines or hydroxyls, produce covalently attached functional groups to GO through the formation of amides or esters. The products are most often characterized by X-ray photoelectron (XPS), Fourier transform infrared (FTIR) and NMR spectroscopies

One of the most common methods of covalent functionalization is the introduction of amine groups. The addition of an aliphatic diamine to EDC-activated graphene oxide produced amine-functionalized graphene at the carboxylic acid groups.

The attachments of polymers to the surface of graphene by atom transfer radical polymerization (ATRP), one of the types of “grafting from” polymerization. It has a fast initiation process and the development of a dynamic equilibrium between dormant and growing radicals [154]. (α -bromoisobutyryl bromide), as ATRP initiator, was attached to the terminal amine, as well as the hydroxyl groups on the basal plane. Polymers were then grown from the surface of the resulting material and increased dispersibility in many solvents (i. e. water and methanol). Aside from activation and amidation/esterification of the carboxyls on GO, it is also possible to convert them into other reactive groups. Generation of amide and carbamate ester groups from the carboxylic acid and hydroxyl groups, respectively, of GO sheets was achieved with the addition of isocyanate derivatives with various aliphatic and aromatic groups [155]. The resulting materials were well dispersed in polar aprotic organic solvents, giving completely exfoliated SLG sheets with a thickness of ~ 1 nm. This dispersion also facilitated the mixing of the GO sheets with matrix polymers, providing new synthesis route to make graphene-polymer nanocomposites [141].

Via the epoxide group of graphene oxide

The epoxy groups can be easily modified through ring-opening reactions under various conditions [148]. An expected mechanism for this reaction involves nucleophilic attack at the α -carbon by the amine. Taking into account the information above, multiple reactions may be occurring simultaneously: amine groups can react with carboxylic acid groups of graphene oxide through the amidation process.

The epoxide ring-opening reaction by the addition of octadecylamine to a dispersion of GO was carried early [152, 156] The resulting suspensions were used for

generation of thin chemically modified graphene (CMG) films by spin-casting or printing of the suspensions. After binding of an ionic liquid (1-(3-aminopropyl)-3-methylimidazolium bromide) to GO, the resulting CMGs were well-dispersed in solvents such as water, DMF, and DMSO, due to the high polarity of the material.

It is worth noting that reactions of the epoxy group of GO have also been used to stabilize solid-phase dispersions of CMGs. Covalent grafting of (3-aminopropyl)triethoxysilane (APTES) to graphene oxide platelets was performed by a nucleophilic S_N2 displacement reaction between the epoxide and the amine groups of APTES [137]. The mechanical properties of composite materials, composed of silica monoliths and the silane-functionalized graphene platelets, were enhanced by the addition of the CMG. The authors suggested that this reinforcement can be induced by possible covalent bonding between the silica matrix and silane groups of the CMG platelets [157].

Non-covalent functionalization

Hydrogen bonding, hydrophobic forces, metal coordination, van der Waals forces, π - π interaction and electrostatic forces are forms of non-covalent interactions. GO can also exhibit non-covalent binding on the sp^2 networks that are not oxidized or engaged in hydrogen bonding. Non-covalent functionalization has been considered to be a desirable and fruitful method for the fabrication of high-quality graphene with improved self-assembled properties.

Most covalent chemical modifications of GO previously discussed occurred at one or more of the various oxygen-containing functional groups present in graphene oxide. Hence, the reactivity observed in materials derived from the reduction of graphene oxide could be caused by residual functional groups left intact after incomplete reduction. In the literature, non-covalent functionalization of graphene sheets through π - π interactions using aromatic organic molecules has rarely been addressed. rGO have been modified by small molecules onto their basal planes via π - π stacking or van der Waals interactions [158, 159]. Pyrene is a π -orbital-rich group that easily forms strong π - π stacking interactions with other polyaromatic materials. Pyrene-tethered precursors have been successfully prepared [160] and attached to aromatic macromolecules such as carbon nanotubes [161], graphene oxide [152] and

fullerene [162]. Liu and co-workers [163] are the first who synthesized pyrene terminated poly(N-isopropylacrylamide) (PNIPAAm) using reversible addition fragmentation chain transfer polymerization, followed by attachment onto the basal plane of graphene sheets via π - π stacking interactions.

The authors of review [137] noticed that adsorption of pyrene, tetracyanoquinodimethane (TCNQ), sulfonated poly(aniline) (SPANI), perylene derivatives and other aromatic species are likely caused by π - π stacking interactions. In the case of poly(styrene sulfonate) (PSS), both π - π stacking and van der Waals interaction could lead to its adsorption.

Water dispersible graphene sheets by non-covalent functionalization, involving GTO and water-soluble pyrene derivative, was synthesized [159]. Lu [164] reported about non-covalent binding between Deoxyribonucleic acid (DNA) or proteins and graphene oxide platelets, demonstrating that this material holds promise as a platform for sensitive and selective detection of DNA and proteins. A hybrid material of GO and doxorubicin hydrochloride (DXR) was also prepared [137]. The authors suggested π - π stacking, as well as hydrophobic interactions between the quinone functionality of DXR and sp^2 networks of GO. These interactions were the primary factors that linked the two units together. In additionally, the authors assumed that strong hydrogen bonding may be present between hydroxyl and carboxylic groups of GO and hydroxyl and amine groups in DXR.

2.6.3. Characterization of Graphene

Identification of the SLG is a problem because they are randomly distributed on the substrate. Raman spectroscopy and atomic force spectroscopy (AFM) are usually used to solve this problem. AFM analysis helps to assess the thickness and number of layers. The choice of substrate is critically important. The apparent contrast of graphene monolayer on a SiO_2/Si substrate (with an oxide thickness of either 300 or 90 nm) was maximized at about 12 % at 550 nm [165]. Graphene flakes give a characteristic colour contrast on a substrate depending on its thickness. In practice, it has been observed that thicker flakes (deposited on 300 nm SiO_2) appeared yellow (>100 nm) to bluish as the thickness decreased. When thickness came to be <10 nm, darker to lighter shades of

purple emerged and indicated the presence of FLG or SLG. AFM thickness of SLG is 0.5-1.5 nm due to chemical contrast.

It has been repeatedly stressed that Raman spectroscopy is a potential candidate for non-destructive and quick characterization of the number of layers of graphene [111, 166, 167]. The major Raman features of graphene and graphite are the two band - G band ($\sim 1580 \text{ cm}^{-1}$) and 2D band ($\sim 2670 \text{ cm}^{-1}$). The G band originates from in-plane vibration of sp^2 carbon atoms and it is a doubly degenerate phonon mode (E_{2g} symmetry) at the Brillouin zone center. The obvious difference between the Raman features of SLG and graphite is the 2D band. The single and sharp second peak is a simple and efficient way to confirm the presence of single-layer graphene. Interesting phenomena are observed in Raman spectroscopic studies of graphene when the G and 2D Raman peaks change in shape, position and relative intensity with a number of graphene layers [165]. Due to the splitting of the electronic band structure of the multilayer material, the 2D band of multilayer graphene can be fitted with multiple peaks [168]. In addition to the differences in the 2D band, the intensity of the G band increases almost linearly as the graphene thickness increases. This can be used to determine the number of layers of graphene.

Unfortunately, in practice, it is not easy to obtain larger amounts of graphene by mechanical exfoliation method. The difficulty of this method is small sample dimensions and low visibility, but their quality is very high with almost no defects.

2.7. Carbon Dots materials

CDs are a new class of water-soluble nanoparticles that were discovered during the electrophoretic purification of SWCNTs in 2004 [169].

The “bottom-up” synthesis involves the pyrolysis or carbonization of small organic molecules. Generally, the organic molecules usually undergo four stages in the formation of CDs: condensation, polymerization, carbonization and passivation. A theoretical review of CDs prepared by “bottom-up” summarized in Figure 7.

Carbon dots obtained under the bottom-up approach commonly have smaller size than GOQDs, starting from 1.3-1.5 nm and ending with 6 nm [170–172]. They can be obtained by low-temperature pyrolysis of individual organic compounds, under solvothermal (hydrothermal) treatment, by microwave-assisted pyrolysis, etc [173–

176]. Due to different carbon sources and synthetic conditions, CDs have different sizes, chemical composition of surface and photoluminescent (PL) properties [177–179]. Due to the unclear mechanism of CDs synthesis, significant variations in the chemical nature of precursors and aggregation of the pyrolytic products, most of the bottom-up synthesis results in the mixture of CDs having different particle sizes and surface properties and thus required chromatographic separation [169, 180]. Thus, at this point, the conventional approach based on the pyrolysis of organic compounds is unable to ensure reproducibility and scale-controlled yield of the luminescent CDs [174, 179, 181].

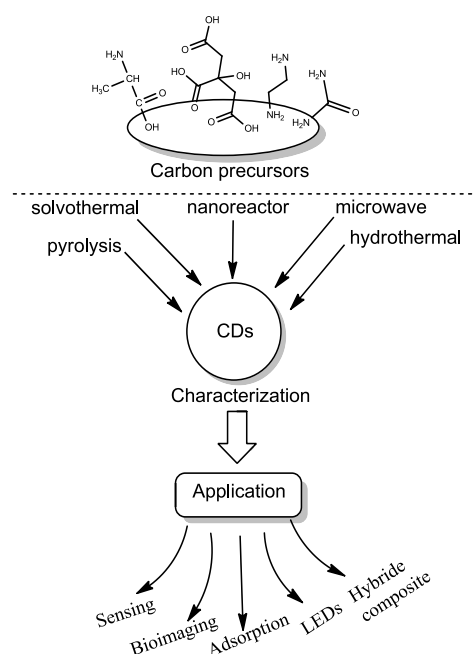


Figure 7 - CDs evolution based on a bottom-up approach

2.7.1. Properties of CDs

CDs exhibit numerous advantages over toxic metal quantum dots such as high photostability, low toxicity, and low cost. Finally, the production and application of CDs are very sustainable. They can be obtained from various organic objects and degrade in a natural environment to CO₂.

Due to their strong photoluminescence, good chemical stability, and biocompatibility CDs have great potential in energy conversion and storage [1], water disinfection [2], food safety [3] analytical chemistry [4–6] for development of chemical- and bio-sensors [6–8], biotechnology and nanomedicine [9–11] in cell

imaging and bio labeling [12–15], for drug release [16], theranostics [9,17], and photodynamic therapy [18], etc.

Besides SWCNTs, a great variety of other macromolecular objects such as nanodiamonds,[182] carbon fibres,[183] and graphene oxide[184] were shredded into smaller pieces using arc discharge,[169] laser ablation,[185] chemical and electrochemical oxidation.[186] This “top-down” synthesis requires harsh thermal (800-900 °C) conditions and thus nanoparticles commonly demonstrated defective graphite crystalline structure denoted as graphene quantum dots (GQDs).[187] In the very first publication, it was already demonstrated that the “top-down” approach resulted in a mixture of GQDs having different particle sizes (commonly 6-10 nm), surface chemistry, and thus different colour and intensity of the luminescence.[175, 179, 188]

Non-selective chemical cutting process, a small yield of GQDs (commonly less than 10%), low quantum yield (QY) of photoluminescence, and a high cost of starting materials required the development of the better approach. In fact, this approach was found even before top-down one. It was used for the “bottom-up” preparation of GO derivatives from simple organic compounds. Later it was discovered that incomplete carbonization can lead to the formation of smaller GO fragments - luminescent carbogenic dots. Such nanoparticles were obtained from different precursors and at different thermochemical conditions and thus they received different names, such as carbon quantum dots, carbon dots, and carbon-rich polymer nanodots.[189–191] Since the correlation between carbogenic dots size and their luminescent properties is very doubtful[192, 193] and all types of luminescent carbogenic nanodots obtained by incomplete pyrolysis of organic matter may belong to the same hierarchical chain,[113, 194] here we will denote all carbogenic dots received in bottom-up approach as CDs.

2.7.2. Synthesis approaches

CDs like as other nanomaterials can be obtained by “top-down” and “bottom-up” routes. A top-down approach is fragmentation or “cutting” of big molecules such as graphite or GO. In opposite, in bottom-up approach small organics used for the preparation of larger nanoparticle structure. In fact, there are a lot of publications where bottom-up and top-down approaches were combined in one process, in which high

temperature (up to 800 °C) pyrolysis of organic matter leading to GO derivatives were combined with the chemical cutting of GO by oxidation agents (NaNO_3 and HNO_3). [195] Ultrasonic strategy to synthesize the GQDs with high QY 27.8% from GO without the addition of any acid in short reaction time [196].

The **electrochemical carbonization** of low-molecular-weight alcohols reached CDs formation [197] in a basic environment. The graphitization degrees and size of these CDs increase with the increasing applied potential. The resulting CDs with amorphous core possess excellent excitation and size-dependent PL characteristics without complicated purification and passivation procedures.

Hu reported the preparation of photoluminescent CDs by **laser irradiation** of a suspension of graphite powder in an organic solvent such as diamine hydrate, diethanolamine, and poly(ethylene glycol) [198]. By organic solvents selection, tunable light emission could be generated and the origin of the luminescence was attributed to carboxylate ligands on the surface of the CDs. One of the fast and simple method is the **microwave irradiation** of organic compounds technique [199]. 2-4 min at 700W was able to prepare N-incorporating CDs.

Hydrothermal or solvothermal synthesis is an inexpensive, environmentally friendly, and non-toxic technique to fabricate novel carbon-based materials from several starting materials. However, specific Teflon autoclave reservoir is needed. Name of the synthesis depends on the solvent. Water used in hydrothermal and other solvents in solvothermal synthesis. Following this approach, hydrophilic and hydrophobic CDs were prepared with a diameter of smaller than 10 nm from carbohydrates carbonization [200]. The hydrophobic CDs were produced by mixing different amounts of carbohydrate with octadecylamine and octadecene before heating to 70–300°C for 10–30 min. The hydrophilic CDs with red and yellow emissions can be fabricated by mixing an aqueous solution of carbohydrate with concentrated phosphoric acid under heating at 80–90°C for 60 min.

Although CDs can be prepared using varieties ways, synthesis of CDs has own drawbacks:

- Carbonaceous aggregation during carbonization.
- Uniformity and size control must be optimized.

- Surface characteristics that are crucial for solubility and selected applications.

External supporting approach

The control of obtaining the homogeneous product in size and shape is still challenging. One of the possible approaches to obtain a uniform material is using of external solid template able to restrict the size and shape of the generated nanostructures.

The main strategies used to improve synthetic conditions of CDs synthesis under the bottom-up approach can be divided into groups: 1) spatial isolation of the carbon sources and 2) nanoreactor-based approach. Spatial isolation has been implemented in the form of solvothermal (hydrothermal) synthesis of CDs and by immobilization of precursors on the surface of solid mater.

Solvothermal synthesis proposed in 2010 is a most used technique today [174, 179]. Difficulties in the synthesis scaling and requirements for tedious purification of CDs are the major problem of it. Spatial isolation can also be achieved during thermal decomposition of citrate salts, where the citrate unit served as the source of carbon while the compensating organic ammonium ($C_{18}H_{37}NH_3^+$) provides the covalently attached surface modifier for micellar structure with $(C_{18}H_{37}NH)(C_4O_{1.8})$ composition [201]. Thermal decomposition of the salt at 300 °C for two hours resulted in carbogenic dots having 6-7 nm size and excitation-dependent luminescence with quantum yield 3% [201]. Spatial isolation was achieved by immobilization of carbon-containing precursors on the surface of solid non-porous materials.[195, 202] The procedure proposed is quite complex and inconclusive, thus no further development has been published.

The synthesis of CDs in nanoreactors is a very attractive approach [17], Figure 8. In contrast to conventional chemical reactors, nanoreactors provide a mesoscopic environment in which the reaction, e.g., reaction media, carriers, and interfaces is subject to nanoscale modulation. The confined space of nanoreactors can increase the probability of reaction collision and the mass transfer of reactive chemical molecules, thereby greatly improving the efficiency of chemical reactions [190].

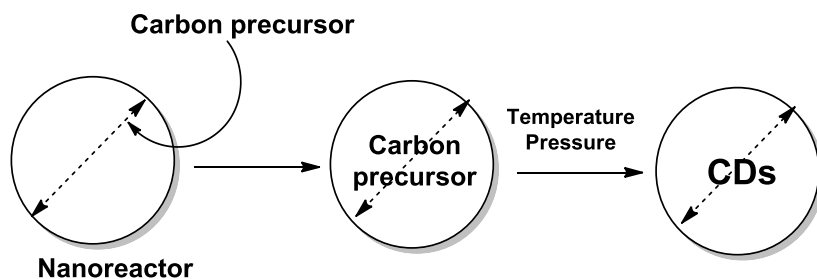


Figure 8 - General scheme of the nanoreactor approach

The preparation of CDs using vesicles and micelles is one of the nanoreactor strategies for the preparation of CDs [203, 204]. Certain progress has already been achieved under this strategy. For example, it was demonstrated that sugar carbonization inside of reverse micelles built from bis(2-ethylhexyl)sulfosuccinate resulted in the formation of fluorescent C-dots with size 1.8-4.0 nm [204]. Fatty acids were used as amphiphilic nanoreactors obtaining “in situ” upon their irradiation (Xe lamp 500 W 4 -12 h) [190]. When nonanoic acid has been used as a carbon source, C-nanoparticles with size 1.6 nm were obtained despite the large size of the vehicle (100 nm). The major disadvantage of the micelles approach is its low thermal stability and critical supersaturation conditions, which are quickly reached due to the water evaporation [204].

Another example of the nanoreactor approach is the utilization of mesoporous metal-organic frameworks (MOFs) for the templated synthesis of CDs such as HKUST-1, ZIF-8, MIL-101 and ZIF-8C [171, 172]. Depending on the cave size of MOFs, C-dots having 1.5, 2.0 and 3.3 nm have been received from glucose after pyrolysis of the composite at 200 °C for 2 h and subsequent dissolution of the host in NaOH. In similar conditions pyrolysis of glucose without template resulted in CDs with 4.5 nm particle size [171]. The precursor adsorption in the MOFs pores was proved from N₂ adsorption experiment, which demonstrates that the pore volume of C-dots@MOFs substantially decreased from 130 to 5 cm³g⁻¹[171].

Several investigations were made using a mixture of CA and organosilanes [192, 202, 205–208]. We believe that the tendency to use Si-organic compounds related to the earlier research, where luminescence of the product received after the silane pyrolysis was mistakenly attributed to the formation of luminescence Si-nanoparticles [209]. In fact, the particles, obtained by the pyrolysis of the mixture of CA with APTES

and CA with n-propylamine are identical [210]. Thus, organosilanes in such types of synthesis perform as an N-doping agent but not as a template.

Several attempts to use molecular sieves and other microporous materials as templates for synthesis of CDs were described [211–216]. In most such cases there were essential contradictions between the size of the pores of the template and the size of the C-particles received. For example, silica ITQ-29 zeolite used for CDs preparation has 1.4 nm pore diameter while the resulted nanoparticles as much as 12 nm [211]. The possible reason for such discrepancies was demonstrated by Giannelis [217]. He used NaY zeolite treated with $\text{H}_2\text{N}(\text{CH}_2)_{10}\text{COONa}$ and citric acid for the preparation of photoluminescent carbogenic dots. The idea of the treatment was to increase the affinity of NaY zeolite toward CA by adding long-chain omega-amino acid, which bounds the zeolite surface and CA. CDs, obtained after the thermal treatment of the composite at 300 °C, were much large (4–6 nm) than pores in NaY (2.2 nm). Thus, the authors logically assumed that CDs were formed on the external surface of the support. Indeed, most crystalline microporous materials have a very small particle size (for example, 1500 × 400 nm) [218]. Such microcrystalline powders have an essential impact on macropores formed by the external surface of the crystallites [219]. Adsorption of hydrophilic precursors on the outer surface of zeolite crystals can result in the formation of CDs that are not confined within the pores of the template. Unfortunately, such a simple conclusion was ignored by most of the researchers who used microporous materials as the host for the preparation of CDs in the template [212].

The application of mesoporous materials in order to confine the growth and shape of carbon nanoparticles and to their agglomeration is rapidly developed in recent years [190, 207, 220–222]. Different inorganic mesoporous materials have been used as scaffolds, such as CaCO_3 [220], Al_2O_3 and $\text{AlO}(\text{OH})$ [193, 221, 222], two-dimensional layered germanate [223], but it seems silica gels are the most appropriate templates for CDs preparation under nanoreactor approach because of next properties:

- a. silica gels have a monomodal (one type) distribution of the pore size;
- b. different samples of silica gels with mesopores from 3 to 11 nm are available and samples with a smaller pore size;
- c. about 99% of the total surface area of silica gels is the area of mesopores;

- d. they have high thermal stability without changing the pore size;
- e. silica demonstrates very weak Bronsted and no Lewis acidities, which is positive to avoid possible side-catalytical reactions with an adsorbed substrate.

The first proof-of-concept on using the mesoporous template in CDs synthesis was made by Zong [170], where carbon precursor was introduced into the pores of an inorganic framework before pyrolysis, which enabling the confinement of the resulted CDs. Experimentally, it was a combination of “bottom-up” (citric acid was used as a carbon source) and “top-down” (composite was pyrolyzed at 300 °C for 2 h on the air in the presence of NaNO_3). Later luminescent CDs were obtained by rapid pyrolysis of citric acid and EDTA within mesoporous templating material (SBA-15) [218]. The calcination was also performed under a mixed bottom-up/top-down approach at a high temperature of 500 °C and in the presence of the oxidizing agents (KNO_3). The authors reported the formation of uniform CDs with average sizes below 4 nm and excitation-dependent photoluminescence [218].

Recently it was demonstrated that nanoreactor synthesis of CDs in the mesoporous template does not require high-temperature treatment (usually 170-250 °C) and oxidizing agents [192, 193, 208, 224]. For example, monodispersed spherical mesoporous silica with pores 3.1 nm was used for the templated synthesis of CDs from APTES on air at 250 °C [206]. Dissolved in HF nanocomposite resulted in luminescent CDs with 3.5 ± 0.9 nm particles, that perfectly fit the size of the pores [192]. Regardless of such mild conditions of the thermal treatment, authors suggest the formation of GOQDs having 7–10 defective graphene layers that are misoriented with respect to each other and contain various oxygen-containing functional groups. The particles received exhibit excitation-dependent PL at 430-500 nm [192]. Interesting research was published recently where silicas with very small pores (1.2 and 3.0 nm) have been used as a host for the templated synthesis of CDs from citric acid [224].

It can be seen from the above that application of mesoporous materials for the synthesis of CDs allows to confine the growth of embedded CDs and prevent their agglomeration. However, the method still results in CDs having different chemical nature and thus PL properties [183, 192, 193, 225, 226], that make their application in

analytical science very doubtful [227, 228]. For example, essential quenching of PL emission by oxygen was reported for CDs obtained by pyrolysis of quaternary ammonium ions trapped in ITQ-29 zeolite [211], while no such effect detected for other C-dots. For some CDs pH-dependent PL is reported [186, 229], while pH-independent for others [230]. Many C-dots demonstrate sharp selectivity towards Fe (III) ions, while to Cu^{2+} , Ni^{2+} and Hg^{2+} for others [227]. Such discrepancy can be caused by the fact that various nanoobjects with different compositions and surface chemistry are perceived as C-dots. Thus, the concept of C-dots requires further development and better separation of the particles is needed before their application. For example, chromatographic separation of as-prepared C-dots allows receiving nanoparticles with excitation-independent PL [169, 180, 224], which is crucial for their applications in bioimaging and for development of optical sensors [174, 202, 231, 232].

In Table 5 characteristics of CDs preparation from porous organo-minerals supports are summarized.

Influence of the precursor chemical nature on CDs properties

Various organic compounds, such as glucose, citric acid (CA), ascorbic acid, glycine, EDTA, etc. have been tested as carbonaceous precursors for bottom-up preparation of CDs, as individual components or in the mixtures.[233] In contrast to the top-down approach, bottom-up synthesis allows obtaining hydrophilic highly luminescent CDs with quantum yield (QY) more than 10% in the one-step process in mild conditions (at 150 – 300 °C), which not requires further activation and stabilization of the particles. Because of simplicity and high QY, bottom-up synthesis is fully dominated today [226].

Although many studies have been reported, the universal fluorescence origin of CDs still remains a question. CDs produced by different reactant and various approaches usually contain different complicated components and structures. However, one important statement was recognized that CDs prepared from conjugated precursor definitely have more sp^2 network than CDs from non-conjugated fragment [234].

Table 5 - Peculiarities of CDs synthesis in mesoporous organo-mineral materials

Nanoreactor	CDs precursor	Thermal condition	Method of CDs elution	PL/excitation, nm	QY, %	Size, nm	Ref.
Mesoporous Al ₂ O ₃	CA polyethyleneimine	200 °C for 6 min	3M NaOH	445/350	4.8	200 for 2000 (nanofibers)	[222, 235]
mesoporous γ-AlOOH		180 °C for 12 h		470/370	-	2.5-4.5	[221]
Mesoporous CaCO ₃	dextran sulphate	200 °C for 180 min		420-470/320	-	3.7-3.8	[220]
Spherical SiO ₂	APTES	250 °C for 5h	48% HF	420/350	-	3.5 ± 0.9	[236]
SiO ₂	Resol+ PEG	900 °C on Air for 2h	2M NaOH	430/360	11-15	1.5–2.5	[195]
Mesoporous silica	CA + NaCl + LiCl + KNO ₃ .	300 °C for 2 h in air	2 M NaOH	410/340	23	1.5–2.5	[170]
SiO ₂	APTES+ CA	180 °C for 3h, hydrothermal	NaOH	435/360	3.3-9.3	2.8 ± 0.3 (in SiO ₂) 2.7 ± 0.3 (after etching)	[202]
SBA-15	furfuryl alcohol+ oxalic acid	850 °C	water	550/370	-	2.5–5.2	[216]
Mesoporous silica with 1.2 and 3 nm pore size	CA	300 °C for 3 h in air	Methanol	465/340	-	-	[224]
Mesoporous silica	APTES	250°C during 5 h in air	40 %HF	-	-	3.3 ± 0.9	[206]
Mesoporous silica	APTES	250°C during 2 h	-	-	-	3	[237]
SBA-15	-	150 °C for 3 h	water	540/340	-	2.4	[213]
Silica nanorods	CA+ NaCl + LiCl + KNO ₃	500 °C 5 min in N ₂	water	420/334	1-5	3.4±0.4	[218]
SiO ₂	CA	170 °C, from 5-600 min	Water/ NaHCO ₃ / NaOH	447/340	-	1.5-3	our

CA is a common and effective carbon source for the preparation of CDs [194, 238–240]. Simple pyrolysis of CA during 30 min lead to the preparation of blue-emitted CDs with QY around 9%. Using organic acid, sugars, natural juices as raw materials, CDs can be obtained with QY 3-13%. Based on summarize data in Table 6, hydrothermal synthesis is the most commonly used approach in the temperature range 120-300°C. CHN, XPS and FTIR analysis help to confirm the presence of functional groups especially carbonyl or carboxylic fragments. Another feature of these particles

is an excitation-dependent behavior of emission spectra. Choice of the precursor is a crucial step for CDs preparation. Including N element in precursor significantly increase QY up to 80%, Table 6.

Table 6 - Summary of representative acids and green synthetic precursors for CDs preparation

Precursor	Method condition	Composition	Particle size, nm	PL behaviour	QY, %	Ref.
CA	Pyrolysis 200°C Atm 30min	46.22, 3.87, 49.91 for C(%), H(%), O (%)	1.4 nm (AFM)	Excitation-independent	9	[238]
Ascorbic acid	Hydrothermal treatment at 180°C, 240 min	FTIR peaks at 3425 and 1637 cm^{-1} (O-H, C=O)	2-2.5 (TEM)	Excitation-dependent	6.79	[230]
Glucose	Alkali- or acid-assisted ultrasonic synthesis	XPS peaks at 286.2 and 288.3 eV (C-O, C=O)	15.7 nm, agglomerates	Excitation-independent; Excitation-dependent	1.1; 2.4	[241]
Strawberry juice	Hydrothermal treatment at 120°C, 12h	XPS 288.2, 286.3, 285.6, 284.6 eV, (C-O, C-N, C-O, C=C)	5.2 (TEM)	Excitation-dependent	6.3	[242]
Sugar cane juice	Hydrothermal treatment at 120°C. 3h	1693 and 1376 cm^{-1} (C=O vibration and symmetric carboxylate stretching)	3 nm		5.76	[243]
Orange juice	Hydrothermal treatment at 120°C, 2.5h	Presence of C=C, C-C, C-OH, C-O-C, C=O, COOH	1.5-4.5	Excitation-dependent	26	[244]
Chitosan	Hydrothermal treatment at 180°C, 12h	59.02, 7.73, 6.51, 26.74 for (C, %), (N, %), (H, %), (O, %)	4-7	Excitation-dependent	43	[245]
Citric acid and ethylenediamine	Hydrothermal treatment at 150–300°C	From FTIR C=O at 1635 cm^{-1} , C-NH-C at 1126 cm^{-1} , N-H at 1570 cm^{-1}	2-6	Excitation-dependent	80	[229]

However, the presence of several components in reactant mixture cause formation by-product and residual of primary precursor, thus purification step is needed. Temperature is an important parameter during formation CDs. Pyrolytic carbonization of CA in ethanolamine (EA) at three different stages of the pyrolytic was investigated process [246]. Three distinct photoluminescent species was obtained. The organic fluorophores with the strongest PL were obtained at the low-temperature stage (180°C). Above 230°C, fluorescent CDs were formed. At 230°C CDs showed excitation-independent emission, however, CDs prepared at 300°C results in excitation-dependent emission. It is important to note that the PL intensity and QY were dramatically decreased.

N,S-doped CDs also exhibit strong blue fluorescence under UV excitation and excitation-dependent emission[247]. CA, cysteamine (CAm), L-cysteine (Cys) were used as precursors. They found that 5-Oxo-3,5-dihydro-2H-thiazolo[3,2-a] pyridine-7-carboxylic acid (TPCA) [247] is the main ingredient and actual fluorescence origin of N, S-CDs.

Besides blue-emissive CDs, multiple-coloured emissive (blue to red light) CDs can be synthesized from CA and urea by varying the reaction conditions (the ratio of CA to urea and the reaction temperature) [248].

Red-, green-, and blue emissive CDs were also received from aromatic isomers of p-, o-, and m-phenylenediamines (PhDA) in ethanol via a solvothermal route[249]. Interesting, p-PhDA in different solvents revealed multiple-colour emissive CDs. The emission peak can be shifted from 540 nm to 614 nm. Based on the investigation of the solvent effect, the red emission of CDs originates from molecular states. Thus, mixing of CA and amines causes the formation of citrazinic acid-derivatives. Aromatization fragments increased with the increasing of the reaction temperature and time. These conjugated molecules are further aggregated to enhance the rigidity of the nanoparticles and form the sp^2 nanodomain via intermolecular interaction, such as p-p stacking and H-bonding. Thus, it forms typical CD structures with an sp^2 nanodomain embedded into the amorphous sp^3 matrix, which is composed of non-conjugated molecules, cross-linked polymers, or amorphous carbon materials [234].

Table 7 - Important characteristics of N-containing CDs

N-Precursor	Method condition	Purification	Particle size, nm	PL behavior	QY, %	Ref.
CA and EDA	Hydrothermal treatment at 150–300°C		2-6	Excitation-dependent	80	[229]
CA and EDA	hydrothermal procedure, 180°C, 5h	centrifugation at 5000 rpm, dialysis for 24 h	-	Excitation-dependent	53	[239]
CA and HMTA	hydrothermal procedure, 180°C, 5h	centrifugation at 5000 rpm, dialysis for 24 h	-	Excitation-dependent	17	[239]
CA and TEOA	hydrothermal procedure, 180°C, 5h	centrifugation at 5000 rpm, dialysis for 24 h	~5 nm	Excitation-dependent	7	[239]
CA and EA	Pyrolysis 180°C (30 min), 230°C (30 min), 300°C (1h)	Dialysis 3500 Da	8 nm	Excitation-dependent and Excitation-independent	50; 15	[246]
CA and diethylenetriamine	Pyrolysis 180°C, 250°C, 300°C (1h)	centrifugation at 8000 rpm, filtration 0.25 µm, dialysis 3500 Da	0.5-2 nm; 6.6 nm; 15.1 nm	CDs-180 and CDs-250 show excitation-independent, when CDs-300 - excitation-dependent	90; 74; 23.5	[194]
CA and Cys	hydrothermal procedure, 200°C, 3h	Dialysis 1000 Da		Excitation-independent	64	[247]
CA and urea	hydrothermal procedure, 140-200°C	centrifugation at 10000 rpm	4-5 nm	Excitation-independent	52.6, 35.1, 12.9	[248]
p,o,m-PhDA	Solvothermal, 180°C, 12h	Silica column	10 nm 8.2 nm 6.0 nm		20.6; 10.4; 4.8	[249]

2.7.3. Mechanism of PL origin

Due to the unclear origin of PL, several accepted luminescence mechanisms such as the surface state, quantum confinement effect and molecular fluorescence were investigated in the literature. *Molecular fluorescence* is attributed to the formation of fluorescent impurities during the bottom-up chemical synthesis that contributes to the majority of emission from CDs samples.

The surface state is correlated with a degree of surface oxidation and surface functional groups. The red-shifted emission of CDs is closely related to the oxygen content on their surface. The higher the degree of surface oxidation, the greater the number of surface defects [176] these defects can trap excitons, and the radiation from the recombination of trapped excitons causes the red-shift emission. On the other hand, the band gap was strongly attributed to the incorporated oxygen species. The band gap reduces with the increase of oxygen content on the CDs surface, that is, red-shifted emission is derived from the increased degree of surface oxidation. Green-emissive and yellow-emissive CDs with the same size distribution and chemical groups showed different degrees of surface oxidation [250]. As mentioned before in the precursor section, *surface functional groups* have a direct influence on the PL of CDs.

Some years ago, *quantum confinement mechanism* was the most popular reason for excitation-dependent emission behavior of CDs. This effect was more observed in a semiconductor crystal. Existing of this phenomenon is closed related to bandgap and size-dependent energy relaxation dynamics. Graphene-based materials are a good example of its demonstration. Authors in [251] fabricated GQDs with different particle sizes (5–35 nm). They noticed that with increasing of GQDs size, the absorption peak energy of the GQDs decreased and the red-shifted behavior of emission was due to the increase of the particle size of GQDs. Combination of some effect can attribute in PL profile. A series of CDs with different emissions were prepared by varying their degree of surface oxidation or their size[252]. Results showed that the degree of surface oxidation and the π -electron system has a significant influence on the energy gaps of the surface states. The higher the extent of surface oxidation or the π -electron system is, the smaller the energy gap of the surface states in the CDs is. That is, the increase of particle size or the degree of surface oxidation leads to a redshift in the emission wavelength of CDs.

2.7.4. Applications

CDs display low toxicity and good biocompatibility. Due to high fluorescence and stability in aqueous solution, CDs are widely used in the field of fluorescence sensing analysis. PL behavior of CDs is sensing to the surrounding environment. Decreasing or increasing of PL intensity can be observed due to the interaction of CDs

with analytes. PL sensing detection of analytes can be carried out in solution or solid phase. Detection of metals, small molecules and bioimaging generally made in solution mode, when adsorbent study, fingerprint sensing in solid one [253].

The most successful feature of CDs is the detection of metals via quenching of PL intensity. Detection of the next metals with LOD were reported Cu^{2+} (5 nmol L^{-1}), [254] Fe^{3+} ($0.239 \text{ } \mu\text{mol L}^{-1}$) [255], Hg^{2+} (0.12 nmol L^{-1}), [256] Cr^{6+} ($0.26 \text{ } \mu\text{mol L}^{-1}$), [257] Au^{3+} (64 nmol L^{-1}) [258] and etc⁷. Authors in these articles reported about possible mechanism of interaction metals with CDs such as fluorescence resonance energy transfer (FRET), inner filter effect (IFE), electron transfer (EIT), aggregation-induced emission enhancement (AIEE) effect, aggregation-induced emission quenching (AIEQ) effect, static quenching effect (SQE), etc. The **AIEE** effect is the phenomenon of fluorescence enhancement which results from the aggregation of fluorescent organic molecules or nanoparticles [260]. The aggregation of CDs usually enhances the extent of π -conjugation and hampers the rotational vibration of their functional groups, resulting in increasing of the radiative rate and the decrease of the non-radiative rate. The **SQE** usually arises from the formation of non-fluorescent complexes between quenchers and the fluorophores in the ground state, not relying on diffusion or molecular collisions. **IFE** is a typical non-irradiation energy conversion model in spectrofluorometry, which only requires a good spectral overlap between the absorption band of the absorber and the excitation/emission band of the fluorophore [176]. Cu^{2+} , Fe^{3+} , and Hg^{2+} are typical metals that can more easily join with functional groups of CDs with **EIT**. Upon excitation, CDs play the role of the electron donors that transferred excited electron forward to the metal receptor and quenching of PL intensity is occurs.

Interesting that CDs were used for the fluorescence analysis of many biomolecules and aromatics compounds such as lysine [261], glucose [262], vitamin B12 [263] tetracycline [264] 2,4,6-trinitrophenol [265], chlorophenols [266] etc. CDs with significant π -network oxygen-contained functional groups such as -OH, -COOH was formed with 2,4,6-trinitrophenol [265] complexes due to π - π stacking interactions.

Based on these sensing behaviors in solution, new CDs-based adsorbent was developed. In 2015 [267] *periodic mesoporous organosilica* embedded with CDs was

proposed as the adsorbent for removal of 2,4-dichlorophenol ($q_{\max}=99.70 \text{ mg g}^{-1}$) and inorganic metal ions in the next order $\text{Hg(II)} > \text{Cu(II)} > \text{Pb(II)}$. Two different mechanisms for organic molecule and metals were proposed. In the first one, the $n-\pi$ electron donor-acceptor interaction between O- and N-containing groups in mesoporous organosilica and the benzene ring in 2,4-dichlorophenol was responsible for adsorption of 2,4-dichlorophenol, while the electrostatic force and complex formation between metal ions and amide groups co-contribute to the improvement of metal ions adsorption. As selective SPE adsorbent for removal of trace cadmium pollutant ($q_{\max}=2420 \text{ } \mu\text{g g}^{-1}$) ions was developed by solid-phase by immobilizing CDs on the *microcarrier cytopore* [268]. In addition, cadmium was determined in fish and mollusc samples with satisfactory recoveries ($\geq 97.4\%$) in batch mode using magnetic (Fe_3O_4) N-doped CDs [269]. *N-doped CDs* into pure *alginate hydrogel beads* could effectively adsorb Gd(III) (201.21 mg g^{-1}) from aqueous solutions [270]. Obtained results showed that in competitive adsorption the adsorbent had a stronger affinity to Gd (III) than to Al (III) , Co (II) , Ni (II) , Zn (II) , and Mg (II) . This behavior can be related that high-valent metal ions were more favorable for binding to adsorption sites than the low-valent. Another similar structure of CDs encapsulated in sodium alginate hydrogel to the detection of tetracycline up to 43.03 mg g^{-1} . Presence of CDs on solid can increased adsorption capacity for removal of aromatic dyes. Hybrids of 5% CDs with magnetic ZnFe_2O_4 nanoparticles can be able to remove of methyl orange up to 181.2 mg g^{-1} [271]. Polyacrylonitrile nano-porous fibres functionalized with N-CDs showed higher adsorption capacity for methyl orange removal (422 mg g^{-1}).

N-CDs decorated on the spherical porous silica gel was used as packing materials for chromatographic column and demonstrate selective behavior for polar compounds in hydrophilic interaction liquid chromatography (HILIC) mode [272]. In 2019 [273], Hybrids of CDs/fatty acid/ Fe_3O_4 was presented as a novel reusable adsorbent for the reliable efficient adsorption (76.23 ng mg^{-1}) and rapid determination of BaP. Last year [274], composite based on CDs/ Fe_3O_4 /CNTs were synthesized and evaluated for carbamazepine removal from water (65 mg g^{-1}). Carbamazepine was good removing at wide pH range regardless of the surface charges, thus $\pi-\pi$ electron donor-acceptor interaction and H-bonding respond for adsorption.

2.8. Conclusion for the theory review

- 1) Contamination of the products with PAHs is an indicator for assessing the eco-health of aquatic environments.
- 2) The concentration of aromatic compounds in lipophilic nature is commonly higher.
- 3) For sample preparation of oil sample before HPLC determination of PAHs, LLE with dimethylformamide and cyclohexane are the most used procedure
- 4) Adsorbents with aromatic functionality (hypercrosslinked polystyrene, rGO) showed high selective to aromatic analytes in oil media.
- 5) π - π interaction is a principal interaction between analyte and adsorbent for selective adsorption
- 6) Recently discovered carbogenic nanoparticles such as carbon nanodots, graphene oxide, graphene oxide nanodots, etc. demonstrated promising features for their application as active sites for selective adsorbents
- 7) Functionalization of carbogenic nanoparticles is the way to create new materials for adsorption of aromatic compounds.
- 8) Presence of large π -electron system and high surface area in graphene derivatives make this nanomaterial very prospective for utilization in electroanalytical chemistry.

3. Experimental section

3.1. Materials and methods

3.1.1. Chemicals and reagents

Silica gels with a different pore size (d) ($\text{SiO}_2(\text{d})$, $\text{d} = 4 \text{ nm}$, 6 nm , 9 nm , 11 nm) and fumed silica (Asil), (3-Aminopropyl)triethoxysilane (APTES, $\geq 98\%$), (3-Mercaptopropyl)trimethoxysilane (MPTMS, 95%), N-[3-(Trimethoxysilyl)propyl]ethylenediamine (EDAS), chloroform anhydrous, toluene anhydrous, diglyme, N,N-Diisopropylethylamine (DIPEA), 9-(chloromethyl)anthracene (9CMA), 9-Anthracenecarboxaldehyde (9ACA), anthracene (Ant), sodium nitroprusside dehydrate (99%), poly(methyl methacrylate) (PMMA), N,N'-Dicyclohexylcarbodiimide (DCC, 99%), acetonitrile (MeCN, $\geq 99\%$), potassium permanganate (KMnO_4 , 99%), sodium borohydride (NaBH_4 , 99%), hydrogen peroxide solution (H_2O_2 , $30\% \text{ (w/w)}$) were purchased from Sigma–Aldrich (USA). Ninhydrin (99%), sulfuric acid (H_2SO_4 , $95\text{--}98\%$) were from QHEMIS (Brazil), graphite and N,N-Dimethylformamide (DMF, 99.8%), sodium bicarbonate (99%) were from Synth (Brazil). Sodium hydroxide (99%) was from Dinamica (Brazil). Citric acid anhydrous (99.5%) was from Proquimios (Brazil), sodium bicarbonate (99%) was from Synth (Brazil). Diethylstilbestrol, estriol (both 97%), sulfamethoxazole (SMZ, 98%) and trimethoprim (TMP, 98%) were from Sigma-Aldrich (USA). To prepare Britton-Robinson buffer (0.04 mol L^{-1}) with 0.5 mol L^{-1} of supporting electrolyte the following reagents were used: boric acid (Neon, 99.5%), acetic acid (Dinamica, 99.7%), phosphoric acid (Vetec, 85%), hydrochloric acid (Merck, 37%), sodium hydroxide (Vetec, 97%), sodium nitrate (Quimica Moderna, $>99\%$). Anthracene was recrystallized from acetone. Toluene was kept in a dark bottle over 3 \AA molecular sieves (4-8 mesh, Sigma-Aldrich) after drying with calcium hydride (from Sigma-Aldrich) and distilled. Empty SPE Tube (with frits) volume 3 mL was used to preparation SPE cartridge packed with synthesized materials. The aqueous solutions were prepared using ultra-pure water from a water purification system (The PURELAB Classic, Elga, UK).

3.1.2. Characterization techniques

The pH value of the solution was measured using a PHS-3E meter with BioTrode lab electrode (Hamilton, USA). The electrical conductivities of supernatant liquids were measured using HI 8633 conductivity meter (HANNA instruments, UK). The specific surface area and pore size of silica gel samples were determined using the nitrogen adsorption-desorption method at 77 K on an ASAP 2020 (Micromeritics, USA). Elemental analyses (% of carbon, hydrogen and nitrogen (CHN)) of chemically modified silicas were determined by PE-2400 elemental analyzer (Perkin Elmer, USA). Thermogravimetric analysis (TGA) was performed on Pyris 1 TGA equipment (Perkin Elmer, USA). The heating rate was 10 °C/min in the working range at 25-900 °C. Fourier transform infrared spectroscopy (FTIR) spectra were obtained in the region 4000-400 cm⁻¹ on FTLA-2000 spectrometer (Thermo Scientific Nicolet). Nuclear magnetic resonance (NMR) spectra in liquid state were recorded on Avance III HD 400 MHz spectrometer (Bruker, USA). Solid-state ¹³C and ²⁹Si nuclear magnetic resonance spectroscopy (CP/MAS NMR) was used to confirm the fixation of modifier in the materials and to estimate the content of different silica substructures. The measurements were performed on an AC300/P spectrometer (Bruker, USA) operating at 100.6 MHz for ¹³C and at 79.5 MHz for ²⁹Si. Adamantane and kaolinite were used as external reference substances for the ¹³C and ²⁹Si NMR experiments, correspondingly. Electronic (UV–Vis) absorption spectra (in 200–450 nm range) were measured by Cary 100 UV-visible spectrophotometer (Agilent, USA). Photoluminescence measurements of liquid samples were made using a model LS 55 luminescence spectrometer (Perkin-Elmer, UK) with 1 cm optical path length quartz cuvettes and solid samples were recorded using Quanta Master (PTI, USA) spectrofluorometer with powder holders. For solution samples, 1 cm optical path length quartz cuvettes were used, when solid samples were recorded using powder holders. The 3D photoluminescence (PL) emission spectra were recorded at room temperature and in ultra-high vacuum (better than 10⁻⁷ mTorr) conditions at the Toroidal Grating Monochromator (TGM) beamline of the Brazilian Synchrotron Light Laboratory (LNLS). Monochromatic photons from 4.5 – 8 eV (~276 to 155 nm), filtered using a quartz window, were used for exciting the samples with emitted light collected by an

optical fibre (aperture: 600 μm) coupled to the chamber by vacuum feedthrough and connected to a R928 Hamamatsu photomultiplier (PMT). The spectra were corrected for the variation in the incident flux of the excitation beam using the excitation and emission spectra of sodium salicylate ($\text{C}_7\text{H}_5\text{NaO}_3$) as standard. The surface composition of composited was analyzed by X-ray photoelectron spectroscopy (XPS), using a K-alpha X-ray photoelectron spectrometer (Thermo Fisher Scientific, UK) equipped with a hemispherical electron analyzer and an aluminium anode X-ray source ($\text{K}\alpha = 1486.6 \text{ eV}$), providing an energy resolution $\sim 1 \text{ eV}$. The morphology of the samples was studied by means of a low-vacuum JSM-6490LV scanning electron microscope (SEM) (JEOL, Japan). Atomic force microscopy (AFM) images were obtained using a Bruker MultiMode 8 microscope. A Si tip with a force constant of 0.4 N m^{-1} and a resonance frequency of 70 kHz were used in tapping peak force method. The samples were diluted in deionized water, ultrasonicated and a single drop was dried on a clean mica surface in a nitrogen flux for 2 h. Statistical analysis of the thickness distribution was performed using Gwyddion 2.53 software. Electrochemical experiments were carried out on an IviumStat potentiostat/galvanostat (Ivium Technologies, The Netherlands) apparatus with a conventional three-electrode cell. Modified carbon paste electrode (CPE) as working electrode, platinum wire as the auxiliary electrode and saturated calomel (SCE) or Ag/AgCl as reference electrodes were used. Differential pulse voltammetry was applied with the following parameters: pulse amplitude of 50 mV , pulse time of 50 ms , step potential of 1 mV and scan rate of 10 mV s^{-1} . The powder X-ray diffraction (XRD) pattern of the CDs product was collected at room temperature using a X'Pert Pro (Panalytical, UK) diffractometer, equipped with a PIXcel one-dimensional hybrid pixel technology position-sensitive device detector and operated with Ni-filtered CuK α radiation ($\lambda = 1.54178 \text{ \AA}$). The transmission electron microscopy (TEM) images were obtained using JEOL FEG JEM 2100F microscope operating at 200 kV . The samples for TEM study were prepared by dropping C-dots suspensions in Milli-Q water onto an ultrathin carbon-coated copper grid and allowing the suspensions to dry in air.

3.2. Preparation of materials

3.2.1. Activation of silica gel

Starting porous silica gels were refluxed under agitation in aqueous nitric acid HNO_3 (3 mol L^{-1}) during 10 h. It was made to hydroxylate the surface and to wash out impurities and trace metals. Subsequently, silicas were filtered and washed with deionized water and dried at 200°C for 4 h under vacuum. Prior to modification, porous and non-porous (Asil) silicas were activated by heating in a muffle at 550°C for 5 h. Activation step is needed to remove the hydrogen bond-absorbed water molecule on the silica gel surface and at high temperature the silanols on the silica surface can also undergo dehydration and condensation to convert into a siloxane bond. These siloxane groups are capable to reversible reaction with water and methanol [275]. Commercial characteristics of the starting silicas before activation are given in Table 8.

Table 8 - Commercial information about silica gel

Silica denoted	Particle size (μm)	Pore size, d (nm)
Asil	0.2-0.3	Non-porous
$\text{SiO}_2(4)$	63-200	4
$\text{SiO}_2(6)$	40-63	6
$\text{SiO}_2(9)$	63-200	9
$\text{SiO}_2(11)$	40-75	11

3.2.2. Synthesis of modified supports

$\text{SiO}_2(d)\text{-NH}_2$. 12 g of the activated silica gel or aerosil was suspended in 110 mL of dry toluene in a round bottom flask equipped with a magnetic stirrer bar and a reflux condenser with a calcium chloride trap to keep out atmospheric moisture. Afterwards, a mixture of APTES (3.0 mL) in 70 mL dry toluene was added to the suspension under constant stirring. The reaction mixture was gently refluxed for 10 h with stirring. After slowly cooling-down to room temperature, the solid phase of N-contained silica gels was separated by filtration, washed in a Soxhlet apparatus with dry toluene during 24 h to remove the excess of silane agent and dried at 115°C for 7 h under vacuum. The completeness of washing of product was tested by the reaction with ninhydrin (1%) to the absence of blue colour of the washing solution. Obtained products were designated as $\text{SiO}_2(d)\text{-NH}_2$ and Asil-NH_2 .

SiO₂(11)-EDA. Preparation of silica gel with ethylenediamine groups (*SiO₂(11)-EDA*) was following a similar approach, but using 9 g of the activated silica gel *SiO₂(11)*, 1.95 ml of EDAS in 100 mL dry toluene and refluxed for 22 h. Post-treatment was carried out similar to *SiO₂(d)-NH₂*.

SiO₂(4)-SH(n). Preparation of silica gel with mercaptopropyl groups was following in similar way as *SiO₂(d)-NH₂*, but 10 g of the activated silica gel *SiO₂(4)* and 2.0 ml of MPTMS in 100 mL dry toluene were used and refluxed for 22 h under inert nitrogen atmosphere. Reproducibility of synthesis methodology was evaluated by preparation two samples *SiO₂(4)-SH(n)*, where n is related to replicates 1 and 2.

3.2.3. Synthesis of anthracene-functional silica gel

SiO₂(d)-Ant-1-t. The procedure was performed for all aminopropyl silica gels with different pore size. Mixture (240 ml) of 9CMA (0.5 g, 2 mmol) and DIPEA (3.0 ml, 17 mmol) in chloroform was introduced into a three-necked 500 ml flask supplied with a mechanical stirrer and reflux condenser with a calcium chloride tube. Aminated silica gels (1.2 g) were added under constant agitation. The synthesis was carried out at room temperature. Progress of the reaction was controlled by UV-Vis spectroscopy of solution above solid at a different synthesis time interval (t, min). For this, an equal portion of the reactive mixture (~40 mL) was collected using a pipette. The supernatant was filtered through a 0.22-micron filter and used for further UV-Vis study. Solid-phase was separated by centrifuge (5 min at 3000 rpm) and washed with chloroform in apparatus Soxhlet to remove the excess of anthracene reactant. The completeness of washing was verified by flame test for Cl-ions (green colour of a flame) and UV-Vis spectroscopy. Finally, the products *SiO₂(d)-Ant-1-t* and *Asil-Ant-1-t* were dried under vacuum at 120 °C for 5 h.

SiO₂(11)-Ant-2b. 9ACA (1.6 g, 8 mmol) in dry toluene (350 ml) was added into a 500 ml two-necked flask equipped with a magnetic stirrer and a Dean-Stark trap with a reflux condenser. The mixture was heated at 95 °C during 30 min to completely dissolving of 9-ACA. Then 5 g of *SiO₂(11)-NH₂* was added under constant agitation and reaction mixture was refluxed for 20 h. After cooling, the solid phase was filtered through a glass Schott filter and washed several times with toluene. The sample was washed with chloroform in Soxhlet apparatus for 5 days. The product was dried under

vacuum at 100 °C for 3 h to obtain SiO₂(11)-Ant-2a. The second step was the reduction of imine bonds. In a 500 ml flask, equipped with a magnetic stirrer, 4.5 g of synthesized imine was mixed with 80 ml NaBH₄ (20 mmol) in diglyme. The mixture was constantly agitated at room temperature under inert dry nitrogen atmosphere during for 28 h. The yellow solid phase was filtered through a glass Schott filter and washed several times with diglyme and then washed with methanol in Soxhlet apparatus for 24 h. To improve reduction, the sample was transferred into the flask with 45 ml NaBH₄ (10 mmol) in methanol and agitated for 24 h. The yellow solid phase was filtered through a glass Schott filter and washed several times with methanol in Soxhlet apparatus for 5 days and then the solvent was changed to chloroform for 28 h. The obtained product was dried at 120 °C during 7 h to obtain SiO₂(11)-Ant-2b.

SiO₂(11)-Ant-3b. 9ACA (2.1 g, 10 mmol) in dry toluene (350 ml) was added into a 500 ml two-necked flask equipped with a magnetic stirrer and a Dean-Stark trap with a reflux condenser. The mixture was heated at 95 °C during 30 min to completely dissolving of 9ACA. Then 5 g of SiO₂(11)-EDA was added under constant agitation and reaction mixture was refluxed for 20 h. After cooling, the solid phase was filtered through a glass Schott filter and washed several times with toluene. The sample was washed with toluene in the Soxhlet apparatus for 4 days. The product SiO₂(11)-Ant-3a was dried under vacuum at 120 °C for 11 h. The second step was the reduction of imine bonds. In a 500 ml flask, equipped with a magnetic stirrer, 4.5 g of synthesized imine was mixed with 80 ml NaBH₄ (15 mmol) in diglyme. The mixture was constantly agitated at room temperature under inert dry nitrogen atmosphere during for 28 h. The yellow solid phase was filtered through a glass Schott filter and washed several times with diglyme and then washed with methanol in Soxhlet apparatus for 7 days. Then the solvent was changed to chloroform for 24 h. The obtained SiO₂(11)-Ant-3b was dried at 120 °C during 8 h. Presence of imine-groups was controlled by reaction with HCl ($1 \cdot 10^{-2} \text{ mol}^{-1}$) and extraction in toluene. The reaction did not lead to a colored organic layer, that's why the product did not wash with HCl.

SiO₂(11)-Ant-4b. In a two-necked flask of 500 ml equipped with a magnetic stirrer, a Dean-Stark trap with a reflux condenser and a calcium chloride trap was used to keep out atmospheric moisture, 9ACA (2.5 g, 12 mmol) in 300 ml of toluene was

introduced under constant agitation. The reaction has been heating prior to boiling of toluene. Dropping funnel with EDAS (2 ml, 9 mmol) in 25 ml toluene was equipped to the flask. During 1 h, all aminosilane was added. After refluxing for 40 h, production of intermediate silane 4a was prepared. 9 g SiO₂ (11) in 100 ml toluene was added to 4a product. Water formation during synthesis was eliminated in a Dean-Stark trap with toluene. After 18 h, the orange product was filtered through a glass Schott filter and washed several times with toluene and then washed with toluene in Soxhlet apparatus for 3 days. Then the solvent was changed to chloroform for 24 h. Obtained imine SiO₂(11)-Ant-4a was dried at 120 °C during 5 h. In a two-necked 500 ml flask, equipped with a magnetic stirrer, NaBH₄ (2.3 g, 60 mmol) in 100 ml methanol was added under inert nitrogen atmosphere. Prepared imine (9.4 g) in 110 ml methanol was added. Hydrogen evolution has been stopped in 2 h. The new portion of NaBH₄ (0.7 g, 20 mmol) was introduced to the mixture and stirred for 1 h. The product was filtered through a glass Schott filter, washed several times with methanol and transferred into Soxhlet apparatus to wash in methanol for 4 days, next solvent was changed to chloroform for 3 days. The obtained material was dried at 120 °C during 5 h. Subsequently, the product was put in a flask with 150 ml (1·10⁻² M) and shaken for 2 h. Due to hydrolysis of imine groups, excess of 9ACA was extracted with toluene. The yellow organic layer was separated by centrifugation 2000 rpm for 5 min. Extraction was repeated to get a transparent organic layer (4 times). Next, final the product SiO₂(11)-Ant-4b was washed with water and dried.

SiO₂(11)-Ant-5b. In a round-bottom flask of 125 ml equipped with a magnetic stirrer and reflux condenser with a calcium chloride trap was used to keep out atmospheric moisture, 9ACA (0.2 g, 1 mmol) in 60 ml diglyme was introduced. EDAS (0.2 ml, 1 mmol) was added under agitation and reflux for 14 h to produce intermediate modifier 5a. Solution of 20 ml NaBH₄ (0.2 g, 5 mmol) in diglyme was transferred into reaction mixture 5a and stirred for 44 h at room temperature. As a result, the color of the mixture was changed from orange to yellow, 5b. The mixture was filtered, and the filtrate was transferred in a two-necked flask with a reflux condenser and SiO₂ (1 g) in 10 ml diglyme was added. Under inert nitrogen atmosphere and constant agitation, the reaction was carried out at 110 °C for 24 h. The solid phase was separated via glass

Schott filter and transferred into the Soxhlet apparatus to wash in chloroform for 24 h. The obtained material was dried at 115 °C during 4 h. Presence of imine-groups was controlled by reaction with HCl ($1 \cdot 10^{-2} \text{ mol l}^{-1}$) and extraction in toluene. The reaction did not lead to colored organic layer, that's why the $\text{SiO}_2(11)\text{-Ant-5b}$ has not been washed with HCl.

3.2.4. Synthesis of GO and modification of silica gel with GOQDs

GO was synthesized from graphite powder using “Improved method” [276]. In brief, 200 mL of a mixture of concentrated H_2SO_4 and H_3PO_4 (9:1 v/v) was added to graphite powder (1.5 g) in a 500-mL round-bottom flask equipped with a mechanical stir bar. Then KMnO_4 (9 g) was added slowly at room temperature under stirring and after the flask was heated to 50 °C for 12 h. The obtained lite-pink mixture was cooled down, poured slowly onto ice (400 mL) with 30% H_2O_2 (20 mL) giving orange suspension. The filtrate was centrifuged (3000 rpm for 15 min), and the supernatant was decanted away. The remaining solid material was then washed in succession with MilliQ water to pH~4, then with HCl (2%) to remove manganese (control with ICP-OES) and other impurities and again with water to pH ~7. For each washing, the mixture was centrifuged (3000 rpm for 20 min) and the supernatant decanted away. The material remaining after this extended, multiple-wash process was washed with ethanol and vacuum-dried 12 h at 45 °C.

Finally, 40 mg of dried product was sonicated in 50 mL of DMF for about 2 h. Obtained brown dispersion was centrifugated at 5000 rpm during for 5 min to remove large particle in the form of precipitation. Obtained supernatant emitted green-blue luminescence in UV light was used for immobilization was named as GOQDs and used for further immobilization. GOQDs were prepared in one-step ultrasonic synthesis [196].

Silica gel modified with GOQDs was labelled as **$\text{SiO}_2(4)\text{-GOQDs}$** . GOQDs were covalently immobilized on silica gel surface via silica-immobilized aminosilane and carboxylic groups of GOQDs as it described elsewhere [277]. $\text{SiO}_2(4)\text{-NH}_2$ (3 g) was added to the suspension of GOQDs in 50 mL of DMF and 40 mg of DCC were added under stirring. The suspension was heated at 85 °C for 60 h with periodic sonification for 30 min. The solid phase was separated by decantation, washed with DMF, methanol

and water under ultrasonic treatment (5 min). Finally, the precipitate was dried at 120 °C for 8 h to obtain about 3 g of SiO₂-GOQDs.

3.2.5. Synthesis of Carbon Dots samples

Without a nanoreactor approach

The CDs was prepared by pyrolysis of citric acid based on the “bottom-up approach” [113]. Approximately 10 g of citric acid was placed into 250 mL two-neck round-bottomed flask and headed to 170 °C using graphite bath under nitrogen atmosphere. During heating, the color of the melted material changed from colorless to yellow. After 30 min, the liquid was an orange color that indicated the formation of CDs. Subsequently, the orange liquid was added into 130 mL of NaOH (10 mg mL⁻¹) solution under vigorous stirring to get pH~7. The obtained sample was named as **CDs-170**.

CDs-200 was prepared by direct pyrolysis of CA [113]. CA (2 g) was loaded in a 10-ml beaker and heated to 200 °C. The CA was liquated, and the color was changed from colorless to pale yellow, orange and finally, it was turned to black solid in about 3 h. To prepare a dispersion of CDs-200, the black solid was dissolved with 50 mL of 10 mg mL⁻¹ NaOH solution and was stored in the refrigerator at 4°C before used.

Adsorbent based on CDs-170 was synthesized in a next way. Aminosilica gel SiO₂(9)-NH₂ (1.0 g) was mixed with an aqueous solution of CDs-170 (25 mL, C(CA)=0.1 mol L⁻¹) at pH 4 and shaken during 24 h to reach equilibrium. The obtained suspension was centrifugated during 10 min at 3000 rpm, decantated and washed two times with ultra-pure water. Therefore, the solid was transferred into a 50-mL round-bottomed flask and heated at 150 °C, using oil bath, under argon atmosphere during 4 h (yield=84% w/w). The solid was designated as **SiO₂(9)-NH₂¹CDs-170**.

CDs obtained via nanoreactor approach

Nanoreactor approach contains several stages in Figure 9: preparation of solid support, hybridization support with CDs, releasing of CDs.

¹ / is composite prepared from adsorption of ready synthesized CDs

Preparation of silica-based embedded composites with citric acid. 1.0 g of SiO_2 , $\text{SiO}_2\text{-NH}_2$, $\text{SiO}_2\text{-EDA}$ were impregnated with 2.0 mL of water solution of citric acid with a concentration of 1.5 g m L^{-1} . The mixture was sonicated for 10 minutes, and excess of liquid was removed by filtration with further blotting of solid with filter paper, receiving a composite denoted as $\text{SiO}_2(\text{d})@\text{CA}$, $\text{SiO}_2(\text{d})\text{-NH}_2@\text{CA}$, $\text{SiO}_2(11)\text{-EDA}@\text{CA}$. To remove excess of precursor, dry diethyl ether (10 mL for 1.0 g of solid) was added to the samples and the mixture was shaken for 20 min. The ether was removed by decantation and the procedure was repeated for 1-4 times. Finally, the samples of silica-based@CA were dried in vacuum (0.1 Torr) at 60°C giving loose powders.

Thermal treatment of silica-based@CA samples. All samples of $\text{SiO}_2(\text{d})@\text{CA}$, $\text{SiO}_2(\text{d})\text{-NH}_2@\text{CA}$ were heated at 170°C under nitrogen. Small portions of the samples were collected at a different time (τ) (from 15 to 720 min) to obtain a set of composites denoted as $\text{SiO}_2(\text{d})@^2\text{CDs-t}$, $\text{SiO}_2(\text{d})\text{-NH}_2@\text{CDs-t}$. One sample ($\text{SiO}_2(9)@\text{CDs-240}$) was additionally heated at 180°C for 20 h under argon. Two samples of $\text{SiO}_2(11)\text{-EDA}@\text{CA}$ were heated at 150°C and 180°C during 10h under nitrogen. The third sample of $\text{SiO}_2(11)\text{-EDA}@\text{CA-T-t}$ was heated at $100\text{-}170^\circ\text{C}$ where small portions of the samples were collected at a different time (t) (from 15 to 600 min).

Releasing CDs from silica-based@CDs composites. Three consequent steps were applied to release CDs. Initially, 1.0 g of silica-based@CDs was transferred to cellulose extraction thimble and washed with water in Soxhlet for 24 h. Water suspension of CDs was filtrated through a $0.22 \mu\text{m}$ membrane, clean from the impurities by dialysis (two days) and stored at 4°C . After washing with water, the solids were additionally washed 3 times with 5 mL of NaHCO_3 (0.1 mol L^{-1}). Finally, 3 mL of NaOH (3 mol L^{-1}) water solution was added to 1.0 g of pre-washed solids at room temperature to dissolve silica support and release nanoparticles CDs. The resulted solution was acidified with a water solution of HCl (34%) and left for 24 h for SiO_2 hydrogel formation. Then CDs were separated from the precipitate by centrifugation, dried in vacuum at 30°C and separated from NaCl by solubilization in $\text{C}_2\text{H}_5\text{OH}$ under

² @ is composite prepared from adsorption of CA onto silica-based materials with further heating

sonification. As prepared CDs were further utilized for all experiments without additional chromatographic separation or dialysis purification.

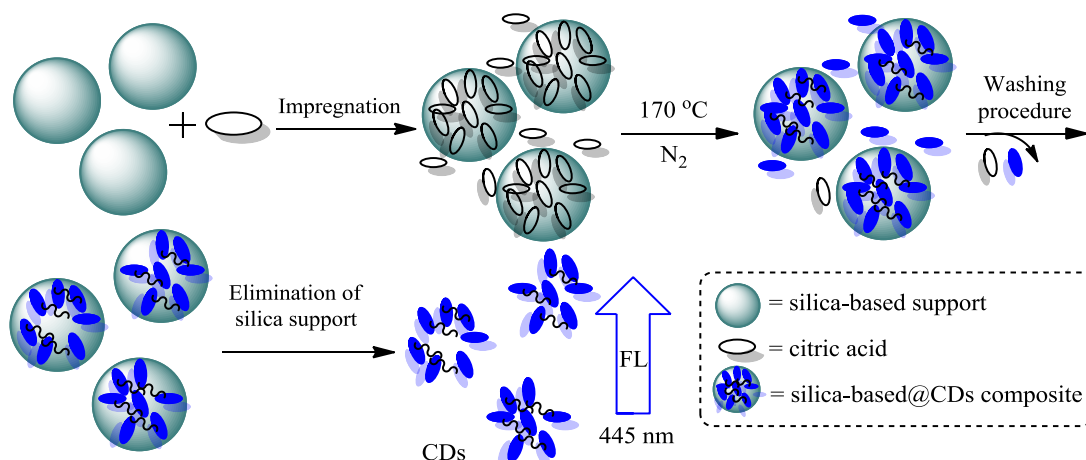


Figure 9 - Scheme of synthesis of CDs using a nanoreactor approach

3.3. The simulation of H⁺ adsorption process

Commonly several models can be used to calculate the protolytic equilibrium constants: ideal adsorption (Langmuir isotherm equation), chemical reactions, energy heterogeneity or the model of polydentate binding. The last one provides the most informative information on the peculiarities of the protonation of amino groups immobilized on the silica surface. The model of polydentate binding was used to simulate the H⁺ adsorption equilibria. The software program CLINP 2.1 has been used to calculate the fitting parameters of the equilibrium models [278].

There is the surface of the amine-containing material considers as an assemblage of independent sorption centers $\overline{(\sim \text{NH}_2)_q}$, each of which contains q fixed amino groups. The binding of H⁺ ions by reaction centers are described as a stepwise process with own values of equilibrium constants $K_i^{(Z)}$ [279] equations 1.1-1.3:

$$\overline{(\sim \text{NH}_2)_q} + \text{H}^+ + \text{Z}^- \xrightleftharpoons{K_1^{(q)}} \overline{(\sim \text{NH}_2)_q \text{HZ}}, \quad (1.1)$$

$$\overline{(\sim \text{NH}_2)_q \text{H}} + \text{H}^+ + \text{Z}^- \xrightleftharpoons{K_2^{(q)}} \overline{(\sim \text{NH}_2)_q \text{H}_2 \text{Z}_2}, \quad (1.2)$$

$$\overline{(\sim \text{NH}_2)_q \text{H}_{q-1}} + \text{H}^+ + \text{Z}^- \xrightleftharpoons{K_q^{(q)}} \overline{(\sim \text{NH}_2)_q \text{H}_q \text{Z}_q}, \quad (1.3)$$

where the bars mark species on the solid phase, i – the step number, Z^- – counter-ion.

The quality of approximation was estimated by the value of χ^2 -criterion:

$$\chi_{exp}^2 = \sum_{k=1}^N \xi_k^2 \quad (1.4)$$

where N is the total number of experimental points; weighted discrepancies $\xi_k = w_k^{1/2} \cdot \Delta_k$; discrepancies $\Delta_k = A_k^{calculated} - A_k^{experimental}$; A is the measured property (equilibrium concentration of $[H^+]$ in solution); the statistical weights of measurements $w_k = \frac{1}{(A_k^{experimental})^2 \cdot \sigma_r^2}$ and σ_r is relative standard deviation of A (0.05 was used in this work).

The model can be considered as adequate in the case of inequality:

$$\chi_{exp}^2 < \chi_{critical}^2 \quad (1.5)$$

where $\chi_{critical}^2$ is the 5% points of the chi-square distribution with $f = N - z$ degrees of freedom, z is the number of fitting parameters.

The specific concentration of sorption centers was calculated as $\overline{(\sim NH_2)_q} = t_q/q$ where t_q – specific concentration of all active amino groups (effective sorption capacity). The average \bar{t}_q is calculated to found optimal fitting parameters:

$$\bar{t}_q = \sum_{j=1}^J t_{qi} \cdot \frac{(\chi_{exp}^2)_j^{-1}}{\sum_{j=1}^J (\chi_{exp}^2)_j^{-1}} \quad (1.6)$$

where J – number of t_q values for which the adequate models were built.

The degrees of formation protonated amine species are calculated as:

$$\alpha_{i,\%} = \frac{\bar{Q}}{\overline{(\sim NH_2)_3} + \overline{(\sim NH_2)_3 HZ} + \overline{(\sim NH_2)_3 H_2 Z_2} + \overline{(\sim NH_2)_3 H_3 Z_3}}, \quad (1.7)$$

where \bar{Q} – equilibrium concentrations of $\overline{(\sim NH_2)_3}$, $\overline{(\sim NH_2)_3 HZ}$, $\overline{(\sim NH_2)_3 H_2 Z_2}$, $\overline{(\sim NH_2)_3 H_3 Z_3}$.

3.4. Determination of the concentration of grafted groups

Concentrations of functional groups on the surface of the obtained materials were determined based on elemental analysis, XPS analysis, thermogravimetric analysis, pH-metric and conductometric titration.

Elemental analysis. The concentration of immobilized groups bonded by one-step surface silanization was calculated from equations 1.8 or 1.9:

$$C_L(\text{mmol/g}) = \frac{10 \cdot P_e}{A_r \cdot n_e}, \quad (1.8)$$

$$C_L (\mu\text{mol} \cdot \text{m}^{-2}) = \frac{10^3 \cdot C_L(\text{mmol g}^{-1})}{S_{BET}}, \quad (1.9)$$

where P_e is the percentage content of the element, %; A_r is the element atomic mass, n_e is the number of atoms of the element under determination in the grafted fragment, S_{BET} is the specific surface area, $\text{m}^2 \text{g}^{-1}$.

The concentration of the groups grafted by the method of assembling them on the surface in more than two steps (for anthracene-based materials) was calculated from equation 1.10:

$$P_e/100 = \sum_{i=1}^i A_r^i \cdot n_e^i \cdot C_L^i \quad (1.10)$$

The symbols in the equation 1.10 are similar to those in the equations 1.8 and 1.9. In this approach, the elemental analysis data of the resulting product can be used for determination concentration of grafting groups.

If the bonded groups are homogeneously distributed in solid, the surface density of functional groups (δ) and the average distance (l) between them are calculated from equations 1.11 and 1.12 [280]

$$\delta(\text{molecules/nm}) = 10^{-6} \cdot C_L (\mu\text{mol/m}^2) \cdot 10^{-18} \cdot N_A, \quad (1.11)$$

$$l(\text{\AA}) = 10 * (1/\delta)^{1/2}, \quad (1.12)$$

where N_A is the Avogadro's number.

XPS analysis. The concentration of immobilized functional groups was calculated from equation 1.13.

$$C_L(\text{mmol g}^{-1}) = \frac{1000 \cdot at(N)}{at(Si) \cdot M(SiO_2) \cdot n(N)} \quad (1.13)$$

where $at(Si)$ and $at(N)$ are the atomic percentage of Si and N in the hybrid, $M(SiO_2)$ is SiO_2 molar mass, $n(N)$ is the number of atoms of the nitrogen in immobilized group.

Thermogravimetric analysis. The concentration of aminopropyl groups on the surface was calculated from thermogravimetric data using equation 1.14 [281] and for two-step modified samples – equation 1.15:

$$C_L, \text{mmol/g} = \frac{\Delta m}{m \cdot M}, \quad (1.14)$$

$$C_L, \text{mmol/g} = \frac{\Delta m_2 - \Delta m_1}{m \cdot M}, \quad (1.15)$$

where $\Delta m/m$ (mg/g) is mass loss of modified silica in the temperature range, corresponding to thermal decomposition of organic fragments per 1 g of sample mass; $\Delta m_2 - \Delta m_1$ is the difference of the mass loss between two-step and one-step modified samples; M is the molar mass of the grafted group, g mol^{-1} .

pH-metric titration. The method of a single sample was used in the pH-metric titration of organosilica suspensions. For this purpose, 10 ml of KCl solution with the ionic strength of 0.1 mol L^{-1} were added to precise weights ($\sim 0.1 \text{ g}$) of the material and titrated with 0.01 mol L^{-1} HCl solution. The mixtures were stored for 24 h to reach equilibrium in the closed bottles at room temperature. The equivalence point was found by linear extrapolation of the graph of the hydroxonium ion quantity in the solution as function of the quantity of added acid using the Gran method.

The back titration of $\text{SiO}_2(\text{d})\text{-NH}_2$ was performed as follows. A 15 ml portion of 0.01 mol L^{-1} HCl solution (2x molar excess) was added to precise weight ($\sim 0.1 \text{ g}$) of amino-modified material and non-modified silica (blank). The suspension was kept for 24 h. Aliquot of 8 mL was placed in a glass beaker and titrated with 0.01 n $\text{Na}_2\text{B}_4\text{O}_7 \cdot 10\text{H}_2\text{O}$. The concentration of the grafted groups was calculated from equation 1.16:

$$C_L, \text{mmol/g} = C_{\text{HCl}}^{\text{SiO}_2} - C_{\text{HCl}}^{\text{xSiO}_2\text{-NH}_2} \quad (1.16)$$

$$C_{\text{HCl}}^{\text{SiO}_2} \text{ or } C_{\text{HCl}}^{\text{xSiO}_2\text{-NH}_2} = \frac{n_0(\text{HCl}) - n(\text{HCl})}{m} \quad (1.17)$$

where $C_{\text{HCl}}^{\text{SiO}_2}$ and $C_{\text{HCl}}^{\text{xSiO}_2\text{-NH}_2}$ are the amount of the acids adsorbed by the non-modified and amino modified silicas, respectively (mmol/g); n_0 and n are initial and final amount of HCl in suspension (mmol); m is weighted sample (g); $C_0(\text{HCl})$ is the initial concentration of the added acid (mol/L); $V_0(\text{HCl})$ is the initial volume of added HCl (ml); V_G is the volume of titrant (borax) determined by the Gran method (ml); C_b is the concentration of titrant (borax); V_{al} is the aliquot volume (ml).

Conductometric titration. The sample (~ 0.1 g) of mercaptopropyl silica gel was placed in 25 ml of aqueous solution of AgNO_3 ($c=5.75 \text{ mmol L}^{-1}$). The suspension was titrated with a 0.1 mol L^{-1} NaCl solution with continuous stirring using a magnetic stirrer. The concentration of the grafted groups was calculated from the formula 1.18:

$$C_L, \text{mmol/g} = \frac{C_0(\text{NaCl}) \cdot V(\text{NaCl})}{m}, \quad (1.18)$$

where $V(\text{NaCl})$ is the volume of NaCl solution in the equivalence point, mL.

3.5. Kinetic studies during synthesis

The experimental dates were estimated with two kinetic models – pseudo-first-order (1.19) and pseudo-second-order (1.20).

$$q_t = q_e (1 - e^{-k_1 t}) \quad (1.19)$$

$$q_t = \frac{k_2 q_e^2 t}{1 + k_2 q_e t} \quad (1.20)$$

where q_e and q_t are the consumed amounts of 9CMA at equilibrium and at various times t (mol g^{-1}), respectively, and k_1 is the rate constant of the pseudo-first-order model (min^{-1}), k_2 is the rate constant of the pseudo-second-order model ($\text{g (mol} \cdot \text{min)}^{-1}$). Furthermore, the initial adsorption rate h ($\text{mol (g} \cdot \text{min)}^{-1}$) can be determined from $h=k_2 q_e^2$.

3.6. Calculation of defect distance in graphene

Two main types of defective graphene are known [135, 282]. In the first one, the honeycomb lattice is largely intact, and the mean defect distance L_D is larger than 3 nm. The I_D/I_G ratio in Raman spectroscopy can be used to evaluate the distance between defects in graphene and for GO it is about 1 (532 nm laser excitation) and increases with an increasing mean distance between two defects from 1 to about 3 nm. In second step, the graphene is dominated by defects, L_D is shorter than 3 nm, and the intact sp^2 -domains between defects are small. The transition between first and second type occurs at a maximum of $I_D/I_G \sim 3.8$ (for a Raman excitation wavelength of 532 nm) [283].

A reliable estimation of the type defect distance for graphene was calculated by using the equation from [284]:

$$L_D = \sqrt{\frac{4.3 \cdot 10^3}{E_L^4} \left(\frac{I_D}{I_G} \right)^{-1}} \quad (1.21)$$

where E_L is laser energy. For 532 nm laser excitation, E_L is 2.33.

3.7. Non-specific adsorption of anthracene

Solvent evaporation method. 300 mg of SiO₂(4) was mixed in glass vials with 1.5 ml of anthracene solution with different concentration (0-7.1 $\mu\text{mol mL}^{-1}$) in ethanol. The vials were stored at room temperature to evaporate solvent. The solid phase was analyzed in three replicates by excitation wavelength at $\lambda_{\text{exc}}=360$ nm. The solid sample was separated into two parts. One part was dried at 50°C, and the third one was not dried.

3.8. Adsorption studies in static mode

MB stock solution ($7.8 \cdot 10^{-2}$ mmol L⁻¹) was diluted with deionized water to the required concentrations ($3.0 \cdot 10^{-2} - 2.0 \cdot 10^{-3}$ mmol L⁻¹) at different pH. SiO₂, SiO₂-NH₂ and SiO₂(9)-NH₂/CDs-170 (50 mg) were mixed with MB (10 mL) and stirred at 300 rpm for 120 min, and then kept for 24 h at room temperature to allow equilibrium. The liquid supernatant was separated from the remained precipitate by centrifuging at 5 000 rpm for 5 min. The residual concentration of MB in the solution was determined via a maximal absorbance at 664 nm.

A similar procedure was carried out for adsorption of CDs-170 and CDs-200 (10 mL) onto 50 mg of silica solid (SiO₂, SiO₂-NH₂, SiO₂-SH, C18) with detection of residual CDs at 325 nm from UV-Vis spectrum. The removal rate (1.22) of MB, CDs and the adsorption capacity (1.23) was assessed by the following equations:

$$R, \% = \frac{C_0 - [X]}{C_0} * 100\% \quad (1.22)$$

where X- MB or CDs-170, CDs-200, C_0 – initial concentration of analyte solution before contact with solid, $\mu\text{mol L}^{-1}$ and $[X]$ concentration of analyte solution after contact with adsorbent, $\mu\text{mol L}^{-1}$.

$$q_e, \mu\text{mol g}^{-1} = \frac{C_0 - [X]}{m} * V \quad (1.23)$$

where m – adsorbent mass, g; V – total volume, L.

Among different available adsorption isotherm equations three isotherms were selected for this study: the Langmuir, Freundlich and Temkin isotherms. The applicability of the non-linear isotherm equation was compared by judging the correlation coefficients, R^2 . Fitting was realized by OriginPro 8.

The Langmuir adsorption isotherm is based on the assumption that all the adsorption sites on the adsorbent surface are energetically equivalent [285]. The maximum adsorption corresponds to a saturated monolayer of solute molecules on the adsorbent surface. The non-linear form of Langmuir isotherm can be represented by the following equation:

$$q_e = \frac{q_{max} * K_L * [c]}{1 + K_L * [c]} \quad (1.24)$$

where q_{max} is the monolayer adsorption capacity ($\mu\text{mol g}^{-1}$) and K_L is Langmuir constants ($\text{L } \mu\text{mol}^{-1}$).

Unlike Langmuir isotherm, Freundlich isotherm assumes heterogeneous surface energies, in which the energy term in Langmuir equation varies as a function of the surface coverage. The well-known linearized form of Freundlich isotherm can be expressed as

$$q_e = K_F * [c]^{1/n}, \quad (1.25)$$

where K_F and n are Freundlich constants with n giving an indication of how favourable the adsorption process.

Temkin isotherm model takes into account the effects of indirect adsorbate/adsorbate interactions on the adsorption process; it is also assumed that the heat of adsorption of all molecules in the layer decreases linearly as a result of increase surface coverage:

$$q_e = \frac{RT}{b} \ln(K_T * [X]) \quad (1.26)$$

where R - molar gas constant $8.314 \text{ J (mol K)}^{-1}$; T - absolute temperature K ; K_T is the Temkin isotherm equilibrium binding constant ($\text{L } \mu\text{mol}^{-1}$); b is the Temkin isotherm constant, J g mol^{-2} .

3.9. Adsorption studies in dynamic mode

SPE adsorption of anthracene as model analyte was carried out in dynamic mode. SPE system was coupled with UV-Vis detector. Solid sample of the adsorbents (250 mg) were packed into empty 3mL SPE tube. Plunger pump was used to push the liquid sample through the packed SPE cartridge with flowrate 1 mL min^{-1} , Figure 10.

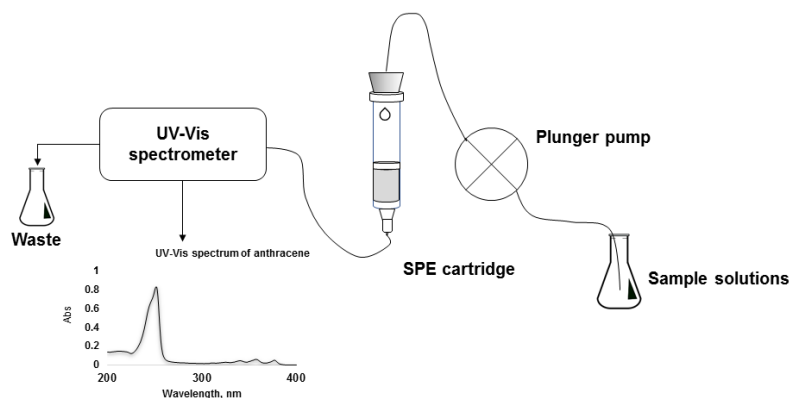


Figure 10 - Schematic diagram of SPE adsorption study

SPE cartridge was connected with quartz flow-through cuvette via Teflon tubes. The cuvette was placed into UV-Vis spectrophotometer and absorption spectra of anthracene were recorded at real time in the wavelength range 225-390 nm with scan rate 600 nm sec^{-1} and cycled every 0.3 min. The concentration of the anthracene was determined for its spectra for absorption bands at 250 nm and 365 nm. The dead volume (V_{dead}) of the system was determined from the blank as $V_{\text{dead}} = 2.0 \text{ mL}$. The breakthrough curves were obtained by subtracted of V_{dead} from experimental results.

Adsorption studies of anthracene with concentration $C_0 = 1 \cdot 10^{-5} \text{ mol L}^{-1}$ was performed from different mobile phases (MP), such as MeCN, acetone, heptane and MeCN/water (1/1, pH=3 and 6).

Before application SPE tubes were conditioned with water (10 min) and then with 10 mL of MeCN. Finally, 10 mL of MP mobile phase was pumped through the column and then a solution of anthracene in corresponding MP. Desorption of anthracene was performed using MeCN, MeCN/water buffer solution with pH 8.5 (90:10) or acetone.

Model solutions, of a) Myristic acid ($2 \cdot 10^{-5} \text{ mol L}^{-1}$) in MeCN:water (50%, pH=3) and b) commercial sunflower oil (1%) in heptane were contaminated with anthracene ($2 \cdot 10^{-5} \text{ mol L}^{-1}$) in corresponding liquid media.

The dynamic adsorption capacity of the SPE columns based on breakthrough curves was determined from equation (1.27- 1.29):

$$C_{10\%} = \frac{C_0 * V_{10\%}}{m} \quad (1.27)$$

$$C_{50\%} = \frac{C_0 * V_{50\%}}{m} \quad (1.28)$$

$$C_{90\%} = \frac{C_0 * V_{90\%}}{m} \quad (1.29)$$

where $C_{10\%}$, $C_{50\%}$ and $C_{90\%}$ are effective dynamic adsorption capacity of SPE cartridge at 10%, 50% and 90% of SPE saturation, $V_{10\%}$, $V_{50\%}$ and $V_{90\%}$ volumes of the solution passed the cartridge to reach corresponding of SPE saturation.

3.10. Calculation of SiO₂-NH₂@CA mass loss

The content of CA ($m(\text{CA})$) on SiO₂-NH₂@CA was calculated using the equation (1.30).

$$\frac{m(\text{CA})}{m(\text{SiO}_2 - \text{NH}_2)} = \frac{m(\text{SiO}_2 - \text{NH}_2@\text{CA})_n - m(\text{SiO}_2 - \text{NH}_2)}{m(\text{SiO}_2 - \text{NH}_2)} \quad (1.30)$$

where $m(\text{SiO}_2 - \text{NH}_2@\text{CA})_n$ and $m(\text{SiO}_2 - \text{NH}_2)$ are mass of the corresponding composites (g), and n – is a number of washing cycles or time of thermal treatment (h).

The molar ration of CA ($n(\text{CA})$) on SiO₂-NH₂@CA was calculated using the equation (1.31).

$$\frac{n(\text{CA})}{n(\text{NH}_2)} = \frac{1000 \cdot m(\text{CA})_n}{m(\text{SiO}_2 - \text{NH}_2) \cdot c(\text{NH}_2) * M(\text{CA})} \quad (1.31)$$

where $c(\text{NH}_2)$ – the concentration of immobilized aminopropyl groups, mmol g⁻¹, $M(\text{CA})$ – the molar mass of CA, g mol⁻¹.

3.11. Calculation of quantum yield of CDs

The relative QYs of the colloidal CDs were estimated with respect to quinine sulfate (QS) as a reference in 0.1 M H₂SO₄ by two approaches such as a single-point and a comparative method.

In the single-point method [229], both absorbance and photoluminescence emission (350 nm excitation) spectra are measured for samples of dilute quinine sulfate and CDs ($A_{350} < 0.01$). The area under each emission spectrum was determined using an optical spectroscopy software SpectraGryph 1.2 to find the integrated fluorescence intensity. Quantum yield was calculated using the following equation (1.32):

$$\text{QY} = Q_R \times \frac{I_S}{I_R} \times \frac{A_R}{A_S} \times \frac{\eta_S^2}{\eta_R^2}, \quad (1.32)$$

where QY= quantum yield of CDs; Q_R = quantum yield of reference; I_S = integrated fluorescence intensity of CDs; I_R = integrated fluorescence intensity of reference; A_S = absorbance of CDs at 350 nm; A_R = absorbance of reference at 350 nm; η_S = refractive index of solvent of CDs; η_R = refractive index of solvent of reference.

QY of quinine sulfate is 54% and refractive index of water solution is 1.33.

The second method involves the use of multiple numbers of solution of reference and sample [286]. Aqueous solutions of different concentrations of quinine sulfate and CDs were prepared. UV absorption (A in the range of 0.1–0.01) and integrated photoluminescence intensity at 350 nm were recorded for each solution. The QY of the CDs can be calculated from the following equation:

$$QY = Q_R \times \frac{K_S}{K_R} \times \frac{\eta_S^2}{\eta_R^2}, \quad (1.33)$$

where K is the slope of the plot of the integrated photoluminescence intensity against absorbance. The subscripts S and R refer to the CDs and reference. UV absorption intensities at 350 nm were kept below 0.05 to minimize any re-absorption effects.

3.12. Preparation of electrode for electrochemical study

Typically, 8 mg of $\text{SiO}_2(4)$ -GOQDs and 12 mg of graphite powder were carefully mixed in agate mortar followed by the addition of mineral oil (5 mg). The prepared homogeneous paste was placed in a Teflon cavity (1 mm in depth and 2 mm in diameter), covered with a platinum disk fused to a glass tube with copper wire as an electric conductor. The manufactured electrode was denoted as CPE/Si/GOQD. Unmodified CPE electrode prepared in the same way without $\text{SiO}_2(4)$ -GOQDs was used for the comparative analyses.

4. Preparation and characterization of silica

To optimize the conditions for the synthesis of grafted anthracene groups and to reveal the main factors controlling the degree of the surface reaction, silicas with various porous structures and nature of the grafted silane were studied.

4.1. Silica gel with immobilized aminogroups

The success of the multi-step reaction on the silica surface primarily depends on the pre-activation of silica gel and the first modification step. The possible total number of the functional group and the main modification pathway are set by initial interaction of silica framework with organosilane. Aminomodification is the beginning block to build our target adsorbent. Therefore, the study in detail silica gel with grafting aminopropyl and diethylenediamine groups is necessary.

4.1.1. Functional analysis of amine-groups on the surface

The quantitative and qualitative methods of organic functional analysis are applied to control the progress of the surface assembly reaction. The interface reaction is complex. Knowing the type and chemical features of functional groups on the surface, a colorimetric assay was used as an express analysis of the conversion of the grafted groups. Ninhydrin solution and salicylaldehyde were used as detection reagent of primary amino-groups. The reaction schemes are presented in Figure 11.

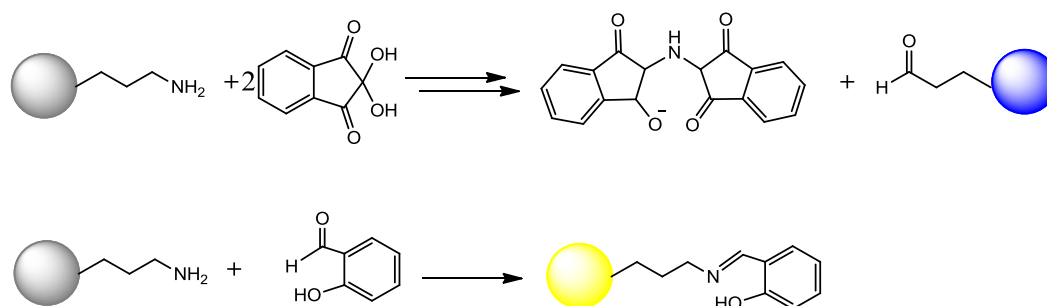


Figure 11 - Schematic illustration of reaction ninhydrin and salicylaldehyde with aminated silica gel

Ninhydrin oxidizes grafted amino-groups and forms a colored blue product known as Ruhemann's purple [287]. In addition, the presence of amino-groups easily detected by the appearance of bright yellow silica after treatment with salicylic aldehyde, Figure 12. Two sample of aminosilica gels were treated with 1% ethanolic solution of ninhydrin and salicylic aldehyde, respectively, than centrifugated and

precipitation was removed with obvious confirmation of immobilization due to colored surface complexes, Figure 12.

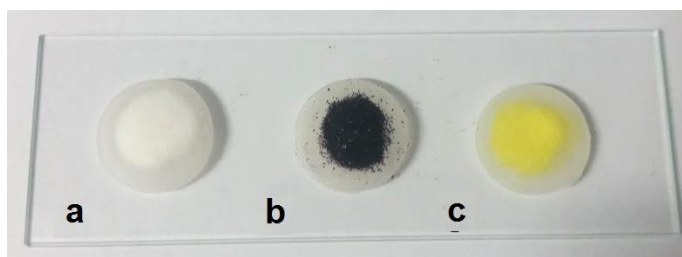


Figure 12 - Digital photographs of aminosilica gel (a), after reaction with ninhydrin (b) and salicylic aldehyde (c)

The degree of aminated silica content can be determined by the measured absorbance of the supernatant liquid. Correlation between account loading of silica with aminopropyl groups versus absorbance of the complex with ninhydrin was studied (Figure 13). With increasing total concentration of immobilized groups, the absorbance of the supernatant linear increased as well. Ninhydrin reagent is indeed sensitive to the presence of amino groups on the surface given that amine concentration on the surface no more than 1 mmol g^{-1} .

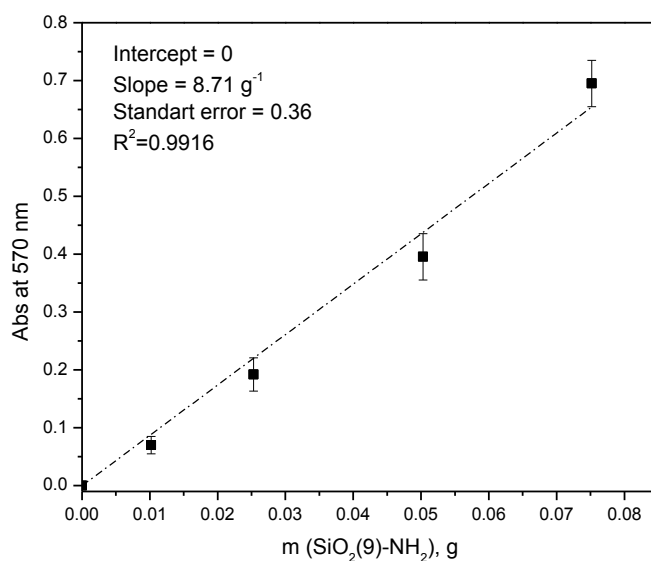


Figure 13 - Formation Ruheman's complex on aminated silica gel

4.1.2. Textural properties

Nitrogen adsorption-desorption isotherms of activated silica origins and aminated silica gels are presented in Figure 14. The calculated textural parameters for

the samples are presented in Table 9. According to IUPAC classification, our porous samples are close to type IV isotherms and associated with H1 hysteresis loop type. Such type of the hysteresis loop is related to capillary condensation taking place in mesopores with narrow pore size distributions [288]. The presented shape of hysteresis is attributed to cylindrical pores. Different pore size has an effect on the quantity of N_2 adsorption. The higher average pore size of pristine and aminated silica gel lead to much more adsorbed N_2 (Figure 14). Non-porous structure of aerosil derivative was confirmed by absence large hysteresis loop due to reversible adsorption and desorption branches (Figure 14). Existence of small hysteresis can be related to the presence of cavities between aerosil aggregates.

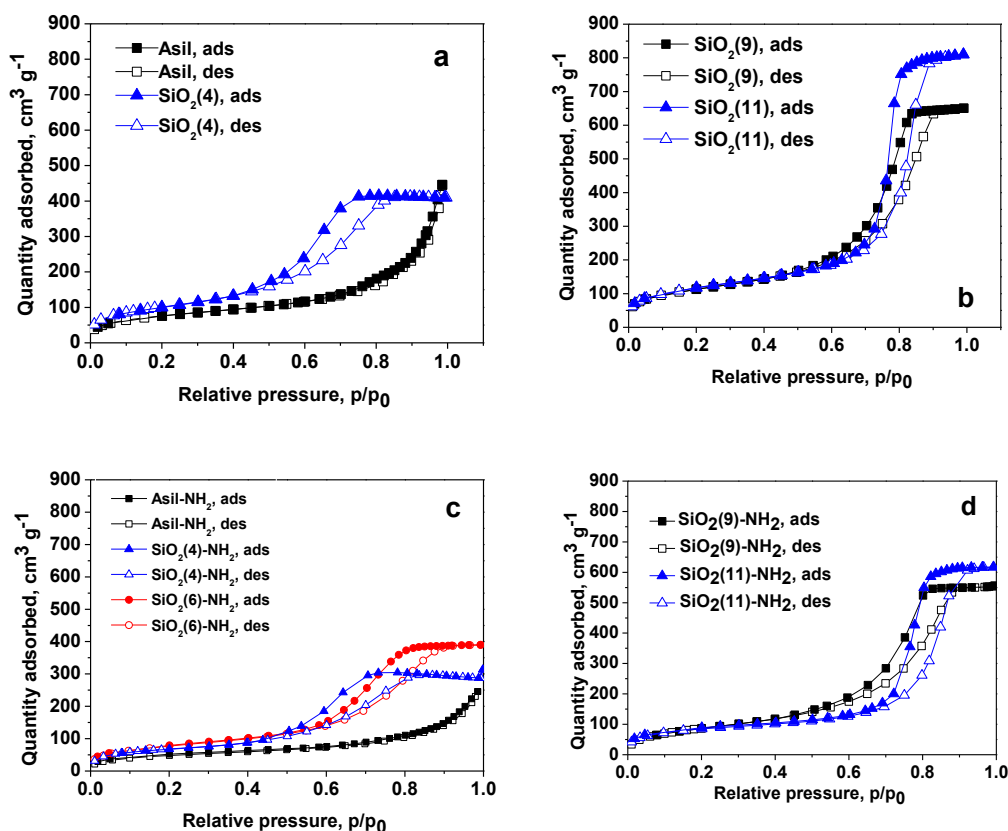


Figure 14 - N_2 adsorption-desorption isotherms of pristine silica gels (a, b) and modified with amino-groups (c, d)

Surface modification show changes in textural characteristics of pure silica matrix (Table 9). Asil derivatives have no pores and exhibit the smallest specific surface area among studied materials. Based on the data, the porosities for the carbon-containing species are a little bit smaller than those for its corresponding modifier-free

samples. Additionally, for non-porous and porous studied materials a reduction in the surface area of the silica gel after organofunctionalization in relation with the unmodified silica gel matrix is observed. This phenomenon can be related to the obstruction of the pores due to the formation of a covering dense layer by the functional groups or to the coalescence of pores [289].

Table 9 - The textural characteristics of the obtained materials

Material	R_{com}^1, nm	R_{BJH}, nm	S_{BET}, m^2g^{-1}	$V_p^{BJH}, cm^3 g^{-1}$	$S_{meso}/S_{BET} (MND^3), \%$
Asil	— ²	—	261	—	—
Asil-NH ₂	—	—	171	—	—
SiO ₂ (4)	2.0	2.8	360	0.77	95.1
SiO ₂ (4)-NH ₂		2.8	237	0.59	99.1
SiO ₂ (6)	3.0	—	480 ¹	0.80 ^b	—
SiO ₂ (6)-NH ₂	—	3.4	279	0.63	99.6
SiO ₂ (9)	4.5	4.6	397	1.00	99.0
SiO ₂ (9)-NH ₂	—	3.9	326	0.94	98.6
SiO ₂ (11)	5.5	4.7	410	1.36	99.6
SiO ₂ (11)-NH ₂	—	4.7	290	1.10	96.1

¹— commercial value

²— no data

³—Modified Nguyen-Do method (cylinders + voids (CV) self-consistent model), desorption branch

Based on the calculation of textural parameters from the desorption branch by Modified Nguyen-Do method (including pore model as cylinders and voids), 95-99 % of all pores are mesoporous type Table 9. Selected samples of SiO₂(d) and SiO₂(d)-NH₂ have a unimodal and narrow distribution of the pores (Figure 15).

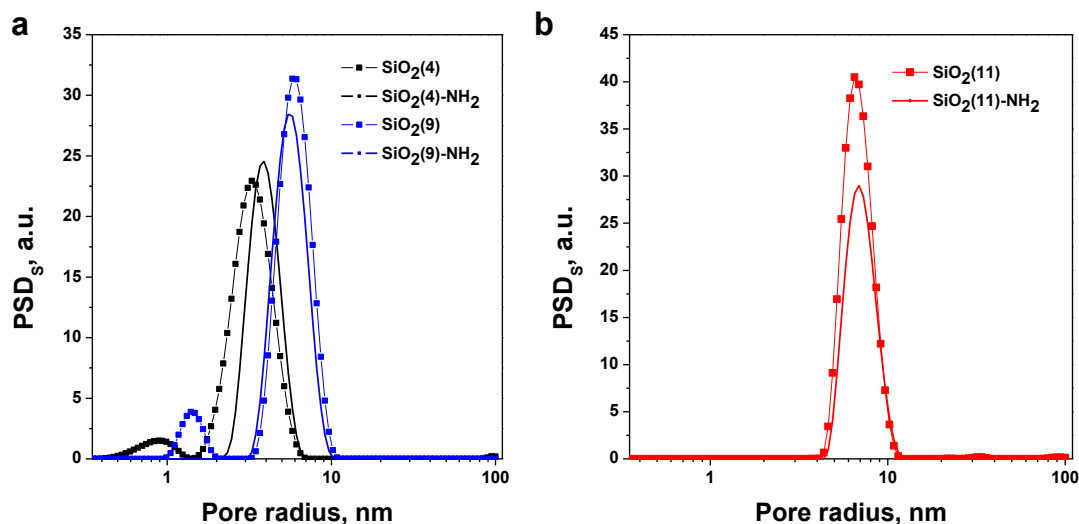


Figure 15 - The incremental pore size distribution of silica and aminopropyl silica gels

The modification of pure silicas with APTES almost did not show influence on pore distribution.

4.1.3. Morphological properties

The surface morphologies of the selected activated silica gel particles are in Figure 16. Primary information from the manufacturer about the morphology of the silica gels was confirmed using SEM techniques. According to Figure 16A, $\text{SiO}_2(4)$ is silica blocks with irregular surface structure and this irregular behavior occurs for silica gels with pore size 6 and 9 nm as well. However, $\text{SiO}_2(11)$ is well-defined spherical particles with a size range 25-70 μm . Asil is pyrogenic silica, which visually identified as a loose, bluish-white powder. Its primary particles are more or less strongly aggregated and agglomerated. SEM micrograph (Figure 16C) shows that agglomerates of about 0.5 to 7 μm form.

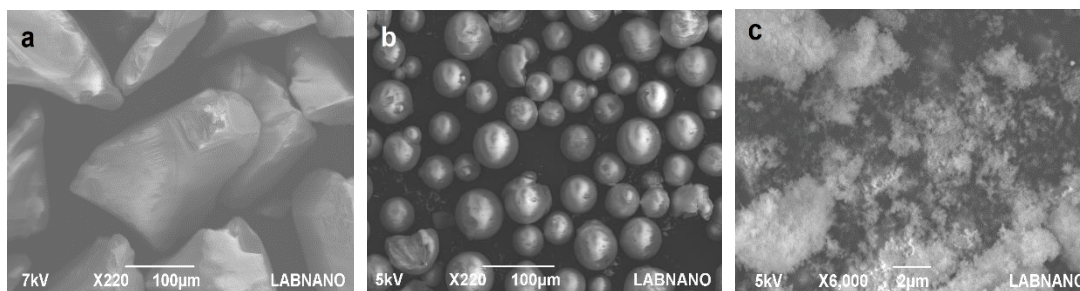


Figure 16 - SEM images of pristine silica gel $\text{SiO}_2(4)$ (a), $\text{SiO}_2(11)$ (b) and Asil (c)

4.1.4. NMR study

Figure 17 shows the ^{13}C NMR spectrum of the $\text{SiO}_2(11)\text{-EDA}$ material. The peaks assigned to C_5 (10 ppm), C_4 (25 ppm), C_1 (40 ppm) and $\text{C}_{3,2}$ (50 ppm) clearly show that the silane modifier is formed on the surface. The spectrum is similar to previously reported [290].

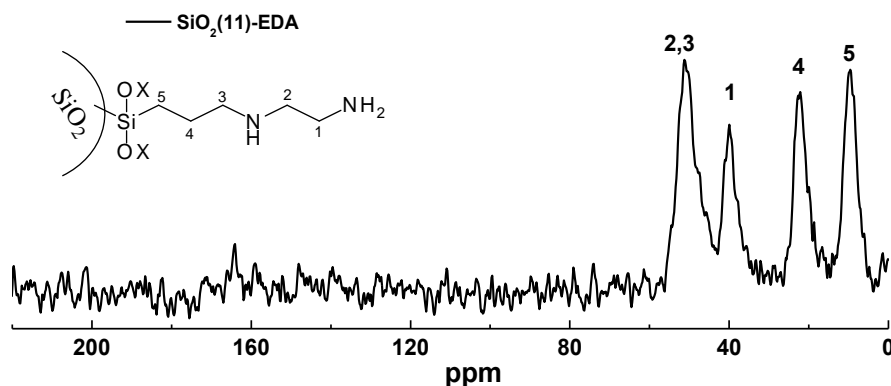


Figure 17 - Solid-state ^{13}C NMR spectrum of $\text{SiO}_2\text{-EDA}$

4.1.5. Structure of the grafted layer

The spectra of pristine Asil, non-porous and average porous aminopropylsilica gels are shown in Figure 18. The FTIR spectra for prepared porous ($d=4\text{-}11\text{ nm}$) aminopropyl silica gels are practically unchanged. Starting aerosil displays well-defined stretching vibration of O-H due to isolated silanol groups at 3752 cm^{-1} . In contrary to non-modified silica, aminated silica gels do not have an intensive band at this frequency. All these samples contain vicinal or unreacted hydrogen-bonded silanol groups at 3545 cm^{-1} , especially $\text{SiO}_2(6)\text{-NH}_2$, and hydrogen-bonded water due to presence broad band at 3350 cm^{-1} . As can be seen from the insert, pristine aerosil does not have any peaks from $1590\text{-}1350\text{ cm}^{-1}$. In contrary, aminated silica gels have several bands in this range responsible for binding functional groups. Prepared aminosilica gels have strong water vibration at 1632 cm^{-1} . The grafted aminogroups are characterized by NH_2 deformation bands. As result, peak position at 1560 cm^{-1} can be defined N-H deformation in protonated amino groups or hydrogen-bonded aminogroups [291]. Confirmation immobilization of propyl fragment was made by the presence of two stretching C-H bands at 2940 and 2863 cm^{-1} along with C-H deformations around

1451-1497 cm^{-1} . Residual bands between 1350-1392 cm^{-1} can be attributed to deformation vibrations ethoxy groups [287].

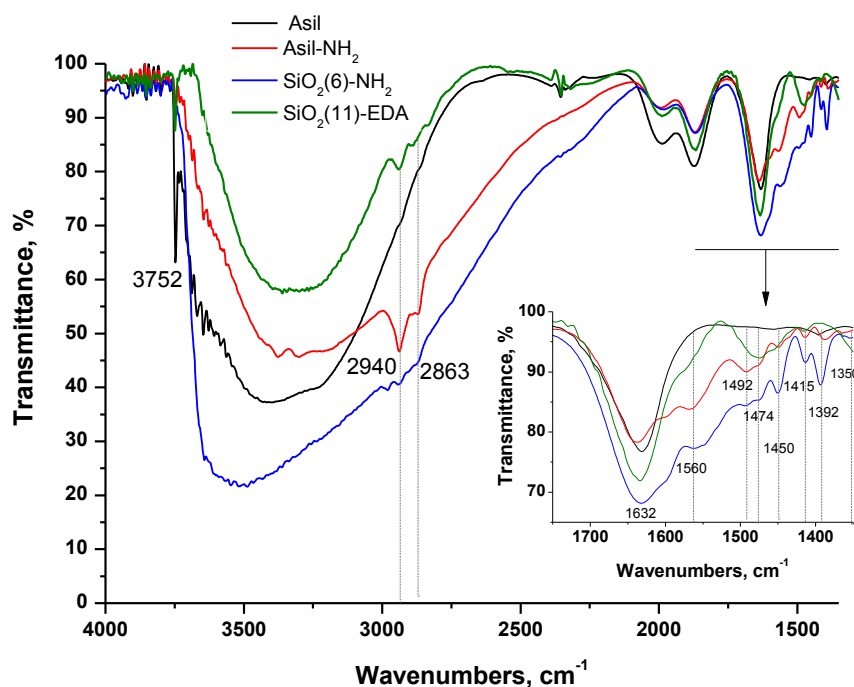


Figure 18 - FTIR spectra of aerosil and aminated silica gel

4.1.6. XPS characterization

The immobilization of aminogroups on the silica was also confirmed by XPS spectroscopy. The XPS survey spectra for the $\text{SiO}_2(4)\text{-NH}_2$ (Figure 19a) and $\text{SiO}_2(11)\text{-EDA}$ (Figure 19d) indicate predominantly O1s, N1s, C1s, Si2s and Si2p peaks centered, respectively, at 532, 401, 286, 155 and 103 eV. The atomic percentage of the element in XPS is an additional assay to characterize element content in the material. Presence of C and N atoms suggests that aminogroups are successfully bonded to the silica surface. The overview spectra show that the nitrogen content of $\text{SiO}_2(11)\text{-EDA}$ is about two times higher in comparison with $\text{SiO}_2(4)\text{-NH}_2$, assuming due to presence two nitrogen-atom in modifier fragment. Based on these percentages, concentrations of immobilized aminogroups were calculated by equation 1.13. The high-resolution C1s XPS spectra of the samples reveal different types of carbon atoms. Using curve-fitting analysis, the C1s XPS spectra of $\text{SiO}_2(4)\text{-NH}_2$ (Figure 19b) and $\text{SiO}_2(11)\text{-EDA}$

(Figure 19e) were deconvoluted into three forms C-C/C-H at 285.0 eV, C-N at 286.3eV and C-O at 287.7 eV.

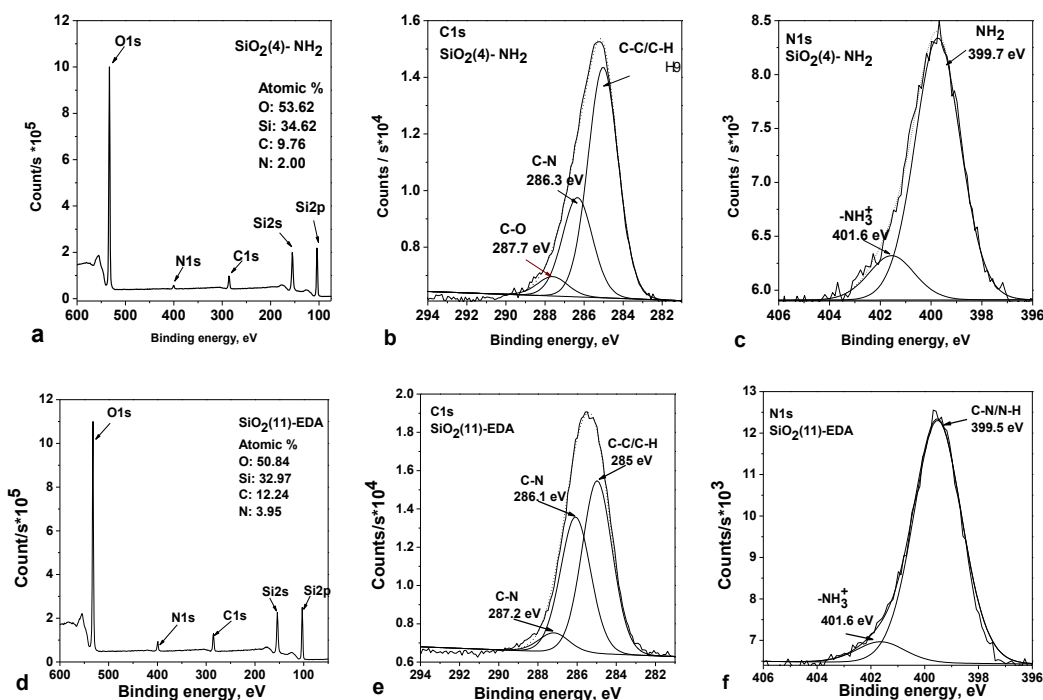


Figure 19 - Survey (a, d) and fitted XPS spectra of the C1s (b, e) and N1s (c, f) regions corresponding to $\text{SiO}_2(4)\text{-NH}_2$ (a, b, c) and $\text{SiO}_2(11)\text{-EDA}$ (d, e, f)

The percentage composition (Table 10) of these forms demonstrates different C contribution in aminated silica. In $\text{SiO}_2(4)\text{-NH}_2$, the predominant type is C-C/C-H (66%), when in $\text{SiO}_2(11)\text{-EDA}$ is C-N (41.4%). The percentage C-O component for both samples is similar. According to N1s form decomposition (Figure 19c, f), the prevalent chemical states of nitrogen represented by the peak at 399.7 eV for H-NH/C-NH bonds and protonated amine or amine bonded with adsorbed water at 401.6 eV. Amount of the second type is higher in $\text{SiO}_2(4)\text{-NH}_2$ (Table 10). The XPS observation agreed well with the FTIR results.

Table 10 - The results of C1s and N1s XPS spectra for SiO₂(4)-NH₂ and SiO₂(11)-EDA

The samples	From C1s C-C/C-H	C-N	C-O	From N1s NH ₂ /C-NH	NH ₃ ⁺	C _L (aminogroups), mmol g ⁻¹
SiO ₂ (4)-NH ₂	66.0	28.4	5.6	85.0	15.0	1.19
SiO ₂ (11)-EDA	52.8	41.4	5.8	92.0	8.0	1.18

4.1.7. Acid-base equilibria at the silica interface

Because of silanol presence and adsorbed water, protonation of bonded aminopropyl groups on silica is a few-step process. The complex character of adsorption may arise from the presence of multiple classes of binding sites with different constant values (energetic heterogeneity) or cooperativity effects. The model of polydentate binding was selected as a tool for detection and quantification of cooperativity effects [279]. It was realized from experimental data from probing of the surfaces of amino silica gels with the H⁺ ions at ionic strength I=0.1 mol L⁻¹.

The adequate fitting of experimental adsorption isotherm was achieved in the model of tridentate binding (q=3). In this model, it is assumed that the surface of aminopropyl silicas can be represented as an ensemble of independent sorption centers, each of which contains three amino groups and the H⁺-binding to that tridentate center is following scheme (Figure 20):

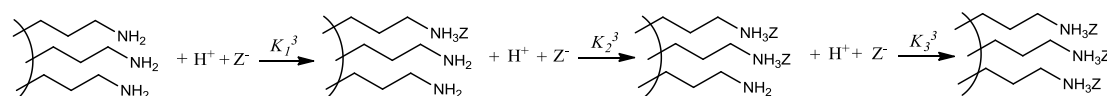


Figure 20 - Protonation of aminopropyl groups fixed on silica surface

The calculated equilibrium constant values are present in Table 11 and the ones similar to early reported [292]. As the values of $K_1^{(3)}$ and $K_2^{(3)}$ exceed $K_3^{(3)}$ considerably, the influence of negative cooperativity effects was concluded (affinity of immobilized amines to the H⁺ ions is decreased with the progress of protonation process). As can be seen from the results of calculations (Table 11), the protonation constants of fixed amino groups are different. This can be attributed to interactions between immobilized amines and weakly acidic silanol groups. It means that the basicity of amines is decreased when they fixed at the surface. Further protonation of the third amine group is unfavorable in this activity center. Thus, adsorption centers on porous aminosilica should be considered as assemblages of interacting immobilized amines and silanol

groups. According to obtained logarithms of the equilibrium constant, the amine groups in Asil-NH₂ are more basic than ones in analogous materials due to less neighbouring silanol groups and denser modified layer.

Table 11 - The results of modeling by polydentate binding

Material	\bar{t}_Q , mmol/g	$\log K_1^{(3)}$	$\log K_2^{(3)}$	$\log K_3^{(3)}$	χ_{exp}^2	$\chi_f^2(5\%)$	f
Asil-NH ₂	0.63	10.18±0.03	8.32±0.03	6.23±0.04	36.0	41.3	28
SiO ₂ (4)-NH ₂	0.67	8.42±0.02	7.08±0.02	5.42±0.02	24.9	44.9	31
SiO ₂ (6)-NH ₂	0.89	8.90±0.02	7.26±0.02	5.63±0.02	42.2	56.3	41
SiO ₂ (9)-NH ₂	0.93	9.35±0.02	7.58±0.02	5.91±0.02	70.4	73.3	55
SiO ₂ (11)-NH ₂	0.68	8.71±0.03	7.61±0.03	5.91±0.03	25.3	38.9	26

The determined equilibrium constants were used to calculate formation degrees of different protonated species on the surface at different pH of solutions using equation 1.7 and presented in Figure 21.

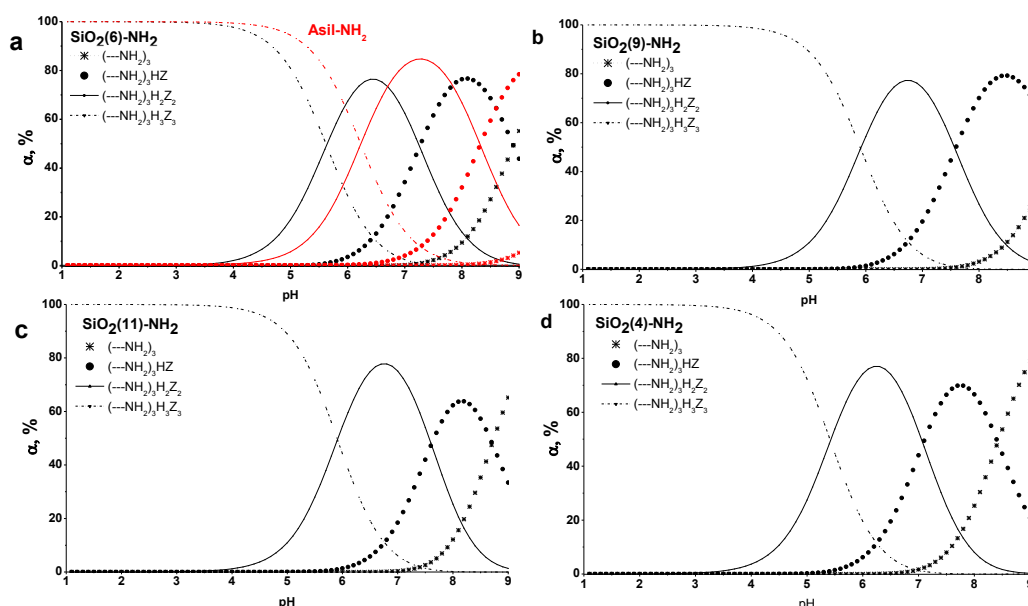


Figure 21 - The formation degrees of different amine-species on the surface at different pH of solutions

At pH <4 almost all amine groups of the tridentate center are protonated on the surface and fixed with counter-ions. In the range of pH 5.5–9.0 different kind of protonated amines are presented. At neutral pH $(\sim \text{NH}_2)_3\text{H}_2\text{Z}_2$ is predominant specie

in the system ($\alpha_i \sim 80\%$), while at $\text{pH} > 8.5$ only $\overline{(\sim \text{NH}_2)_3\text{H}^+ \text{Z}^-}$ and non-protonated amines exist.

4.1.8. Quantification of functional group loading

Elemental analysis

The results of the elemental analysis on carbon, hydrogen and nitrogen of analyzed materials are presented in Table 12.

Table 12 - The results of elemental analysis

Material	N, %	C, %	H, %	C_L^N *, mmol g ⁻¹	C_L^C *, mmol g ⁻¹	C_L^{H**} , mmol g ⁻¹
Asil-NH ₂	1.29	2.88	0.74	0.92	0.80	0.73
SiO ₂ (4)-NH ₂	1.30	3.76	1.15	0.92	1.04	1.14
SiO ₂ (6)-NH ₂	1.35	4.37	1.36	0.96	1.21	1.35
SiO ₂ (11)-EDA	3.57	5.35	2.30	1.27	0.89	1.76

The first step of modification is a root of the target product and it is advisable to compare the results of the elemental analysis on several elements. The percentage content of H usually has auxiliary character due to the content of variable adsorbed water on silica. Concentrations of grafted aminopropyl groups with 4 and 6 nm pore size determined from carbon loading are higher than those ones from nitrogen. It is can be related with solvent adsorption or incomplete hydrolysis of ethoxy-groups of silane. Nitrogen loading is more accurate information about the concentration of aminogroups.

Thermogravimetric analysis

Thermal decomposition of organic fragments and thermal stability of selected aminopropyl silicas were analyzed in the temperature range 25-900 °C (Figure 22) and concentrations of bonded groups were calculated from TGA data using equations 1.14-1.15 and organized in Table 13.

Commonly, the process of mass loss of chemically modified silica in the low-temperature region (<200 °C) is attributed to desorption of physically adsorbed water, that's why region before 220 °C is not shown. At 250-350 °C water desorption observed due to the condensation of vicinal silanol groups, followed by dehydroxylation of silica gel at temperatures higher than 600 °C [293]. The endothermic effect in the curve from differential thermal analysis (curves are not

shown) in the low-temperature zone is responsible for desorption of physically adsorbed water and in high-temperature – the start of the destruction of the organic fragment.

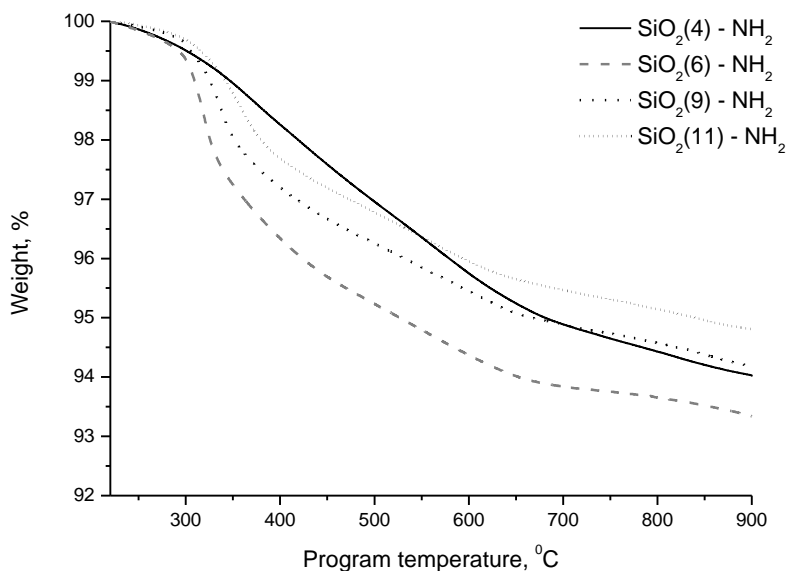


Figure 22 - TGA thermograms of aminosilicas

The TGA thermograms show the intensive weight loss step <700 °C, which corresponds to the decomposition of aminopropyl groups. After 700 °C can be observed some mass loss due to water evolution, associated with dehydroxylation of isolated silanols on silica surface. As can be seen from plots, weight loss decreased in amine with increasing pore diameter from 6 nm to 11 nm. SiO₂(4)-NH₂ does have weight decline at 350°C.

Table 13 - The estimated concentrations of selected samples by TGA

Materials	The temperature range, °C	The fragments	Δm , mg g ⁻¹	C _L , mmol g ⁻¹
SiO ₂ (4)-NH ₂	220-720	-(CH ₂) ₃ -NH ₂	48.0	0.83
SiO ₂ (6)-NH ₂	220-700	-(CH ₂) ₃ -NH ₂ -OH	62.0	1.07 or 0.89
SiO ₂ (9)-NH ₂	220-670	-(CH ₂) ₃ -NH ₂	50.0	0.86
SiO ₂ (11)-NH ₂	220-670	-(CH ₂) ₃ -NH ₂	44.0	0.76

Comparison of concentrations by various methods

The concentration of immobilized groups was calculated by several independent methods and results are presented in Table 14. Each method has their benefits and drawbacks. As shown in the table, the values obtained by elemental analysis are higher than those measured by the other methods. However, this excess of amino groups can be inaccessible for further coupling reactions in aqueous solution. Active aminogroups in aqueous solution can be estimated by direct or back pH-titration. According to maximum attainable adsorption of H⁺ ions, it may be concluded that more than 90% of immobilized amino groups are accessible for the H⁺ probe. All applied methods showed that SiO₂(6)-NH₂ is the most concentrated sample with aminogroups prepared SiO₂(d)-NH₂. Based on TGA data, lower immobilization of aminopropyl groups was shown in sample SiO₂(11)-NH₂ with higher pore size.

The nature of the surface coverage with grafted molecules and their distribution are the factors that determine the differences in the properties of grafted and native molecules. The distance between the grafted molecules influences on the protolytic properties of the grafted ligands, the stability of formed complexes on the surface and the mechanisms of surface coverage by the modifier. Chemical modification can presumably lead to three basic types of the distribution of bonded modifier molecules over the surface, namely random, island-like, and uniform [294].

Table 14 - Concentrations of immobilized aminogropus

Materials	Elemental analysis, mmol g ⁻¹	TGA, mmol g ⁻¹	Direct titration, mmol g ⁻¹	pH- Back pH-titration, mmol g ⁻¹
Asil-NH ₂	0.92±0.1	—	0.61±0.05	0.57±0.06
SiO ₂ (4)-NH ₂	0.92±0.2	0.83±0.1	0.6±0.1	0.76±0.1
SiO ₂ (6)-NH ₂	0.96±0.14	1.07±0.10	0.8±0.1	0.9±0.1
SiO ₂ (9)-NH ₂	—	0.86±0.1	0.87±0.04	0.8±0.1
SiO ₂ (11)-NH ₂	—	0.76±0.1	0.66±0.07	0.68±0.02
SiO ₂ (11)-EDA	1.27			

Values of concentrations of grafted aminogroups (less than 1 mmol/g) lead to the presence of monolayer coating of silica surface. Assuming that homogeneous distribution of immobilized amino groups provides uniformly covers the surface and it opens the possibility to estimate the surface density of the active binding centers (δ) and the average intermolecular distance between bonding two amino groups (l) via equation 1.11 and 1.12. Calculated values are present in Table 15.

Table 15 - The density of binding sites and average intermolecular distance between neighboring groups in hybrid nanoparticles

Material	C_L^{back} , $\mu\text{mol}/\text{m}^2$	δ , molecules/ nm^2	l , Å
Asil-NH ₂	3.3		
SiO ₂ (4)-NH ₂	3.2	2.11	6.9
SiO ₂ (6)-NH ₂	3.2	1.73	7.6
SiO ₂ (9)-NH ₂	2.45	1.59	7.9
SiO ₂ (11)-NH ₂	2.34	1.58	8.0

According to data in Table 15, the surface density of fixed aminogroups decreases with increasing pore size from 4 to 11 nm. The average distance between two isolated silanols is 7 Å [295], in our case, the distance increased with pore size of aminosilica 6.9-8 Å. Thus, silanol groups can be replaced by amino groups due to close intermolecular distance up to 7 Å. According to these values, the surface coverage close to or lower than the monolayer – 2.11 and 1.59 amino groups by nm^2 , as compared to the maximum theoretical value of 2.05 groups per nm^2 [296].

4.2. Silica gel with immobilized mercapto-groups

CDs are the particles enriched in oxidized groups. Due to using citric acid as start materials, final CDs have a fragment of acid transformation. Unfortunately, the exact structure of CDs is unknown, but the properties of these functionality can be analyzed and predicted. Adsorption of prepared CDs in solution on different silica-based support can demonstrate affinity power of CDs. Silica gel with modified mercaptopropyl groups was also used for this aim. Characterization of this adsorbent is present below.

4.2.1. Synthesis and analysis of mercaptopropyl silica

Silica gel with immobilized mercaptopropyl-groups was prepared by a one-step modification of the $\text{SiO}_2(4)$ surface with silane containing target groups in toluene anhydrous. Surface thiol-groups can be partly oxidized by atmospheric oxygen to disulfides ($-\text{S}-\text{S}-$) [297]. As a result, natural oxidation of thiol-groups to disulfides by atmospheric oxygen reduces activity and adsorbent capacity of binding functional groups. The synthesis was carried out under an inert nitrogen atmosphere to prevent the possibility of $-\text{S}-\text{S}-$ bond formation and retain the thiol groups on the surface of the adsorbent. Similar to amino-groups, functional analysis was applied as an express assay to confirm the presence of mercapto-groups on the surface. Sodium nitroprusside is an analytical reagent for the detection of thiols. The reaction schemes are presented in Figure 23.

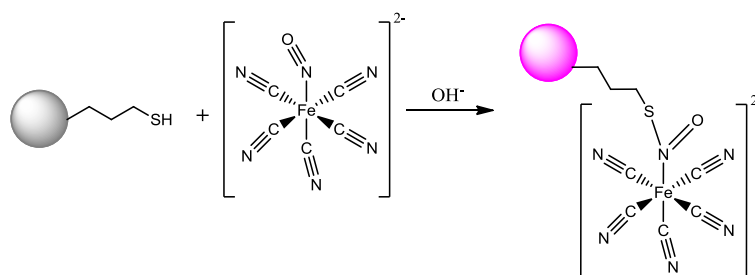


Figure 23 - Schematic illustration of reaction ninhydrin and salicylaldehyde with aminated silica gel

Nitroprusside's test was first introduced by the detection of cysteine [298]. Sodium nitroprusside is a water-soluble sodium salt comprised of Fe^{2+} complexed with nitric oxide (NO) and five cyanide anions. Suspension of silica gel modified with mercapto-groups with the solution of sodium nitroprusside in alkaline medium gives a

purple color that confirms the presence of -SH groups. Non-modified silica gel gives no positive reaction. Figure 24 shows wet solid samples after nitroprusside's test.

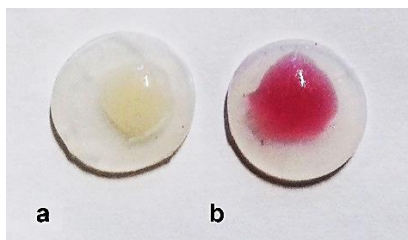


Figure 24 - Digital photo of $\text{SiO}_2(4)$ (A) and $\text{SiO}_2(4)\text{-SH}$ (B) after reaction with sodium nitroprusside in alkaline medium

4.2.2. Textural properties

Nitrogen adsorption-desorption isotherms of pristine silica and silica with modified with mercaptopropyl groups are presented in Figure 25. The calculated textural parameters for the samples are presented in Table 16.

Nitrogen adsorption-desorption isotherms show that $\text{SiO}_2(4)$ and $\text{SiO}_2(4)\text{-SH}(n)$ exhibit characteristic type IV isotherms with a steep increase in adsorption at $p/p_0 = 0.6\text{--}0.8$. Permanency of hysteresis loop after modification attest to the preservation of mesoporous structure. However, hysteresis of modified silica gel is more closed than in case of pure silica gel and can be related to presence of particle aggregation.

Pore size and pore volume of modified silica gel were decreased after surface modification. Interesting, behavior in surface area is different for two $\text{SiO}_2(4)\text{-SH}(n)$ samples. Compared to origin $\text{SiO}_2(4)$, S_{BET} of $\text{SiO}_2(4)\text{-SH}(1)$ decreased due to modification silica pore with mercaptopropyl groups. However, S_{BET} of $\text{SiO}_2(4)\text{-SH}(2)$ increased. It can be related to some reasons. The first one is imprinting of functional groups on the surface and formation of the roughness of the particle surface [299]. The second one is related to the deposition of MPTMS and attachment of thiol groups on the surfaces and inside the pores of $\text{SiO}_2(4)$ [300]. In this case, MPTMS is hydrolyzed and condensed with silanol groups located on the surface and pore walls of the silica. As a result, functional silane layers on the surfaces of silica are formed with increasing BET surface area, and reduction of pore volume and pore size.

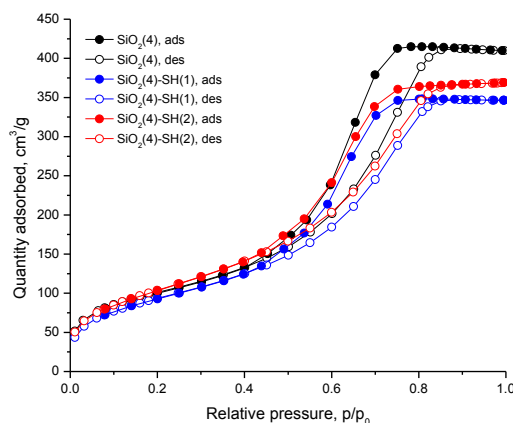


Figure 25 - N₂ adsorption-desorption isotherms of pristine silica gels and modified with mercaptopropyl-groups

Table 16 - The textural characteristics of the obtained materials

Material	R_{BJH} , nm	S_{BET} , m ² g ⁻¹	V_p^{BJH} , cm ³ g ⁻¹	S_{meso}/S_{BET} (MND), %
SiO ₂ (4)	2.8	360	0.72	95
SiO ₂ (4)-SH(1)	2.3	341	0.54	100
SiO ₂ (4)-SH(2)	2.3	385	0.57	100

4.2.3. FTIR characterization

The spectra of pristine Asil and SiO₂(4)-SH(n) are shown in Figure 26. The samples have stretching vibration of O-H groups due to isolated silanol groups at 3752 cm⁻¹ and broad band in the region of 3100-3700 cm⁻¹ is related to hydrogen-bonded water on silica surface. The band at 1640 cm⁻¹ is referred to O-H bending vibration of the adsorbed water molecules. Immobilization of S-organic fragment can be considered successful because of the presence of new bands after modification pristine silica gel. After anchoring the SH-silylating agent on the surface of silica, SiO₂(4)-SH(n) has several bands at 1456 and 1412 cm⁻¹ are referred to C-H bend of methylene group and the weak band at 2580 cm⁻¹ is assigned to S-H stretching frequency. C-S and C-S-H stretching vibrations tend to give rise to very weak absorptions in the infrared spectrum.

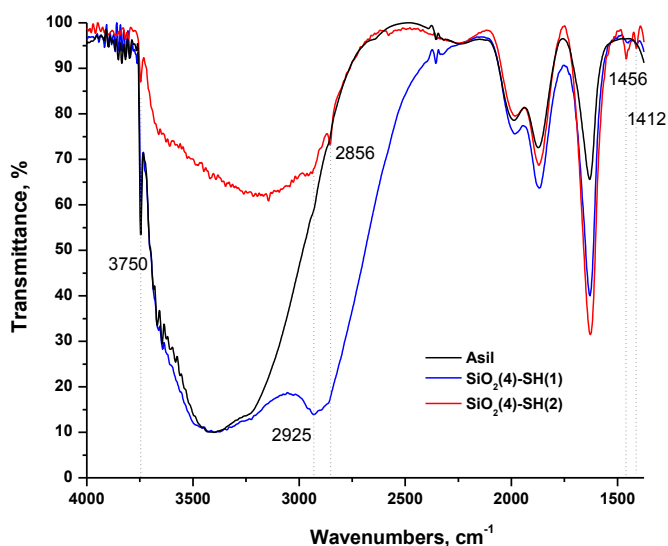


Figure 26 - FTIR spectra of aerosil and silica gel with mercaptopropyl groups

4.2.4. Quantification of immobilized groups

Conductometric titration

Because of the high affinity of thiols for soft metals such as Cd^{2+} , Pb^{2+} , Ag^{+} and Hg^{2+} , thiol-functionalized silica exhibited a high adsorption capacity against these ions [301, 302]. Feature of formation metal-sulfide interaction was used to determinate the binding concentration of functional groups by indirect conductometric titration. It is based on the titration of excess Ag^{+} ions with a solution of sodium chloride after their interaction with the immobilized thiol groups [303].

The curves of the back-conductometric titration of the $\text{SiO}_2\text{-SH}(n)$ samples have two regions and the position of its crossing corresponds to the concentration of the attached thiol groups Figure 27. The conductivity of the $\text{SiO}_2\text{-SH}(n)$ suspensions slowly decrease to the equivalence point because the mobility of Ag^{+} ions ($6.24 \cdot 10^{-8} \text{ m}^2 \text{ s}^{-1} \text{ V}^{-1}$) [304] is higher than that of Na^{+} ions ($5.19 \cdot 10^{-8} \text{ m}^2 \text{ s}^{-1} \text{ V}^{-1}$) [304] for which they were substituted. An excess of sodium chloride resulted in an increase in the suspension conductivity because of the high mobility of the chloride ions ($7.91 \cdot 10^{-8} \text{ m}^2 \text{ s}^{-1} \text{ V}^{-1}$) [304]. According to titration curves, Figure 27, equivalence points and concentration of the attached thiols are almost equal for both materials $\text{SiO}_2(4)\text{-SH}(1)$ and $\text{SiO}_2(4)\text{-SH}(2)$, 0.60 and 0.62 mmol g^{-1} , respectively.

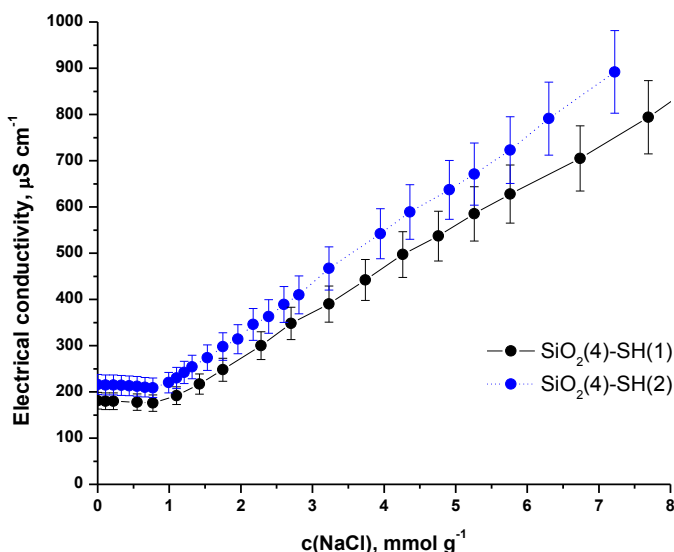


Figure 27 - Plots of electrical conductivity of suspensions of SiO₂(4)-SH(n) versus added sodium chloride

Elemental analysis

The results of the elemental analysis on carbon, hydrogen of analyzed materials are presented in Table 17. Due to similar values of concentration estimated by conductometric titration, element analysis was carried out only for SiO₂(4)-SH(2). The concentration of grafted mercaptopropyl groups was estimated based on the percentage content of C atom.

Table 17 - The results of elemental analysis

Material	C, %	H, %	C_L^C *, mmol/g	C_L^{H**} , mmol/g
SiO ₂ (4)-SH(2)	2.02	0.69	0.56	0.76

Thermogravimetric analysis

Thermal stability of SiO₂(4)-SH(2) was analyzed in the temperature range 225–900 °C (Figure 28). The weight loss observed before 225 °C was not shown due to the removal of physisorbed water [305]. At 225–420 °C, flat profiles changed into a rapidly declining curve corresponding to the decomposition of the grafted silane.

SiO₂(4)-SH(2) material shows a total mass loss of 33.5%. However, the sharp weight loss (30%) occurred up to 420 °C, which could correspond to the decomposition of the mercaptopropyl groups. However, the continuous decomposition took place

together with the condensation of remaining silanol groups to yield the final residue of siloxane [301].

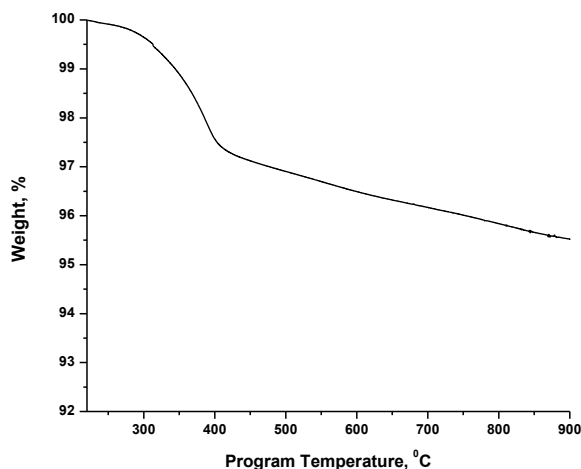


Figure 28 - TGA thermograms of aminosilicas

Based on estimated weight loss of the organic unit, the grafted concentration of thiol-groups was calculated, Table 18.

Table 18 - The estimated concentrations of selected samples by TGA

Materials	The temperature range, °C	The fragments	Δm , mg g ⁻¹	C _L , mmol g ⁻¹
SiO ₂ (4)-SH(2)	225-420	-(CH ₂) ₃ -SH	30.0	0.40±0.1

Comparison of concentrations by various methods

The concentration of immobilized thiol-groups was calculated by elemental, thermogravimetric and conductometry analyses and results are presented in Table 19. As shown in the table, the values obtained by conductometric titration are closed to both samples and higher than two other methods. Reasons for this difference can be the incomplete combustion during elemental analysis or the accessibility of functional groups. Values of concentrations of grafted thiol-groups (less than 1 mmol g⁻¹) lead to the presence of monolayer coating of silica surface. Assuming that homogeneous distribution of immobilized thiol-groups provides uniformly covers the surface and it opens possibility to estimate the surface density of the active binding centers (δ) and the average intermolecular distance between bonding two thiol-groups (l) via equations 1.11 and 1.12. Calculated values are present in Table 19.

Table 19 - Concentrations and density of immobilized groups

Materials	Elemental analysis, mmol g ⁻¹	TGA, mmol g ⁻¹	Conductometric titration, mmol g ⁻¹	C _L , μmol m ⁻²	δ, molecules nm ⁻²	l, Å
SiO ₂ (4)-SH(1)	—	—	0.60±0.20	1.76	1.07	9.67
SiO ₂ (4)-SH(2)	0.56±0.05	0.40±0.1	0.62±0.02	1.61	0.97	10.2

According to data in Table 19, the surface concentration of SiO₂(4)-SH(1) higher than SiO₂(4)-SH(2). As a result, two thiol-fragment in SiO₂(4)-SH(2) lie further apart comparing with SiO₂(4)-SH(1) surface.

4.3. Conclusions of the chapter 4

- 1) It has been demonstrated that N-contained silane was grafted with a higher yield than S-contained silane.
- 2) Qualitative analysis of functional groups by formation colorimetric surface complex can be used for express test of successful immobilization.
- 3) Ninhydrin solution and salicylic acid are able to identify aminogroups and sodium nitroprusside was used for mercaptopropyl groups.
- 4) The surface concentration of the functional groups of aminopropyl groups depends on the pore size and as result surface area.
- 5) The increasing pore size of silica gel from 0 to 11 nm lead to decreasing of surface concentration of aminopropyl groups from 3.3 to 2.3 μmol m⁻².
- 6) The molar concentration of grafted functional groups can be estimated based on CNH, TGA, pH and conductometric titration.
- 7) According to mean value with a confidence interval, concentration of aminopropyl groups is lead in range 0.5-0.96 mmol g⁻¹, while concentration of mercaptopropyl was found 0.4-0.62 mmol g⁻¹.

5. Anthracene-immobilized silicas

Since adsorption properties of organo-silicas depend on a various parameter such as the composition of the immobilized layer, its density and geometry, samples of SiO₂-Ant were obtained using several approaches. In these approaches, silica gels with different pore sizes were used. Composition of the immobilized layer was also varied by using aminosilica or ethylenediamine silica. N-alkylation and condensation reactions were performed to immobilized different anthracene derivatives. Finally, 9 sets of samples of SiO₂-Ant were received, which are identified in Table 20.

Table 20 - Identification of the anthracene-containing silicas and their descriptions

SiO ₂ (d)-Ant-1-t*	Organosilica with nominal pore size d = 6, 9 and 11 nm), having immobilized anthracene fragments obtained by N-alkylation of SiO ₂ -NH ₂
Asil-Ant-1-t	Non-porous silica having immobilized anthracene fragments obtained by N-alkylation of Asil-NH ₂
SiO ₂ (11)-Ant-2a	Organosilica with nominal pore size 11 nm, having immobilized anthracene fragments obtained by condensation of SiO ₂ -NH ₂ with 9-aldehyde derivatives of anthracene, imine
SiO ₂ (11)-Ant-2b	The same as SiO ₂ (11)-Ant-2a after reduction with NaBH ₄ , amine
SiO ₂ (11)-Ant-3a	The same as SiO ₂ (11)-Ant-2a but SiO ₂ -EDA have been used instead of SiO ₂ -NH ₂ , imine
SiO ₂ (11)-Ant-3b	The same as SiO ₂ (11)-Ant-3a after reduction with NaBH ₄ , amine
SiO ₂ (11)-Ant-4a	Anthracene-containing silane was obtained from EDAS by condensation with 9-aldehyde derivatives of anthracene and further silane immobilization on silica, imine
SiO ₂ (11)-Ant-4b	The same as SiO ₂ (11)-Ant-4a after reduction with NaBH ₄ , amine
SiO ₂ (11)-Ant-5b	The same as SiO ₂ (11)-Ant-4a but silane synthesis was performed in diglyme with a further reduction of the product by NaBH ₄ , amine

*- synthesis time, min

5.1. Synthesis of silica with immobilized anthracene derivatives

Two approaches were used in SiO₂-Ant synthesis: a) surface assembling, where target products were prepared in step-by-step synthesis on silica surface; and b) silane immobilization where target silane was prepared first and then immobilized on silica surface, Figure 29.

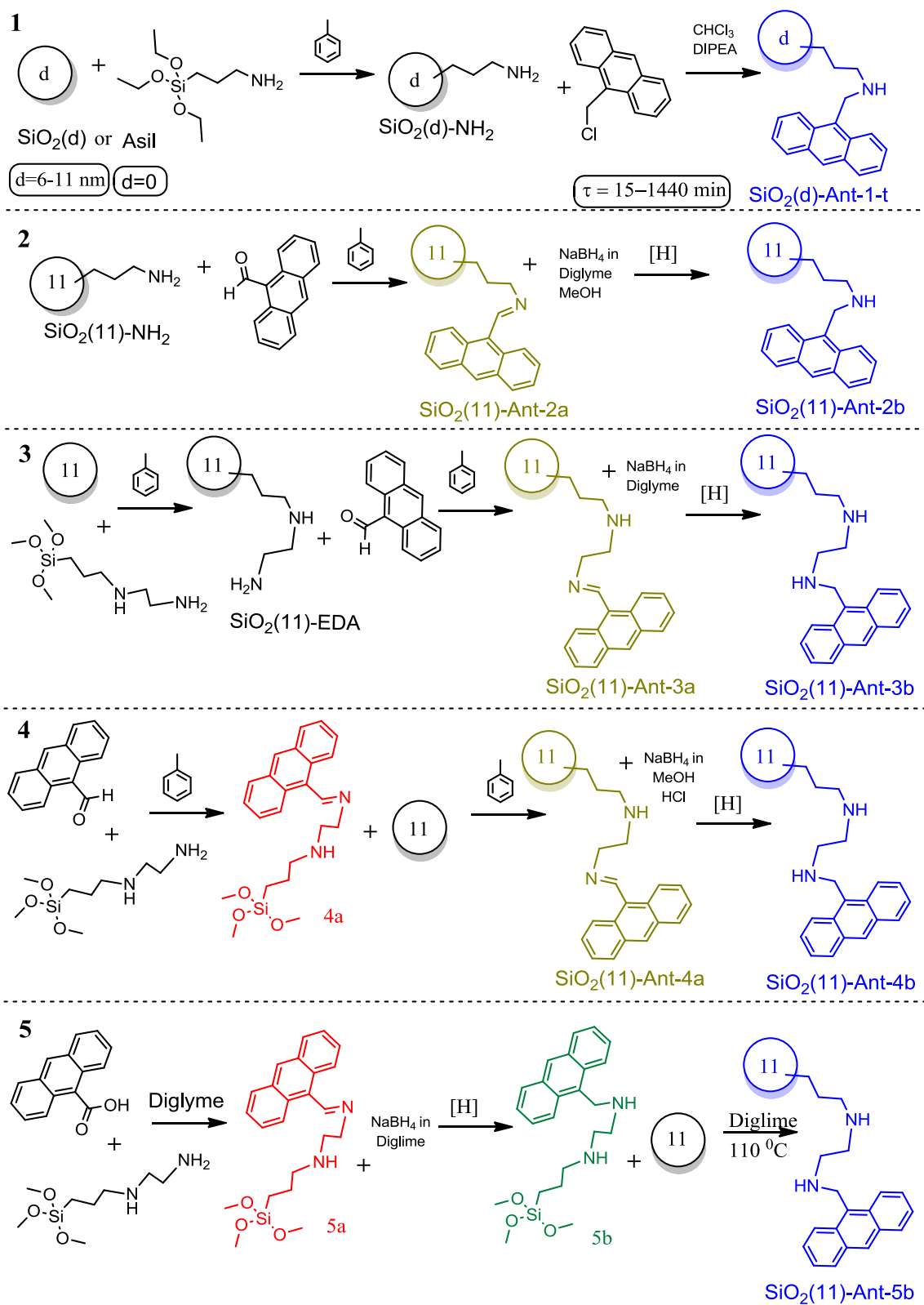


Figure 29 - The summarized scheme of synthesis of the anthracene-based silica gels

The first step is preparation of mono ($\text{SiO}_2(\text{d})\text{-NH}_2$) and diamine ($\text{SiO}_2(11)\text{-EDA}$) silica gels using classical grafting protocol. Secondly, the N-alkylation approach was used to functionalize aminopropyl silica gels with 9CMA in chloroform and in the presence of excess amounts of Hunig's base (known as DIPEA). Previously, acetonitrile was considered as solvent based on the experience of authors [306] that dissolved 9CMA (6.62 mmol) in 50 ml of acetonitrile. However, in practice 9CMA (2 mmol) could not be dissolved completely in 50 ml and even in 500 ml. After examination the most appropriate solvent, chloroform was selected. DIPEA is a relatively non-nucleophilic tertiary amine and used as a base catalyst for reaction. Two isopropyl groups and one ethyl group sterically hinder access to nitrogen making a very poor target for the nucleophilic attack [307]. Presence of DIPEA should not interfere with the interaction between fixed aminopropyl and 9CMA with forming quaternary ammonium salts. DIPEA was taken in 15-fold excess with respect to the theoretical maximum capacity of the aminated silica gel (1 mmol g^{-1}) to neglect reagent consumption during the synthesis. Initial aminopropyl silica gel play the role of insoluble reactant, thus 9CMA was used in two-fold excess and progress of the reaction was checked by it. 9CMA has characteristic peaks in the UV-Vis region and supernatant was easily verified for the presence of an excess of 9CMA. The main challenge was washing off the obtained product in Soxhlet to complete remove of non-reacted anthracene precursor. The desorption of 9CMA from pores to washing solution is quite a long process, because of small pore size and conformational rearrangements of presented functional groups upon contact with a solvent. After addition of a fresh portion of solvent to supposedly sample, 9CMA moved to solvent volume.

The continuous extraction of 9CMA excess has occurred for 2-7 days depending on the sample. Previously [308, 309], difficulties in washing have not been indicated in detail, although it is important for the further use of materials as solid-phase adsorbents.

Initial aminosilica gel is a white powder. During connection with anthracene reactant the color has been changing into yellow-orange product. Similar color changing was occurred in [310] after the introduction of 9CMA unit to amine-derivative. As it is known (link metal adsorption), aminopropylsilica gel with Cu^{2+}

forms blue surface complex. After the addition of Cu^{2+} solution, anthrylmethyl-aminosilica gels have greenish color via overlapping blue color of the new complex and yellow product.

Different silicas non-porous and porous were used as matrices. It is reasonable to compare surface behavior of the non-porous functionalized silica gel with porous because porous supports affect the amount of the adsorbed reactants. Asil-Ant-1-t is a reference product in case absence of physical adsorption of reactant in silica pores. Similar to pyrene molecules [311], two molecules of anthracene can interact at a close distance and form excimers. Long-standing synthesis is a risk of receiving high loading sample with excimer complex. The synthesis was carried out at room temperature in order to prevent the fast formation of anthracene-anthracene interaction on the surface. The different pore size of pristine silica matrix was used to investigate the excimer effect during synthesis. Using photoluminescence study of anthrylmethyl-aminopropyl silica gel recorded from solid samples, the effects of changing the silica pore size on the formation of excimers from anthracene molecules confined in the mesopores was studied. Products with a pore size of 6 nm gave less excimers than materials synthesized with 11 nm pores [311]. Kinetics assay was studied to estimate the effectiveness of the synthesis process of modified materials. The approach helps to understand optimal synthesis conditions for preparation of solid phase with an optimal degree of modification. The free 9CMA in solution was monitored with UV-Vis at 373 nm. The non-free 9CMA was bound via covalent grafting with amino groups (in case of Asil-NH₂ or SiO₂(d)-NH₂) and physically adsorbed due to porous structure of matrix (in case of SiO₂(d)-NH₂). As a result, consumed quantity of 9CMA at different synthesis time, q_t , was calculated and two common kinetic models were employed to simulate the modified progress, equation 1.19 and 1.20. The pseudo-second-order model was only one which able to fit experimental data with high correlation coefficient (R^2), Figure 30.

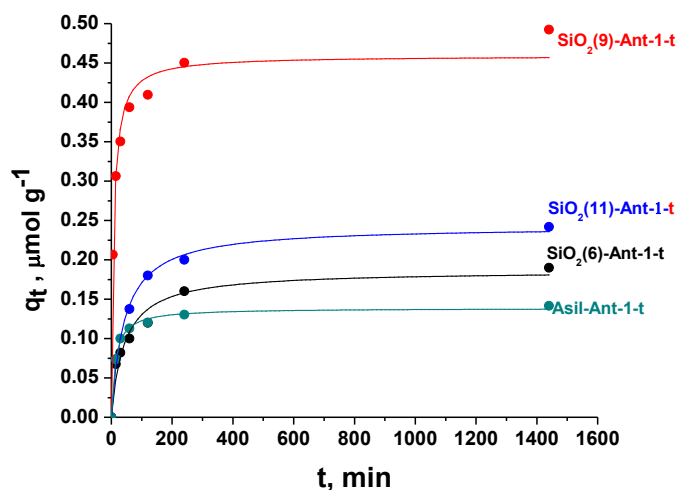


Figure 30 - Plot of consumed quantity of 9CMA by aminated silicas at different synthesis time (points – experiment; lines-model of pseudo-second-order)

The obtained modeling kinetic parameters and correlation coefficients are presented in Table 21. Covalent binding of 9CMA on Asil-NH₂ can be observed only between functional groups on the surface. As a result, Asil-Ant-1-t showed the least value of calculated adsorption capacity. It is a fact that adsorption efficient increases with the surface area of the material. Among normalized adsorption capacity by the surface area of selected materials, SiO₂(9)-Ant-1-t shows the maximum due to high surface area of initials aminosilica gel SiO₂(9)-NH₂ (326 m² g⁻¹ versus 290 m² g⁻¹ for SiO₂(11)-NH₂). The reaction reached the equilibrium at room temperature in approximately 120 min for all samples. Based on the obtained concentration of fixed aminopropyl groups via the back-titration approach, conversion of an amine into anthracene groups was calculated. However, theses value is in excess due to physically adsorbed some part of 9CMA. Excess conversion increased in order Asil-Ant-1-t ≈ SiO₂(6)-Ant-1-t (22%), SiO₂(11)-Ant-1-t (47%), SiO₂(9)-Ant-1-t (78%).

Table 21 - The parameters of kinetic modeling for anthracene modified silica gel

Model	Modeling parameters	Asil-Ant-1-t	SiO ₂ (6)-Ant-1-t	SiO ₂ (9)-Ant-1-t	SiO ₂ (11)-Ant-1-t
Pseudo-second order	q _e calc., mmol g ⁻¹	0.11±0.05	0.19±0.06	0.46±0.10	0.24±0.06
	q _e calc., μmol m ⁻²	0.73±0.10	0.68±0.05	1.9±0.20	1.1±0.10
	k ₂ , g mmol ⁻¹ min ⁻¹	0.187	0.126	0.293	0.098
	R ²	0.950	0.956	0.981	0.994
	ω ^{back} , %	22.1	21.3	77.6	47.0

Formation of intermediate Schiff base product was a basic approach to the synthesis of the second group of anthracene-based silica gel differs in the procedure. Order of reactants addition and solvent type were principal distinctions. For the preparation of *SiO₂(11)-Ant-2a* and *SiO₂(11)-Ant-3a*, initially 9ACA was mixed with animated silica gel (SiO₂(11)-NH₂ and SiO₂(11)-EDA, respectively) in dry toluene, Figure 29. The reaction of imine formation is a reversible equilibrium that generates water as a by-product. A Dean-Stark trap was used to collect water produced during a chemical reaction and to prevent oligomerization of the alkoxysilane groups during the synthesis of protected silane via the reaction between the aldehyde and the amine. Initially, sodium borohydride in diglyme and MeOH was used to reduce the double bond. After the reduction step of imine silicas, the color of the samples became lighter.

Another reactant combination was chosen for SiO₂(11)-Ant-4a and SiO₂(11)-Ant-5a. In SiO₂(11)-Ant-4a, at the beginning, 9ACA reacted with EDAS in toluene and afterwards SiO₂(11) was added, (4a and SiO₂(11)-Ant-4a, respectively), Figure 29. Imine was reduced in methanolic solution of NaBH₄, (SiO₂(11)-Ant-4a). However, in SiO₂(11)-Ant-5a toluene was substituted in diglyme, and reduction step was carried out before addition of SiO₂(11). NaBH₄ is less reactive than lithium aluminium hydride and is, therefore, more chemoselective in its action. Reduction step was carried out at room temperature in methanol and NaBH₄ acts on obtained double bond of imine-silane and present excess of 9ACA. After the reduction step, the solution above solid-phase shows a new fluorescent spot on the TLC plate (hexane:EtOAc=80:20) under 365 nm, which may be related to reduced anthracene-9-methanol from aldehyde

excess. Soxhlet washing in methanol after reduction was necessary to remove unreacted reactant-derivatives.

Finally, qualification assay was applied to check the presence of unreduced imine functional groups. The dried solid products ($\text{SiO}_2(11)\text{-Ant-(2-5)a}$) have been mixed with HCl ($1 \cdot 10^{-2}$ M) and extracted in toluene. If materials have imine units, contact with HCl turns it into orange flaky solid and organic layer colored in yellow. $\text{SiO}_2(11)\text{-Ant-2a}$, $\text{SiO}_2(11)\text{-Ant-3a}$, $\text{SiO}_2(11)\text{-Ant-5a}$ did not show the presence of imine excess, when $\text{SiO}_2(11)\text{-Ant-4a}$ give colored layer and additional washing step with HCl was performed with further vacuum dry step.

5.2. Textural characterization

Textural features of studied materials were investigated based on nitrogen adsorption-desorption isotherms. The analysis directly shows the difference between non-porous and porous materials, Figure 31.

All porous analyzed samples represent IV type isotherm according to the IUPAC classification that associates with H1 hysteresis loop. Usually, it is related to the absence of macropores [288]. The presented shape of hysteresis is attributed to cylindrical pores. However, the overall profiles of the adsorption-desorption isotherms and them hysteresis loop were retained for all porous modified samples, which indicates that the porous structure of the silica gel was not appreciably altered with modification. In case of aerosil-derivation, isotherms classified as type II and referred to adsorption on non-porous solids or type III with polymodal covering. In our case, the isotherms of modified aerosil are almost reversible. Existence of small hysteresis can be related to presence of cavities between aggregates or inter-particle pores. Interestingly, $\text{SiO}_2(11)\text{-Ant-5a}$ is not similar to its analogous, Figure 32.

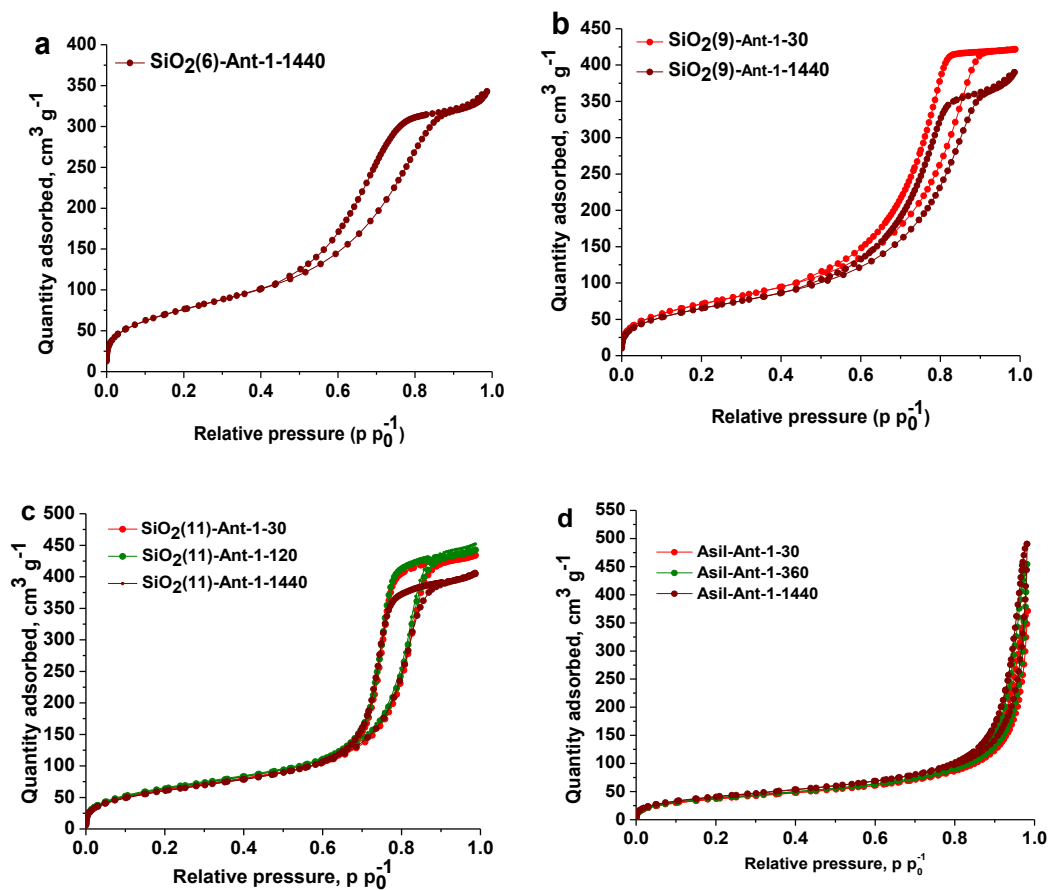


Figure 31 - N_2 adsorption-desorption isotherms of $\text{SiO}_2(6)\text{-Ant-1-t}$ (a), $\text{SiO}_2(9)\text{-Ant-1-t}$ (b), $\text{SiO}_2(11)\text{-Ant-1-t}$ (c), aerosil-based materials (d)

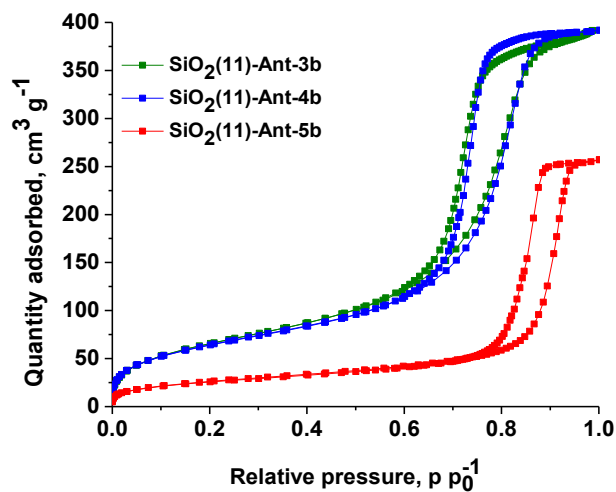


Figure 32 - N_2 adsorption-desorption isotherms of $\text{SiO}_2(11)\text{-Ant-3b}$, $\text{SiO}_2(11)\text{-Ant-4b}$, $\text{SiO}_2(11)\text{-Ant-5b}$

Relative pressure of hysteresis start was shifted from 0.7 to 0.8, which indicates about changes were introduced in the porous structure of the silica during chemical modification. Qualitative proof of the surface modification can be monitored by changing the porous characteristic of materials after the modification step. According to Table 22 specific surface area and pore volume of prepared materials are comparatively lower than those of the corresponding pristine silica gels. Attachment of anthryl molecules at the porous silicas $\text{SiO}_2(\text{d})$ with increasing of synthesis time causes a reduction of the total pore volume and the internal pore size. Contact with organic solvent leads to aggregation of individual aerosil particle with decreasing of surface area after modification.

In additionally, for non-porous and porous studied materials a reduction in the surface area of the silica gel after organo-functionalization in relation with the unmodified silica gel matrix is observed. This phenomenon can be related to the obstruction of the pores due to the formation of a covering dense layer by the functional groups or to the coalescence of pores Figure 33.

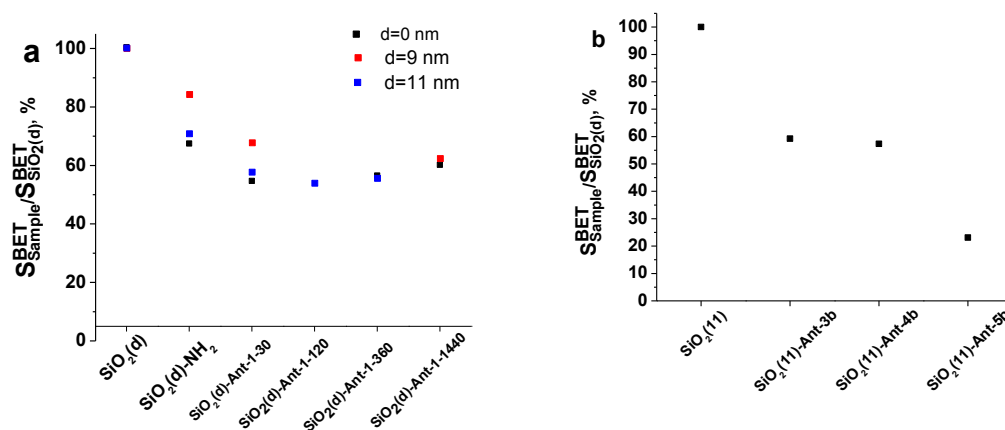


Figure 33 - Plots of relative changes of S_{BET} during synthesis

Table 22 - The textural characteristics of the obtained materials

Material	Average pore size, nm	S_{BET} , m^2g^{-1}	V_p , $\text{cm}^3 \text{g}^{-1}$
Asil		260.7	
Asil-Ant-1-30		136.0	
Asil-Ant-1-360		141.1	
Asil-Ant-1-1440		151.1	
$\text{SiO}_2(6)$	6.0 ^a	480.0	0.80
$\text{SiO}_2(6)$ -Ant-1-1440	5.6	278.37	0.51
$\text{SiO}_2(9)$	10.1	387.4	1.01
$\text{SiO}_2(9)$ -Ant-1-30	6.8	262.0	0.64
$\text{SiO}_2(9)$ -Ant-1-1440	7.2	239.1	0.59
$\text{SiO}_2(11)$	12.2	410.2	1.25
$\text{SiO}_2(11)$ -Ant-1-30	7.8	227.3	0.66
$\text{SiO}_2(11)$ -Ant-1-120	7.8	234.1	0.68
$\text{SiO}_2(11)$ -Ant-1-1440	7.6	221.0	0.62
$\text{SiO}_2(11)$ -Ant-3b	6.9	242.8	0.59
$\text{SiO}_2(11)$ -Ant-4b	7.2	235.1	0.59
$\text{SiO}_2(11)$ -Ant-5b	13.2	94.8	0.39

^a data from the manufacturer.

5.3. Solid state ^{13}C NMR

Significant information about immobilization of pendant groups on the pristine silica substrate can be obtained through solid-state ^{13}C NMR spectra, as presented in Figure 34. At the beginning, the spectrum of $\text{SiO}_2(11)$ -EDA has four distinct signals at 9.6, 22.4, 40.1 and 51.0 ppm are related to different carbon atoms in 3-n-propylethylenediamine groups [290] labeled in figures. These peaks help to conclude that the alkyl chain was in fact bonded to the silicon atom. Interesting to compare sample before and after reduction imine bond of $\text{SiO}_2(11)$ -Ant-3a. After reaction of aminated silica gel with 9ACA, new peaks have been appeared. The spectrum of $\text{SiO}_2(11)$ -Ant-3a confirmed the presence of the imine bonds $-\text{C}=\text{N}$ with the resonance at 162.0 ppm and low intensity [312]. Aromatic carbons of anthracene rings related to broad peak at 124-130 ppm. Taking in account reduction step, the new peak at 30.0 ppm was assignable to the reduced carbon atoms connecting to three

benzene rings. In addition, presence of peak at 210.0 ppm can be related to carbonyl groups [313] due to hydrolysis of imine groups during reduction lead or non-washed 9ACA precursor. $\text{SiO}_2(11)$ -Ant-3b in aromatic region has shoulder with the intersect of peaks that can be corresponded to several form of anthracene onto silica gel. $\text{SiO}_2(11)$ -Ant-4b has similar spectrum, but with worse resolution and with the weak resonances at 168.6 ppm was assigned to the residual imine groups which did not react reduced with NaBH_4 . For last $\text{SiO}_2(11)$ -Ant-5b sample shifts of the pristine alkyl carbon signals attributed from 0-55 ppm to 20-80 ppm are also observed. This affect can be attributed to some structural transformation between silane and 9ACA.

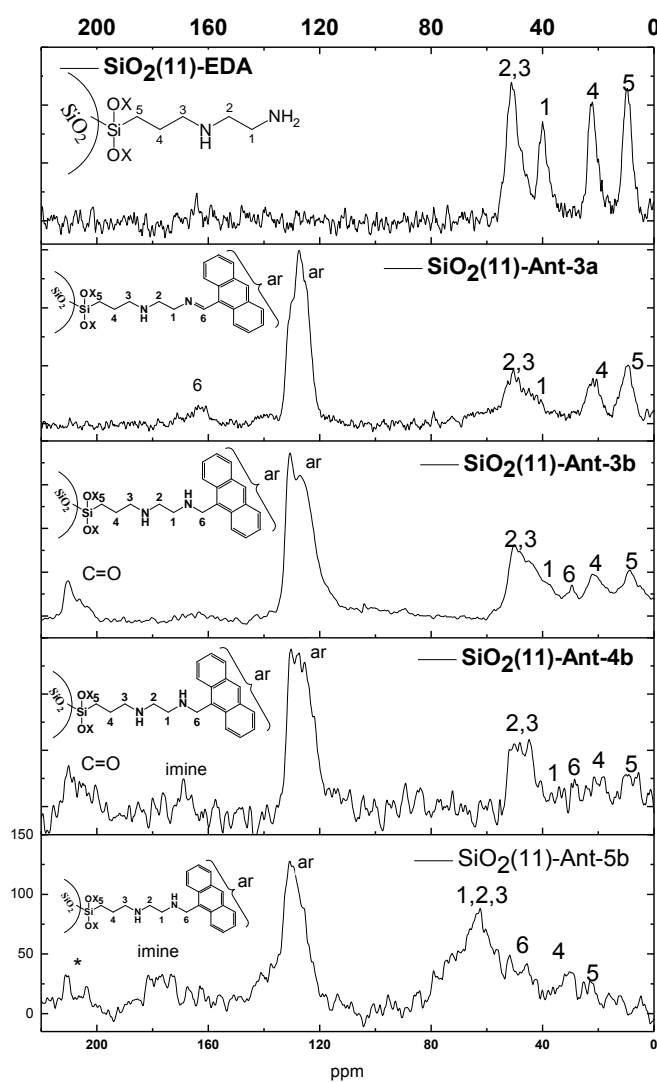


Figure 34 - ^{13}C CP/MAS NMR solid state spectrum of $\text{SiO}_2(11)$ -EDA derivatives; (*) - Spinning sidebands

5.4. FTIR characterization

Anthracene silica gels obtained by N-alkylation were characterized by FTIR analysis. Due to similar composition of functional groups, representation of FTIR spectra of silicas modified with anthracene groups was made by Asil-derivatives, Figure 35. The broad band covering the range from 3000 to 3700 cm^{-1} can be assigned to hydrogen-bonded and sharp band at 3740 cm^{-1} in Asil-Ant-1-1440 contribute to isolated Si-OH groups. With increasing synthesis time, the intensity of bands in the range 1650-1300 cm^{-1} is also gone up. Both spectra display aliphatic stretching (2870 and 2936 cm^{-1}) and banding (1448 and 1470 cm^{-1}) vibrations of C-H bonds that attribute to from aminopropyl segment. Bands of aromatic molecules generally are weak. C=C and C-H vibration of anthracene groups can be related with observed bands at 1634 cm^{-1} and 1412 cm^{-1} , respectively. The residue of unconverted primary aminopropyl groups can be related to band at 1573 cm^{-1} . Thus, immobilization of anthracene fragment was reached successfully.

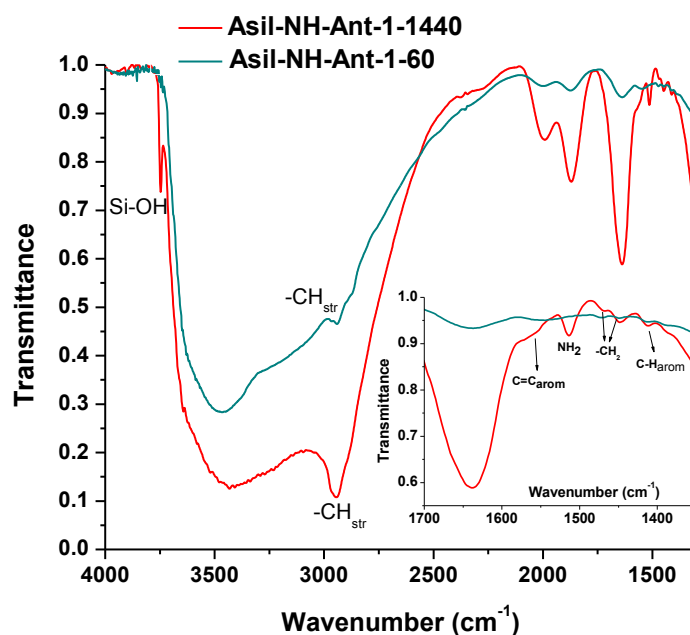


Figure 35 - FTIR spectra on Asil-Ant-1-t

5.5. XPS characterization

XPS survey scan of anthracene-based silica gel $\text{SiO}_2(11)$ -Ant-1-1440 (not shown) revealed predominantly the presence of matrix component Si2s and Si2p (34.2%), O1s (53.9%) and modifier components N1s (2.1%) and C1s (9.8%). The

deconvolution of the C1s spectrum of anthracene-silica gel differs from pristine aminopropyl silica gel, Figure 36a. High-resolution C1s spectra of each sample have three components in range 282-290 eV. Based on energy position, these peaks of SiO₂(11)-NH₂ and SiO₂(11)-Ant-1-1440 can be related to next bonds C-O (287.6 and 288.2 eV), C-N (286 and 286.4 eV), C-C/C-H (285 and 285.1) [314], respectively. Some shifts towards long energy zone are observed for SiO₂(11)-Ant-1-1440. It can be related to the presence another carbon form that overlaps with the deconvoluted dominant component. In addition, the obvious feature of C1s spectrum of SiO₂(11)-Ant-1-1440 is presence a shake-up peak with binding energy at 292.1 eV. This kind of peak is a characteristic of pi-pi* transition [315] in conjugated systems or aromatic groups. Although C=C groups have not been clearly identified, pi-pi* transition confirmed the existence of anthracene fragment onto silica gel. Aromatic C=C content may be included in a peak at 285.1 eV. Two N-containing forms can be obtained after fitting N1s XPS spectrum of SiO₂(11)-Ant-1-1440. There are one peak at 399.8 eV corresponds to primary or secondary N-H amines and another peak at 401.7 eV related to hydrogen-bonded amine [316]. Successful coupling of anthracene groups on the aminosilica surface is further confirmed by fluorescence measurements.

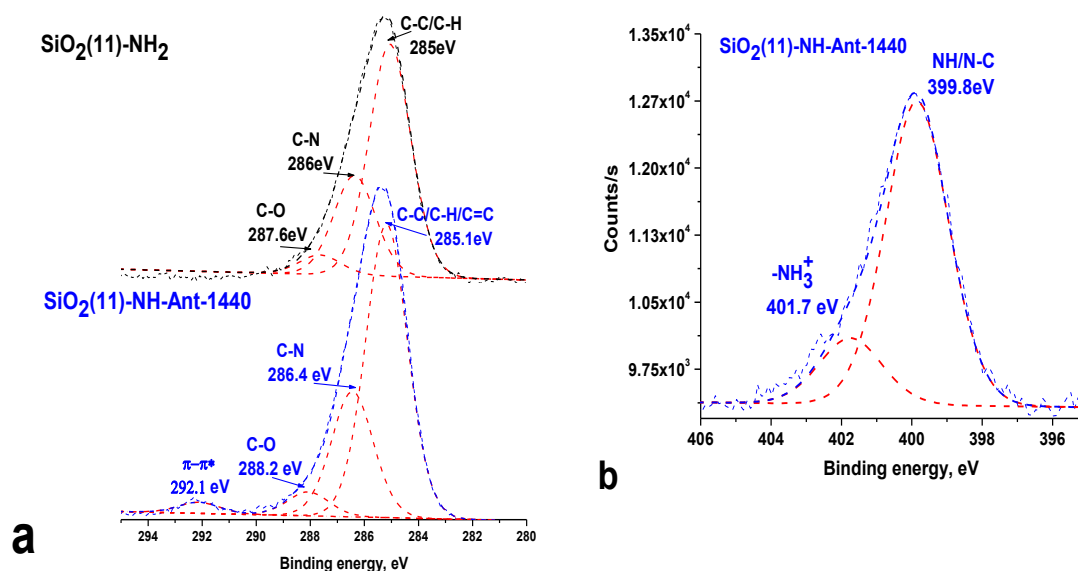


Figure 36 - High-resolution C1s spectra of aminopropyl and anthracene-based silica gel (a) and N1s spectrum of anthracene-based silica gel (b)

The deconvolution of the C1s region of 3-n-propylethylenediamine silica gel SiO₂(11)-EDA similar to SiO₂(11)-NH₂, when the appearance of peaks at 285.0, 286.0,

287.2 eV corresponds to the presence of C-C/C-H, C-N, C-O bonds, respectively, Figure 37. The obvious difference was noted in relation percentages of C-C/C-H to C-N. In $\text{SiO}_2(11)\text{-NH}_2$ sample this relation is C-C/C-H:C-N=66%:28%, while in $\text{SiO}_2(11)\text{-EDA}$ sample equal 53%:41% and can be related to a higher number of N element in grafting groups. C1s XPS spectrum of $\text{SiO}_2(11)\text{-Ant-2b}$ is close to $\text{SiO}_2(11)\text{-Ant-3b}$ with two fitted peaks C-C/C-H at 285 eV and C-N at 286 eV with percentage 80%:20 and 85%:15%, respectively for the samples. $\text{SiO}_2(11)\text{-Ant-5b}$ has an interesting spectrum with two new peaks at 288.0 eV and 292.0 eV responder to C-O and $\pi\text{-}\pi^*$ transition.

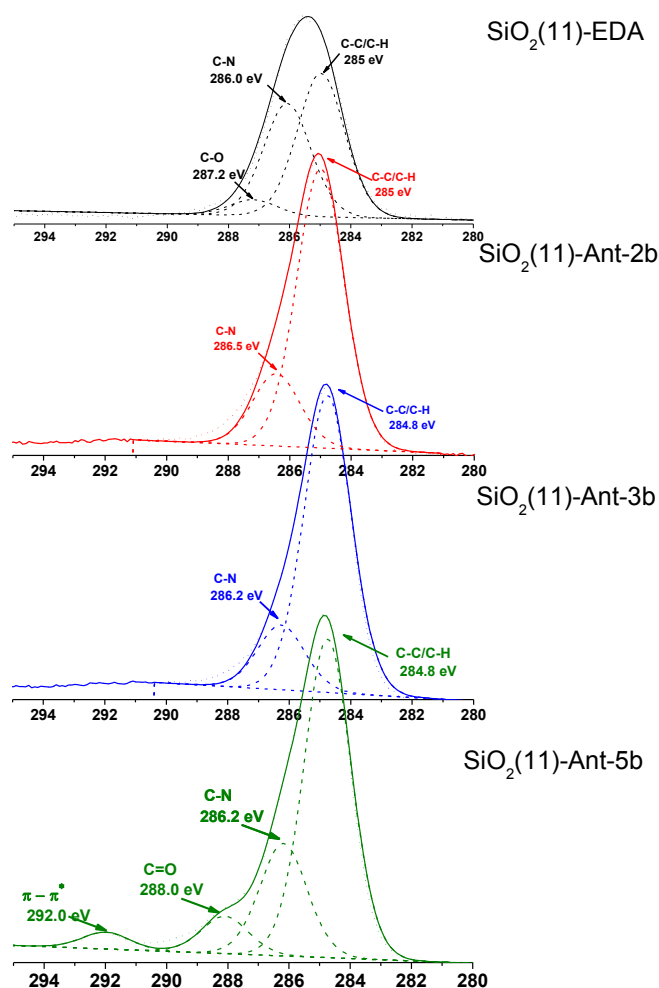


Figure 37 - High resolution C1s spectra of $\text{SiO}_2\text{-EDA}$ and reduced imine anthracene silica gels

5.6. Thermogravimetric analysis

Thermal decomposition of organic fragments and thermal stability of selected silica-based materials was analyzed using TGA. The low-temperature mass loss is

responsible for the desorption of physically adsorbed water from the silica surface of the carrier [317] that's why region before 220°C is not shown, Figure 38. After 700 °C can be observed some mass loss due to water evolution associated with dehydroxylation of isolated silanols on silica surface. The high-temperature effects correspond to the thermal destruction of the organic layer. Aminopropyl silica gels decompose at 250-700°C and anthracene-based materials break down to 900°C with stepwise processes of mass loss. The value of mass loss at this range can be used for the calculation of the total organic loading. The results of such calculations are present in Table 23. Non-porous Asil-NH₂ shows the lowest concentration of aminopropyl groups 0.66 mmol g⁻¹. However, decreasing of pore size of aminated silicas from 11 to 6 nm lead to higher grafting of functional groups from 0.76 to 1.07 mmol g⁻¹. Calculation of concentration of grafted groups bonded using multi-step synthesis is complicated by the presence of simultaneous processes of decomposition. The concentration of anthrylamine groups can be calculated by the difference in its mass loss and pristine aminopropyl silica gel. Anthracene-based functional groups of Asil-Ant-1-1440 covered about 17% of total groups, while SiO₂(6)-Ant-1-1440 showed 21%.

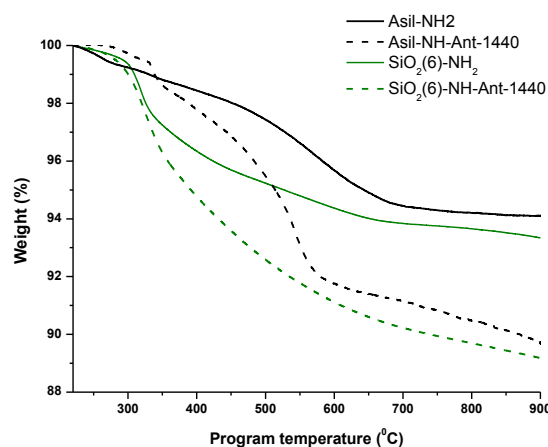


Figure 38 - TGA thermograms of pristine aminopropyls and anthracene-based silica gels

Table 23 - The estimated concentrations of selected samples by TGA

Materials	The temperature range, °C	The fragments	Δm , mg/g	C_L , mmol/g	ω , %
Asil-Ant-1-1440	220-675	-CH ₂ -Ant	68	0.11	17
SiO ₂ (6)-Ant-1-1440	220-680	-CH ₂ -Ant	90	0.22	21

5.7. Element analysis

The results of elemental analysis on carbon, hydrogen and nitrogen of selected materials are presented in Table 24.

Table 24 - The results of elemental analysis

Material	N, %	C, %	H, %	C_L^N , mmol g ⁻¹	C_L^{N*} , mmol g ⁻¹	C_L^{Ant*} , mmol g ⁻¹
SiO ₂ (6)-Ant-1-1440	1.14	6.10	0.98	0.81	0.63	0.18
SiO ₂ (9)-Ant-1-1440	1.16	5.94	0.98	0.83	0.66	0.16
SiO ₂ (11)-Ant-1-1440	1.05	4.61	0.80	0.75	0.64	0.11
SiO ₂ (11)-Ant-2b	0.82	6.61	0.85		0.33	0.25
SiO ₂ (11)-Ant-2a	0.98	7.46	0.87		0.43	0.27
SiO ₂ (11)-Ant-3b	1.76	9.13	2.78		0.33	0.30
SiO ₂ (11)-Ant-4b	2.13	9.12	3.87		0.51	0.25

Multistep modification at silica surface lead to the presence of more type of functional groups. The first step of modification is a root of the target product and it is advisable to compare the results of the elemental analysis on several elements. Nitrogen loading is more accurate information about the concentration of fixed N-contained groups.

After the second stage of surface modification to obtain anthracene-based material, carbon content was increased due to reaction with 9CMA and 9ACA. In this case, the concentration of bonded groups from nitrogen loading C_L^N describes the total concentration of N-containing groups. Due to incomplete transformation aminopropyl into anthraceneaminopropyl groups, the resulting anthracene-based material is multifunctional (a mixture of various grafted groups) and determination of the concentration needs a specific approach. Proposed way suggests the presence of different chemical forms on the surface which can contribute to the elemental composition. This approach allows determining the concentration of grafted groups

even if the elemental analysis was carried out only for the final multi-step product. Matrix model was applied. In Table 25 are presented an example of a matrix for SiO₂(6)-Ant-1-1440. The system of three equations (analysis on three elements) with three unknowns' concentrations of these groups were solved and results were presented in Table 24 denoted as *. It was observed that summing up values of concentration residual aminopropyl groups C_L^N * and anthracene modified fragment C_L^{Ant} * obtained with matrix method was total concentration of residual and modified aminopropyl groups $C_L^N * + C_L^{Ant} * = C_L^N$. After N-alkylation synthesis (SiO₂(d)-Ant-1-τ), surface of silica gels contains 0.11-0.18 mmol g⁻¹ of anthryl-aminopropyl targeted groups.

However, Schiff base reaction is a route that leads to higher loading of anthryl fragment 0.25-0.30 mmol g⁻¹.

Table 25 - Matrix model to calculate the concentration of SiO₂(6)-NH-Ant-1440

System of equations	Potential grafted groups	C_L^X
$\begin{cases} 12 \cdot 3 \cdot x + 12 \cdot 18 \cdot y + 0 \cdot z = 6.10 \cdot 10^{-2} \\ 1 \cdot 10 \cdot x + 1 \cdot 20 \cdot y + 2 \cdot z = 1.14 \cdot 10^{-2} \\ 14 \cdot 1 \cdot x + 14 \cdot 1 \cdot y + 0 \cdot z = 0.98 \cdot 10^{-2} \end{cases}$	-Si(OH) ₂ -(CH ₂) ₃ -NH ₂	X=N
	-Si(OH) ₂ -(CH ₂) ₃ -NH-CH ₂ -Ant	X=Ant
	H ₂ O	X=H ₂ O

5.8. Surface functionality

CHN and TGA were analyses that able to evaluate the molar concentration of organic modifier on the silica surface. Previous consumed values of 9CMA during kinetic assay showed overstatement concentration of anthracene value and can be used as preliminary surface modification order, Table 21, Table 26. The concentration of immobilized groups was calculated by several independent methods and results are presented in Table 26. For a better representation of functional groups location, obtained concentration in mmol g⁻¹ was converted to surface specific concentration in μmol m⁻² using results of the textural characteristics, Table 22.

The molar concentration can be normalized by the surface area of analyzed materials. In this case, due to the smallest surface area, Asil-NH₂ has surface concentration 5.4 μmol m⁻², while SiO₂(9)-NH₂ and SiO₂(11)-NH₂ have in two times less 2.6 μmol m⁻². Similar situation observed for sample with anthracene-based samples. The nature of the surface coverage with grafted molecules and their distribution are the factors that determine the differences in the properties of grafted

and native molecules. The distance between the grafted molecules influences on the protolytic properties of the grafted ligands, the stability of formed complexes on the surface and the mechanisms of surface coverage by the modifier.

Table 26 - Summarized information about concentrations of grafted Ant and density of immobilized groups

Materials	C_L^{kinet} , $\mu\text{mol m}^{-2}$	C_L^{CHN} , $\mu\text{mol m}^{-2}$	C_L^{TGA} , $\mu\text{mol m}^{-2}$	ω^{CHN} , %	δ , molecules nm^{-2}	l_i , Å
Asil-Ant-1-1440	0.73±0.10	0.93±0.20	0.73±0.10	28.2	0.56	13.4
SiO ₂ (6)-Ant-1-1440	0.68±0.05	0.65±0.10	0.79±0.05	20.3	0.40	15.8
SiO ₂ (9)-Ant-1-1440	1.9±0.20	0.67±0.10	—	27.3	0.40	15.8
SiO ₂ (11)-Ant-1-1440	1.1±0.10	0.50±0.06	—	21.4	0.30	18.3
SiO ₂ (11)-Ant-3b	—	1.24±0.10	—	50%	0.75	11.5
SiO ₂ (11)-Ant-4b	—	1.28±0.10	—	33%	0.77	11.4

Assuming that homogeneous distribution of immobilized amino groups provides uniformly covers the surface and it opens the possibility to estimate the surface density of the active binding centers (δ) and the average intermolecular distance between fixed two aminopropyl or two anthracene-aminopropyl groups (l_i) [101, 318].

According to values of aminopropyl density onto obtained porous samples, the surface coverage close to or lower than the monolayer – 2.05 and 1.56 amino groups by nm^2 , as compared to the maximum theoretical value of 2.05 groups per nm^2 (study based on SiO₂ with pore size 4.2-12.0 nm) [319]. Non-porous Asil-NH₂ has a little bit higher density. Special attention should be paid to the nearest neighbor distance between anthracene moieties. Feature of aromatic pi-conjugated molecules in close position to each other is forming excimer complex. The critical distance of excimer formation for pyrene molecules on silica surface is 3-5 Å [101]. The condition of the excimer anthracene-anthracene formation in solution was estimated to be 8-10 Å in chloroform [306]. The average distances between two anthracene molecules in Asil-Ant-1440 and SiO₂(d)-Ant-1440 samples are in the range 13.5-18.3 Å that are in two times higher than magnitude to the distance between two amino groups in initial fixed amines. Obtained values are much more than 10 Å thus no interactions between two closely located anthracene subunits should be observed. Previously studies show exceptions. With the calculated average anthracene distance ranges from 12.3 to 34.9 Å, emission spectra of solid silica gels with anthracene fragment had a characteristic

band at 500 nm. Additional studies of surface photoluminescence properties of modifying materials are needed.

5.9. Solid-state photoluminescence of anthracene-containing materials

Similar to pyrene molecules [311], molecules of anthracene can interact with each other due to π - π stoking forming excimers. Certainly, behavior of the anthracene molecules in solution and on the surface is different. Particularly, it was demonstrated that anthracene adsorbed in silica gel with a pore size of 6 nm gives less excimers than those adsorbed in 11 nm pores [311]. We studied this effect for anthracene adsorbed of SiO_2 and $\text{SiO}_2\text{-NH}_2$ to prevent miss-interpretation of the results and minimize unwanted formation of the excimers on silica. Thus, photoluminescence of anthrylmethyl-aminopropyl silica gel, SiO_2 and $\text{SiO}_2\text{-NH}_2$ with adsorbed anthracene were studied. Effect of changing the silica pore size on the formation of excimers from anthracene molecules confined in the mesopores was also studied.

5.9.1. Photoluminescence study of anthracene adsorbed on SiO_2

Anthracene solution and pristine silica gel can be used as modeling objects for the preliminary pattern of photoluminescence study of modified solid sample. Static adsorption of anthracene on silica gel was analyzed to evaluate interaction with silica matrix. After excitation solution of anthracene at 360 nm, the only one overlap occurs at 380 nm, which corresponds to the transition from vibration level $v=0$ at ground state S_0 to $v=0$ at ground state S_1 , (label as “0-0” Figure 39). Excitation spectra were recorded at emission wavelength of 402 nm that corresponds to the most intensive band. As shown in inset Figure 39, there is a good linear relationship between photoluminescence intensity at 402 nm and initial concentration of anthracene without demonstration inner effect in range $0\text{-}5.6 \mu\text{g ml}^{-1}$ in ethanol. Comparing photoluminescence intensity before and after adsorption on silica sorbent, the low values of anthracene retention $0\text{-}8\%$ were obtained.

Anthracene can be adsorbed on the silica surface via π -cloud interactions with silanol functionalities [320]. Due to previously thermal treatment of silica gel with the removal of silanol groups, insignificant interaction between anthracene and residual silanol groups was observed.

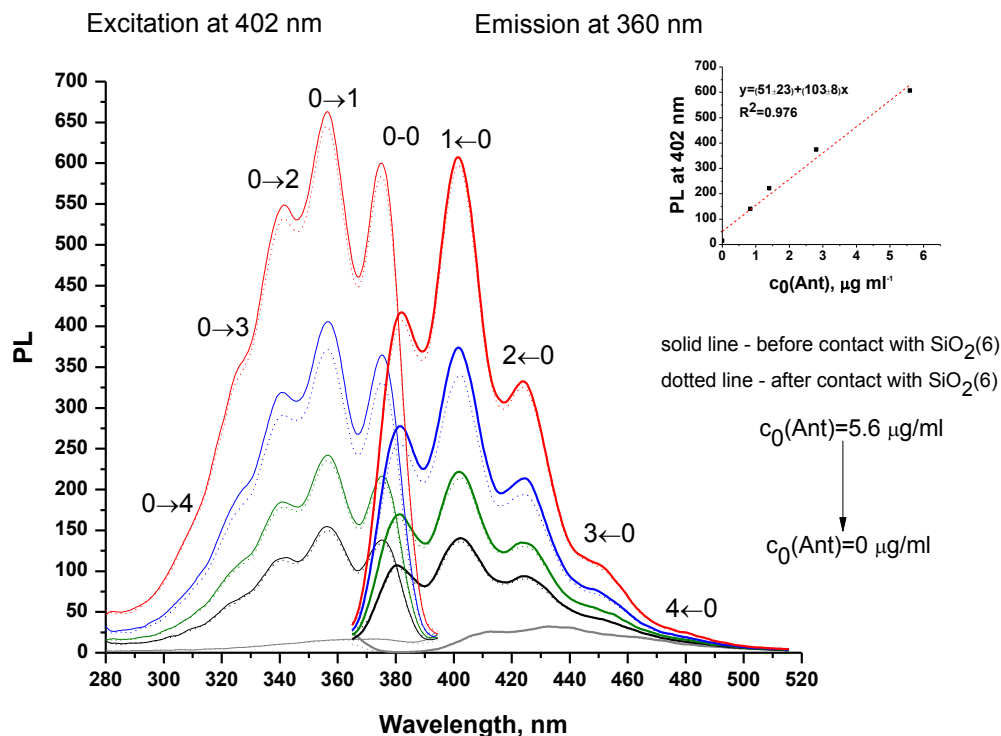


Figure 39 - Photoluminescence spectra of anthracene solution before and after adsorption, exc 360 nm (solvent=ethanol, V=5 mL, m=300 mg, time=120 min)

Photoluminescence behavior of anthracene precipitated on silica surface was evaluated. Based on low adsorption of anthracene, it was introduced by impregnation method with following evaporation of the solvent. According to volume pore of $\text{SiO}_2(6)$ ($V_p=0.8 \text{ cm}^3 \text{ g}^{-1}$) minimum fixed volume of solution with different quantities of anthracene were added to silica gel to gel solid composites $\text{SiO}_2(6)@\text{Ant}$. Emission spectra of bulk $\text{SiO}_2(6)@\text{Ant}$ samples excited at 360 nm had broad peak overlapping in range 370-385 nm, thus the optimized excitation wavelength was found as 340 nm. Normalized emission spectra of $\text{SiO}_2(6)@\text{Ant}$ after evaporation of solvent have clearly defined peaks, Figure 40. The peak at 400 nm is the most intensive for composite $\text{SiO}_2(6)@\text{Ant}$ with loading $0.7\text{-}2.7 \mu\text{mol g}_{\text{SiO}_2}^{-1}$. Increasing of anthracene loading leads to the predominance of the peak at 420 nm. Its effect can be observed because of closely packed anthracene molecule into the pore of silica gel and as a result the self-absorption effect is occurs.

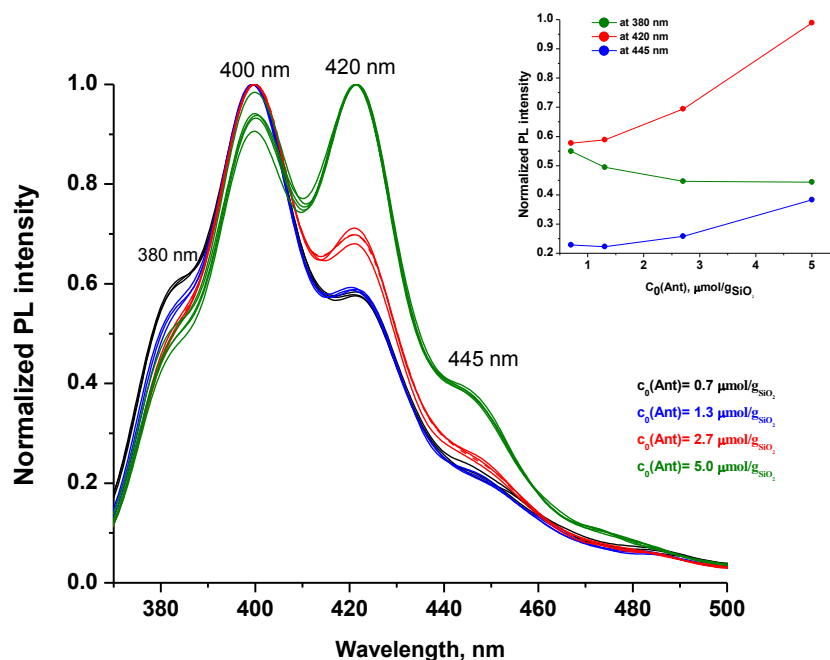


Figure 40 - Normalized PL spectra of solid bulk samples of $\text{SiO}_2(6)@\text{Ant}$, exc=340 nm, T=298K, m=100 mg

As a fact, the temperature has an influence on fluorescence intensity, Figure 41. Composites with low loading with prepared and spectra were recorded before and after dried at 50°C . Bulk composites were crushed to decrease the amount of emission light passing through the sample and as a result minimized the inner filter effect. Absolute photoluminescence intensity increased with temperature in surface loading $0.05\text{-}0.25 \mu\text{mol g}(\text{SiO}_2)^{-1}$.

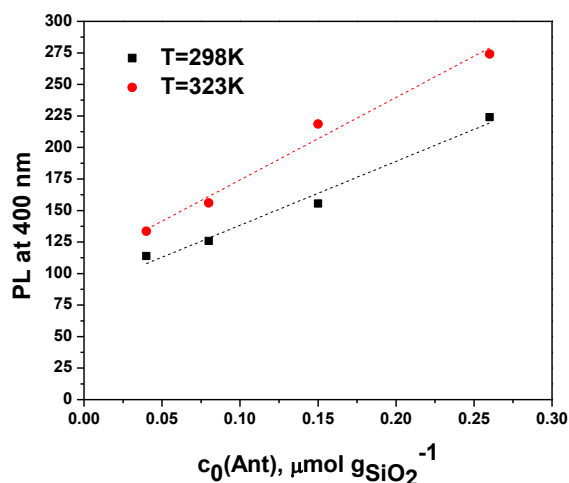


Figure 41 - PL intensity of solid sample of silica gels with introduced anthracene at different concentrations without heating ($T=298\text{K}$) and after heating at 323K , $\text{exc}=340\text{ nm}$

5.9.2. Photoluminescence study of silicas with immobilized anthracene

As it was mentioned earlier, changing of the pore size can essentially change photoluminescent spectra of $\text{SiO}_2\text{-Ant}$ because of excimer formation, Figure 42.

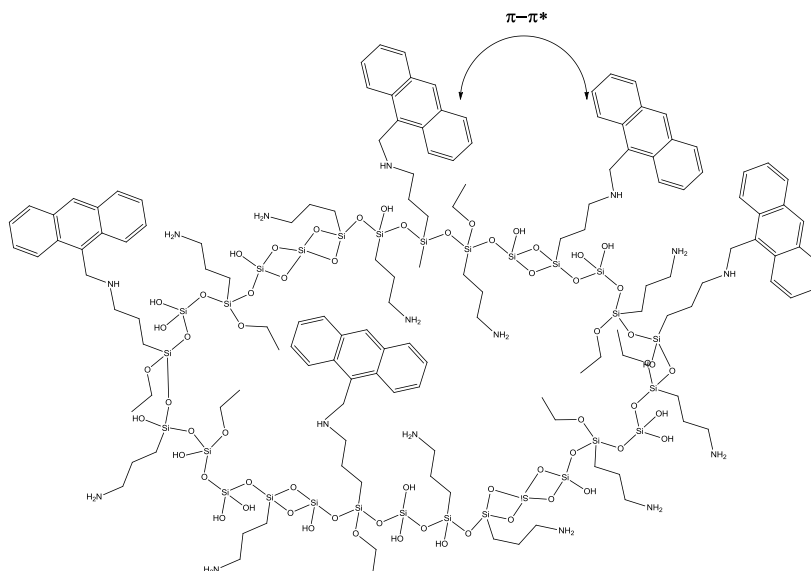


Figure 42 - Scheme of silica gel surface modified with anthracene groups

It was performed by direct recording emission spectra from the solid sample. Asil-Ant-1-t has anthracene fragments only on the surface, therefore it can play the role of assessment grafted layer without interaction with functional groups into pores. The emission spectra in Figure 43a were obtained by exciting Asil-Ant-1-t at 340 nm . From the data, two distinct peaks associated with the pyrene monomer are visible at 384 and

405 nm in all three samples. Comparing with spectra of non-covalently bonded anthracene on silica surface, Asil-Ant-1- τ spectra show redshifts of all peaks in 10 nm. The peaks intensity at 480 nm increases with time of synthesis and as a result of the loading of anthracene-based loading. In addition, some bathochromic shift from 426 to 430 nm is observed. Fluorescence aspect mainly related to the π -conjugate system of the fluorophore. After increasing account of anthryl fraction on aerosil, the conjugated degree of π electron increased with the shift of emission maximum to the longer wavelength [321]. After 1440 min intensity of the band at 480 nm is dominant. These phenomena can be related to concomitant interchain π - π stacking interactions [322] between alkylamino-anthracene groups on the silica surface. Formation of surface excimer complexes on non-porous Asil-Ant-1- τ materials after 240 min time of synthesis can be assumed. Although the calculated distance between anthracene moieties of Asil-Ant-1-1440 was 13.5 Å, emission peaks imply that the anthryl-groups are “clustered” within the interaction distance necessary for excimer formation.

However, the excimer formation is much less noticeable for the much porous materials SiO₂(11)-Ant-1-t, Figure 43b. This observation suggests that the amine groups on the SiO₂(11)-NH₂ surface are distanced enough (8 nm) to prevent the anthracene molecules from aggregating and forming excimers. Calculated values of average intermolecular distance between two anthrylaminopropyl groups on Asil-Ant-1-1440 (18.3 nm) is higher than in Asil-Ant-1-t (13.5 nm), Table 26.

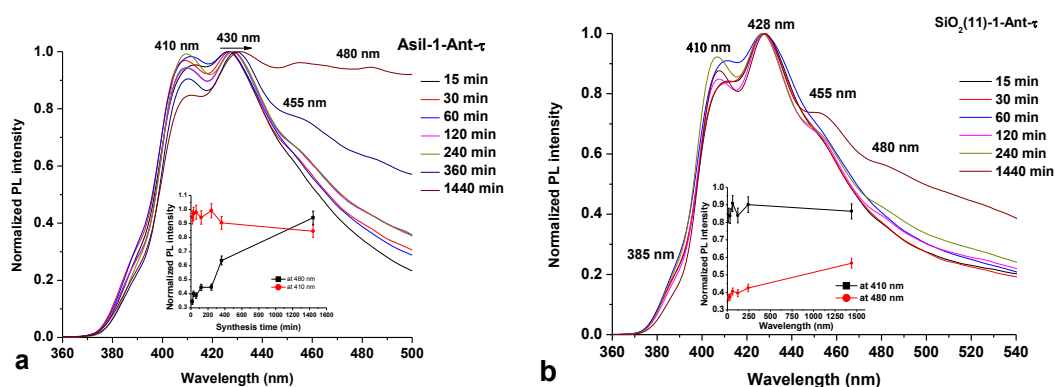


Figure 43 - Normalized PL spectra of solid Asil-Ant-1-t (a) and SiO₂(11)-Ant-1-t (b), exc=340 nm

5.9.3. 3D UV spectra of anthracene-based silicas

Three-dimensional fluorescence spectrum is one kind of matrix spectrum which is composed of the excitation wavelength (Y), emission wavelength (X) and fluorescence intensity (Z). 3D spectra of silica gel with immobilized aminoanthracene groups were recorded by the scanning range of excitation wavelength from 4.5-8 eV (276-155 nm) and emission wavelength was in range 350-700 nm. 3D spectra and corresponding contour images of Asil-Ant-1-t prepared at 15, 360 and 1440 min are present in Figure 44. At 15 min, excitation energy 4.5-5.5 eV leads to emission of anthracene molecule in solid with four obvious bands of monomer at 388, 407, 430 and 455 nm. These values were similar to values obtained upon excitation by visible energy at 340 nm. The maximum intensity of photoluminescence observed at excitation 5 eV (248 nm). Rising synthesis time up to 360 min shows a new emission band at 455 nm and higher energy may be used to excite those materials. The increasing number of the anthryl conjugation degree leads to the easy excitation of the sample and producing fluorescence. However, absolute photoluminescence emission decreases with synthesis time. Due to using UV light as an excitation source, photochemical decomposition may occur with a decrease or even suppression of fluorescence. Interesting 3D spectrum and contour image obtained for Asil-1-Ant-1440 sample. In addition to previously noted monomer bands, the new broad and intensive band centered at 525 nm is observed. This new unstructured band can be assigned to the formation of excimers between neighboring anthracene groups. Besides, exciplex complex in the excited state at this wavelength can be formed. Fixed amines could provide charge-transfer interactions with photo-excited anthracene. During the synthesis anthracene contain on silica gel was a variable component, while amine unit was unchanged. After 15 min of synthesis, the concentration of immobilized groups on silica surface was in excess comparing to anthryl units without an unstructured band at 525 nm on the fluorescence spectrum. Increasing intensity at 525 nm occurs with anthryl loading particularly from 120 min. Thus, band at 525 nm must be attributed to the formation of anthracene–anthracene excimers rather than to the amine–anthracene exciplexes. Presence of co-existence of monomer and excimer form is focused in range 4.75-5.5 eV. At higher energy unstructured band is a dominant component of spectrum up to 6.5 eV.

Analyzing optical behavior $\text{SiO}_2(11)$ -Ant-1-t, excitation energy needed to produce maximum emission is changed from 5 to 4.75 eV for synthesis time 15 and 240 min, respectively, Figure 45. In this type samples formation of excimer complex was not prevailing. It's correlated with the calculated average intermolecular distance between two anthrylaminopropyl groups 18.3 Å which is not favorable to formation exciplexes. $\text{SiO}_2(6)$ -Ant-1-1440 and $\text{SiO}_2(9)$ -Ant-1-1440 have equal value of intermolecular distance (15.8 Å) and normalized intensity of unstructured band centered at 525 nm, Figure 46. Absolute values of photoluminescence monomer band decreased to 240 min and from 240 to 1440 min increasing of the impact of excimer band is occurred in case $\text{SiO}_2(9)$ -Ant-1-t samples. Relation of excimer band at 525 nm to monomer at 407 nm raised greatly for 1440 min.

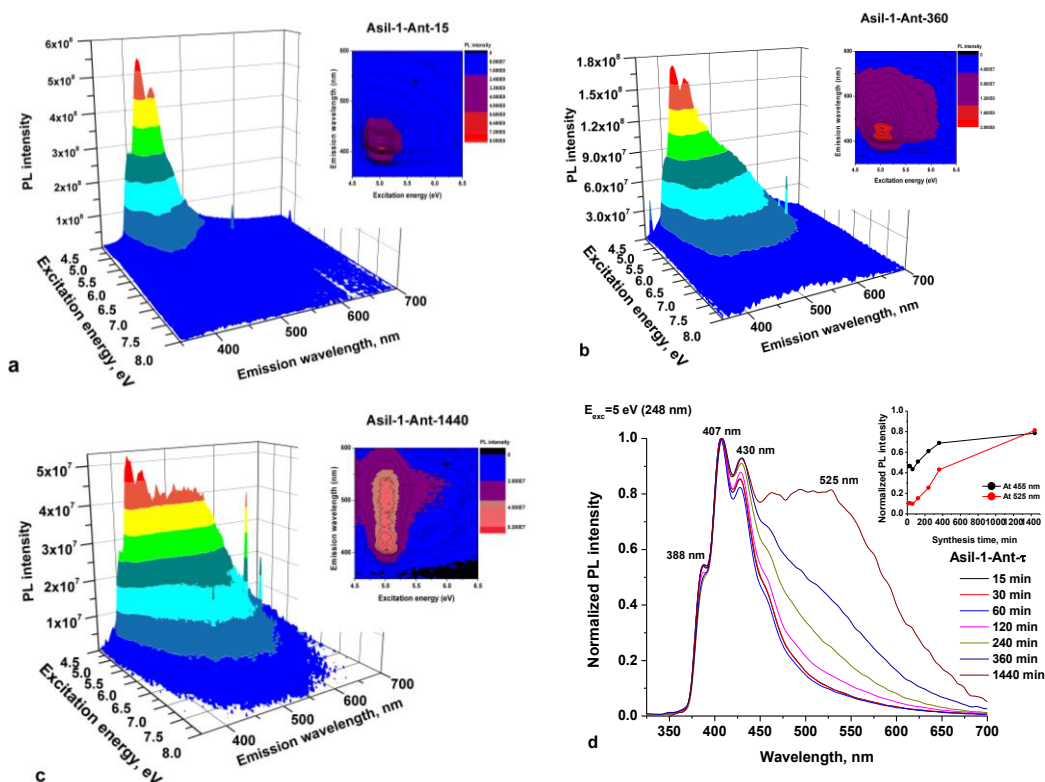


Figure 44 - Solid 3D Photoluminescence spectra of Asil-1-Ant-15 (a), Asil-1-Ant-360 (b), Asil-1-Ant-1440 (c) and normalized spectra of Asil-1-Ant-t (d)

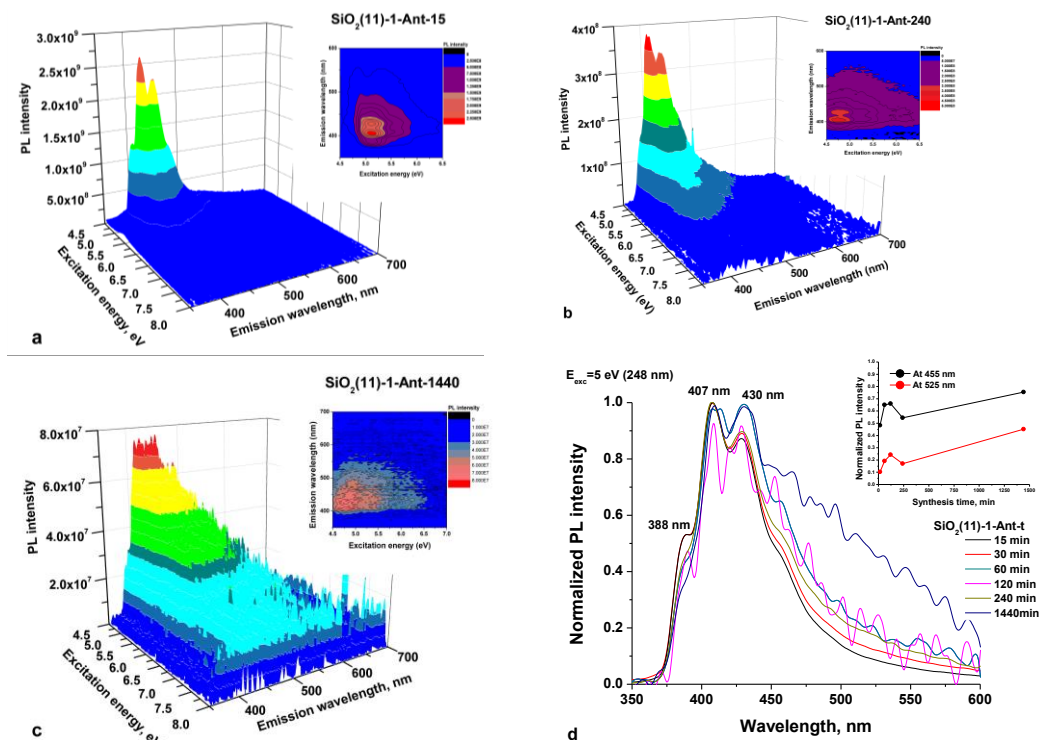


Figure 45 - Solid 3D Photoluminescence spectra of $\text{SiO}_2(11)\text{-1-Ant-15}$ (a), $\text{SiO}_2(11)\text{-1-Ant-240}$ (b), $\text{SiO}_2(11)\text{-1-Ant-1440}$ (c) and normalized spectra of $\text{SiO}_2(11)\text{-1-Ant-t}$ (d)

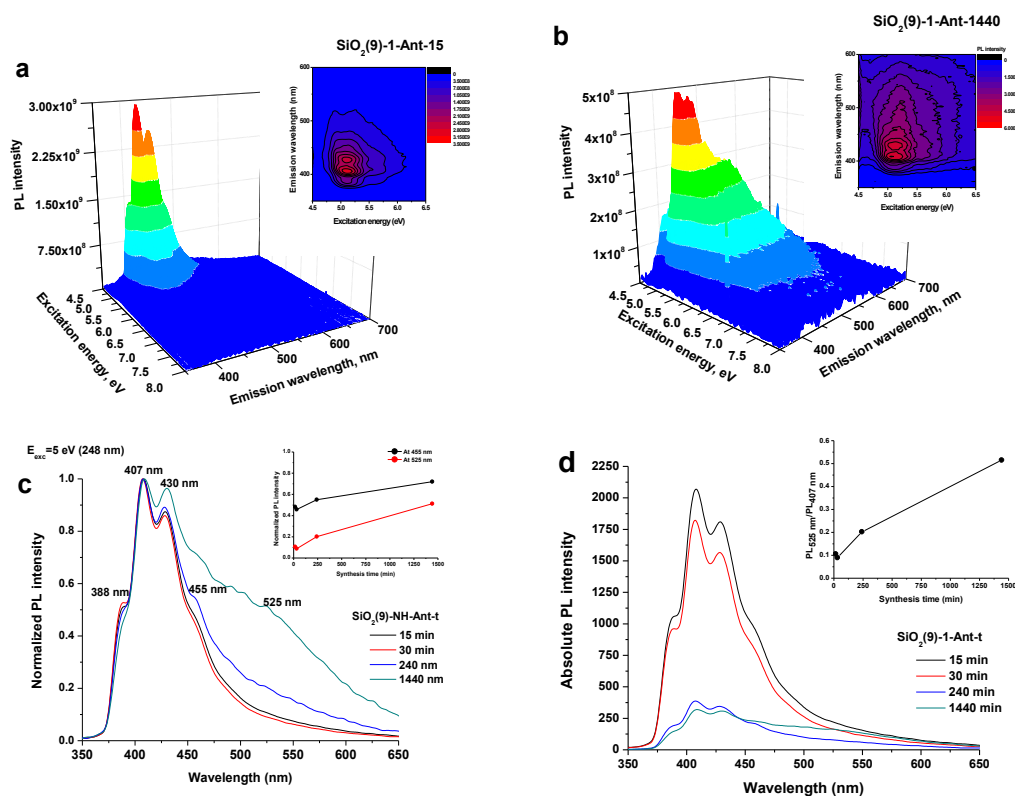


Figure 46 - Solid 3D Photoluminescence spectra of $\text{SiO}_2(9)\text{-Ant-1-15}$ (a), $\text{SiO}_2(9)\text{-Ant-1-1440}$ (b), normalized spectra of $\text{SiO}_2(9)\text{-1-Ant-t}$ (c) and absolute spectra of $\text{SiO}_2(9)\text{-1-Ant-t}$ (d) excited at 5eV

5.10. Conclusions of the chapter 5

- 1) Surface assembling on silica surface and silane immobilization were successfully used for the preparation of silica gel modified with anthracene moieties.
- 2) Silane immobilization leads to the higher content of anthracene groups.
- 3) Kinetic study of surface covering during the synthesis of silica gel modified with anthracene groups via N-alkylation shows that at 120 min saturation of modification is occurred.
- 4) It has been established that increasing pore size of silica gel leads to increasing of loading degree of anthracene-derivatives.
- 5) Solid state MAS NMR, XPS and PL analyses confirmed the identity of grafted functional moieties.
- 6) It was demonstrated that bulk silica does not adsorb anthracene from solution.
- 7) Formation of excimer complexes between the neighbor immobilized anthracene groups can be monitored using solid fluorescence spectroscopy.
- 8) The presence of anthracene excimers on the adsorbent surface can be evaluated from peak intensity at 480 nm.
- 9) Excimer on non-porous anthracene-immobilized silica have been formed more quickly than on the porous ones.

6. Graphene-based materials

6.1. Synthesis approach

Hybrid SiO₂-GOQDs materials can be obtained by adsorption and further chemical anchoring of the earlier prepared GOQDs on the support surface [3, 22, 49]. An alternative way is incomplete pyrolysis of small organic compounds trapped inside of the adsorbed pores [50]. In the latter case, the porous matrix can better confine size and shape of the resulted GOQDs [51, 52]. However, preparation of SiO₂-GOQDs inside the host porous system can have an undesirable influence on its application, since it can essentially reduce the specific surface area of the resulted hybrid material. For example, SBA15-GQDs hybrid nanocomposite obtained by incomplete pyrolysis of pyrene adsorbed in SBA15 pores has only 26 m² g⁻¹ while specific surface area of the pristine host is 719 m² g⁻¹ [51]. Therefore, the first scheme has been selected and GOQDs were prepared from graphite in one-step ultrasonic synthesis with further immobilization of appropriate nanoparticles in the porous system of mesoporous silica. This choice is also supported by the recent studies that have confirmed infiltration of GOQDs into the pores system of the carrier [23, 53]. Samples of GO were prepared from graphite powder by oxidation with KMnO₄ in the mixture of concentrated H₂SO₄ and H₃PO₄ since it was demonstrated that addition of H₃PO₄ to the acid mixture improved safety of the process and led to the successful increase in the reaction yield [54].

Because SiO₂-GOQDs shall be used as an ion-selective electrode, it was important to obtain metal-free nanocomposite [51], because even traces of electrocatalytically active metal ions such as Mn can corrupt properties of the electrode [45, 55, 56]. To ensure Mn-free composition of GO samples, the concentration of Mn ions in washing solutions was monitored. The results presented in Figure 47 demonstrate that water is less sufficient washing reagent than 2% HCl for removal of Mn²⁺ ions impurities from GO. This fact can be explained by good adsorption properties of GO towards metal ions [1, 57]. It seems simple washing with water cannot eliminate residuals of Mn on GO surface.

Covalent immobilization of GOQD on silica surface via the well-established procedure of SiO₂(4)-NH₂ acylation in anhydrous solvent (DMF) by carboxylic

functional groups of GOQDs in the presence of DCC [10][14]. Because of different density, excess of GOQDs was separated from the final product by multiple decantations alternating with the ultrasonic treatment of SiO_2 -GOQDs in DMF. Finally obtained green-grey product demonstrates greenish luminescence under irradiation with UV light at 365 nm. Similar photoluminescence was observed earlier for silica-immobilized GOQDs [20]. Chemical analysis of SiO_2 - NH_2 and SiO_2 -GOQDs demonstrate that carbon content in the samples increased from 2.89 to 3.22%, while nitrogen does not change. This indicates that about 3.3 mg of GOQDs has been immobilized on one gram of SiO_2 -GOQDs, which constitute 25% from initially loaded for synthesis (13 mg g^{-1}).

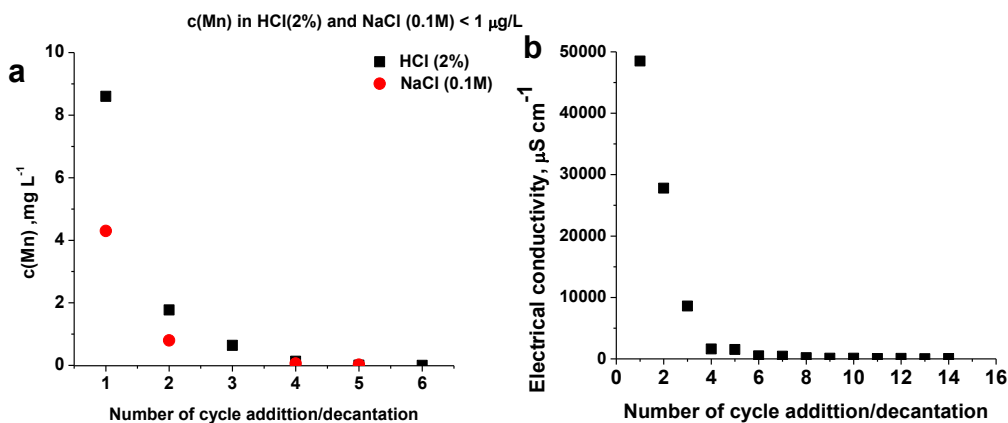


Figure 47 - Effect of washing on $c(\text{Mn})$ in supernatants (a) and monitoring of electrical conductivity with water washing (b)

6.2. Nitrogen adsorption-desorption measurements

From Figure 48, it can be seen that $\text{SiO}_2(4)$ -GOQDs has the same character of N_2 adsorption/desorption isotherm that pristine $\text{SiO}_2(4)$ - NH_2 . This suggests that immobilization of GOQDs does not change porous structure of silica support having typical Type IV isotherm with a distinct hysteresis loop of H1 in the p/p_0 range of 0.4–1.0, which exhibited predominant presence of cylindrical mesopores in the frameworks. However, slightly higher average pore volume and pore size for $\text{SiO}_2(4)$ - NH_2 and larger surface area for $\text{SiO}_2(4)$ -GOQDs (Table 27) suggest incorporation of GOQDs to the porous structure of hybrid material. Graphene has high theoretical surface area and due to similar fragment in GOQDs structure, surface area of composite

SiO₂(4)-GOQDs was increased. Absence of macropores and increased surface area of the hybrid material indicates that GOQDs does not block porous structure of silica.

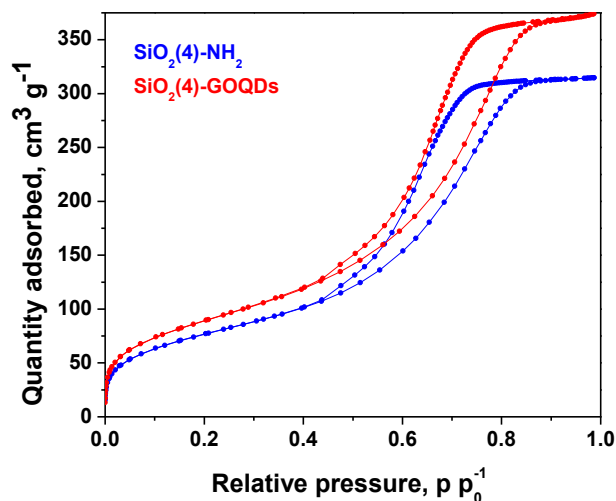


Figure 48 - N₂ adsorption/desorption isotherms of SiO₂(4)-NH₂ (blue curve) and SiO₂(4)-GOQDs (red curve)

Table 27 - The textural characteristics of the obtained materials

Material	Average pore size, nm	Pore volume, cm ³ g ⁻¹	S _{BET} , m ² g ⁻¹
SiO ₂ -NH ₂	5.4	0.67	278
SiO ₂ -GOQDs	5.2	0.56	324

6.3. SEM

The morphology of GO and SiO₂-GOQDs was investigated by SEM technique. Freeze-dried GO demonstrates a closely packed lamellar structures reflecting their multilayered microstructure, (Figure 49a inset). With the exfoliation of graphite oxide into GO, the edges of the GO sheets become crumpled, folded, and closely restacked. GO sheet has the rough surface of the film (Figure 49). SEM image of SiO₂-GOQDs obviously demonstrates that silica particles have not wrapped by GO and thus porous structure of the hybrid SiO₂-GOQDs composite is open. This coincides with the conclusions obtained from N₂-adsorption isotherms.

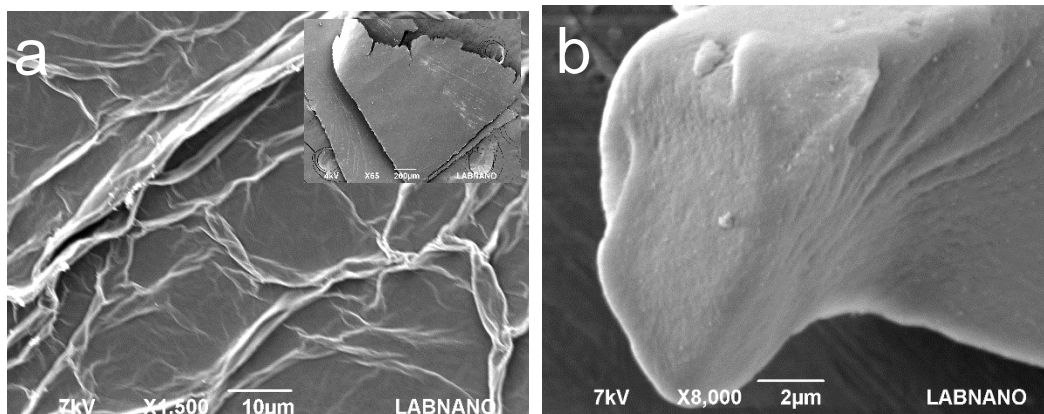


Figure 49 - SEM images of GO(a) and SiO₂-GOQDs (b)

6.4. Fluorescence spectroscopy

Direct prove of GOQDs immobilization on SiO₂ surface was obtained from photoluminescent spectra of SiO₂(4)-GOQDs. It is known that neither aminosilica nor GO exhibit photoluminescence, but SiO₂-GOQDs exhibit strong luminescent band with some maximum peaks at 404, 425 and 450 nm (Figure 50) that can be attributed to the presence of different particle of GOQDs. These peaks equally to GOQDs in water suspension [323] and other hybrid silica-based materials with loaded GOQDs [324, 325].

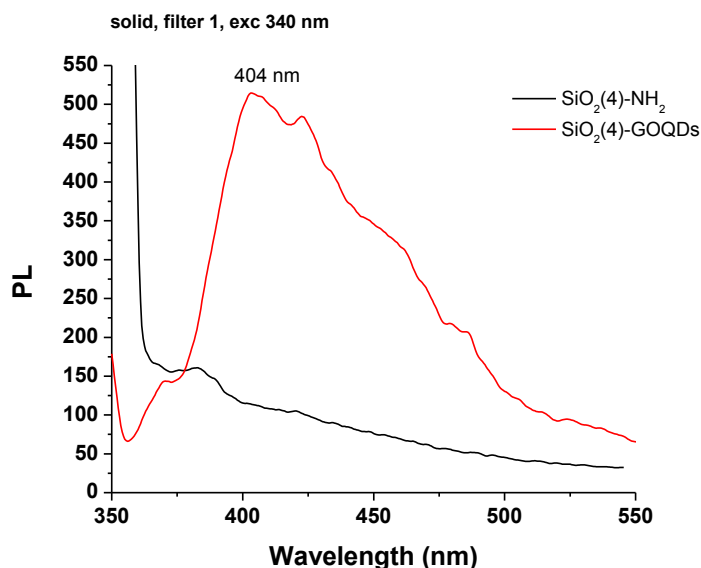


Figure 50 - Photoluminescent spectra of solid samples SiO₂(4)-NH₂ (black line) and SiO₂(4)-GOQDs (red line) under excitation light at 340 nm

6.5. Raman spectroscopy

In order to investigate the successful synthesis of GOQDs and immobilization of the nanoparticles, the Raman spectra of the samples were recorded. From Figure 51 it is evident that the Raman spectrum for GOQDs shows two distinct peaks at 1585 cm^{-1} and at 1372 cm^{-1} .

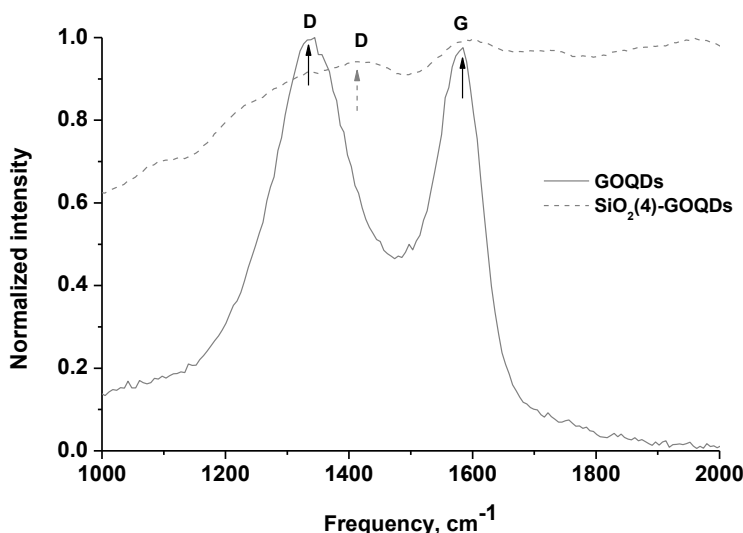


Figure 51 - Raman spectra of GOQDs (—) and SiO_2 -GOQDs (- -)

The appearance of the D peak at 1372 cm^{-1} for GOQDs originates from the stretching vibration of sp^3 -hybridized carbon atoms, which induces defects and disorders due to oxidation. G peak originates from the stretching vibration of sp^2 -carbon atoms of GOQDs and observed at 1585 cm^{-1} . The ratio between the intensities of characteristic bands (I_D/I_G) gives an indication of the functional group insertion [326]. For experimental samples $I_D/I_G < 1$ presumably indicating a decrease in the fraction of aromatic sp^2 domains in GOQDs with increasing the number of detection oxygen-containing sites [327]. Further similar evidence for oxygen-containing groups in GOQDs was received from FTIR, NMR MAS and XPS of the SiO_2 -GOQDs hybrid material.

Regardless of strong fluorescence background and low carbon content (3.3 mg g^{-1}) we were able to record Raman spectrum from SiO_2 -GOQDs and it confirms immobilization of GOQDs, Figure 51. Ordered G band was detected at about 1585 cm^{-1} that matches the position of G band of individual GOQDs indicating

inessential interaction between silica scaffold and the basal plane of immobilized GOQDs. Contrary, the position of D-band in hybrid material is shifted to 1412 cm^{-1} Figure 51, suggesting anchoring of GOQDs via oxygen-containing sites. It is obvious that not all such sites of GOQDs react with immobilized aminosilane fragments in $\text{SiO}_2\text{-NH}_2$. Therefore D-band in Raman spectra of $\text{SiO}_2\text{-GOQDs}$ is proliferated, Figure 51.

6.6. FTIR characterization

The FTIR spectra of $\text{SiO}_2\text{-GOQDs}$, as well as Raman spectra, suggest the presence of oxygen-containing sites in GOQDs, including C(O)O-H ($\nu_{\text{O-H}}$ at 3390 cm^{-1}), CO-H ($\nu_{\text{O-H}}$ at 3250 cm^{-1}), carboxyl ($\nu_{\text{C=O}}$ at 1730 cm^{-1}) and epoxy ($\nu_{\text{C-O}}$ at 1225 cm^{-1}) moieties [328], Figure 52.

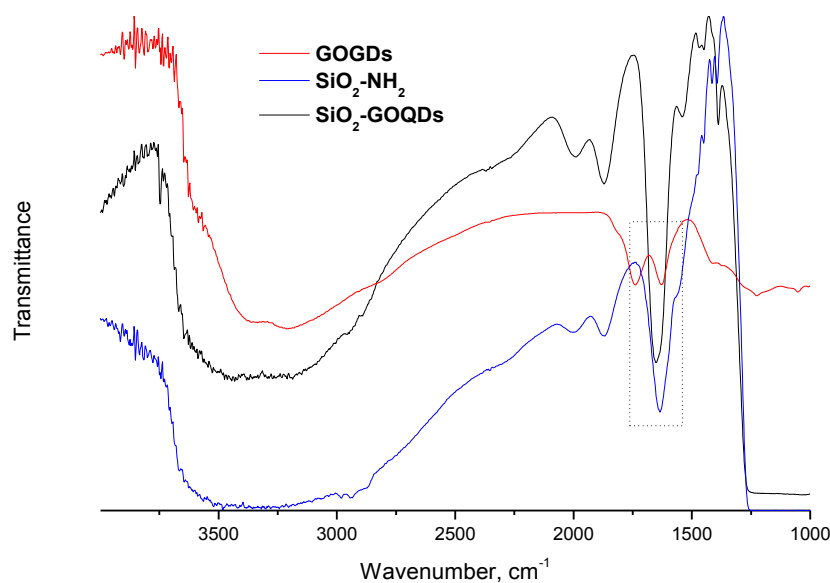


Figure 52 - FTIR spectra of GOQDs, $\text{SiO}_2\text{-NH}_2$, $\text{SiO}_2\text{-GOQDs}$

Apart of silica gel matrix, the pristine $\text{SiO}_2\text{-NH}_2$ shows several bands at about 2950 cm^{-1} (ν_{CH_3} and ν_{CH_2}), and at peaks at 1560 , 1475 , 1450 , 1420 and 1390 cm^{-1} that correspond to stretching vibrations of propylamine chain. FTIR spectrum of GOQDs essentially changed on immobilization. Particularly, stretching vibration of carboxylic group at 1730 cm^{-1} disappeared, and bands at 1650 cm^{-1} and 1574 cm^{-1} corresponding to stretching vibration of C=O and bending vibrations of N-H in NHC(O) fragment of immobilized moiety developed instead, Figure 52. Band near 1650 cm^{-1} can be related

to presence of water, however, after modification of aminosilica with GOQDs band position shifts from 1637 cm^{-1} to 1650 cm^{-1} . From these observations, covalent immobilization of GOQDs via carboxyl fragments of the nanoparticle and aminogroup of the silane can be assumed [328, 329].

6.7. MAS ^{13}C NMR spectroscopy of $\text{SiO}_2(4)$ -GOQDs.

The $\text{SiO}_2(4)$ -GOQDs has less than for percent of total carbon, therefore ^{13}C MAS NMR spectrum of this nanocomposite is very noise, Figure 53.

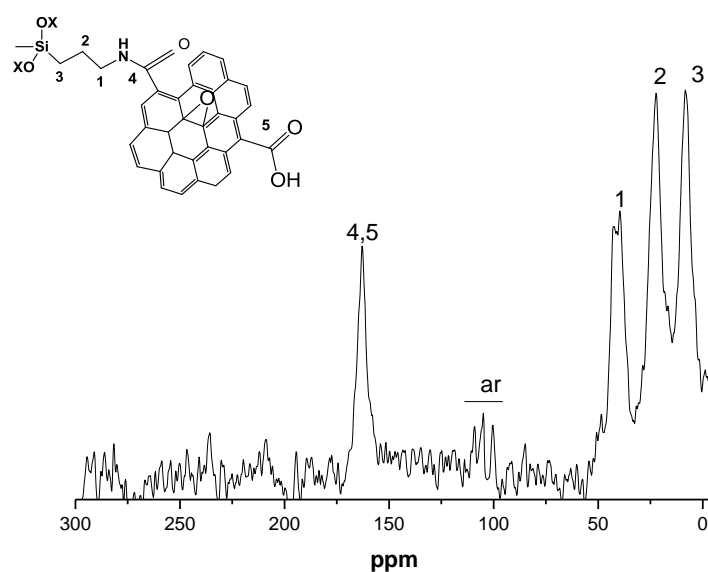


Figure 53 - CP/MAS ^{13}C NMR spectrum of SiO_2 -GOQDs

Nevertheless, we were able to record the spectra and identify the signals. Intensive peaks at 10, 25 and 40 ppm were correspondingly assigned to $\text{Si}-\text{C}_\alpha\text{H}_2$, $\text{CH}_2-\text{C}_\beta\text{H}_2$ and $\text{C}_\gamma\text{H}_2-\text{NH}-$ in immobilized moiety, Figure 53. The signal at 165 ppm was identified as carbonyl fragment of GOQDs [330, 331], while series of signals at 100-115 ppm were assigned to sp^2 carbons in the basal plane of graphene [332]. Consequently, ^{13}C NMR spectrum of SiO_2 -GOQDs as well as FTIR and Raman demonstrate an essential fraction of oxygen-containing fragments in GOQDs and prove immobilization of the GOQDs in the porous scaffold of silica.

6.8. XPS spectroscopy

XPS spectra of SiO₂-GOQDs further confirmed successful immobilization of nanoparticles. It is also demonstrated that SiO₂-GOQDs is Mn-free material since its XPS does not contain Mn 2p peaks at 641.3 and 653.2 eV [333], Figure 54.

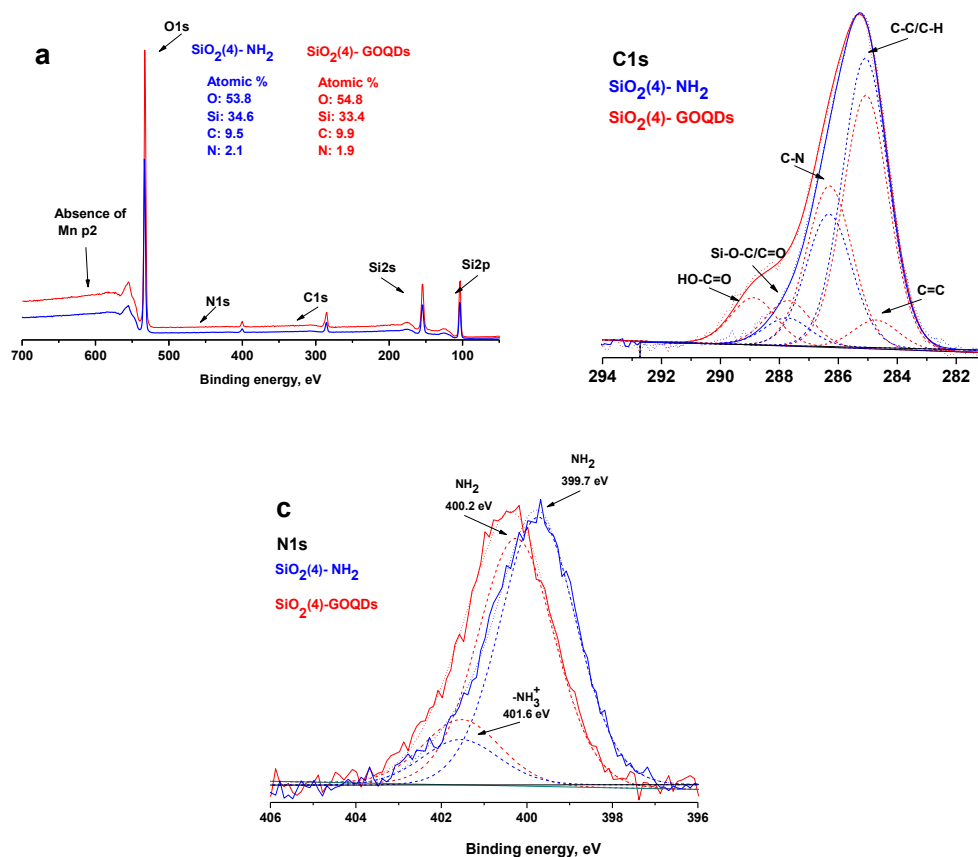


Figure 54 - Survey (a) and fitted XPS spectra of the C1s (b) and N1s (c) of SiO₂-GOQDs and pristine SiO₂-NH₂ with deconvoluted data regions corresponding to SiO₂-NH₂ and SiO₂-GOQDs

The high-resolution XPS spectra demonstrate the essential difference between C1s bands for SiO₂-NH₂ and SiO₂-GOQDs, Figure 54b. The C1s band from SiO₂-NH₂ can be deconvoluted into three components that were attributed to C-C, C-N and C-O bonds in SiO₂-immobilized aminopropyl fragments, Table 28. The relative intensity of C-C and C-N peaks in the spectrum is about 3:1, which correlates with the composition of the immobilized fragment. Also, about 6% of carbon atoms in SiO₂-NH₂ bonded with oxygen, suggesting incomplete hydrolysis of ethoxy groups of aminosilane in the immobilization process, as it is demonstrated in Figure 54 (inset). In addition to the peaks noticed for SiO₂-NH₂, C1s band of SiO₂-GOQDs shows additional peaks

(Figure 54b), attributed to C=C and C=O bonds in O-C=O or N-C=O fragments (Table 28), indicating successful immobilization of GOQDs [334].

Table 28 - XPS results of SiO₂(4)-NH₂ and SiO₂(4)-GOQDs

SiO ₂ (4)-NH ₂				SiO ₂ (4)-GOQDs				
C1s								
Type	C-H, C-C	C-N	C-O	C=C	CH, C-C	C-N	C-O	OCO
eV	285.1	286.3	287.7	284.7	285.1	286.2	287.7	288.9
%	69	25	6	5	47	31	8	9
N1S								
	NH ₂	NH ₃ ⁺		NH		NH ₃ ⁺		
eV	399.7	401.6		400.2		401.6		
%	86	14		79		21		
C _L = 1.01 mmol g ⁻¹				C _L = 0.95 mmol g ⁻¹				

Figure 54c shows the high-resolution N1s XPS spectra of the hybrids. Band of pristine SiO₂-NH₂ consist of peak attributed to neutral and protonated primary amine. On GOQDs immobilization fraction of H-bonded amines is essentially increased, while another fraction of amine fragment were transformed to amide, Table 28. This effect reflects peculiarity of the surface reaction of the immobilized amine with nanoparticles containing several carboxyl fragments. It is obvious that only a few carboxyl groups of GOQDs can acylate immobilized amines due to steric restrictions. Others will be ionized and will protonate the remaining amines, as it is illustrated in Figure 55.

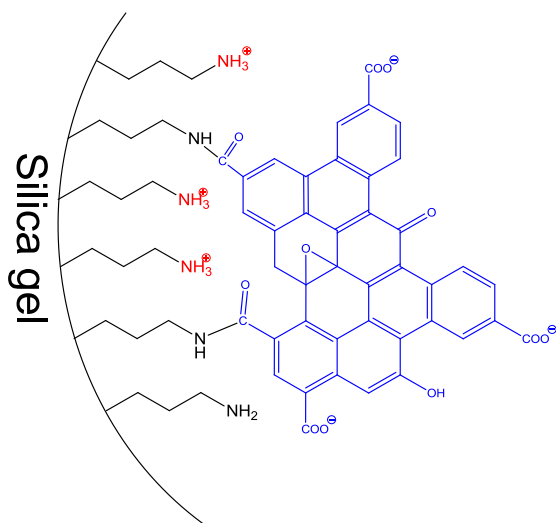


Figure 55 - Schematic structure of surface layer in SiO₂-GOQDs

6.9. Electrochemical application of SiO₂(4)-GOQDs

6.9.1. Critical information about analytes

Among the drugs used in medicine, antibiotics and hormones are required special attention. The residue of the antibiotics in the environment has resulted in bacterial resistance, which could seriously affect human health and ecological balance [335]. Sulfamethoxazole (SMX) with trimethoprim (TMP) also known as co-trimoxazole is an antibiotic combination used to treat a variety of bacterial infections, however chronic toxicity and even potential endocrine disruption were reported.

Metabolism, growth, movement and reproduction of living organism are served by hormones which are agents of the endocrine system. During for many years scientific and medical concern focused on environmental estrogens named endocrine disruptors (ED) that can cause cancerous tumours, birth defects, and other developmental disorders of the endocrine system even at low concentration. Diethylstilbestrol (DES) and Estiol (ET) are class representative that can act as ED [336]. DES had been used for clinical therapy to prevent spontaneous abortion until 1973 when was showed possible deleterious estrogenic and carcinogenic effects [337]. ET is a natural hormone produced during pregnancy, however, in excess can causing impairment to growth and reproduction. DES as a cheap and better absorbed analogue of the natural hormone oestradiol-17 β was used as growth-promoter for cattle, sheep and poultry in many countries [338]. DES was administered as an implant under the skin of young animals or as a feed additive. Although it had been prohibited as a growth promoter for years, these estrogens are still found in the river [339], fish [340], milk [341] and meat [342] of some livestock in many countries due to illegally using.

As a result, the food chain is a possible way to penetrate antibiotics and environmental estrogens into a human when can stay longer than natural estrogen due to higher stability and slower metabolization rate. Therefore, it is necessary to control its abuse and to develop sensitive and effective analytical methods for its determination. DES, EST and mixture (in concentration ratio 5:1) of SMZ/TMP were selected as analytes, Figure 56.

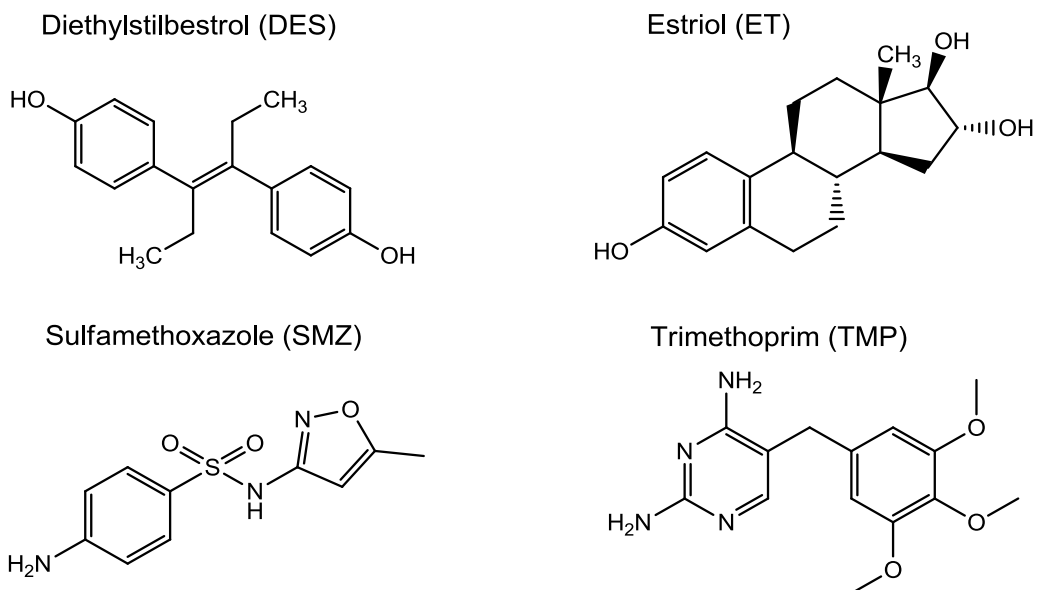


Figure 56 - Chemical structure of the tested analytes

6.9.2. Electrochemical properties of the carbon paste electrode modified with SiO₂(4)-GOQDs

Carbon paste electrode (CPE) was selected for modification because it is cheap, can be reproducibly prepared in any laboratory and SiO₂(4)-GOQDs can be easily integrated into an electrode. Two antibiotics and two hormones were selected for investigation, Figure 56. DES is the first synthetic estrogens that had been widely used in the treatment of estrogen-deficiency disorders. Nowadays, DES is often illegally used as growth-promoter for cattle, sheep and poultry in many countries [338]. Although it had been prohibited as a growth promoter for years, these estrogens are still found in the river [339], fish [340], milk [341] and meat [342].

All selected analytes have aromatic rings that can form π - π stacking complexes with GOQDs, but they also have various polar fragments, which can weaken or enhance such interaction and thus change the sensitivity of the electrochemical analysis.

First, CPE electrode modified with SiO₂(4)-GOQDs was tested in differential pulse voltammetry (DVP) oxidation of a mixture, containing sulfamethoxazole and trimethoprim (5:1). The results were compared with those, obtained on CPE electrode without any additives.

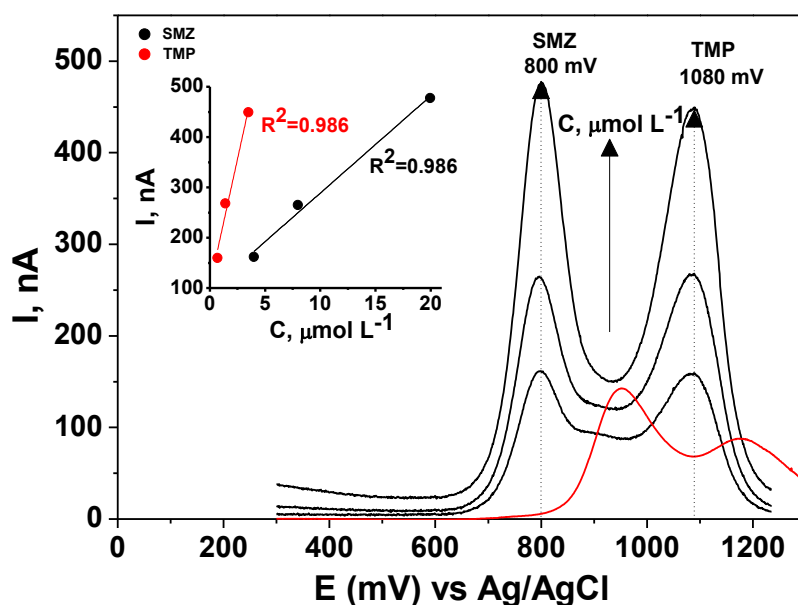


Figure 57 - DPV analysis of sulfamethoxazole (SMZ) and trimethoprim (TMP) on modified with SiO₂-GOQDs (black line) and bulk (red line) carbon paste electrodes. The analytes were presented in a mixture (5:1) with next concentration of SMZ: 4.0, 8.0 and 20 $\mu\text{mol L}^{-1}$ of SMZ and bulk test at 4.0 $\mu\text{mol L}^{-1}$ of SMZ

From the data presented in Figure 57a, it can be seen that electrode modified with SiO₂-GOQDs higher response to TMP (87% of enhancement) and only 14% for SMZ. Further, the oxidation peaks are shifted to lower potentials for both components but differently (-155 mV for SMZ and -95 mV for TMP). This effect increases the difference in anodic peaks of analytes to 280 mV making determination of SMZ and TMP in their simultaneous presence more reliable. The modified electrode demonstrated linear signal response *vs.* concentration of the analyte, Figure 57a(inset). Improved sensitivity and better separated peaks demonstrate the positive effect of SiO₂(4)-GOQDs on electrochemical analysis of SMZ and TMP by DVP.

The significant improvement of electrocatalytic performance of the modified electrode was also observed in DVP analysis of both selected hormones, Figure 58. In DES analysis the modified electrode demonstrated 7.6-fold enhancement of sensibility and by 2.2-fold in EST analysis compared to the bare electrode, Figure 58. Similar to antibiotic analysis, the oxidation peaks of both hormones are shifted to lower potentials for SiO₂-GOQDs modified electrode that demonstrates better interaction of the analytes with active centers of the electrode.

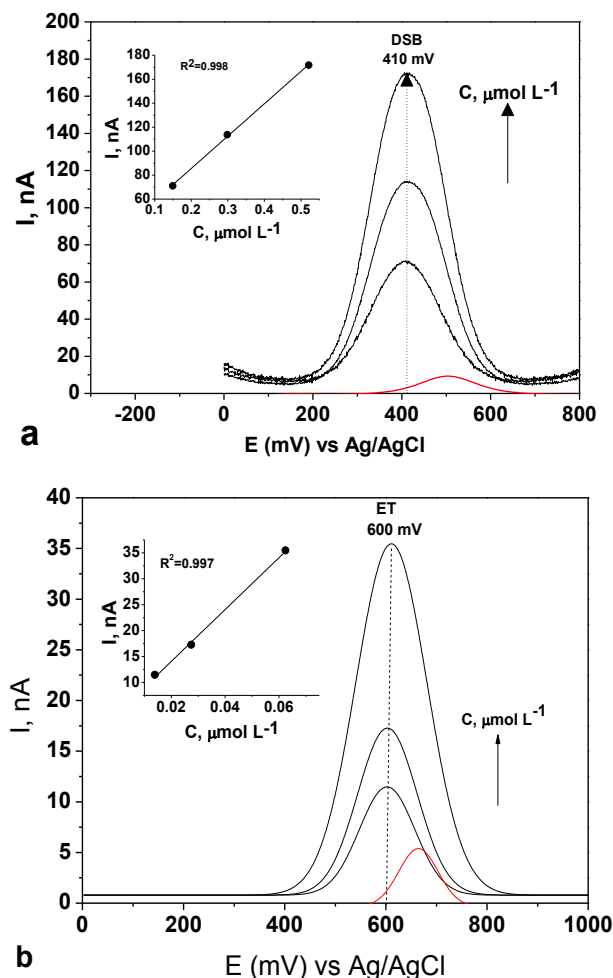


Figure 58 - DPV analysis of DES (a) and ET (c) on modified with SiO₂-GOQDs (black line) and bulk (red line) carbon paste electrodes. Concentration of the analytes: DES - 0.15, 0.30 and 0.52 $\mu\text{mol L}^{-1}$ (black lines) and 0.15 $\mu\text{mol L}^{-1}$ (red line), ET - 0.014, 0.027, 0.062 $\mu\text{mol L}^{-1}$ (black lines) and 0.014 $\mu\text{mol L}^{-1}$ (red line). Supporting electrolyte: 0.04 mol L⁻¹ of BRbs (pH 5.8), 0.5 mol L⁻¹ of NaNO₃.

The large difference between peak potentials (200 mV at CPE/Si/GOQDs comparing with 160 mV at non modified CPE) indicates the applicability of the electrode based on Si/GO for the simultaneous analysis of these hormones. It is shown on inset figures Figure 58a,c(inset), the peak currents linear increase with increasing of analyte concentrations, thus electrode can be used for calibration plot.

These results are interpreted considering the textural characteristics and chemical nature of the Si/GO. As it was shown in previous work [343], silicas with a high surface area form porous silica-graphite paste network, where graphite particles keep its conductivity, thus enhancing electrochemical response. Presence of graphene fragments in Si/GO plays an important role in accumulating of analytes near the

electrode surface due to π - π stacking interactions between biomolecules and condensed ring of graphene chair. In addition, graphene enhances the charge transfer process for CPE/Si/GOQDs electrodes compared to CPE.

DPV for increasing concentration of selected analytes were recorded. From every voltammogram the background was subtracted to register more well-defined peaks [344]. Based on obtained curves the calibration graph was drafted, insets in Figure 57a, Figure 58a,c, in agreement with the following equations:

$$I-I_0(\text{nA})=(19\pm2)*C(\text{SMZ}, \mu\text{mol}^{-1})+(95\pm20) \quad 1.34$$

$$I-I_0(\text{nA})=(100\pm14)*C(\text{TMP}, \mu\text{mol}^{-1})+(106\pm30) \quad 1.35$$

$$I-I_0(\text{nA})=(270\pm7)*C(\text{DES}, \mu\text{mol}^{-1})+(32\pm3) \quad 1.36$$

$$I-I_0(\text{nA})=(500\pm20)*C(\text{EST}, \mu\text{mol}^{-1})+(4\pm1) \quad 1.37$$

The validation parameters such as sensitivity, range of linear response, LOD and LOQ were evaluated. The LOD and LOQ were calculated as $\text{LOD} = 3S_b/b$, $\text{LOQ} = 10S_b/b$ where S_b is the standard deviation of the blank ($n = 10$) and b is the slope of the calibration curve.

6.10. Conclusions of the chapter 6

- 1) Ultrasonic treatment of GO was promoted to the introduction of GOQDs on aminosilica gel.
- 2) Modification with GOQDs increased surface area of the composite from 278 cm^{-1} to 324 cm^{-1} .
- 3) The results demonstrate the great potential of GOQDs in electrochemistry.
- 4) In contrast to GO nanoparticles of GOQDs can infiltrate in the porous system of the support and thus maintain high surface area of the electrode.
- 5) CPE modified with SiO_2 -GOQDs demonstrated enhanced sensitivity towards DES and EST and less profound towards TMP and SMZ.
- 6) The fact higher sensitivity of CPE modified with SiO_2 -GOQDs toward DES and EST was explained by essential π - π stacking interaction between immobilized GOQDs and selected hormones.
- 7) Oxidation peaks for all analytes were shifted to lower potentials for about 100 – 150 mV, demonstrating better interaction between the analytes and active centers of the electrode.

7. Carbon Dots based materials

Two synthetic approaches in “bottom-up” mode were used for preparation CDs namely pyrolysis of CA and nanoreactor approach. To prevent problem with identification silica composites with CDs, next symbols were used. “/” is used to identify CDs prepared from pyrolysis of CA and “@” is determinate composites prepared from nanoreactor approach.

7.1. CDs prepared without nanoreactor approach

In this chapter, the optical, morphological and adsorption properties of CDs prepared via pyrolysis of citric acid is described.

7.2. Synthesis and optical properties of CDs

In this chapter, the results of CDs preparation by pyrolysis of CA is presented. Pyrolysis of organic compounds is very complex and incomplete pyrolysis which is commonly used for CDs preparation even more complex and unclear. Therefore, the reaction conditions such as precursor, temperature, pressure and time are crucial criteria. Preparation of CDs was carried out at atmospheric pressure, in an inert nitrogen atmosphere to prevent oxidation of CA by oxygen. Commonly for CDs synthesis decomposition of CA is recommended to perform in the temperature range of 150-200 °C [226]. There was a consensus that CDs have been produced when CA is melted and forms an orange liquid. Thus, we studied the influence of temperature treatment on the visual transformation of CA via UV-VIS spectroscopy. At 95-150°C no changes were observed with CA. At above 160 °C it began to melt. Subsequently, in 35 min the color of the melted acid was changed from colorless to pale yellow, and then orange referring to the formation of CDs. In UV-VIS spectra this process is accompanied by absorption peak at 335 nm, Figure 59. After 35 min of treatment at 170 °C the intensive shoulder with maximum at 335 nm can be identified in the spectrum, therefore the first sample of the resulted mixture was selected for further investigation, denoted as **CDs-170**. Addition of **CDs-170** to the alkaline solution turns its color to a dark red, but after vigorously shaking color it changed back to orange.

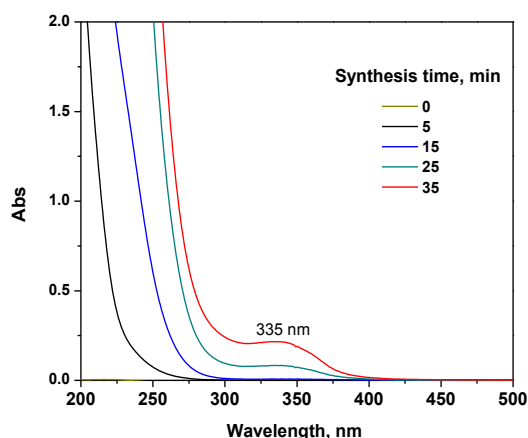


Figure 59 - UV-vis spectra of the neutralized solution of melted CA

In the very first article [113] of CDs preparation by thermal decomposition of CA the authors mentioned about the formation of the black solid product after a long time of treatment and named it “graphene oxide”. However, the fluorescence of the black product after its dissolution in NaOH cast doubt on the conclusion of the authors. Thus, we decided to obtain and study the second sample obtained by CA pyrolysis at 200 °C for 180 min and denoted as CDs-200.

CDs-200 dispersion in NaOH was brown, but after neutralization to pH 7, it was turned into yellowish solution.

In UV–VIS spectra of CDs-200 two absorption peaks at 250 nm and 335 nm can be seen, Figure 60. Presumably, these peaks can be assigned to $\pi \rightarrow \pi^*$ and $n \rightarrow \pi$ electronic transition in CDs surface [58]. It can be seen that UV spectra of both samples are very similar, and it seems pyrolysis of CA at 200 °C does not result in formation of GO. Further proof was obtained from PL spectra of CDs-170 and CDs-200, Figure 61.

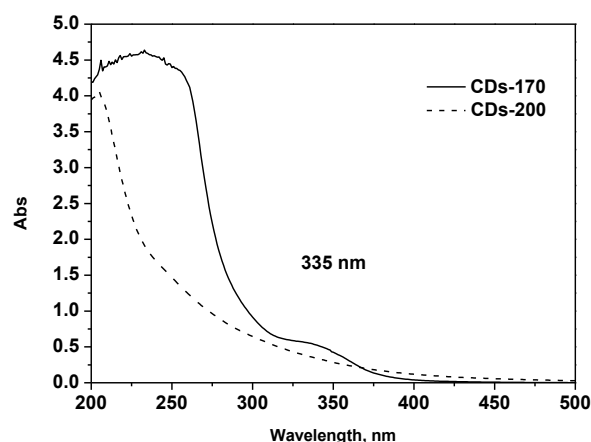


Figure 60 - UV-Vis spectra of CDs-170 and CDs-200 at pH 5

Emission spectra of both CDs-170 and CDs-200 show excitation-dependent feature. However, CDs-170 demonstrates an emission band at 465 nm while excited at 380 nm. CDs-200 has an emission band at 496 nm when excited at 420 nm.

The PL peaks for both samples shifts to longer wavelength as the excitation wavelength gradually increases, Figure 61 (inset a,b). Until now the phenomenon of excitation-dependent PL CDs is unclear. Such factors as different particle size distribution in CDs product, graphitic structure with the diverse surface state, various type of oxidation functional groups commonly attributed to red-shift in the emission spectrum of CDs [345]. Since the solution of CDs has essential absorption at 335 nm, we determined the correlation between CDs concentration and solution absorption. Dilution factor was used to facilitate quantification CDs dispersion due to direct proportionality of the concentration and dilution factor ($c \sim V_0/V_f^3$). First, we determined the level of dependence between CDs suspension pH and its absorption/luminescence.

³ V_0 – aliquot volume, mL; V_f – final volume after dilution, mL

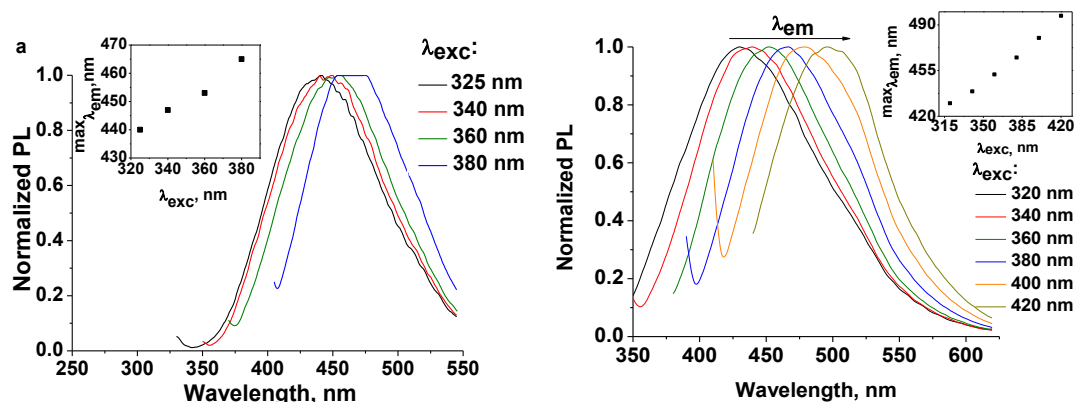


Figure 61 - Normalized PL spectra of CDs-170 (a) and CDs-200 (b) with different excitation wavelengths; the relationship between excitation and an emission wavelength of PL spectra (inset a,b)

PL spectra of CDs-170 solution demonstrates its maximum intensity at pH 3, Figure 62a. The dependence of the CDs PL from pH can be explained by protonation/deprotonation process of the carboxyl groups on their surface. In addition, the lower PL intensity in the highly acidic medium could be related to particle aggregation as a result of hydrogen bonding formation between carboxylic acid moieties on the surface of CDs [346]. Thus this behavior can indicate that pH-sensing phenomenon occurs due to the presence of the functional groups on CDs surface and not defect in the structure of the dots [347]. Contrary to PL, the absorbance of CDs at 335 nm only slightly depends on pH, increasing from pH 2 to 4.5, Figure 62b.

An interesting effect was observed for CDs suspension with dilution. In UV-Vis spectra dilution of CDs linearly correlates with absorbance, Figure 62c. In contrast, PL intensity does not change linearly with concentration, Figure 62d. The PL intensity of CDs-170 dispersion increased with increasing dilution factor of CDs up to 0.05 value, Figure 5. However, a further increase in CDs concentration led to a decrease in the photoluminescence intensity. This could be attributed to self-quenching of CDs, or the particles aggregation at high concentration of CDs [28, 29]. In order to achieve the highest fluorescent intensity and to avoid particles aggregation, the dilution factor of CDs solution in the next experiment section was being fixed below 0.02 (dilution in 50 times).

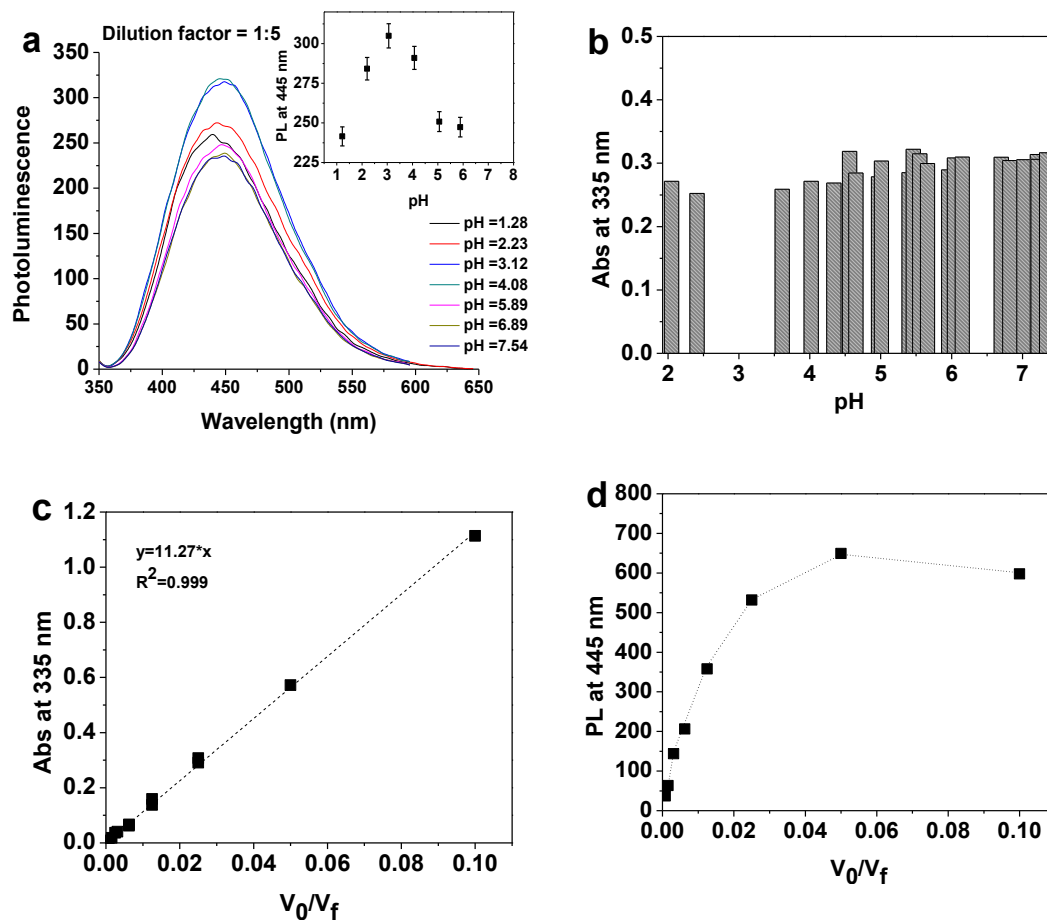


Figure 62 - PL spectra of CDs-170 (a) and their absorbance dependence (b) at different pH and influence of concentration of CDs on absorbance (c) and PL (d)

The as-prepared CDs can be swiftly dispersed in NaOH and HCl aqueous solutions. However, the presence of other ions can show some influence. The colloidal stabilities of CDs-170 and CDs-200 were investigated at various ionic strength forming by salt NaCl (0-0.1 mol L⁻¹), Figure 63. As shown in Figure 63 PL intensity of CDs-200 and the position of the emission peak remains unchanged with increasing of NaCl concentration. However, CDs-170 is more sensitive.

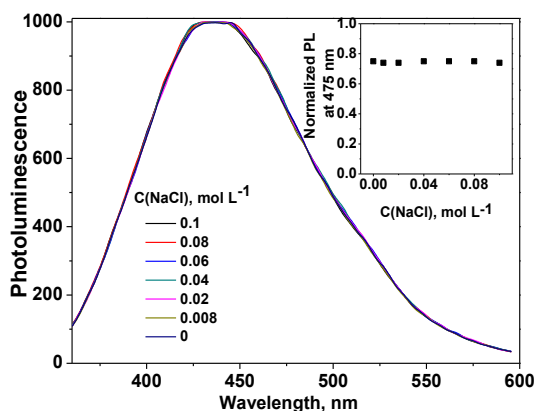


Figure 63 - PL spectra of CDs-200 in NaCl aqueous solution and effect of NaCl content on PL intensity of peak maximum (insets)

7.3. XRD of CDs, TEM and AFM microscopy

The size and morphology of CDs-170 were investigated by TEM and AFM microscopy, Figure 64. TEM image shows spherical morphology of CDs with the mean diameter of the particles is about 5 nm. CDs organized in small groups, probably due to some agglomeration. Such agglomeration already was demonstrated for C-dots [206]. The HRTEM result indicates that the particles are amorphous carbon particles and in rare cases, the particles possess well-resolved lattice spacing of 0.34 nm corresponding to the (200) in-plane lattice spacing of graphitic carbon. AFM image demonstrates well-dispersed particle distribution, Figure 64b. Obtained nanoparticles show mainly height range 5-8 nm Figure 64c,d. From length profiles, some larger particles 20 nm are found, as well as nanosheets (probably graphene-derivative).

The XRD profile of solid CDs-200 has prominent broad (002) peak centered at 21° (Figure 64d) which is commonly attributed to the amorphous highly disordered carbon atoms in CDs and corresponds to the inter-layer distance of 0.42 nm.

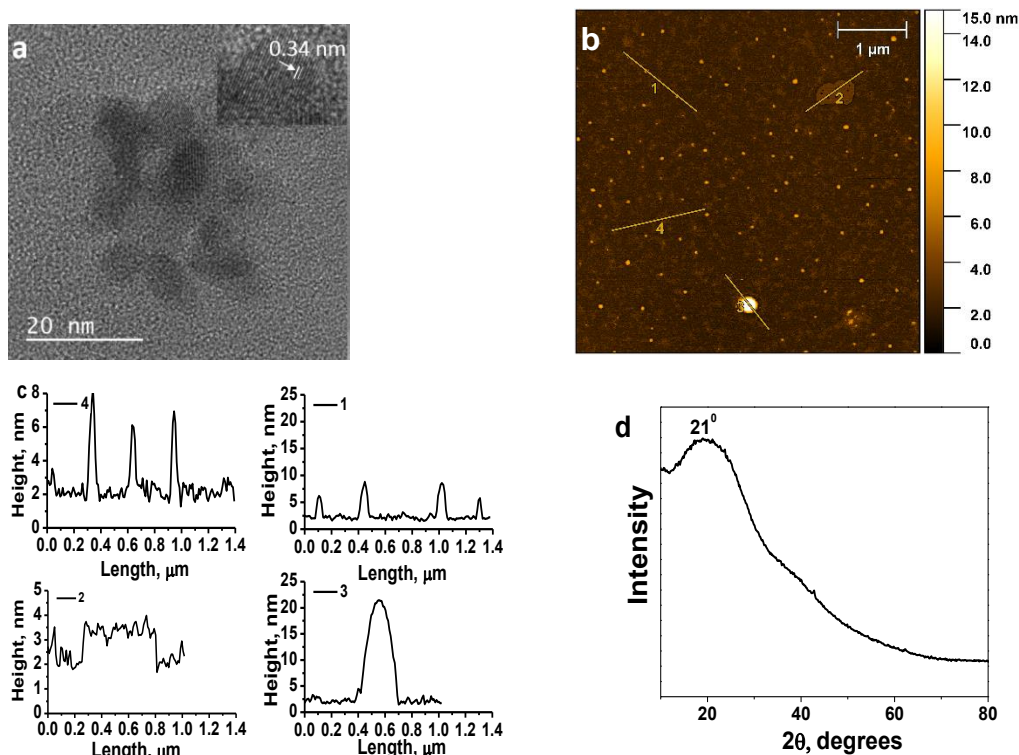


Figure 64 – TEM (a) with HRTEM (a,inset), AFM image (b) with length profiles (c) of CDs-170 and XRD pattern of CDs-200 (d)

7.4. FTIR characterization

FTIR spectrum of CDs-170 was obtained to investigate the surface functionality of the as-prepared CDs, Figure 65. Solvent from the dispersion of CDs was evaporated and the obtained product was mixed with pure KBr to get solid tablet. The broad absorption band at around 3400 cm^{-1} corresponds to the O–H stretching vibration. The peak at 2940 cm^{-1} is attributed to the C–H stretching vibration. The characteristic peaks at 1647 , 1566 and 1394 cm^{-1} correspond to the C=O, C=C and O=C–O stretching vibration, respectively [348]. In addition, bands centered at 1290 cm^{-1} can be related to ether C–O vibration. The peaks reason at $1165\text{ cm}^{-1} - 1080\text{ cm}^{-1}$ are corresponding to CH bending vibration.

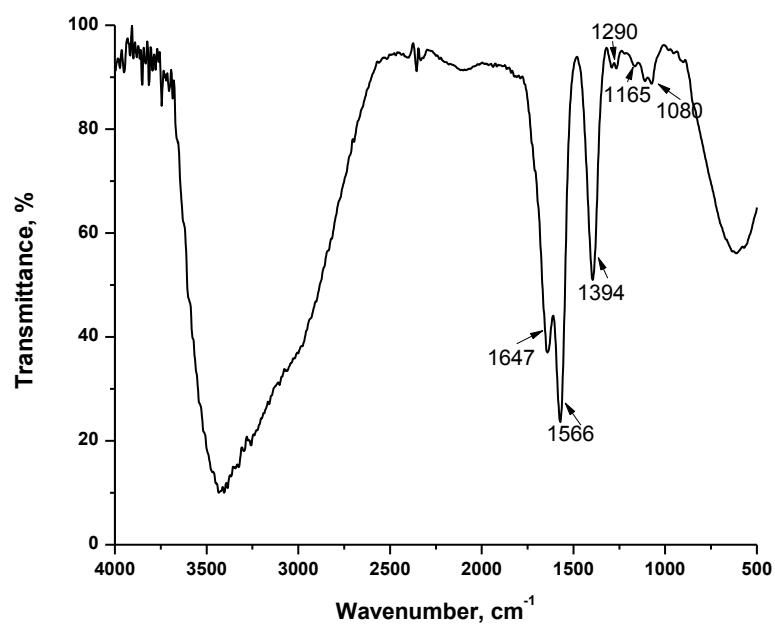


Figure 65 - FTIR spectrum of CDs-170

7.5. Raman

The Raman spectrum of solid CDs-200 shown in Figure 66.

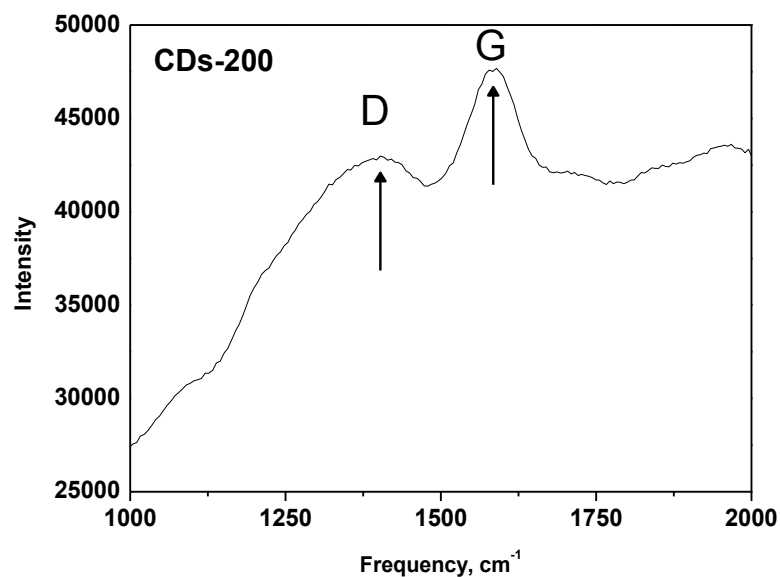


Figure 66 - Raman spectrum of solid CDs-200

One important observation is an intensive background due to fluorescence that makes complicated interpretation of the Raman spectrum. Besides, two prominent

peaks D band (1404 cm^{-1}) and G band (1585 cm^{-1}) are presented and indicate the sp^3 -bonded carbon defects in CDs and sp^2 clusters due to aromatic groups inside CDs, respectively [349]. The I_D/I_G ratio is found to be 0.9, which is higher than those of the reported carbon dots [29,30]. Graphitization degree and long-time pyrolysis have an effect on this ratio via decreasing of sp^3 fragment in structure [350].

7.6. Adsorption study of CDs on silica-based support

Commonly used SPE adsorbent is silica modified materials. Application of CDs in sorption field requires the integration of CDs dispersion onto the solid carrier. SiO_2 , $\text{SiO}_2\text{-NH}_2$, $\text{SiO}_2\text{-SH}$ and C18 were tested as a solid support to an analyzed affinity for CDs dispersion. The concentration of CDs has been recalculated based on initial loading of CA in synthesis. Obtained values was the next $C_0(\text{CDs-170})=0.4\text{ mol L}^{-1}$ and $C_0(\text{CDs-200})=0.13\text{ mol L}^{-1}$.

Initially, static adsorption of CDs-170 and CDs-200 on silica-based support was carried out at different pH, Figure 67. Pristine silica gel almost did not adsorb CDs in pH range 1-8 ($R<10\%$). $\text{SiO}_2(4)\text{-SH}(2)$ shows some improvements in adsorption of CDs-170 at pH 1-3 from 5 to 10% and in the case of CDs-200 10-40%. Aminated silica gel able to collect more than 70% of CDs loading. Acidity did not affect extraction efficiency at pH from 3.5 to 5.5 which has a maximum value of 100%. It shows that the weakly acidic pH range is the best medium for interaction between grafted aminopropyl groups of silica gel with carboxylic groups of CDs. Based on the results of polydentate modeling, $\text{SiO}_2(6)\text{-NH}_2$ (Chapter 4.1.7.2) possesses 82% of completely protonated adsorption centers $(\text{---NH}_2)_3\text{H}_3\text{Z}_3$ and 18% $(\text{---NH}_2)_3\text{H}_2\text{Z}_2$. CDs can consist fragment of carboxylic acid with different dissociation constant (pK_a) similar to CA precursor ($\text{pK}_{a1}=3.14$; $\text{pK}_{a2}=4.76$; $\text{pK}_{a3}=6.39$). We can suggest that the presence of partly dissociated carboxylic groups is interacted with protonated amines forming ammonium/tertiary salt/complex. According to the previously optical study of CDs, optimum pH was at 4.0-5.0.

Influence of NaCl presence on adsorption study was carried out with detection of PL and absorbance intensity after equilibrium, Figure 68. Adsorption of CDs-200 in all studied NaCl concentration range ($0\text{-}0.1\text{ mol L}^{-1}$) reached $80\pm 10\%$ and comparable results can be obtained by PL and UV-Vis spectroscopy. PL response for CDs-170

results (Figure 68a) shown a little bit lower data than UV-Vis spectroscopy. However, repeatability of absorbance results was better than PL, because PL spectroscopy is a more sensitive technique and presence of some solid particle (e.g. silica) can interfere measurement. Thus, the next adsorption study was estimated based on UV-Vis results.

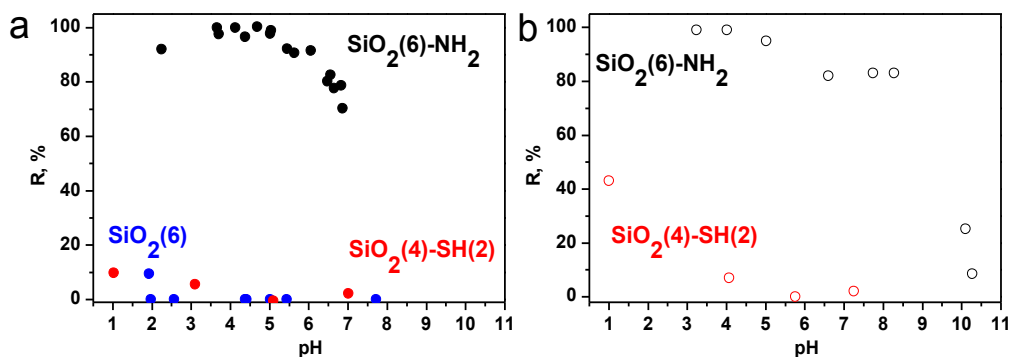


Figure 67 - Effect of pH on percentage removal of CDs-170 (a) and CDs-200 (b) by $\text{SiO}_2(6)\text{-NH}_2$, $\text{SiO}_2(6)$, $\text{SiO}_2(6)\text{-SH}(2)$ (initial concentration = 80 dilution, adsorbent dosage: 5 g L^{-1} , contact time: 120 min)

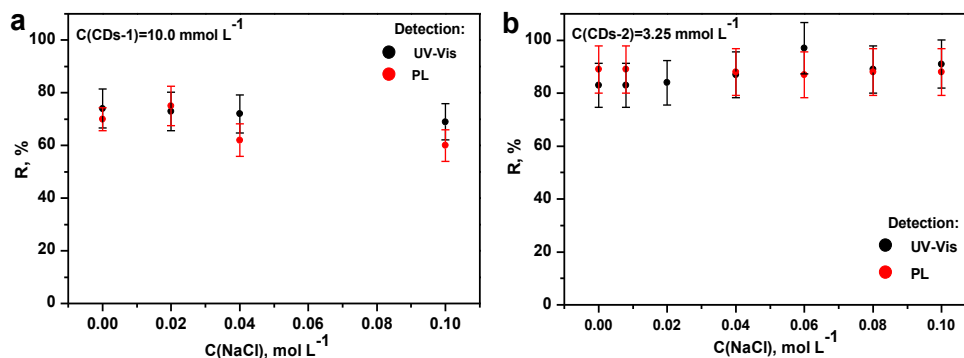


Figure 68 - Effect of NaCl concentration on percentage removal of CDs-170 (a) and CDs-200 (b) by $\text{SiO}_2(6)\text{-NH}_2$ (adsorbent dosage: 5 g L^{-1} , contact time: 120 min, pH 5)

Photoluminescence behavior in solid-state CDs is usually shown a self-quenching effect. Upon excitation of hybrids of adsorbed CDs-170 on $\text{SiO}_2(6)\text{-NH}_2$ in vacuum UV range from 4-7 eV (310-177 nm) peaks of CDs at 470 nm are observed, Figure 69. Comparing aqueous solution with solid composite, the maximum emission peak was red-shifted from 445 nm to 470 nm that phenomenon was observed early [351]. Solid obtained after CDs adsorption from the acid medium, $\text{SiO}_2(6)\text{-NH}_2/\text{CDs-pH-1}$, show more intensive PL peak at 470 nm than composite $\text{SiO}_2(6)\text{-NH}_2/\text{CDs-pH-4}$. As was noticed from Figure 67, adsorption in pH=4 revealed the highest adsorption efficiency thus decreasing in solid PL intensity can indicate surface self-quenching of

CDs due to interaction of functional groups or increasing concentration of closed-localized CDs.

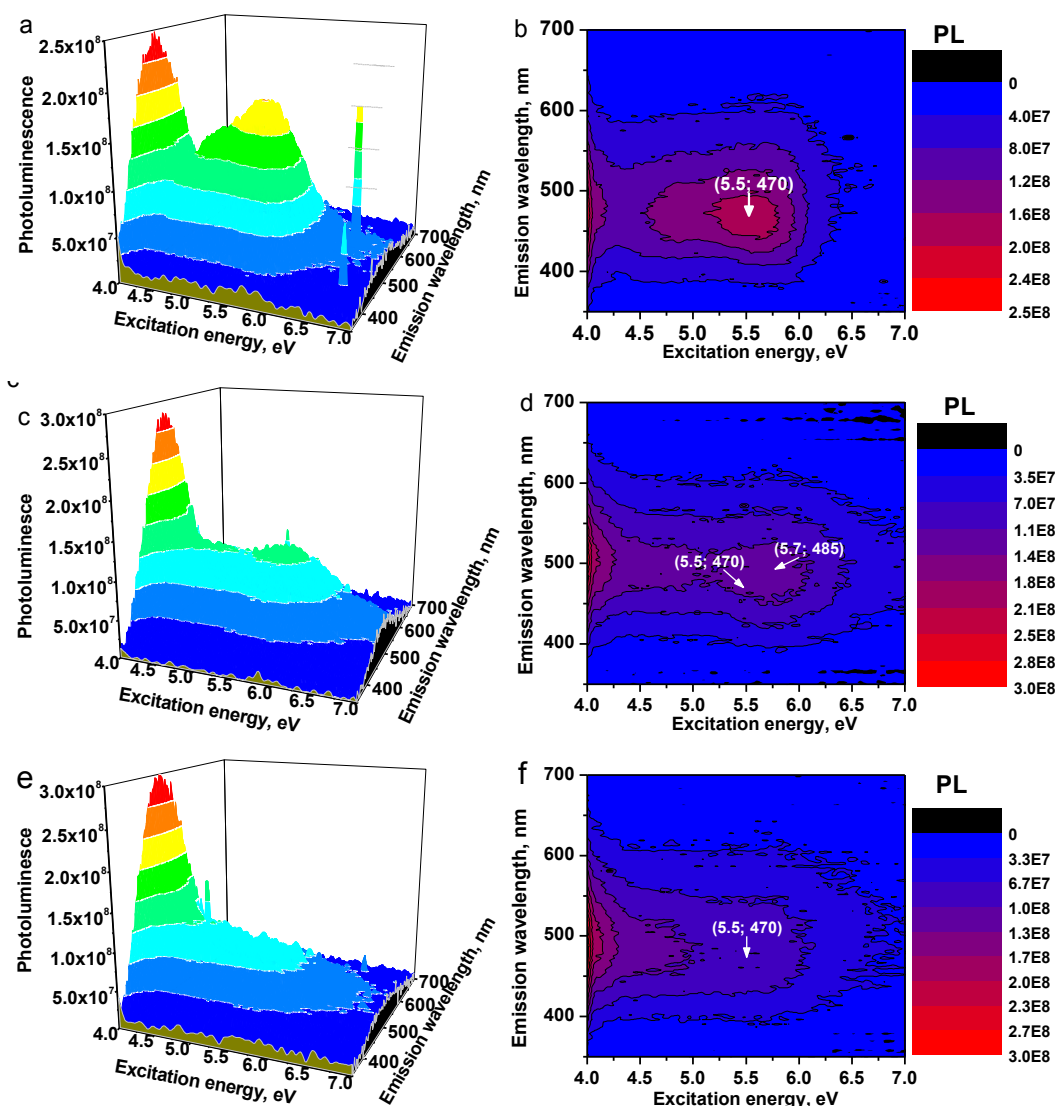


Figure 69 - Solid-state 3D PL spectra and its excitation-emission-intensity spectra of CDs-170 adsorbed on SiO₂(6)-NH₂ at pH=1 (a), pH=4 (b), pH=7 (c)

7.7. Effect of adsorbent dose

The influence of adsorbent dose on the fixing of CDs-170 is shown in Figure 70. The aminosilica gel amount was taken between 4–145 mg in 10 mL solutions. It was shown that the adsorption efficiency of aminosilica gel for CDs decreased when the adsorbent dose increased. It can be related to the unsaturation of the adsorption active sites involved in the adsorption process. the adsorption capacity was decreased from 3.5 to 0.5 mmol g⁻¹ when the adsorbent dose was increased from 0.5 to 14.5 g L⁻¹. With

increasing adsorbent dose, the number of CDs adsorbed onto the unit weight of adsorbent was reduced causing a decrease in equilibrium adsorption capacity [285]. However, the removal rate of CDs increased from 20% to 100%. Thus 5 g L^{-1} was selected optimum para further experiments using 50 mg of adsorbent and 10 mL of solution.

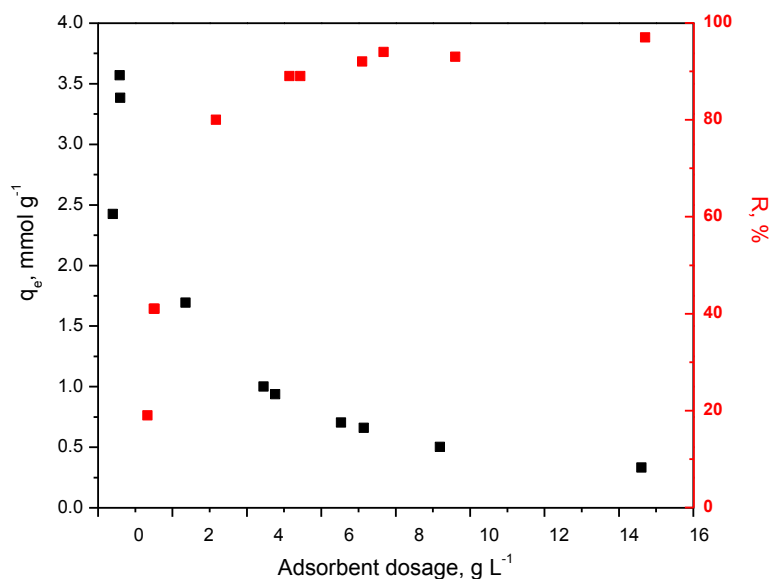


Figure 70 - Effect of adsorbent mass on percentage removal of CDs-170 in ($C_0=5.0 \text{ mmol L}^{-1}$, total volume: 10 ml, pH =5, contact time: 120 min)

7.8. Adsorption isotherms

CDs-170 and CDs-200 were adsorbed on silica gel with different functionality at pH 5. Interesting, CDs-170 show selectivity in relation to the aminated surface of silica gel, Figure 71a. $\text{SiO}_2(6)$ and $\text{SiO}_2(4)\text{-SH}(2)$ did not adsorb CDs-170. It seems that silanol groups on $\text{SiO}_2\text{-NH}_2$ did not participate in the interaction with CDs and adsorption process took place exclusively due to immobilized aminopropyl groups. According to Figure 71b, aminated silica gels have higher adsorption efficiency, however, $\text{SiO}_2(6)$ and C18 (in $\text{MeOH:H}_2\text{O}=70:30$) can be able also to hold up 20% and 25%, respectively. We suggest that CDs-200, unlike the CDs-170, include in the structure some aromatic or aliphatic fragments which can form hydrophobic interaction with C18-alkyl chain or silanol functionalities via π -cloud overlap.

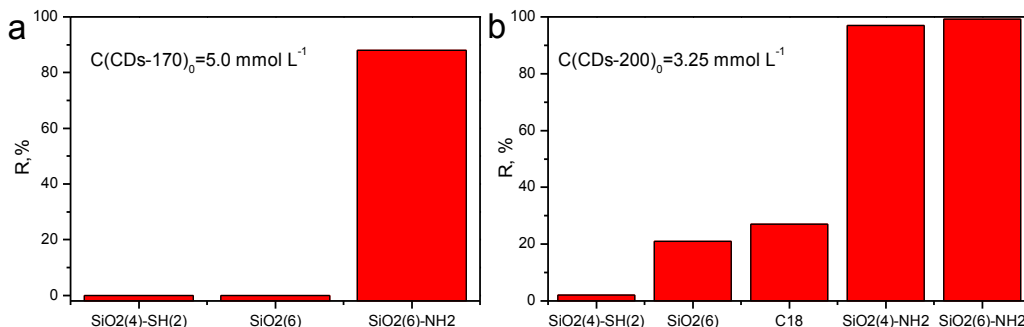


Figure 71 - Evaluation of adsorption CDs-170 (a) and CDs (b) depends on adsorbent

7.9. Isothermal adsorption equilibrium study

Adsorption isotherms are usually used to describe the adsorption mechanism and some parameters can express the surface properties and affinity with the adsorbent. To further comprehend the adsorption progress, we employ the Langmuir, Freundlich and Temkin non-linear isotherm models to fit the experimental data, Figure 72. The relative parameters calculated from these models at room temperature are listed in Table 29. As mentioned previously, SiO₂(6) did not adsorb CDs-170. Based on a comparison of the correlation coefficient R^2 values, all three models are good estimators of isotherm behavior of CDs-170 and CDs-200 adsorption by the aminopropyl silica gel.

Based on CDs-170 adsorption results, correlation coefficient R^2 from the Langmuir model fitting is a little bit lower than the Freundlich model and can be said about some energy heterogeneity of adsorption centers. A normal Langmuir isotherm usually can fit experimental data if the value for $1/n < 1$. As illustrated in Table 29, the value of $1/n$ is 0.44, which indicated favorable adsorption. From Langmuir modeling, the maximum adsorption capacity of SiO₂(6)-NH₂ was 5.6 mmol g⁻¹. The concentration of immobilized aminogroups is 0.9 mmol g⁻¹ obtained from back-pH titration (table7). It is energy probably that interaction of fixed amino group with carboxylic group occur via coordination 1:1. However, from adsorption results 6-7 CDs should be coordinate across fixed aminogroups. Due to the primary representation of CDs concentration via CA loading, CDs molecules can be formed from 6-7 molecular fragments of CA.

From the initial linear region (Henry region), the partition coefficient (obtained from the slope of plotted q_e vs $[\text{CDs}]$) was found, Table 30. The high value, 75500 mL g⁻¹ revealed strong affinity between solid and CDs-170. Based on good results obtained from the Temkin model at all tested concentration levels, it can be suspected that there

was electrostatic interaction between deprotonation carboxylic groups of CDs-170 and protonated aminogroups during the adsorption process.

All these three models adequately fitted adsorption of CDs-200 on silica gel with immobilized groups as well. In this case, two aminopropyl silica gel with different pore size were tested, Table 29. From Langmuir modeling, the maximum adsorption was almost the same 1.0 and 1.1 mmol g⁻¹ for SiO₂(6)-NH₂ and SiO₂(4)-NH₂, respectively. Obtained results are very closed to the grafted concentration of immobilized groups (). According to the Langmuir model, the adsorption occurs on a homogenous surface by monolayer coverage and no subsequent interaction between adsorbed species. It seems that most of the immobilized aminogroups in selected adsorbents took part in interaction with carboxylic groups as 1:1. During long-time synthesis, most carboxylic groups of carboxylic acid were decomposed or carbonized and the number of residual -COOH groups was lower than in CDs-170 sample. The constant K_L , K_T , K_d and b were higher, but not significantly, for SiO₂(6)-NH₂ than for SiO₂(4)-NH₂ that can be related to the number of grafted groups per 1 g of silica gel.

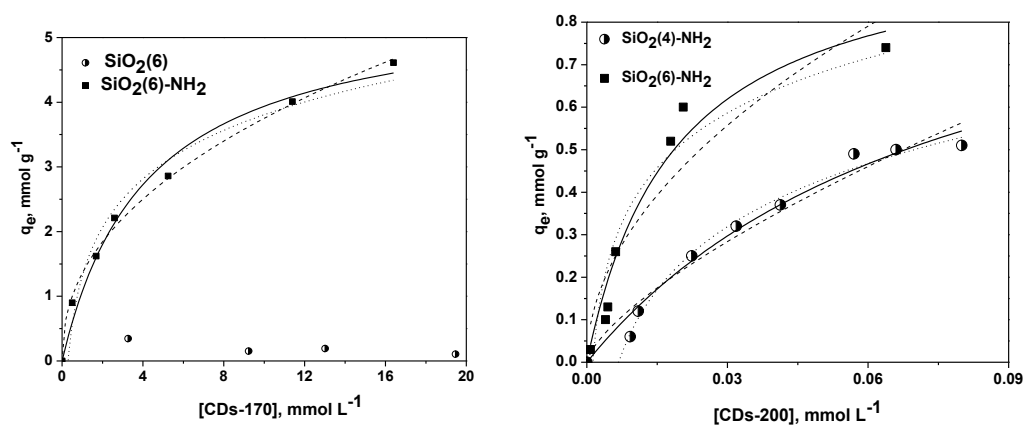


Figure 72 - Adsorption isotherms of CDs-170 (a) and CDs-200(b) by silica-based adsorbents (adsorbent dosage: 5 g L⁻¹, contact time: 120 min, pH 5). The solid lines are Langmuir model simulation; the dashed lines are Freundlich model simulation; the dotted lines are Temkin model simulation

Table 29 - The isotherm parameters for the adsorption of CDs onto silica gel modified with aminopropyl groups

Model parameters									
CDs-170	Freundlich			Langmuir			Temkin		
Solid	K_F (mmol g ⁻¹)(L mmol ⁻¹) ^{1/n}	1/n	R ²	K_L (L mmol ⁻¹)	q_e (mmol g ⁻¹)	R ²	b (mmol ² J ⁻¹ g ⁻¹)	K_T (L mmol ⁻¹)	R ²
SiO ₂ (6)-NH ₂	1.36	0.44	0.996	0.24	5.6	0.986	2290	3.34	0.976
CDs-2	Freundlich parameters			Langmuir parameters			Temkin isotherm		
Solid	K_F (mmol g ⁻¹)(L mmol ⁻¹) ^{1/n}	1/n	R ²	K_L (L mmol ⁻¹)	q_e (mmol g ⁻¹)	R ²	b (mmol ² J ⁻¹ g ⁻¹)	K_T (L mmol ⁻¹)	R ²
SiO ₂ (4)-NH ₂	3.29	0.70	0.960	12.5	1.1	0.978	11567	148	0.990
SiO ₂ (6)-NH ₂	3.27	0.50	0.859	52.7	1.0	0.953	13300	775	0.880

Table 30 - Linear partition coefficient of CDs on aminated silicas

	CDs-170 on SiO ₂ (6)-NH ₂	CDs-200 on SiO ₂ (6)-NH ₂	CDs-200 on SiO ₂ (4)-NH ₂
K_d , m g ⁻¹	75.5	200	191

7.10. Desorption assay

Force of CDs bonding with the adsorbent surface can be estimated using desorption assay. From Figure 62, Figure 67 can be seen that pH=1 is not favorable for adsorption of CDs on aminosilica gel. Application basic solution as desorption agent can be acceptable due to the starting of silica dissolution. Adsorption and desorption were carried out using batch mode. CDs-170 was adsorbed onto SiO₂(9)-NH₂ from concentration range 0-25 mmol L⁻¹ at pH=4. After removing the solution above solid, HCl (1M) was added as a desorption reagent to obtain pH 0.5-1. As a result, the desorption degree was 65-75%, Figure 73a. However, about 25-35% of CDs-170 exhibited more strong interaction with an adsorbent.

Using the solid phase of CDs with aminosilicagel (SiO₂(d)-NH₂/CDs) as adsorbent, the stability of functional groups is needed. Surface propylammonium salt of CDs can be converted into strong amide bond producing after its heating >100 °C.

Influence of thermal treatment of $\text{SiO}_2(9)\text{-NH}_2/\text{CDs-170}$ on desorption degree was analyzed, Figure 73b. After heating of adsorbed CDs onto $\text{SiO}_2(9)\text{-NH}_2$ at 150°C during 2 h, desorption degree decreased from 79 to 8%. The strong acid environment could not release adsorbed CDs from a solid surface due to forming covalent amide-bond and these hybrids can be used as adsorbent.

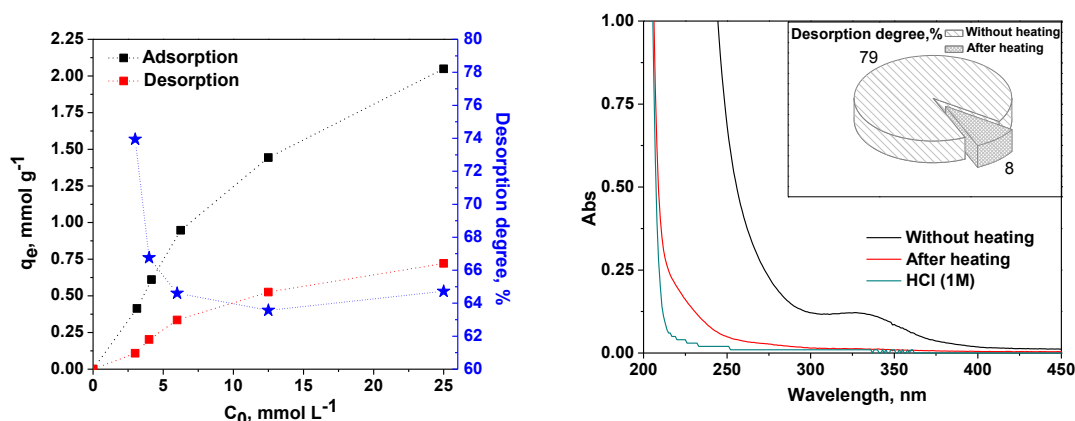


Figure 73 - CDs-170 loading on aminosilica before and after desorption (a) and desorption degree after heating (b)

7.11. Preparation of adsorbent

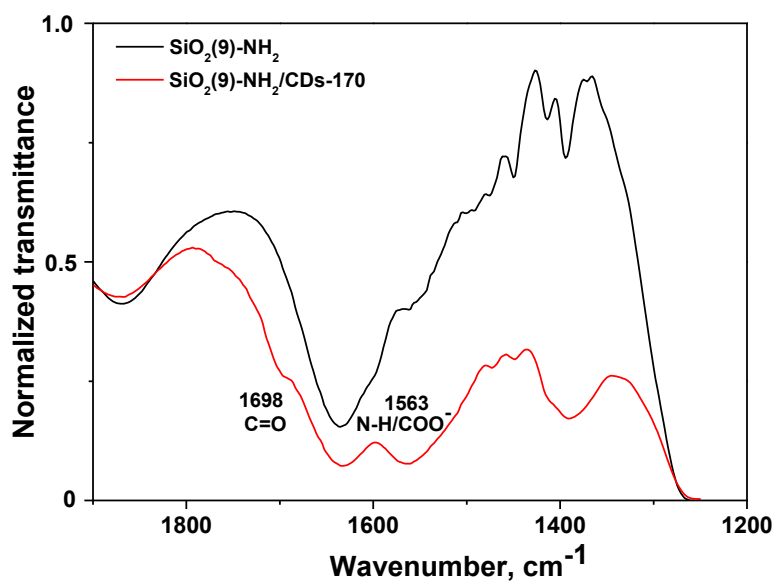


Figure 74 - FTIR spectra of pristine aminosilica gel and with CDs loading

Based on previous experiments, the adsorbent in form of CDs adsorbed on aminosilica gel was prepared according to the procedure described in the chapter 0. Adsorption loading of CDs-170 in $\text{SiO}_2(9)\text{-NH}_2/\text{CDs-170}$ reached up 70% of initial concentration and this value correspond to 0.86 mmol/g . From FTIR spectrum, well-

defined new peak of carboxylic component was found. As seen in Figure 73, confirmation of CDs presence can be assigned due to COO^- , C=O and N-H presence with wavenumbers at 1563 and 1698 cm^{-1} , respectively [352].

7.12. Adsorption study of organic dye onto silica-based materials

Silica gel was used as an effective adsorbent for removing of cationic dye from aqueous solution in contrast to aminated solid. We suggest that incorporation of CDs on aminopropyl silica gel can increase affinity to cationic dye. MB was used as a model analyte, Figure 75a, and the adsorption capacity of MB was investigated by batch tests. UV-Vis spectrum of MB consists of two bands at 613 nm and 663 nm in visible light range, Figure 75b.

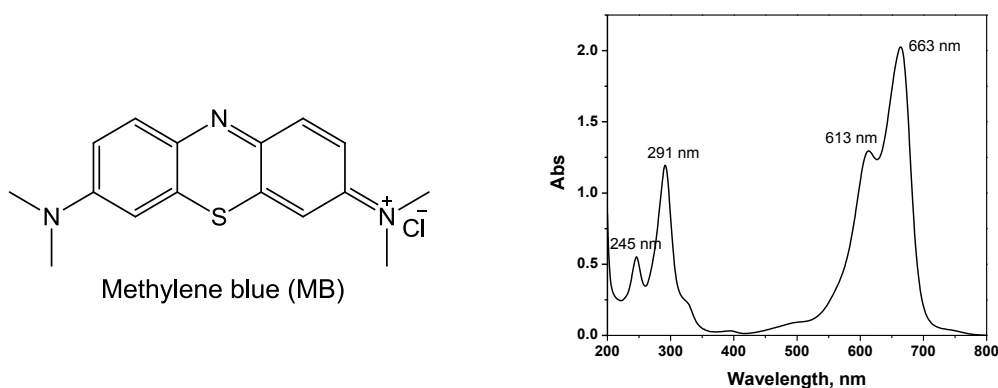


Figure 75 - Chemical structures of MB and its UV-Vis spectrum

The effect of pH is a crucial factor of the general adsorption process, which can affect the chemistry properties for both dye molecules and adsorbents. MB is a cationic dye with a pK value of 3.8 [285] and exists in aqueous solution as positively charged ions at pH greater than 3.8. As a charged species, the degree of its adsorption onto the adsorbent surface is primarily influenced by the surface charge on the adsorbent, which in turn is influenced by the solution pH. In general, the negatively charged form of analytes is favorably adsorbed by the adsorbent at lower pH values due to the presence of a higher number of H^+ ions. In contrast, cations are adsorbed due to the negatively charged surface sites adsorbents at high pH values. Figure 76 shows the effect of the solution pH on removal efficiency by the different adsorbent. $\text{SiO}_2(9)$ exhibited the best result since it's used for adsorption cationic dye up to $\text{pH}=9$. In a strong acid medium, adsorption of MB on $\text{SiO}_2(9)\text{-NH}_2$ and $\text{SiO}_2(9)\text{-NH}_2/\text{CDs-170}$ did not observe

due to repulsive electrostatic interaction between both positively charged analyte and adsorbent. The adsorption capacity of $\text{SiO}_2(9)\text{-NH}_2$ and $\text{SiO}_2(9)\text{-NH}_2/\text{CDs-170}$ was increased from 0-15% and 0-80%, respectively, in pH range 4-7. This can be explained on the basis of a decrease in competition between positively charged H^+ , H_3O^+ and MB for surface sites and also by the decrease in positive surface charge on the adsorbent, which results in a lower electrostatic repulsion between the surface and MB [285]. However, removal efficient removal of MB by $\text{SiO}_2(9)\text{-NH}_2/\text{CDs-170}$ was higher than $\text{SiO}_2(9)\text{-NH}_2$ in 5 times at pH=7 due to the presence of carboxylic groups on the aminated surface.

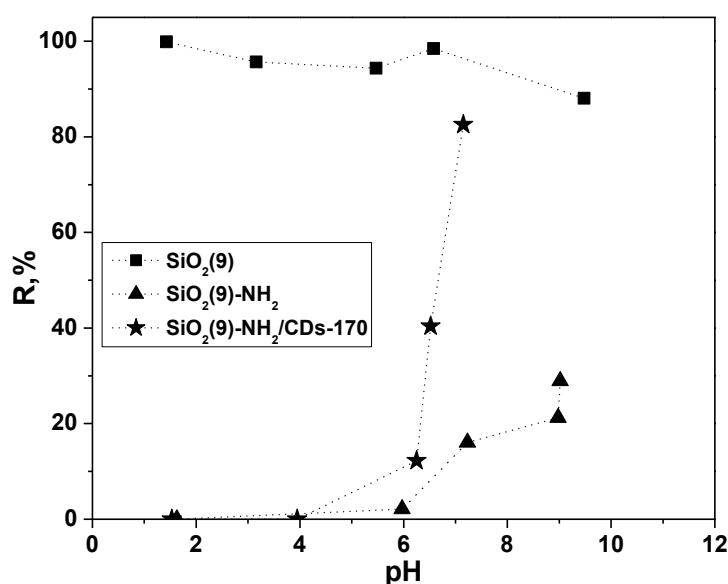


Figure 76 - Effect of pH on the equilibrium adsorption capacity of MB onto $\text{SiO}_2(9)$, $\text{SiO}_2(9)\text{-NH}_2$ and $\text{SiO}_2(9)\text{-NH}_2/\text{CDs-170}$ ($C_0=1.56 \text{ mmol L}^{-1}$, $m=50 \text{ mg}$, $V=10 \text{ mL}$)

Figure 77 shows the fitting of adsorption data using the Langmuir and Freundlich models for the adsorption of MB on $\text{SiO}_2(9)$, $\text{SiO}_2(9)\text{-NH}_2$, $\text{SiO}_2(9)\text{-NH}_2/\text{CDs-170}$ and the fitting parameters with K_d from Henry region are summarized in Table 31. Langmuir model could not fit resulted in adsorption data of MB on $\text{SiO}_2(9)\text{-NH}_2$. In addition, $1/n$ coefficient from Freundlich fitting was 2.02 that indicates unfavorable monolayer adsorption and cooperation effect between adsorbed MB and MB in solution. According to rest adsorbents, the regression coefficients, R^2 suggest that the Langmuir model fits the adsorption data better, which implies that both $\text{SiO}_2(9)$ and $\text{SiO}_2(9)\text{-NH}_2/\text{CDs-170}$ possess homogeneous adsorption surface and the adsorption of MB on these two adsorbents is likely monolayer. For these both adsorbents, maximum

adsorption loading was calculated as 17.1 and 3.7 $\mu\text{mol g}^{-1}$. K_d of MB onto adsorbent increased in the next order: $\text{SiO}_2(9) > \text{SiO}_2(9)\text{-NH}_2/\text{CDs-170} > \text{SiO}_2(9)\text{-NH}_2$.

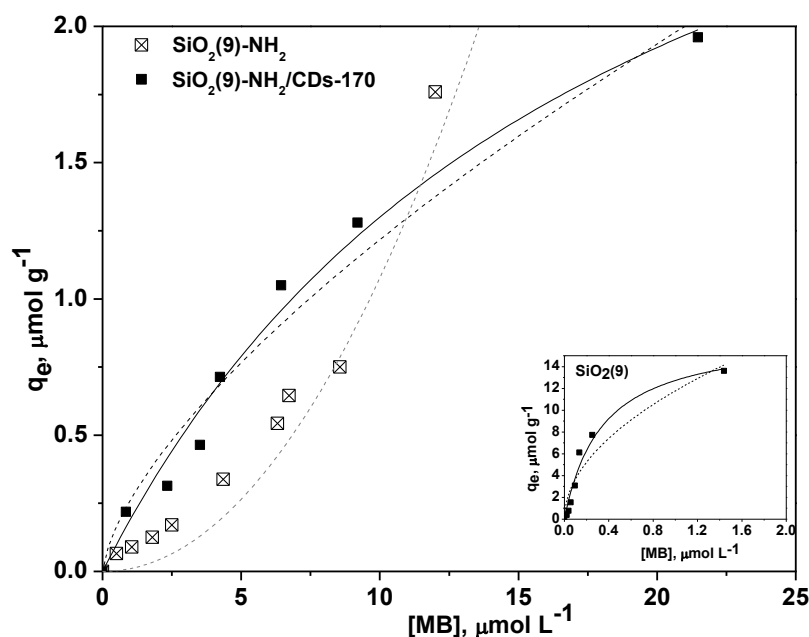


Figure 77 - Adsorption isotherms of MB by silica-based adsorbents ($m=50$ mg, $V=10$ mL, contact time: 120 min, pH 7). The solid lines are Langmuir model simulation; the dashed lines are Freundlich model simulation

Table 31 - The isotherm parameters for the adsorption of MB onto silica-based materials

Model parameters							
MB	Freundlich			Langmuir		Henri	
	K_F ($\mu\text{mol g}^{-1}$)($\text{L}\mu\text{mol}^{-1}$) ^{1/n}	1/n	R^2	K_L ($\text{L}\mu\text{mol}^{-1}$)	q_e ($\mu\text{mol g}^{-1}$)	R^2	K_d (mL g^{-1})
Solid							
$\text{SiO}_2(9)$	11.8	0.51	0.905	2.94	17.1	0.968	195
$\text{SiO}_2(9)\text{-NH}_2$	0.01	2.02	0.989	-	-	-	-
$\text{SiO}_2(9)\text{-NH}_2/\text{CDs-170}$	0.26	0.67	0.967	0.054	3.7	0.983	85

7.13. Carbon Dots obtained from nanoreactor approach

The general idea of this approach is the preparation of CDs strictly inside of the mesoporous template to ensure the confinement of all the nanoparticles. In order to achieve this, the next parameters of the template synthesis ought to be controlled:

- the total surface of the template is represented by mesoporous;
- the total volume of the solution used for impregnation shall be less than the total volume of the template pores;
- Excess of the precursor shall be removed from the outer surface of the template.

Therefore, special attention was given on the porous characteristics of the template and on the distribution of the precursor on the surface of the scaffold.

7.14. Morphological properties of host silicas

For proper preparation of CDs under the nanoreactor approach, it is critical to use the hosts with suitable pore size. It is generally accepted that CDs have a particle size of less than 10 nm [174, 177, 353]. Therefore, in contrast to earlier publications where microporous zeolites with small particle size have been used, silica gels with 4–11 nm nominal pore diameter and large particles (40–200 μm) is used in the current research, Table 32. The latter shall reduce CA adsorption on an external area of the particles and so prevent the formation of CDs outside of the pores. Since porous characteristics of the host are essential for the nanoreactor approach, they were justified from nitrogen adsorption experiment. From N_2 adsorption isotherms (Figure 14) it was demonstrated that the mesoporous structure is dominated for the selected samples. It was confirmed that the selected silica samples have the desirable pore sizes from 4.9 to 10.2 nm, with 0.7–1.25 $\text{cm}^3 \text{g}^{-1}$ pore volume. Accordingly, the mesopores contribute more than 95% (commonly 99.7% \pm 0.3) to the overall porosity of the silica gels, $S_{\text{meso}}/S_{\text{BET}}$ (%) values in Table 32.

Table 32 - Morphological characteristics of silica templates and the concentration of immobilized amines.

Silicas as denoted	Particle size (μm)	S_{BET} ($\text{m}^2 \text{g}^{-1}$)	$S_{\text{meso}}/S_{\text{BET}}$ (%)	Average pore size (nm)	Volume pore ($\text{cm}^3 \text{g}^{-1}$)	Concentration of immobilized groups* (mmol g^{-1})	Maximum loading of CA on $\text{SiO}_2\text{-NH}_2$, (g g^{-1})
$\text{SiO}_2(4)$	63-200	360.3	94.9	5.5	0.72	0	1.12
$\text{SiO}_2(4)\text{-NH}_2$		278.0	100	4.9	0.47	0.8 ± 0.2	0.73
$\text{SiO}_2(6)$	40-63	— ^[b]	—	6.0 ^[a]	0.80	0	1.24
$\text{SiO}_2(6)\text{-NH}_2$		278.6	100	5.4	0.59	0.8 ± 0.1	0.91
$\text{SiO}_2(9)$	63-200	387.4	99.8	6.9	1.01	0	1.57
$\text{SiO}_2(9)\text{-NH}_2$		325.8	99.9	6.1	0.86	0.9 ± 0.1	1.35
$\text{SiO}_2(11)$	40-75	400.2	99.6	10.2	1.25	0	1.94
$\text{SiO}_2(11)\text{-NH}_2$		290.0	99.4	9.1	0.95	0.7 ± 0.2	1.47

* - determined from direct pH-metric titration, [a] - data of the manufacturer, [b] - no data

As it is expected, the pore size of the templates is slightly decreased upon immobilization of the aminosilane, that makes $\text{SiO}_2\text{-NH}_2$ suitable for nanoreactor synthesis of CDs with particle size less than 10.2 nm, Table 32.

7.15. Preparation of silica-based@ nanocomposite

A crucial aspect of the nanoreactor synthesis of CDs is verification that a major part of the precursor is localized in the host pores. To ensure this, the volume of CA solution used for the preparation of silica-based@CA composites was limited by pore volumes of the silica gels. Also, high loading of hydrophilic silanol groups on the silica surface ensures good affinity of CA to the host. Considering high solubility of CA in water (up to 1.5 g in 1 mL of water) the maximum capacity of the template towards the precursor was estimated as 0.73-1.35 g of CA per 1.0 g of $\text{SiO}_2\text{-NH}_2$ and 1.12 – 1.94 g of CA per 1.0 g of SiO_2 , Table 32. Nevertheless, after the treatment of silica gel even with a small volume of liquid, wet material is always obtained due adsorption of some part of the water solution on inter-particle space. In order to obtain $\text{SiO}_2\text{@CA}$ having the precursor in the pores only, this interparticle liquid having dissolved compounds must be removed before the pyrolysis. To prove the importance of such pre-treatments, a sample labelled as $\text{rSiO}_2(11)\text{@CA}$ was prepared according to the procedures

recommended in [170, 211, 286]. By comparison of mass the silica sample before and after treatment with CA, it was found that loading of CA on $\text{rSiO}_2(11)@CA$ constitute of 112% of maximum pore capacities for this material. Therefore, after drying $\text{rSiO}_2(11)@CA$ is a compact glued agglomerate. After two consecutive rinsings of $\text{rSiO}_2(11)@CA$ with ether, CA loading is reduced to 60% of maximum pore capacity. The ether has been used for several reasons: a) CA is much less soluble in it than in water, which allows gentle control of CA removing procedure; b) ether is not miscible with water and so it will hardly penetrate into the $\text{SiO}_2@CA$ pores already fulfilled with water and thus will remove CA mainly from the outer surface of the template; c) ether is more lipophilic, it less drenches the template surface and thus ether solution can more completely be separated from the solid residuals by filtration than water. Such samples of $\text{SiO}_2@CA$ present itself as a loose dry powder. The SEM images confirm the difference between $\text{rSiO}_2@CA$ particles and $\text{SiO}_2(11)@CA$ particles (Figure 78), demonstrating a lot of CA microcrystals located on the external surface of $\text{rSiO}_2@CA$ and absence of those on $\text{SiO}_2(11)@CA$. The results presented in Figure 78 prove that washing of $\text{SiO}_2@CA$ with ether essentially reduces the amount of CA adsorbed on the outer surface of the template. Indeed, as-prepared $\text{rSiO}_2@CA$ form compact glued agglomerates (Figure 78a), while ether washed $\text{SiO}_2@CA$ can be seen as a loose powder with no sign of CA crystals out of the porous structure (Figure 78b).

CA onto amino-contains materials can adsorb more than onto non-modified silica gel due to higher affinity. Figure 78d demonstrates that rinsing of oversaturated $\text{SiO}_2(9)-\text{NH}_2@CA$ with ether essentially reduces CA loading. Particularly, it is clear that one cycle of ether washing is enough to get $\text{SiO}_2(9)-\text{NH}_2@CA$ with about maximum loading of CA (details in Table 32). Even distribution of CA on SiO_2-NH_2 surface was also proved by energy-dispersive spectroscopy (EDS) of $\text{SiO}_2-\text{NH}_2@CA$ (Figure 79).

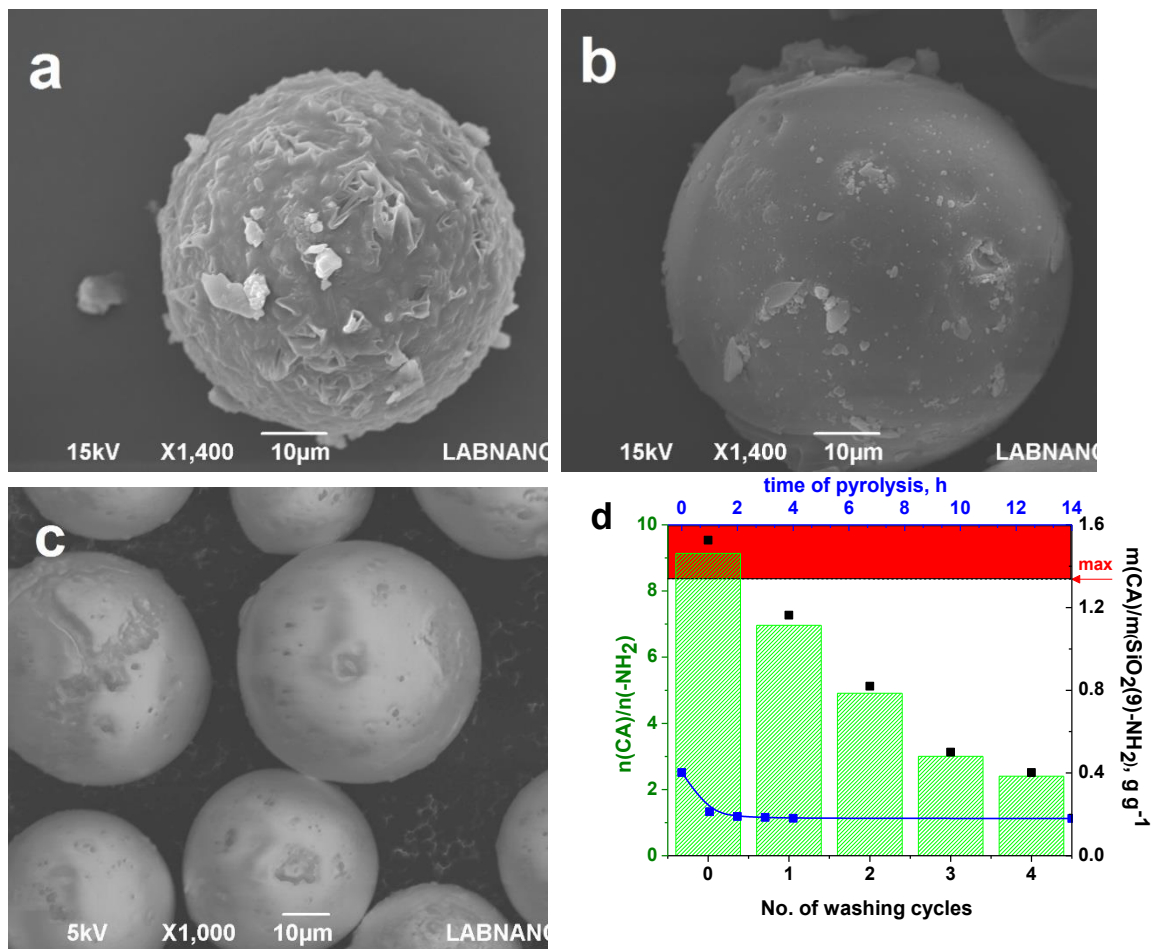


Figure 78 - SEM images of $rSiO_2@CA$ (a), $SiO_2(11)@CA$ (b), pristine $SiO_2(11)$ (c) and CA content on $SiO_2(9)-NH_2@CA$ after 0-4 of washing cycles with ether (bottom axis) and further thermal treatment (upper axis) (d)

Thus, the importance of the procedure for removing CA excess from an outer surface of silica composite was considered. In order to do so, wet samples of as-prepared silica-based@CA were blotted with filter paper until dry and then were washed out with two portions of diethyl ether. The ether is not miscible with water; therefore, it was expected that ether will not penetrate the pores of wet silica-based@CA filled by water and so will remove the excess of CA from the external surface of the particles only.

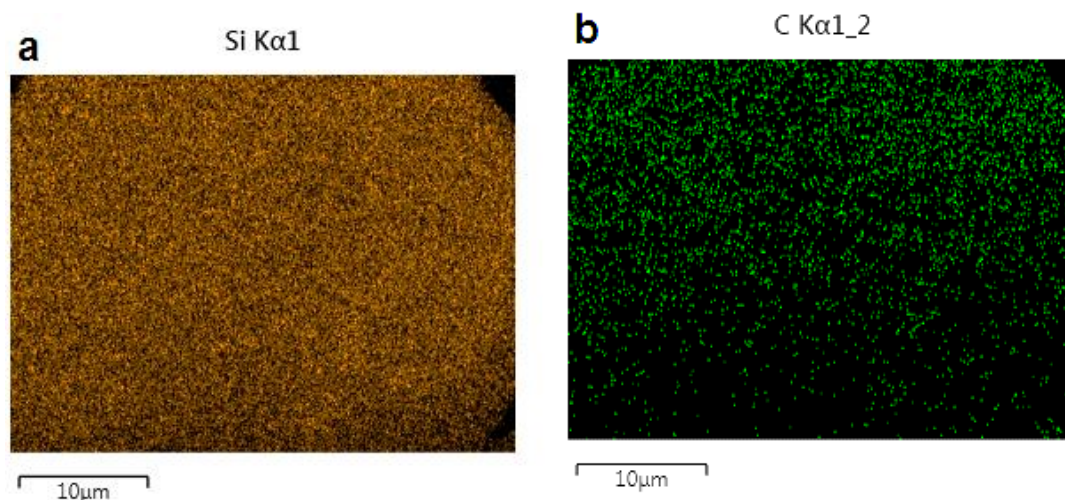


Figure 79 - EDS elemental mapping of silicon (a) and carbon (b) on $\text{SiO}_2\text{-NH}_2\text{@CA}$

7.16. Thermochemical treatment of $\text{SiO}_2\text{-NH}_2\text{@CA}$

The formation of CDs in silica-gel nanoreactors can be easily observed by monitoring of the samples PL. It was demonstrated that after 5-15 min of thermal treatment at 170 °C, visible blue luminescence is already developed for $\text{SiO}_2\text{-NH}_2\text{@CDs}$ samples. To confirm the quick formation of silica-encapsulated CDs, thermogravimetric analysis of $\text{SiO}_2\text{-NH}_2\text{@CA}$ sample was performed. The analysis was made for the sample obtained after four cycles of ether rinsing, having about 0.4 g of CA for 1.0 g of $\text{SiO}_2\text{-NH}_2$, Figure 78d. Considering the concentration of immobilized silane (Table 32), such loading corresponds to 2-3 molecules of CA per one molecule of the immobilized amine, Figure 78d. The sample with three times less loading of CA than maximum capacity $\text{SiO}_2(9)\text{-NH}_2$ has been chosen to ensure capturing of CA exclusively in $\text{SiO}_2\text{-NH}_2$ pores and also because QY of CDs is commonly highest for such molar ration of amine to CA [193, 205, 210]. $\text{SiO}_2(9)\text{-NH}_2\text{@CA}$ lost about 50% of its mass under the thermal treatment at 170 °C for the first hour, then no essential difference in the sample mass have not been observed even after 14 h of further treatment, Figure 78d. From this experiment, quick decomposition of CA inside of $\text{SiO}_2\text{-NH}_2$ pores can be concluded. Therefore, further samples of $\text{SiO}_2\text{-NH}_2\text{@CDs}$ were obtained mainly in the time frame of 15-240 min.

7.17. Synthesis of SiO₂@CDs, SiO₂-NH₂@CDs and SiO₂-EDA@CDs

SiO₂(d), SiO₂(d)-NH₂ and SiO₂(11)-EDA materials were used as a host for CDs precursor. After impregnation with the precursor and pre-treatment, samples of SiO₂@CA and SiO₂-NH₂@CA were thermally treated in an inert atmosphere at 170 °C for 5-720 min and then subsequently washed with water, NaHCO₃, and NaOH to release CDs, Table 33. One test sample of SiO₂(4)-NH₂@CA at 200°C was prepared during 600min.

Table 33 - Overview of the host samples used for the preparation of CDs from citric acid precursor

Temperature: 170 °C																
Host	Pore diameter, nm				Time of pyrolysis, min								Post-treatment			
SiO ₂	5.5	6.0	6.9	10.2									600			
SiO ₂ -NH ₂	4.9	5.4	6.1	9.1	5	15	30	60	120	240	360	720	H ₂ O	NaHCO ₃	NaOH	
Temperature: 100-180 °C																
Host	Pore diameter, nm				Time of pyrolysis, min								Post-treatment			
Temperature, °C:					100	110	130	150	170		150	180				
SiO ₂ (11)-EDA	10.2				60	60	60	60	15-600	600	600		H ₂ O	NaHCO ₃	NaOH	

Based on the theoretical review, CDs prepared from ethylenediamine precursor showed high QY. SiO₂(11)-EDA host was also used to preparation of composites. One batch sample of SiO₂(11)-EDA@CDs-T-t obtained after heating at 100, 110-150°C and collected at each 60 min, and at 170°C during 15-600 min, Table 33. Additionally, two samples were received after heating the sample at 150°C (SiO₂(11)-EDA@CDs-150-600) and 180°C (SiO₂(11)-EDA@CDs-180-600) during 600 min.

7.18. Characterization of silica-based@CDs composites

7.19. FTIR spectroscopy

FTIR spectra are crucial to revealing the difference in the chemical composition of CDs [194, 232, 238]. FTIR spectra of silica gel embedded CDs have some limitations due to overlapping of guest and host absorption. Particularly, FTIR spectra of silica-based@CDs reveal the narrow band at 3744 cm⁻¹, broad intensive bands at 3700-3000 cm⁻¹ and at 1900-2200 cm⁻¹, which are attributed to stretching vibrations of silanol and siloxane groups of silica template, Figure 80. The spectrum of

$\text{SiO}_2(6)@\text{CDs-180}$ reveal itself as a superposition of the host and the guest (CDs) and in addition to the bands of silica, $\text{SiO}_2(6)@\text{CDs-180}$ sample demonstrates well-defined peaks at 1775 cm^{-1} and 1702 cm^{-1} that can be attributed to stretching vibration of C=O fragments in $-\text{C(O)}(\text{OR})$ and $-\text{COOH}$ functional groups of silica-adsorbed CDs. These bands prevent observation of stretching vibrations from O-H and N-H groups of C-dots. Functional group region of FTIR spectra of CDs contains several absorption bands, but most intensive is $\nu(\text{C=O})$ at $1620\text{--}1650\text{ cm}^{-1}$ [183, 190, 229, 238].

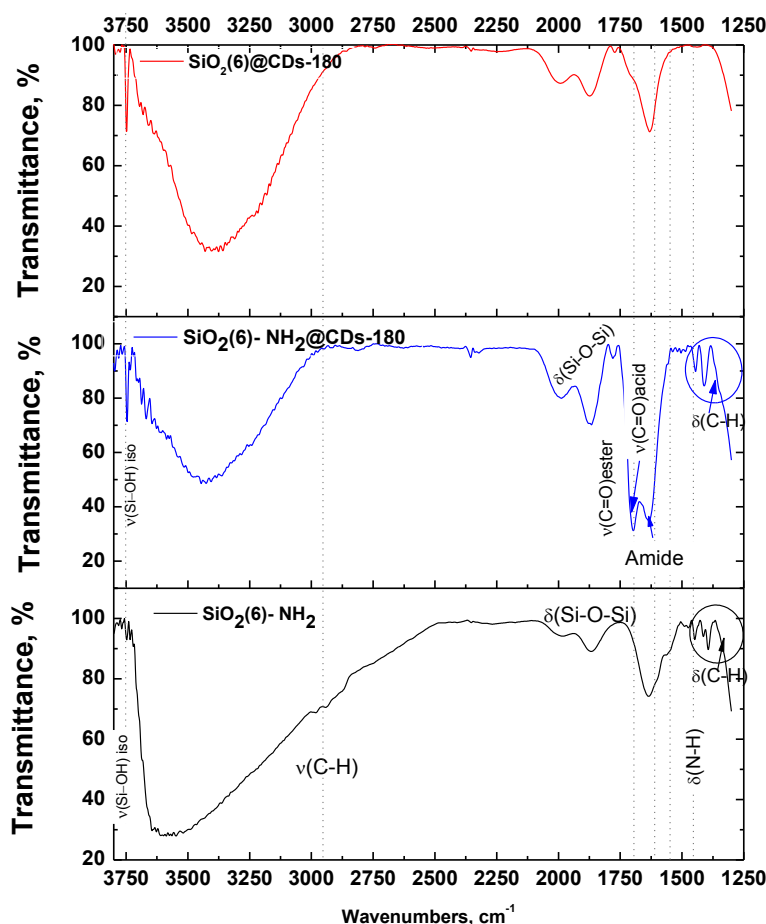


Figure 80 - FTIR spectra of $\text{SiO}_2(6)@\text{CDs-180}$, $\text{SiO}_2(6)\text{-NH}_2@\text{CDs-180}$ and $\text{SiO}_2(6)\text{-NH}_2$

Contrary, FTIR spectra of $\text{SiO}_2\text{-NH}_2@\text{CDs}$ demonstrate two equally intensive absorptions at 1648 and 1700 cm^{-1} (Figure 80), confirming the presence of two kinds of fictional moieties in C-dots - $>\text{C=O}$ and $-\text{NH-C(O)-}$, correspondingly [194].

Figure 81 shows the FTIR results of composites $\text{SiO}_2(11)\text{-EDA@CDs-150-600}$, $\text{SiO}_2(11)\text{-EDA@CDs-180-600}$ and evaporated product of water Soxhlet extract from $\text{SiO}_2(11)\text{-EDA@CDs-150-600}$.

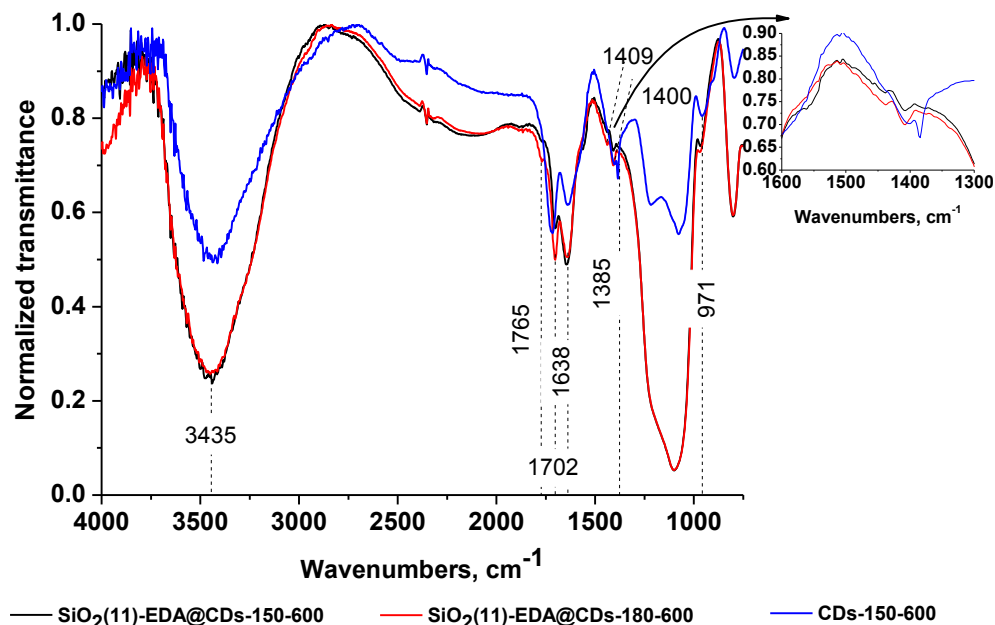


Figure 81 - FTIR spectra of CDs-150-10h and composites $\text{SiO}_2(11)\text{-EDA@CDs-150-600}$, $\text{SiO}_2(11)\text{-EDA@CDs-180-600}$

All spectra have two kinds of functional moieties of -C=O and -NH-C(O)- at 1702 cm^{-1} and 1638 cm^{-1} , respectively, and them similar to bands in $\text{SiO}_2(6)\text{-NH}_2\text{@CDs-180}$. Thus amide-derivation is observed onto $\text{SiO}_2(11)\text{-EDA}$ support as well. Profile of the spectra is similar except for the relative intensity of certain bands. In general, the broad absorption peak centered at 3435 cm^{-1} are associated with multiple structures of O-H. CDs-150-600 is more dehydrative than composites. Relative enhancement of the typical stretching vibration of COOH bonds at 1702 cm^{-1} in CDs-150-600 comparing to composites indicate an increase in the degree of oxidation of the CDs and free carboxylic groups. However, stretching vibrations of C=C at 1560 cm^{-1} ($\text{SiO}_2(11)\text{-EDA@CDs-150-600}$), and C-N= at 1438 cm^{-1} (for both composites) bonds were observed for each sample, indicating the formation of polyaromatic structures between aminosilica carrier and citric acid during the reaction process. It can be moieties of IPCA fragmentation.

7.20. XPS spectroscopy

XPS survey, C1s and N1s high-resolution spectra and the best deconvolution into individual components measured for samples SiO₂(6)@CDs-180, SiO₂-NH₂, SiO₂-NH₂@CDs, CDs-150-10h and composites SiO₂(11)-EDA@CDs-150-600, SiO₂(11)-EDA@CDs-180-600 are demonstrated in Figure 82, Figure 83. XPS findings were used to further investigate the chemical nature of the embedded CDs into the matrix.

The XPS survey spectra for the SiO₂(6)@CDs-180 (Figure 82) indicate predominantly O1s, C1s, Si2s and Si2p peaks centered, respectively, at 532, 286, 155 and 103 eV.

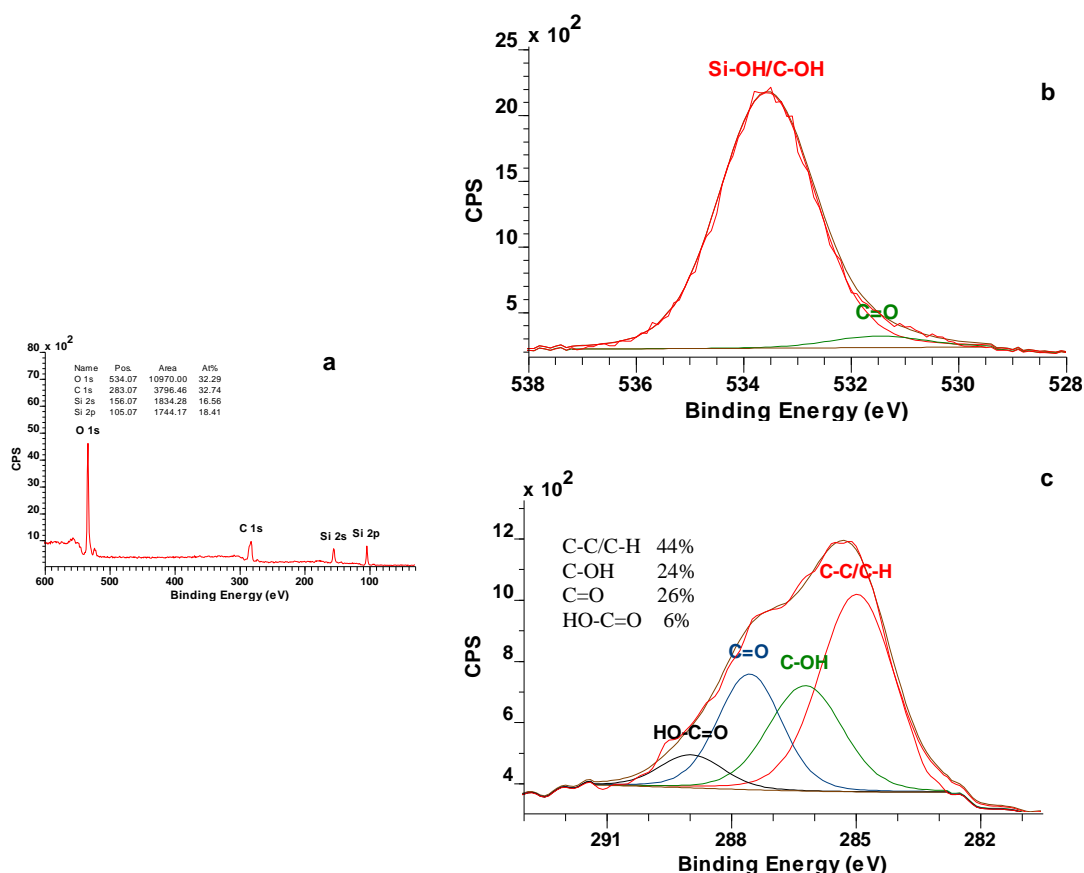


Figure 82 - Survey (a) and high resolution fitted XPS spectra (b, c) of SiO₂(6)@CDs-180 in O1s (b) and C1s (c) regions

The high-resolution C1s XPS spectra of samples revealed different types of carbon atoms in CDs. Curve fitting analysis of high-resolution XPS of C1s reveals bands at 284.5 eV, 286.3, 287.5 and 289 eV that can be assigned to C–C (44%), C–OH (24%), carbonyl (26%) and carboxyl (6%) groups, correspondingly, Figure 82(c). This

kind of XPS is very typical for CDs and demonstrates the formation of partly decarboxylated CDs. A weak band at 551.5 eV attributed to carbonyl fragments in CDs can be seen in high-resolution O1s XPS spectrum of SiO₂(6)@CDs-180, Figure 82b.

The XPS survey spectra both SiO₂-NH₂ and SiO₂-NH₂/CDs demonstrate predominantly O1s, N1s, C1s, Si2s and Si2p peaks centered at 532, 401, 286, 155 and 103 eV, respectively, Figure 83d. From the atomic ratio between silicon and nitrogen in SiO₂(4)-NH₂ concentration immobilized aminosilane was determined as 0.95 mmol g⁻¹ that matches the value defined by chemical analysis (Table 14). After impregnation of aminosilica with CA and its thermal treatment the atomic ratio between carbon and silicon increases from 0.28 (for SiO₂(4)-NH₂) to 0.51 (for SiO₂(4)-NH₂@CDs-720) indicating the formation of silica-incapsulated C-dots. It is important to mention that silicon to nitrogen atomic ratio remains the same (0.0575 ± 0.0005) for both nanocomposites indicating the thermal stability of immobilized amines. From carbon to nitrogen atomic ratio the composition of such encapsulated C-dots was estimated as C/N = 9/1. In the high-resolution XPS spectra the C1s band can be deconvoluted into three (SiO₂(4)-NH₂) peaks at 285, 283.3 and 287.7 eV, which are attributed to aliphatic (C-C), oxygenated (C-O) and nitrous (C-N) carbons, respectively [229, 354], Figure 83b. The N 1s band can be deconvoluted into two peaks at 399.7, and 401.6 eV, representing neutral and protonated alkyl amine[218], Figure 83c.

High-resolution XPS spectra of SiO₂-NH₂@CDs are essentially different from pristine SiO₂-NH₂. The C1s band in spectra can be deconvoluted into four peaks attributed to graphitic C=C (285.6 eV), nitrous C-N (286.8 eV) and oxygenated carbon species, such as carbonyl and carboxylic (288.8 and 289.7 eV), Figure 83e. The N1s XPS spectrum of SiO₂-NH₂@CDs clearly demonstrates changing in chemical environmental of N atom after the thermal treatment, revealing new dominating (93%) band at 400.9 eV, which can be attributed to the amide, Figure 83f.

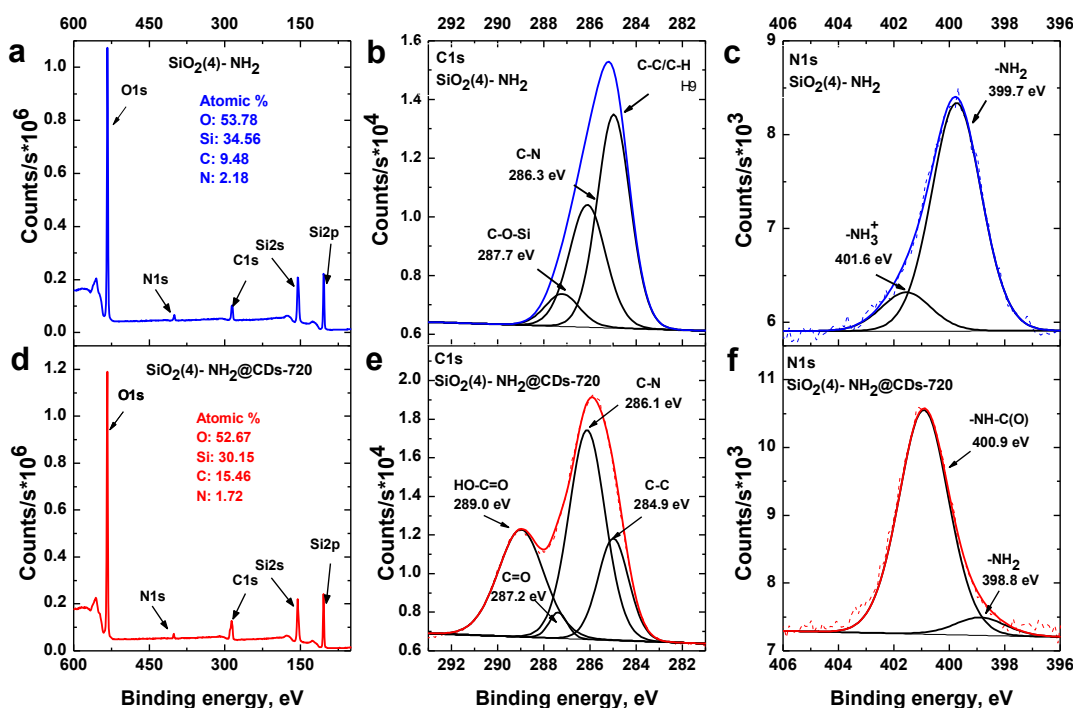


Figure 83 - Survey (a, d) and fitted XPS spectra of the C1s (b, e) and N1s (c, f) regions corresponding to $\text{SiO}_2(4)\text{-NH}_2$ (a, b, c) and $\text{SiO}_2(4)\text{-NH}_2\text{@CDs-720}$ (d, e, f).

The XPS survey spectra of SiO_2 -EDA-derivatives demonstrate the same predominantly elements peaks. Interesting, C, N, O atomic percentages in the sample were different. C content increased in the next sample $\text{CDs-150-600} > \text{SiO}_2\text{-EDA@CDs-180-600} > \text{SiO}_2\text{-EDA@CDs-150-600} > \text{SiO}_2\text{-EDA}$, Figure 84a. CDs-150-600 is almost C-containing materials of CDs due to removal of the silica-based matrix. $\text{SiO}_2\text{-EDA@CDs-180-600}$ and $\text{SiO}_2\text{-EDA@CDs-150-600}$ have similar C-content due to the sample mass proportion of support and CA. $\text{SiO}_2\text{-EDA}$ has only 10 % of C due to the absence of CA onto the material. N-contain for silica-based materials exhibited equal values. For CDs materials, O element is taken part of silica matrix and oxidized groups of CDs. $\text{SiO}_2\text{-EDA@CDs-180-600}$ has lower O-element than $\text{SiO}_2\text{-EDA@CDs-150-600}$ due to higher thermal treatment that provides carboxylation and forming less carboxylic groups. High-resolution C1s XPS spectra of $\text{SiO}_2\text{-EDA-based@CDs}$ are similar to $\text{SiO}_2\text{-NH}_2\text{@CDs}$ with the presence of C-C/C=C, C-N, C=O and HO-C=O bands, Figure 84.

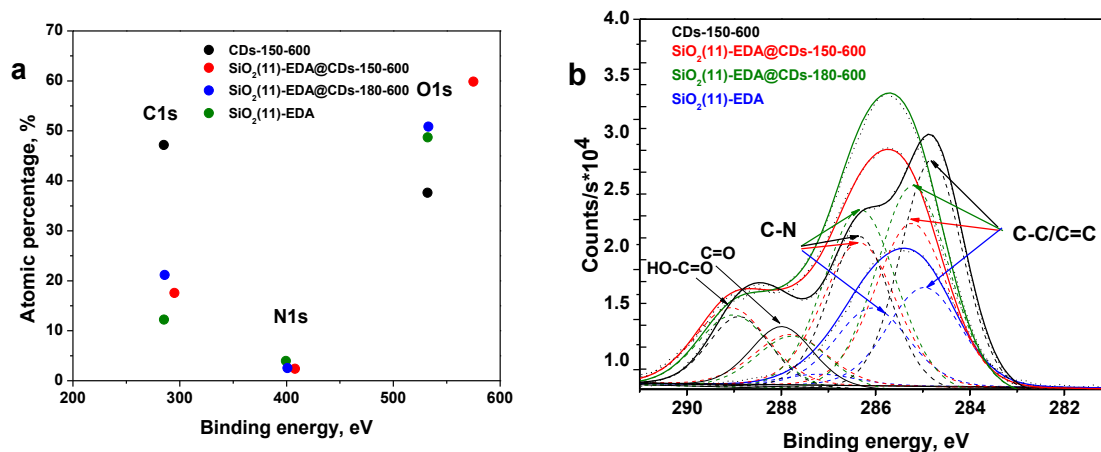


Figure 84 - Atomic percentage from the survey (a) and fitted XPS spectra of the C1s corresponding to CDs-150-600, SiO₂(11)-EDA@CDs-150-600, SiO₂(11)-EDA@CDs-180-600, SiO₂(11)-EDA

7.21. Photoluminescence of solid composites SiO₂@CDs- τ .

The incipience of CDs has been monitored by measuring the photoluminescence from solid samples of SiO₂@CDs obtained for different time of thermal treatment, Figure 85.

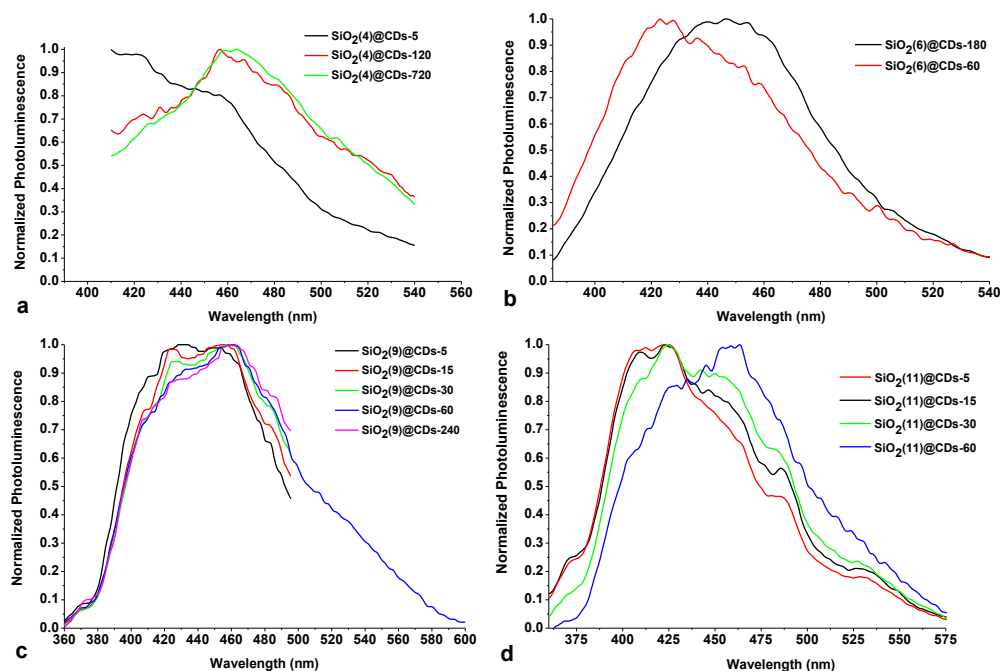


Figure 85 - Normalized PL spectra of SiO₂(d)@CDs-t

It seems that CDs are formed in silica pores very quickly. At least, the luminescence of SiO₂@CDs can already be detected after 5 min of SiO₂@CA treatment of at 170 °C. However, the position of PL maximum (420 nm) for SiO₂@CDs obtained

for such a short time (5-60 min) does not match with PL of CDs obtained from CA by conventional methods (445 nm). Together with the peak at 420 nm, PL spectra of all $\text{SiO}_2@\text{CDs}$ exhibit peak at 450 nm, Figure 85. Thus, PL spectra of $\text{SiO}_2@\text{CA}$ commonly exhibit a wide band, which consists of two peaks at 420 and 450 nm.

While the peak positions do not essentially depend on the time of $\text{SiO}_2@\text{CDs}$ thermal treatment and the size of the host pores, the relative intensity of long-wave emission rises with time for all studied $\text{SiO}_2@\text{CDs}$ that can manifest the development of CDs with higher decarboxylation degree. Absolute intensity of $\text{SiO}_2@\text{CDs}$ reaches its maximum for 15-30 min of $\text{SiO}_2@\text{CA}$ thermal treatment and then sharply decline for all studied samples, Figure 8a. After 100 min of the treatment, no further depression of PL is observed, Figure 86b. The photoluminescence spectra of $\text{SiO}_2@\text{CDs}$ clearly demonstrate the formation of CDs captured in silica pores. But it is also clear that those CDs have different sizes and shapes since they exhibit multiple maxima in PL spectra of $\text{SiO}_2@\text{CDs}$. The nature of the PL band at 420 nm shall be further investigated.

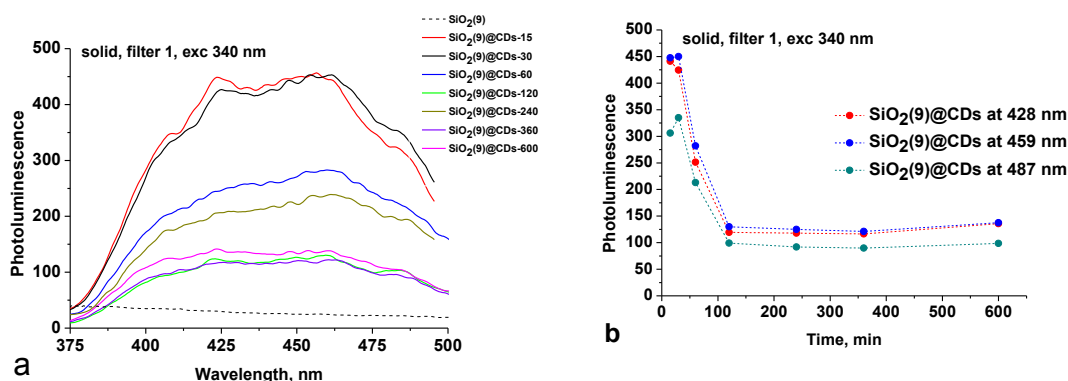


Figure 86 - Photoluminescence spectra of $\text{SiO}_2(9)@\text{CDs}$ -t for different time of the thermal treatments (a), and changes of photoluminescent intensity versus time (b)

The $\text{SiO}_2@\text{CDs}$ composites also demonstrate photoluminescence that occurs under excitation with high energy radiation (165-276 nm, 7.5-4.5 eV). For example, $\text{SiO}_2(6)@\text{CDs}$ generates wide emission with a maximum at 525 nm, Figure 87b. From two-dimensional mapping, as a function of the excitation energy, it can be seen that the peak position of photoluminescence emission almost does not change in the function of excitation energy, Figure 87a. The most intense photoluminescence for $\text{SiO}_2(6)@\text{CDs}$ is observed at 4.0-4.2 eV (310-295 nm). It seems $\text{SiO}_2(6)@\text{CDs}$ can be useful for adsorption and transformation of short wave UV radiation.

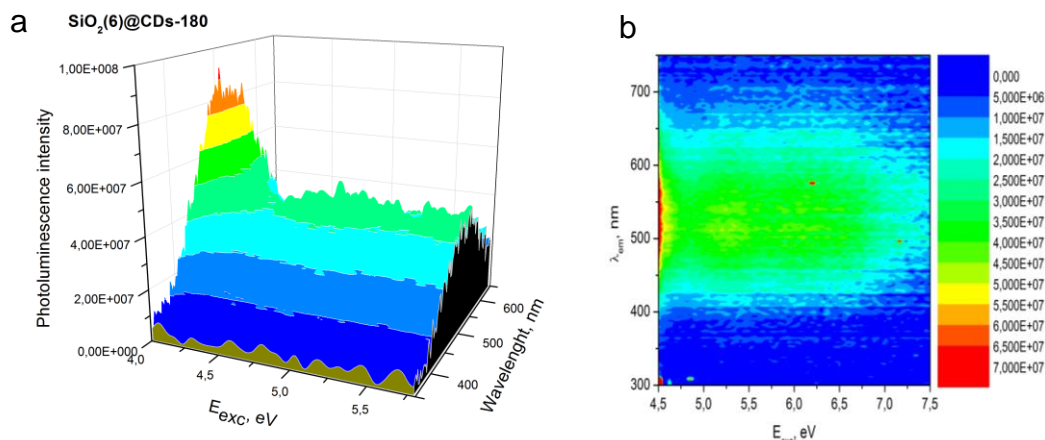


Figure 87 - 3D photoluminescent spectra and excitation-emission map of $\text{SiO}_2(6)\text{@CDs-180}$ (a, b)

The PL spectra of all $\text{SiO}_2\text{-NH}_2\text{@CDs}$ samples consist of the broad asymmetrical band, where several peaks can be distinguished with maximums at 428 and 455 nm, Figure 88. No essential difference in the position of maximums in PL spectra of C-dots captured in aminosilica templates with different pore size was noted, but relative intensities of the peaks are different. Generally speaking, the intensity of short-wave shoulder in PL spectra of $\text{SiO}_2\text{-NH}_2\text{@CDs}$ increases with increasing the pore size of the host and decreases with the time of thermal treatment, Figure 88.

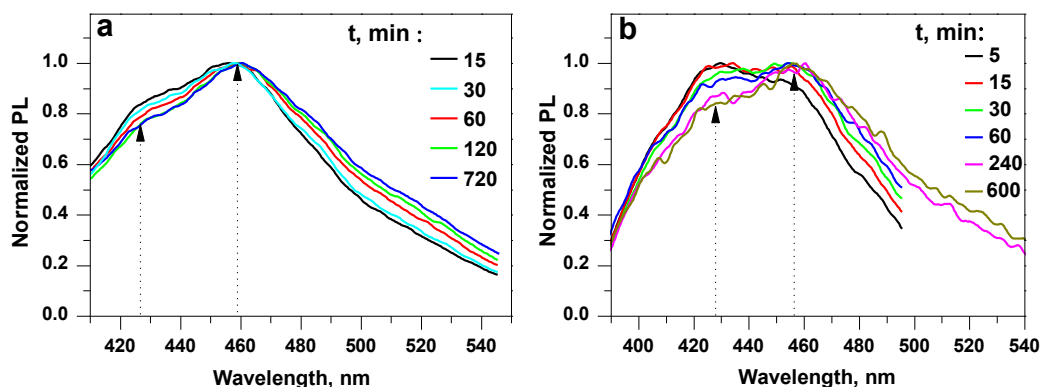


Figure 88 - Normalized PL spectra of $\text{SiO}_2(4)\text{-NH}_2\text{@CDs-t}$ (a) and $\text{SiO}_2(9)\text{-NH}_2\text{@CDs-t}$ (b) obtained after the different time (t, min) of the thermal treatment of $\text{SiO}_2(d)\text{-NH}_2\text{@CA}$.

A sharp decline in absolute photoluminescence intensity was observed for all solid samples with the time of thermal treatment in the range of 5 - 50 min. After that time, the photoluminescence of $\text{SiO}_2\text{-NH}_2\text{@CDs}$ samples is stabilized. For the preparation of CDs with persistent properties from $\text{SiO}_2\text{-NH}_2\text{@CA}$, thermal treatment of the composite shall be performed for at least 120 min at 170 °C. Longer heating (up

to 12 h) has no essential effect on $\text{SiO}_2\text{-NH}_2\text{@CDs}$ PL and also does not lead to further mass loss of the composite. According to normalized PL solid spectra of $\text{SiO}_2(11)\text{-EDA@CDs-T-t}$, Figure 97, redshift of maximum PL peak position was observed. It can be related that with increasing of thermal treatment some grown particle can occur.

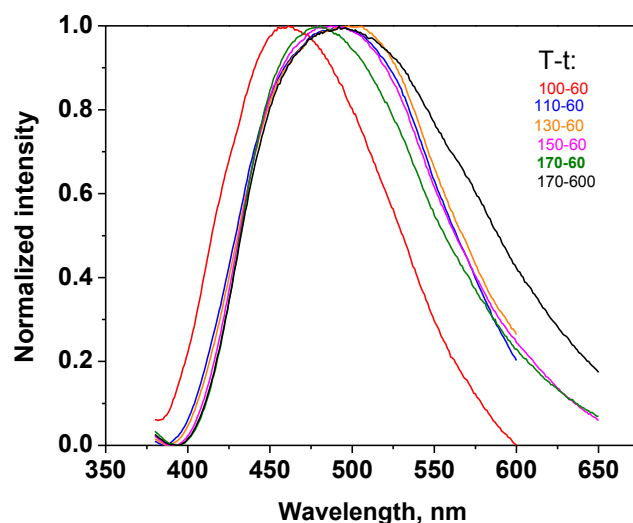


Figure 89 - Normalized PL spectra of $\text{SiO}_2(11)\text{-EDA@CDs-T-t}$ obtained after the different time (t, min) and the thermal treatment (T, °C) of $\text{SiO}_2(11)\text{-EDA@CA}$

7.22. Elution of CDs from the host

To elute the resulted CDs from the silica host three consecutive steps were applied. First, they were exhaustively washed with water until the conductivity of the washing solution and no light absorption was observed in UV spectra, Figure 90a,b. Then 0.1 mol L^{-1} of NaHCO_3 water solution was used for the same purposes. Finally, SiO_2 scaffold was dissolved in NaOH . It has been found that water elutes strongly luminescent CDs from all samples of $\text{SiO}_2\text{@CDs-t}$. Four washing cycles were enough to remove most of the trapped CDs, Figure 90a. Further washing of $\text{SiO}_2\text{@CDs-t}$ with NaHCO_3 and even solubilization of the host in NaOH no reveal an essential quantity of the CDs, except for the samples treated for 600 min, Figure 90c,d. The weak affinity of the CDs to the SiO_2 host can be concluded from this experiment. It also can be assumed that silica gel is a more appropriate host for confining of CDs particles then earlier used zeolites since it releases CDs by treatment with water and not requires solubilization of the host in alkali solution.

During the thermal treatment of $\text{SiO}_2\text{@CA}$ most of the CDs are growing inside of the host pores with no essential interaction with the surface of silica. Such type of CDs particles can be eluted by water from the hosts. Immersing of $\text{SiO}_2\text{@CDs}$ into NaHCO_3 solution promotes ionization of silanol groups of silica surface and carboxylic fragments on CDs surface. Negatively charged silica surface stimulates further elution of the negatively charged CDs.

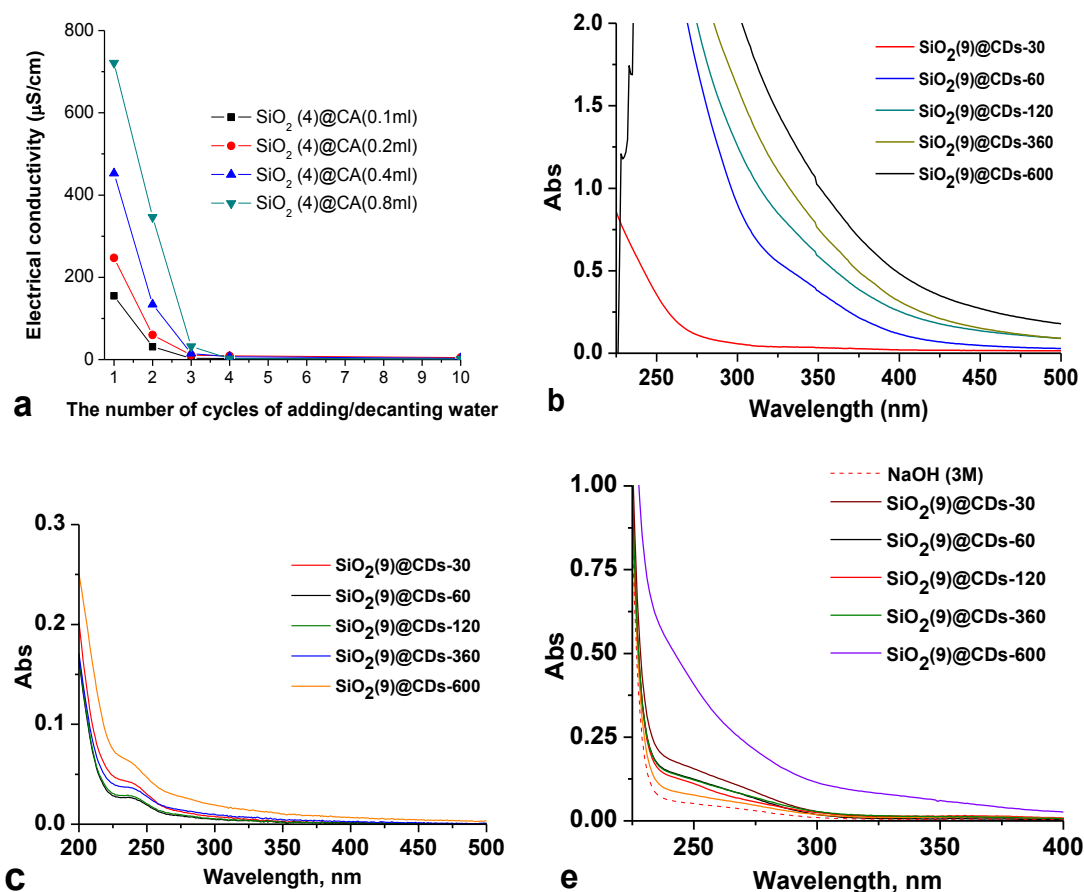


Figure 90 - (a) Electroconductivity of the supernatant solution obtained after immersing of $\text{SiO}_2(4)\text{@CDs-60}$ (0.5 g) to 10 ml of water with further filtration and cycling the procedure; (b-d) UV-VIS spectra of the supernatant solutions, obtained by successive treatment of $\text{SiO}_2(4)\text{@CDs-60}$ with water (b), $0.1 \text{ mol L}^{-1} \text{NaHCO}_3$ (c), $3 \text{ mol L}^{-1} \text{NaOH}$ (d) after different time of the thermal treatment.

During the thermal treatment of $\text{SiO}_2\text{@CA}$ most of CDs are growing inside of the host pores with no essential interaction with the surface of silica. Such type of CDs particles can be eluted by water from the hosts. Immersing of $\text{SiO}_2\text{@CDs}$ into NaHCO_3 solution promotes ionization of silanol groups of silica surface and carboxylic

fragments on CDs surface. Negatively charged silica surface stimulates further elution of the negatively charged CDs.

Since PL spectra of $\text{SiO}_2\text{-NH}_2\text{@CDs}$ and $\text{SiO}_2\text{-EDA@CDs}$ exhibit complex multiband emission, it is obvious that several types of CDs were formed inside of the pores under the thermal treatment of amine-based@CA. In contrast to most of the earlier published results (for example [193, 211, 217]), it was found that an essential part of unbound CDs can be eluted from amine-based @CDs by water. Nevertheless, it was found that not all the CDs can be extracted from amine-based@CDs even by exhaustive washing with water in Soxhlet. After such treatment, solid amine-based@CDs still exhibited strong PL. This luminescence of the solid remains even after washing the samples with NaHCO_3 solution, which promotes deprotonation of carboxylic groups on CDs surface and thus their elution from the host carrier due to electrostatic repulsion with ionized $\equiv\text{Si-OH}$ groups. Thus, silica-fastened CDs were purified by the dissolution of the silica matrix in NaOH .

Such different elution behavior of CDs can be explained by the chemical reaction between a part of the adsorbed precursor with immobilized aminogroups of the template, leading to firm immobilization of the resulted CDS inside of the pores, as it is demonstrated, as an example for $\text{SiO}_2\text{-NH}_2\text{@CDs}$, in Figure 91. As it is presented in Figure 78, the molecular ratio (η) of CA to immobilized aminosilane (NH_2) on $\text{SiO}_2\text{-NH}_2\text{@CA}$ is in the next range: $3 < \eta_{\text{CA}/\eta_{\text{NH}_2}} < 8$. Thus, some molecules of CA are firmly holding in the template due to the formation of immobilized salt, Figure 91. Upon heating, this salt can turn to amide,[355] and further to covalently immobilized CDs, Figure 91. Because large excess of precursor, not all CA are turning to C-dots. It is particularly true for samples of $\text{SiO}_2\text{-NH}_2$ with large pores due to their higher capacity towards CA. For the same reason PL spectra of $\text{SiO}_2(4)\text{-NH}_2\text{@CDs}$ and $\text{SiO}_2(9)\text{-NH}_2\text{@CDs}$ are different: in the aminosilica template with larger pores hold two types of CDs, while one type dominates in smaller pores. The proposed model of C-dots formation inside of $\text{SiO}_2\text{-NH}_2$ pores is also confirmed by XPS N1s (Figure 83, Figure 84) and FTIR (Figure 80, Figure 81) spectra of $\text{SiO}_2\text{-NH}_2\text{@CDs}$ and $\text{SiO}_2\text{-EDA@CDs}$ where amide moieties can be clearly seen.

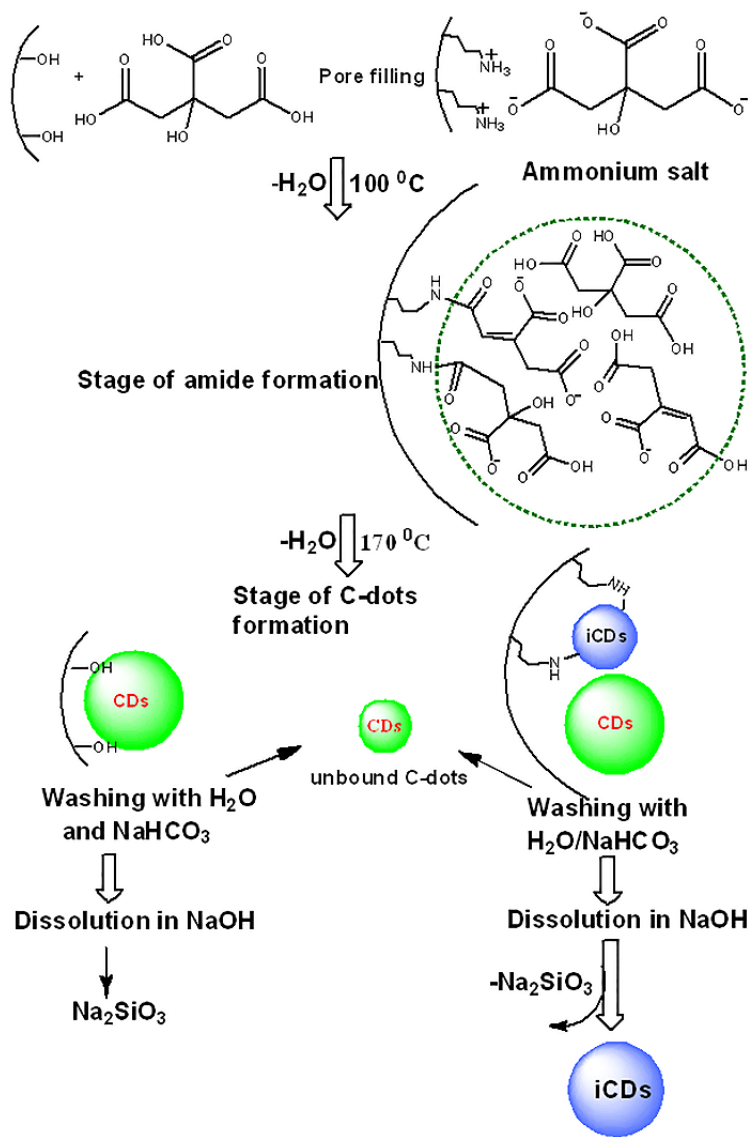


Figure 91 - Scheme of C-dots formation from CA encapsulated in $\text{SiO}_2\text{-NH}_2$ pores.

7.23. Characterization of CDs

7.24. Microscopy

The size and morphology of CDs were investigated by high-resolution transmission electron microscopy (HRTEM), atomic force microscopy (AFM), Energy-Dispersive Spectroscopy (EDS) and Electron Energy Loss Spectroscopy (EELS). First of all, with the help of EDS and EELS chemical nature of found nanoobjects was identified as carbogenic particles. EDS analyses in HRTEM with a large area silicon drift detector (SDD) of several nanoparticles were done. There are several elements detected by the EDS, such as C, Cu, Si, Cr, Fe and Co, etc, with three

of them have relatively strong signal: C, Cu and Cr. Since we used Cu grid with C support for the TEM study, we cannot confirm what elements the nanoparticles contain with the EDS results only. However, the EDS results indicate possible elements in the nanoparticles. Usually, the strong Cu signal is from the Cu grid and other elements, such as Cr, Fe and Co are from the sample holder. EELS detects the energy loss of the electrons beam in TEM passing through the sample and the secondary electrons do not have any effect on the EELS spectrum. As a result, EELS can give very local elemental information with very high spatial resolution and no signal from the adjacent particles and sample holder. A very strong C signal was found in the energy range of 290-340 eV. No EELS signal for other elements was detected. With all the data, we can conclude that the nanodots in our study are CDs.

Two different types of CDs were analyzed: CDs eluted from $\text{SiO}_2(11)\text{-NH}_2$ @CDs by water, and CDs obtained by dissolution of the templates with 4.9 nm ($\text{SiO}_2(4)\text{-NH}_2$ @CDs) and 9.1 nm ($\text{SiO}_2(11)\text{-NH}_2$ @CDs) pores. TEM images confirmed that all C-dots are well dispersed and have about spherical morphology, Figure 92. The mean diameter of the particles is about 5 nm for all encapsulated CDs, but their size distribution profiles are essentially different. The CDs obtained from the template with 4.9 nm pore diameter have a narrow asymmetrical distribution of the particle size, with about 81% of the particles with size ≤ 5 nm, Figure 92d. Surprisingly CDs obtained after removing the template with 9.1 nm pore diameter have only slightly bigger particles from 3 to 8 nm and symmetrical character of size distribution profile, Figure 92f. Size distribution profile for water extracted CDs is much wider than for CDs from template with an essential contribution (56%) of small (about 3 nm) CDs, Figure 92b. About 95% of water extracted CDs have the particle size 2.5-5.5 nm. These CDs often organized in small groups (Figure 92a), probably due to some agglomeration during extraction in the Soxhlet. Such agglomeration already was demonstrated for CDs [206].

The HRTEM (Figure 92 insets) results indicate that most particles are amorphous carbon particles and in rare cases, the particles possess well-resolved lattice spacing of 0.34 and 0.20 nm, corresponding to the (200) and (100) in-plane lattice spacing of graphite, correspondingly [356], as shown in Figure 92a,c,e.

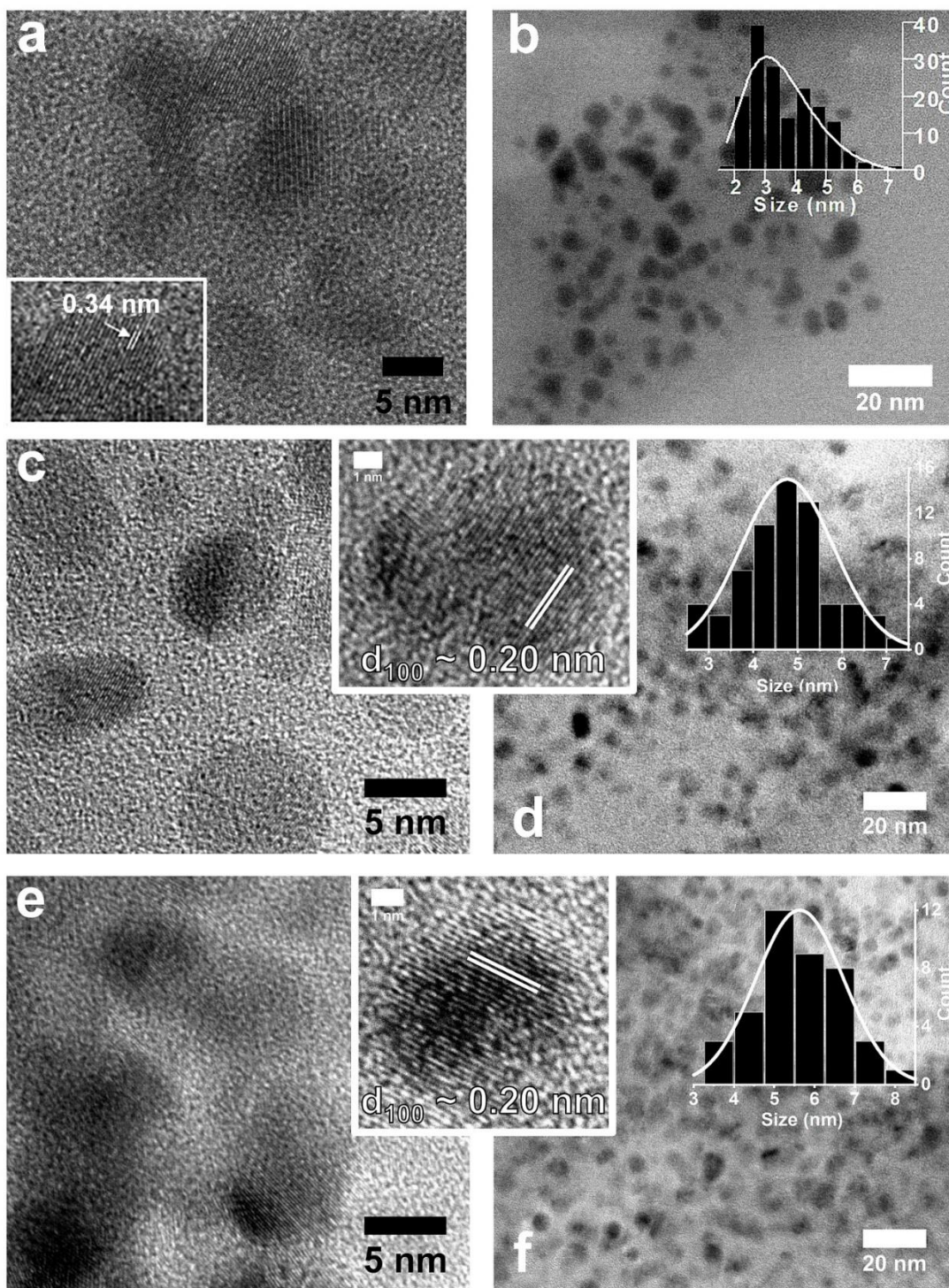


Figure 92 - TEM and HRTEM (in insets) images with the size distribution profiles of water extracted CDs (a, b) and CDs obtained by dissolution of $\text{SiO}_2(4)\text{-NH@CDs-240}$ (c, d) and $\text{SiO}_2(11)\text{-NH@CDs-600}$ (e, f).

AFM technique was used to probe the sample topography and measure particle height. AFM image of CDs prepared from $\text{rSiO}_2\text{@CDs}$ according to the procedure

shows the wide distribution of the particle's height mainly from 5 to 8 nm, Figure 93a. The CDs obtained from $\text{SiO}_2(4)\text{@CDs-180}$ have a smaller height (2-4 nm) and narrower distribution profile, Figure 93b.

These data support the results, obtained from SEM microscopy of $\text{rSiO}_2\text{@CA}$ particles (Figure 78), suggesting the possible formation of CDs on the outer surface of the silica template. If so, the growth of such particles is not confined by the template, and CA pyrolysis can lead to formation CDs with size, larger than the size of silica pores. On the contrary, the experimental procedure proposed in current research demonstrated the narrow distribution of the CDs particle height. Thus, the importance of the pre-treatment of $\text{SiO}_2\text{@CA}$ nanocomposites for removing CA excess that can be adsorbed on the outer surface of silica is feasible.

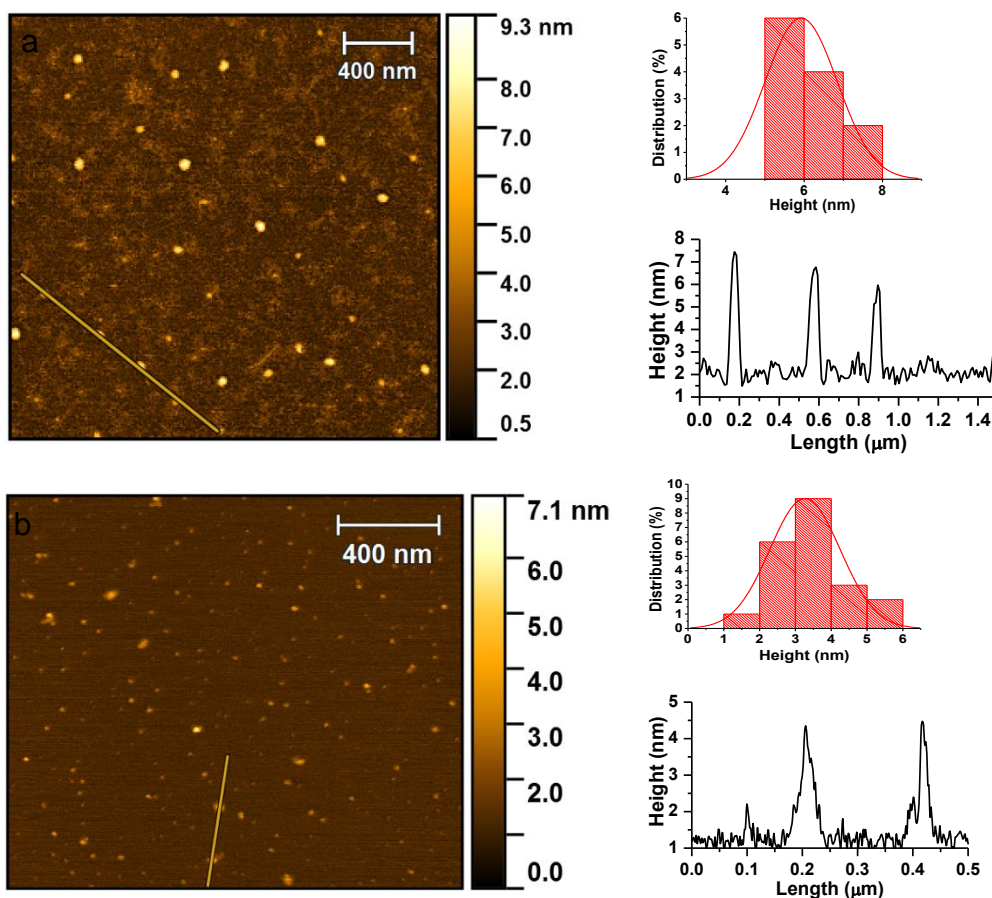


Figure 93 - AFM images (left), height distribution (upper right) and profile (lower right) of the CDs obtained from $\text{rSiO}_2\text{@CDs}$ (a) and $\text{SiO}_2(4)\text{@CDs-180}$ (b) after their elution with water

AFM images demonstrate that CDs eluted from $\text{SiO}_2\text{-NH}_2\text{@CDs}$, Figure 94, are spherical particles with a height about 1-3 nm. By taking to account the results of AFM

and TEM microscopies, it can be concluded that CDs eluted from $\text{SiO}_2\text{-NH}_2\text{@CDs}$ are flattened spheroids with 2-4 nm of height, and 5 nm in lateral size, and so consist of 5-10 defective graphene layers with various oxygen-containing functional groups.[192]

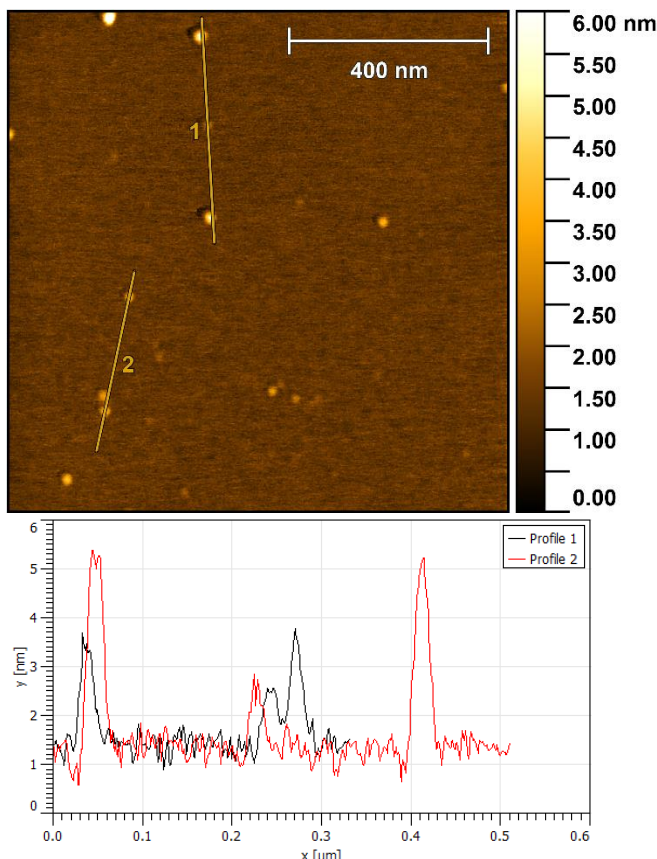


Figure 94 - AFM images and height profiles of CDs eluted from $\text{SiO}_2(11)\text{-NH}_2\text{@CDs-600}$

The XRD profiles of the CDs received in nanoreactors have a well-defined single diffraction peak centered at 23.2° , suggesting that the carbonizing of CA would produce graphite structures [238]. XRD of conventional CDs-200 obtained by pyrolysis of CA at 200°C during 180 min, Figure 64 revealed much broader 2θ patterns, suggesting so less-organized hexagonal graphite structure.

7.25. Photoluminescence of CDs obtained in nanoreactors

All CDs eluted from SiO_2 hosts exhibit emission band centered at 447 nm, Figure 12. The band intensity essentially depends on the time of $\text{SiO}_2\text{@CA}$ thermal treatment and reaches its maximum for CDs obtained from $\text{SiO}_2\text{@CDs-60}$ (Figure 95a-c). The PL band symmetry of CDs deteriorates with increasing of the maternal host pore size, reviling short-wavelength shoulder, Figure 95d.

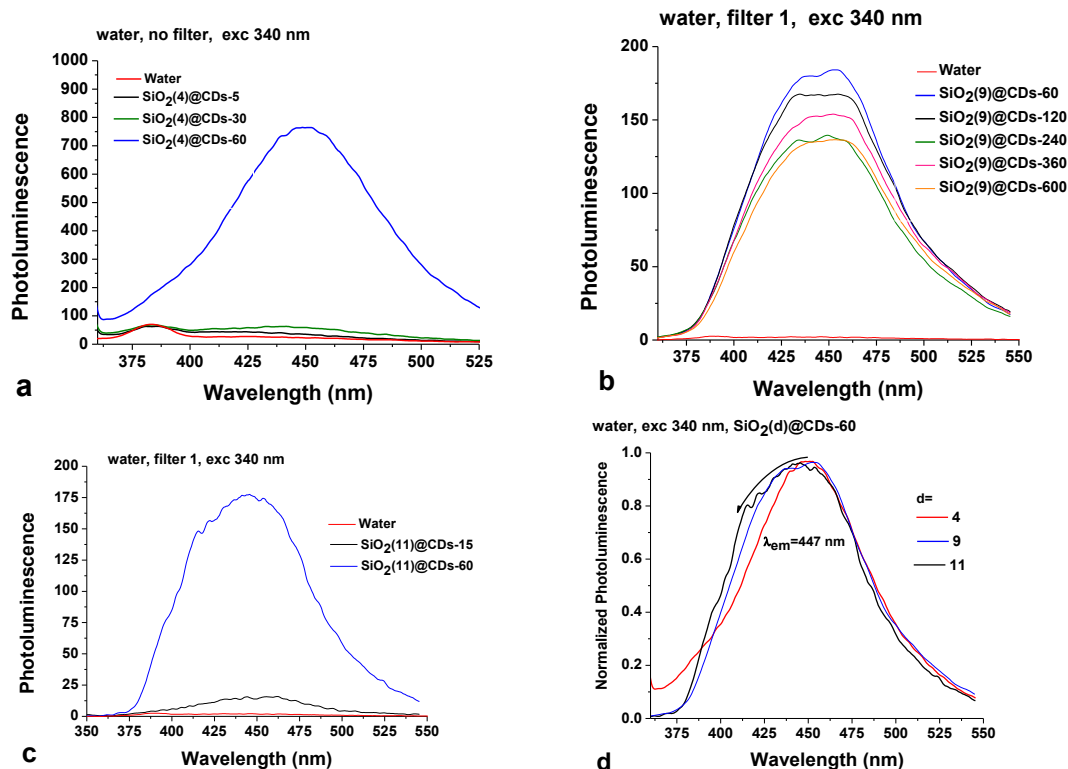


Figure 95 - Photoluminescence emission spectra of the first supernatant obtained by the washing of $\text{SiO}_2(d)@\text{CDs}-\tau$ with water (a-c), and normalized PL spectra of $\text{SiO}_2(d)@\text{CDs}-60$ for $d = 4, 9$, and 11 (d)

This observation is in consensus with those obtained for $\text{SiO}_2@\text{CDs}$ (Figure 85) and can indicate the formation of less decarboxylated CDs for small treatment time (less than 60 min) in silica gel with larger pores.

Photoluminescent spectra of as-prepared CDs show resemblance with PL spectra of $\text{SiO}_2\text{-NH}_2@\text{CDs}$ (Figure 88): both spectra demonstrate wide emission band where two maxima at 428 and 450 nm can be distinguished, Figure 96. It seems encapsulation does not change PL properties of water extracted CDs. These CDs can be easily and completely removed from $\text{SiO}_2\text{-NH}_2@\text{CDs}$ by water (Figure 91), which evidence suggests that these particles are unbound with the template surface.

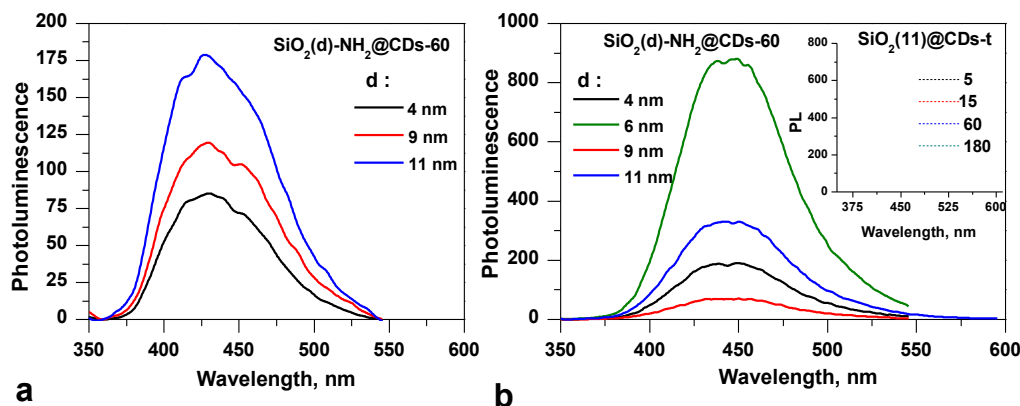


Figure 96 - PL spectra of water extracted CDs(a) and CDs (b) obtained after removing of solid support in $\text{SiO}_2(\text{d})\text{-NH}_2\text{@CDs}$ and $\text{SiO}_2(11)\text{@CDs-t}$. The excitation wavelength of 340 nm

All CDs encapsulated in $\text{SiO}_2\text{@CDs}$ are unbound and can be washed out from the nanocomposite with water. It can be seen from very weak PL of dissolved $\text{SiO}_2\text{@CDs}$ samples after they were exhaustively washed with water, Figure 96b (inset). In contrast to $\text{SiO}_2\text{@CD}$, CDs obtained by dissolving of $\text{SiO}_2\text{-NH}_2\text{@CDs}$ demonstrate strong PL emission with one maximum at 445 nm. The position of the maximum is constant and does not depend on the size of the template pores and time of CDs synthesis, (Figure 96b). In contrast to solid PL intensity of $\text{SiO}_2(4)\text{-NH}_2\text{@CDs}$ and $\text{SiO}_2(4)\text{@CDs}$, PL of CDs rises with time preparation and after 120-200 min it stabilizes.

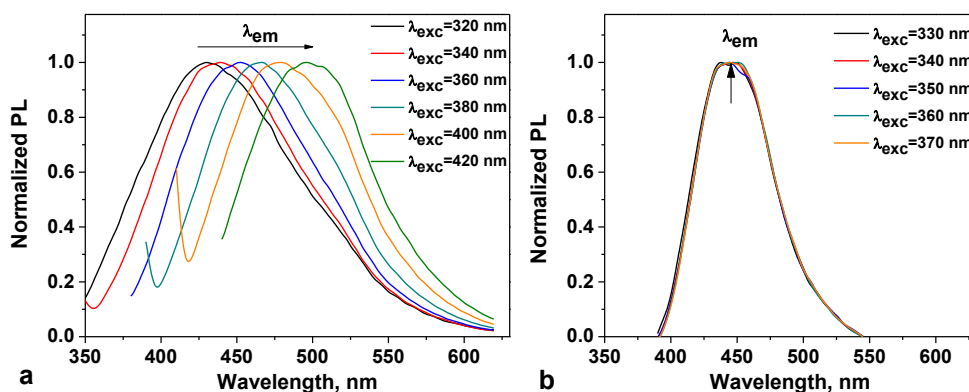


Figure 97 - Normalized PL spectra of CDs-200(a) and CDs after etching of $\text{SiO}_2(4)\text{-NH}_2\text{@CDs-240}$ (b)

Luminescent properties of CDs obtained after removal of solid support were compared with the conventional one. The results, presented in Figure 97 demonstrate

that, in contrast to convenient CDs, the CDs obtained by dissolving of $\text{SiO}_2\text{-NH}_2\text{@CDs}$ exhibit excitation-independence profile with maximum emission at 445 nm.

Excitation-independence emission behavior of CDs obtained by dissolving of $\text{SiO}_2(11)\text{-EDA@CDs-180-600}$ exhibit non-changed peak position at 460 nm upon excitation 320-400 nm. The red-shift in maximum position from 445 nm to 460 nm was observed by changing the functionality of nanoreactor from aminopropyl to ethylenediamine moieties. However, an excitation-independence character was salvaged.

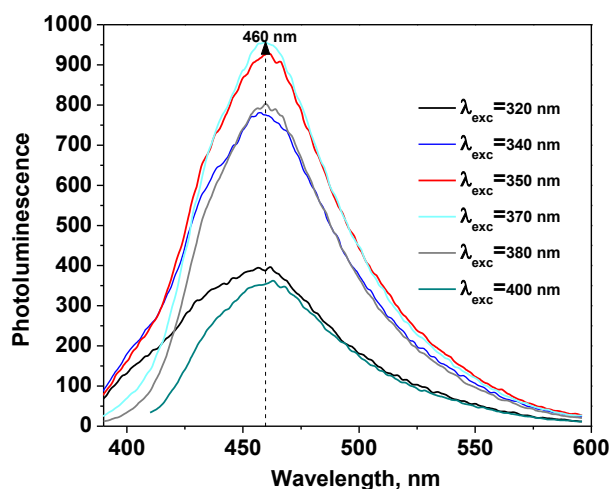


Figure 98 - PL spectra of CDs after etching of $\text{SiO}_2(11)\text{-EDA@CDs-180-600}$

7.26. Quantum Yield

Quantum yield was determined for CDs obtained from $\text{SiO}_2(\text{d})\text{@CDs-t}$, $\text{SiO}_2(\text{d})\text{-NH}_2\text{@CDs-t}$ thermally treated for $t=60\text{--}600$ min by the single-point method (equation 1.32) and $\text{SiO}_2(11)\text{-EDA@CDs-T-t}$ by single-point method (equation 1.32) and a comparative method (equation 1.33). The results presented in Table 4 demonstrate that the CDs obtained in $\text{SiO}_2(\text{d})\text{-NH}_2$ host exhibited higher QY than in SiO_2 . QY upon excitation at 350 nm showed higher QY at 340 nm. In addition, QY of CDs released after dissolving of silica support, showed some improvement in QY than in water elution.

Table 34 - QY of CDs obtained from SiO₂(4)@CDs-720, SiO₂(d)-NH₂@CDs-t by single-point method

Sample	Eluent	QY at 340 nm, %	QY at 350 nm, %
SiO ₂ (4)@CDs-720	Water	0.03	
SiO ₂ (4)-NH ₂ @CDs-720	Water	1.24	
SiO ₂ (4)-NH ₂ @CDs -30	NaOH, 3 mol L ⁻¹	2.79	3.88
SiO ₂ (6)-NH ₂ @CDs -15	NaOH, 3 mol L ⁻¹		16.85
SiO ₂ (6)-NH ₂ @CDs -60	NaOH, 3 mol L ⁻¹		6.28
SiO ₂ (6)-NH ₂ @CDs -180	NaOH, 3 mol L ⁻¹		3.61
SiO ₂ (9)-NH ₂ @CDs-15	NaOH, 3 mol L ⁻¹	4.68	
SiO ₂ (9)-NH ₂ @CDs-60	NaOH, 3 mol L ⁻¹	2.52	
SiO ₂ (9)-NH ₂ @CDs-120	NaOH, 3 mol L ⁻¹	2.12	
SiO ₂ (9)-NH ₂ @CDs-240	NaOH, 3 mol L ⁻¹	1.38	
SiO ₂ (9)-NH ₂ @CDs-360	NaOH, 3 mol L ⁻¹	1.85	
SiO ₂ (9)-NH ₂ @CDs-600	NaOH, 3 mol L ⁻¹	0.60	
SiO ₂ (11)-NH ₂ @CDs-15	NaOH, 3 mol L ⁻¹	5.04	
SiO ₂ (11)-NH ₂ @CDs-30	NaOH, 3 mol L ⁻¹	4.01	
SiO ₂ (11)-NH ₂ @CDs-60	NaOH, 3 mol L ⁻¹	2.99	
SiO ₂ (11)-NH ₂ @CDs-120 (replica 1)	NaOH, 3 mol L ⁻¹	2.31	
SiO ₂ (11)-NH ₂ @CDs-120 (replica 2)	NaOH, 3 mol L ⁻¹	2.56	
SiO ₂ (11)-NH ₂ @CDs-240	NaOH, 3 mol L ⁻¹	2.03	
SiO ₂ (11)-NH ₂ @CDs-420	NaOH, 3 mol L ⁻¹	1.98	

However, the best QY was obtained after water washing of SiO₂(11)-EDA@CDs-150-600 and SiO₂(11)-EDA@CDs-180-600, Table 35. A single-point method and a comparative method showed closed values and the highest one corresponds to SiO₂(11)-EDA@CDs-150-600. In addition, pH influence on QY (single-point method) was analyzed, Figure 99. QY of CDs from SiO₂(11)-EDA@CDs-150-600 increased in pH range 1-7.5 and then decreased up to 50% at pH 11. QY of CDs from SiO₂(11)-EDA@CDs-180-600 increased in pH range 1-4 and then almost hold constant value 12-14% from pH 4 to 12.

Table 35 - QY at 350 nm of water extracted CDs from SiO₂(11)-EDA@CDs-T-t

Samples	QY (Equation 1.32), %	QY (Equation 1.33), %
SiO ₂ (11)-EDA@CDs-150-600	90	71
SiO ₂ (11)-EDA@CDs-180-600	18	14

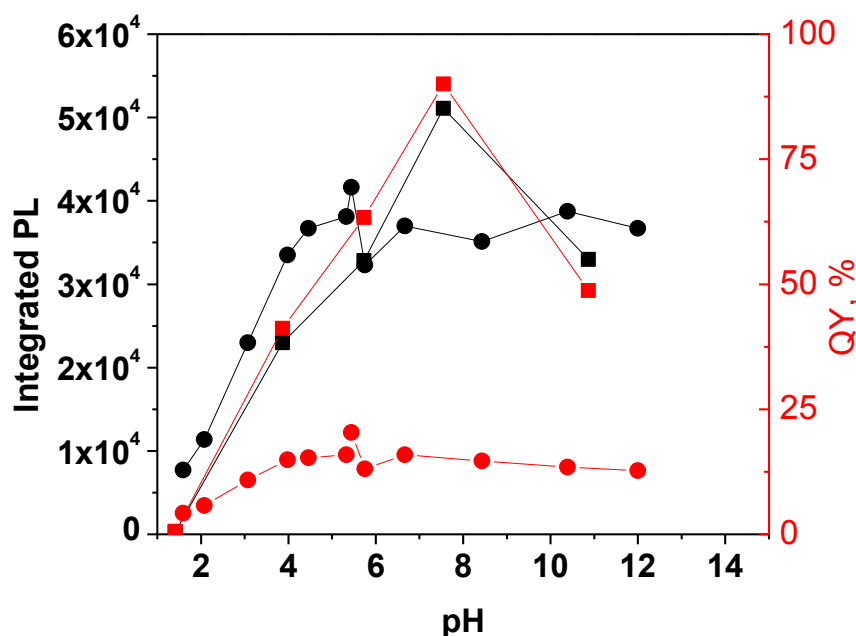


Figure 99 - Integrated PL intensity (black line) and QY (red line) of extracted CDs-150 (sphere) and CDs-180 (square) at different pH.

7.27. Conclusions for Chapter 7

- 1) It was proven that rinsing of silica-based@CA with ether allows manipulating with CA loading into the host pores.
- 2) XPS spectra of silica-embedded CDs suggest the formation of partly decarboxylated carbon nanoparticles.
- 3) In silica gel with larger pores, a short time (less than 100 min) of SiO₂@CA pyrolysis resulted in the formation of the particles, which exhibit strong blue-shifted PL with a maximum at 420 nm.
- 4) Increasing of pyrolysis time leads to the formation of luminescent solids with red-shifted (450 nm) PL.
- 5) These particles eluted with water demonstrate PL at 447 nm. Time of SiO₂@CA thermal treatment has no visible effect on CDs PL, except those obtained for very short (less than 60 min) time of the pyrolysis.
- 6) Summarizing the results of FTIR, XPS TEM and PL spectroscopy it can be concluded that CDs are firmly bound to silica surface due to the formation of a

covalent amide bond with immobilized amino-silanes. Thus, they can be considered as N-doped C-dots, while unbound CDs can be pure carbogenic particles.

- 7) The excitation- independent PL has resulted from a similarity in the surface chemistry for all of the CDs. Excitation-independent PL makes CDs attractive for the development of optical sensors and bioimaging.
- 8) Increasing the template pore size from 4.9 up to 9.1 nm has no effect on the size of CDs, which remains constant at about 5 nm.
- 9) The PL emission of CDs obtained from $\text{SiO}_2\text{-NH}_2\text{@CDs-t}$ (for $t > 120$ min) also remains constant regardless of the template pore size. This makes the proposed methodology of CDs preparation very robust.
- 10) QY of CDs eluted from $\text{SiO}_2\text{-EDA@CDs}$ composites show enhancing up to 18-90% comparing to $\text{SiO}_2\text{@CDs}$ and $\text{SiO}_2\text{-NH}_2\text{@CDs}$.

8. Application of nanocomposites for SPE preconcentration of anthracene

Solid-phase extraction is one of the most popular sample preparation methods. The selection of the appropriate extraction system is an important stage in the elaboration of the analytical procedure. In this case, the knowledge of the interactions between isolated compounds, sorbent and elution solvents seems to be important.

Continuous extraction on fixed bed adsorbent is the type of technique in which the contact between adsorbate and adsorbent has mainly occurred in dynamic conditions. The performance of SPE fixed-bed column is studied by breakthrough curves, i.e., a representation of the pollutant-effluent concentration versus time or volume profile in SPE cartridge. From this profile, the extraction ability of sorbents in SPE cartridge is evaluated, particularly: (i) the bed capacity; (ii) the volume of sample loaded, (iii) the nature and volumes of conditioning solvents and eluents. The breakthrough point is usually defined as the point when the ratio between outlet concentration - C and initial concentration - C_0 of analyte becomes > 0.10 . In industrial application, the adsorbent from the column is usually replaced when the ratio $C/C_0 = 0.50$ ($V_{50\%}$ or $C_{50\%}$). The dynamic capacity of the column is calculated for $C_{50\%}$ [357]. After $C_{50\%}$ the column can still operate until the ratio $C/C_0 = 0.90$. This point is termed as the operating limit of the column. The column will be completely exhausted when the pre-determined inlet concentration is almost equal to the outlet concentration ($C/C_0=1$).

8.1. Adsorption of anthracene on SPE cartridges from the organic mobile phase

All SPE cartridges were prepared equally using 200 mg of the adsorbent. The seed of the mobile phase was limited as 1 mL min^{-1} . Next cartridges were studied for anthracene adsorption: 1) C18 (standard), 2) $\text{SiO}_2(11)\text{-EDA@CDs-150-600}$, 3) $\text{SiO}_2(11)\text{-EDA@CDs-180-600}$, 4) $\text{SiO}_2(11)\text{-Ant-5b}$, 5) $\text{SiO}_2(4)\text{-GOQDs}$, 6) $\text{SiO}_2(11)\text{-Ant-1}$, and 7) $\text{SiO}_2(4)\text{-NH}_2\text{@CDs-200-600}$.

As it was mentioned in the chapter 2.2, the most difficult and ambitious task is adsorbents that can extract aromatic compounds from organic solvents. There is no problem to extracting non-polar PAHs from an aqueous solution. Due to high

lipophilicity of PAHs they are easily removed by conventional hydrophobic adsorbents, like C18. PAHs are practically insoluble in water, so their determination in aqueous solutions is not reliable. In contrast, PAHs is very easily concentrated in fats and oils. If they are analyzed in such objects, separation of fatty macro components from PAHs is required. Common C18 column has no selectivity towards PAHs and thus the SPE column is quickly saturated. Therefore, it was crucial to study PAHs adsorption from organic solvents like acetonitrile, acetone, hexane, which are commonly used for sample preparation. In this research, anthracene has been used as a model compound because it possesses the same properties as other PAHs but has the smallest conjugated system of aromatic rings and thus weakest affinity to the adsorbents with specific π - π interaction. In other words, if the proposed adsorbent extracts anthracene, it will surely extract other PAHs.

The results of anthracene adsorption from acetonitrile solution on all studied SPE cartridges in dynamic conditions are presented in Figure 100. First, the breakthrough curves were analyzed, Figure 100a.

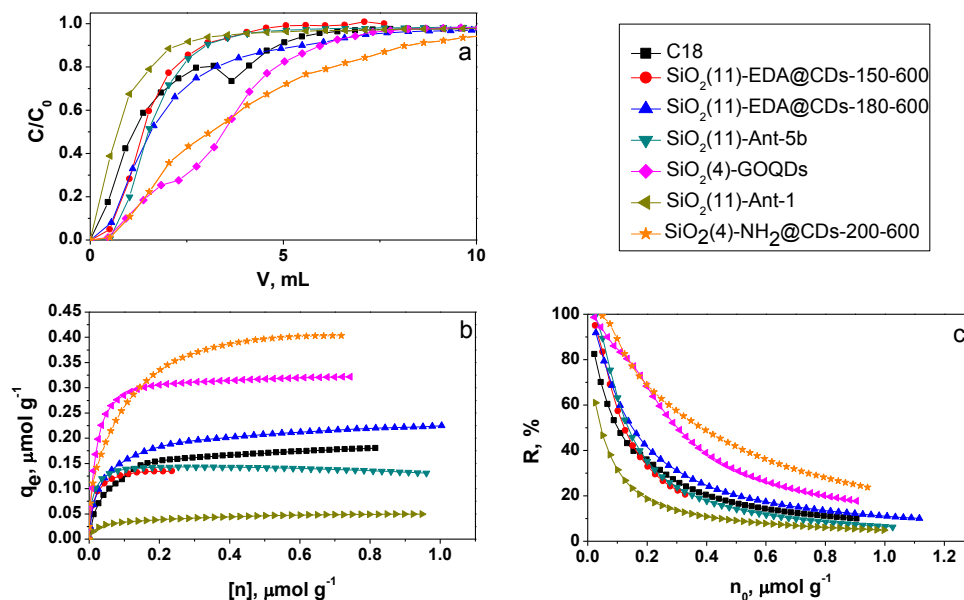


Figure 100 – Adsorption of anthracene from MeCN in dynamic conditions on various SPE cartridges: a) the breakthrough curves, b) dynamic adsorption capacity of SPE the cartridges, c) adsorption rate (R , %). The adsorbent mass 200 mg, anthracene concentration $1 \cdot 10^{-5} \text{ mol L}^{-1}$

From Figure 100 presented it can be seen that all SPE cartridges demonstrate similar breakthrough curves, except those with carbon nanoparticles (SiO₂(4)-GOQDs

and $\text{SiO}_2(4)\text{-NH}_2@\text{CDs-200-600}$). They also demonstrate two-times higher total capacity than C18 cartridge, Figure 100b. Maximum operation capacity ($C_{90\%}$) of the adsorbents decreases in the next order: $\text{SiO}_2(4)\text{-NH}_2@\text{CDs-200-600} > \text{SiO}_2(4)\text{-GOQDs} > \text{SiO}_2(11)\text{-EDA}@\text{CDs-180-600} > \text{C18} > \text{SiO}_2(11)\text{-Ant-5b} > \text{SiO}_2(11)\text{-EDA}@\text{CDs-150-600} > \text{SiO}_2(11)\text{-Ant-1}$. The adsorbents with immobilized anthracenes demonstrated the lowest capacity and lowest adsorption affinity towards anthracene in solution.

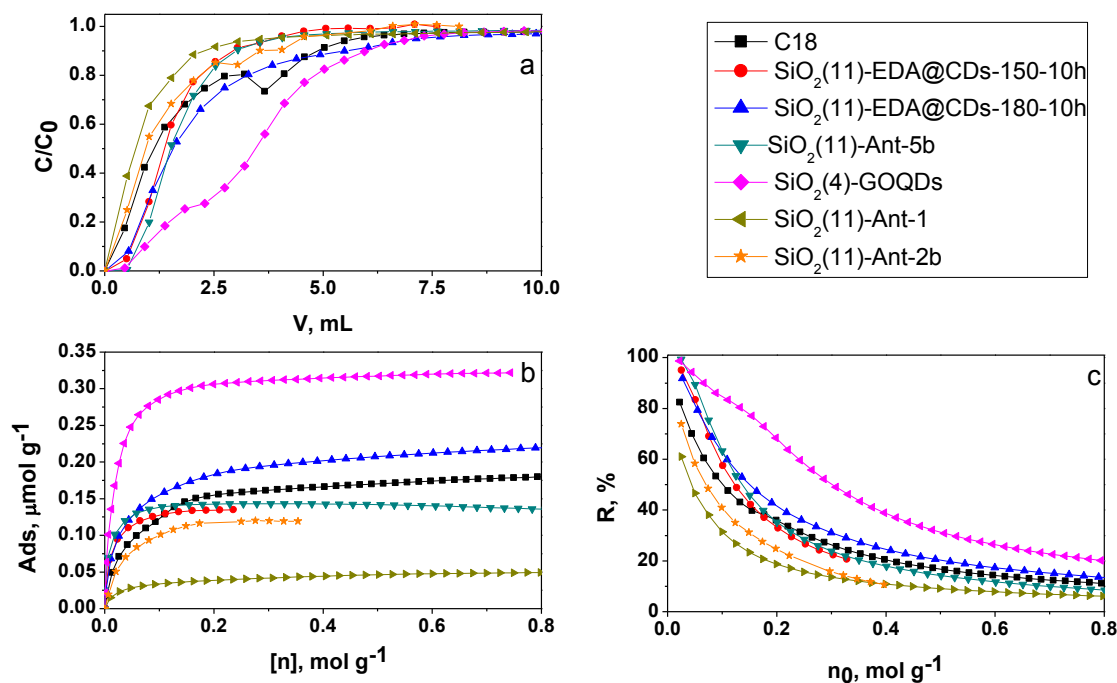


Figure 101 - Adsorption of anthracene from acetone in dynamic conditions on various SPE cartridges: a) the breakthrough curves, b) dynamic adsorption capacity of SPE the cartridges, c) adsorption rate ($R, \%$). The adsorbent mass 200 mg, anthracene concentration $1 \cdot 10^{-5} \text{ mol L}^{-1}$

Adsorption of anthracene from acetone solution on experimental SPE cartridges is about the same as from acetonitrile (Figure 101), except for $\text{SiO}_2(4)\text{-NH}_2@\text{CDs-200-600}$, which demonstrates about the same capacity as C18, Figure 101b.

From the breakthrough curves, fundamental parameters of SPE cartridges were calculated and summarized in Table 36.

Table 36 - Parameters of SPE cartridges used for dynamic adsorption of anthracene.

Adsorbent	V _{10%} , mL	V _{50%} , mL	V _{90%} , mL	C _{10%} , nmol g ⁻¹	C _{50%} , nmol g ⁻¹	C _{90%} , nmol g ⁻¹	K _d , mL g ⁻¹
From 100% MeCN							
C18	0.27	1.1	4.8	12.8	52.0	229	2260
SiO ₂ (11)-EDA@CDs-150-10h	0.62	1.34	2.8	31.0	67.0	140	2700
SiO ₂ (11)-EDA@CDs-180-10h	0.62	1.53	5.3	31.0	76.0	263	2965
SiO ₂ (11)-Ant-5b	0.73	1.49	3.1	36.0	74.0	153	3163
SiO ₂ (4)-GOQDs	0.9	3.45	6.0	43.0	164	286	3290
SiO ₂ (11)-Ant-1	0.12	0.71	2.2	6.0	35.0	108	1770
SiO ₂ (11)-NH ₂ @CDs-200-10h	0.85	2.97	8.4	42	145	410	3469
From 100% acetone							
C18	0.28	1.12	4.8	13.8	55.3	237	1694
SiO ₂ (11)-EDA@CDs-150-10h	0.62	1.35	3.3	31.0	67.3	165	1602
SiO ₂ (11)-EDA@CDs-180-10h	0.57	1.6	5.5	29.0	79.4	273	1425
SiO ₂ (11)-Ant-5b	0.77	1.50	3.3	40.0	74.0	163	2291
SiO ₂ (4)-GOQDs	0.92	3.46	6.0	44.3	167	289	1901
SiO ₂ (11)-Ant-1	0.15	0.70	2.3	7.4	34	113	1532
SiO ₂ (11)-Ant-2b	0.22	0.92	3.3	11.0	45	161	2225

The results presented allow analyze tendencies for the adsorbents of the same class. For example, the affinity of CDs-containing adsorbent towards anthracene is increased with the temperature of the particle preparation from SiO₂(4)-NH₂@CDs-150-600 to SiO₂(4)-NH₂@CDs-200-600, Figure 100. The same is observed for SiO₂(11)-EDA@CDs, Figure 101. SiO₂(11)-EDA@CDs-180-600 has on 50% higher capacity and affinity to adsorb anthracene than SiO₂(11)-EDA@CDs-150-600, Table 36. As it was mentioned in chapter 2.3, higher temperature of the thermal treatment promotes the formation of basal graphene structure with less defected sp² conjugated aromatic system. Such systems have higher density of π -electrons, and thus stronger tendency to form π - π stacking complexes. This results in increasing affinity towards PAHs.

Among three adsorbents with immobilized anthracene-derivatives, having equal pore size, column capacity is increased in next order SiO₂(11)-Ant-5b > SiO₂(11)-Ant-

2b > SiO₂(11)-Ant-1. It can be related to higher number of anthracenes loading via Schiff base than N-alkylation.

From linear area of the dynamic adsorption curve distribution coefficients (K_d) of anthracene was calculated for selected adsorbents. The results are presented in Table 36. Generally speaking, K_d of anthracene in acetone are lower than those in acetonitrile. For example, K_d for SiO₂(4)-GOQDs in acetone is 1901 mL g⁻¹, while in MeCN is 3290 mL g⁻¹.

8.2. Anthracene adsorption from mixed-solvent systems

Commonly for SPE preconcentration of apolar compounds mixed solvent systems have been used. Water in these mixed solvent systems is used to increase the distribution coefficient and thus recovery degree of the analyte. In this research, we also studied the most common solvent mixture such as MeCN:water =50:50 v/v, Figure 102.

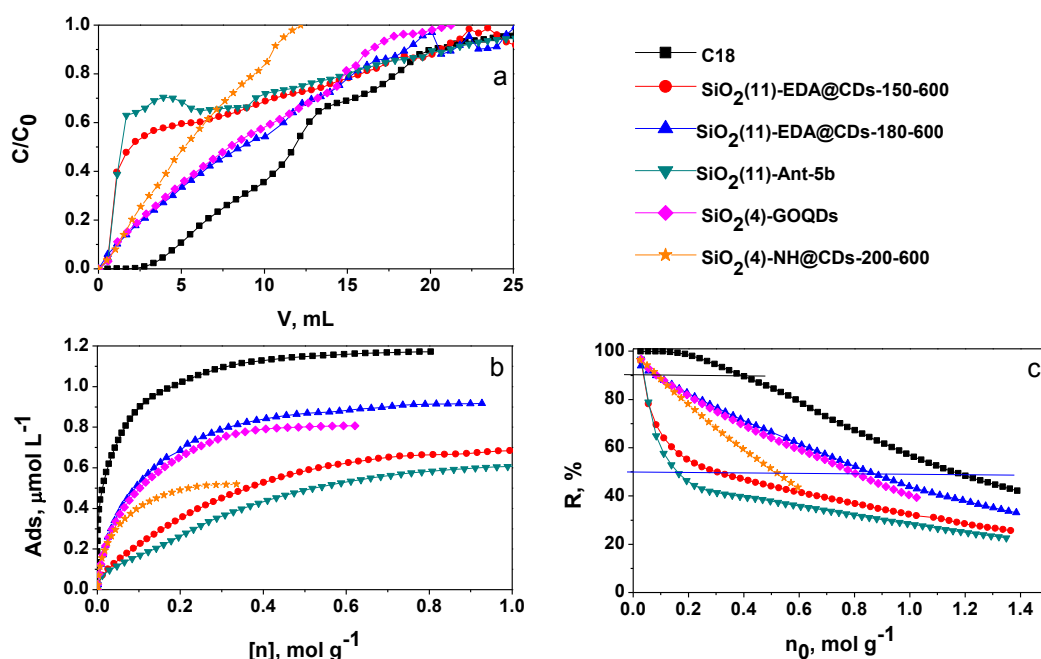


Figure 102 - Adsorption of anthracene from MeCN:H₂O=50:50 with pH=3.0 in dynamic conditions on various SPE cartridges: a) the breakthrough curves, b) dynamic adsorption capacity of SPE the cartridges, c) adsorption rate (R, %). The adsorbent mass 200 mg, anthracene concentration $1 \cdot 10^{-5}$ mol L⁻¹

As it was expected addition of polar solvent essentially increased K_d for all adsorbent toward apolar anthracene (Table 39), but the most pronounced increase was

observed for C18 adsorbent. The K_d value for this adsorbent is amplified in more than 2 times while for others as maximum as 1.5 times. As a result, C18 adsorbent became more efficient in the extraction of individual anthracene from acetonitrile/water mixture than the proposed adsorbents, Figure 102.

Table 37 - Dynamic adsorption parameters from the breakthrough curves

Adsorbent	V _{10%} , mL	V _{50%} , mL	V _{90%} , mL	C _{10%} , nmol g ⁻¹	C _{50%} , nmol g ⁻¹	C _{90%} , nmol g ⁻¹	K _d , mL g ⁻¹
MeCN:water = 50:50, pH=3							
C18	4.85	11.8	20	239	582	987	4866
SiO ₂ (11)-EDA@CDs-150-600	0.67	1.9	19.9	33	95	993	3123
SiO ₂ (11)-EDA@CDs-180-600	1.22	8.6	18.5	61	427	918	4284
SiO ₂ (11)-Ant-5b	0.67	1.3	19.9	33	64	981	2923
SiO ₂ (4)-GOQDs	1.22	7.9	16.4	59	256	791	3990
SiO ₂ (11)-NH ₂ @CDs-200-600	1.22	5.3	11	60	259	537	3826
MeCN:water = 50:50, pH=6							
C18	3.9	7.8	20	192	384	986	5046
SiO ₂ (11)-EDA@CDs-150-600	0.9	4.9	15.9	45	244	793	4052
SiO ₂ (11)-EDA@CDs-180-600	0.6	1.7	19.6	30	84	973	3086
SiO ₂ (11)-Ant-5b	0.7	1.4	22.3	35	69	1100	2837
SiO ₂ (4)-GOQDs	1.4	7.8	22.5	68	376	1085	4554
SiO ₂ (11)-NH ₂ @CDs-200-600	0.7	3.0	7.1	34	146	347	3540

The total adsorption capacity of C18 cartridge is increased in about 3 times, indicating the essential impact of hydrophobic interaction between the adsorbent and analyte. Consequently, the addition of water to mobile phase levels selectivity of the proposed adsorbents raising from to π - π stacking interaction and increases non-specific hydrophobic interaction for all adsorbents.

Since driving forces of anthracene adsorption in the water-containing mobile phase is dispersive interaction, properties of the adsorbents shall not very much depend on the media pH. Indeed, as it can be seen from Figure 103, changing of the media pH from 3 to 6 does not essentially change characteristics of the cartridges, Figure 102. With changing of pH distribution coefficients of the adsorbents have changed within error.

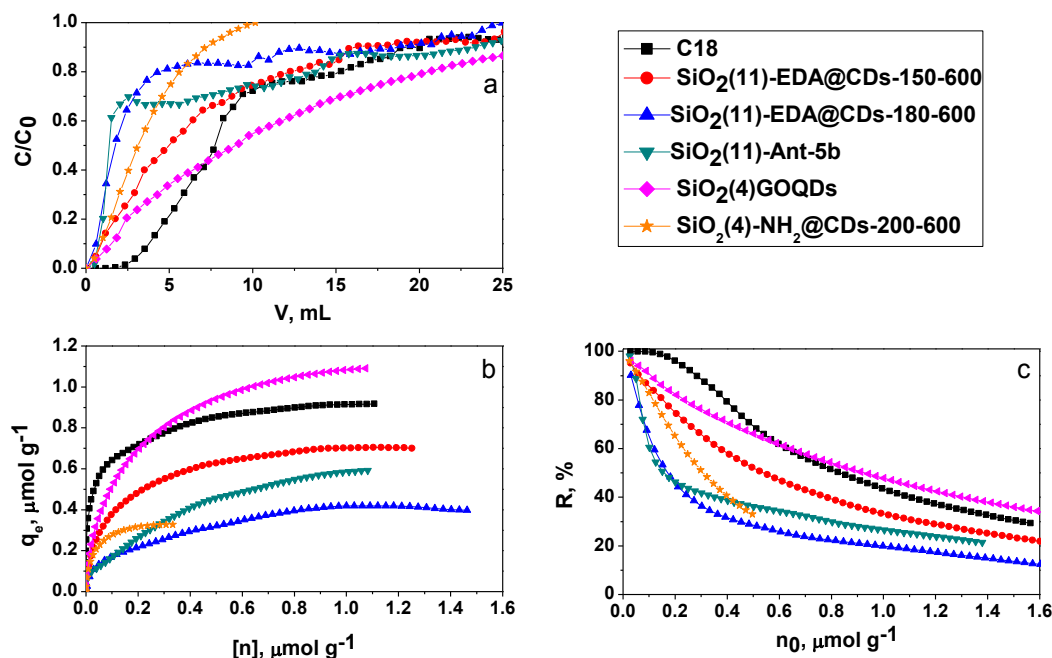


Figure 103 - Adsorption of anthracene from MeCN:H₂O=50:50 with pH=6.0 in dynamic conditions on various SPE cartridges: a) the breakthrough curves, b) dynamic adsorption capacity of SPE the cartridges, c) adsorption rate (R , %). The adsorbent mass 200 mg, anthracene concentration $1 \times 10^{-5} \text{ mol L}^{-1}$

8.3. Adsorption of anthracene form solution with interfering compounds

As it was indicated an earlier major problem in the determination of PAHs is an analysis of objects with a high content of lipophilic compounds such as vegetable oils, for example. Contamination of vegetable oil with PAHs is a perfect indication of its quality and also can be used to identify the origin of oil production. Vegetable oil is composed primarily by triacylglycerols and phospholipids.

In the current research, we investigated next two model samples contaminated with anthracene: 1) myristic acid, C₁₃H₂₇COOH (MY) and 2) sample of sunflower commercial vegetable oil.

MY is the third most common saturated fat in the oil [358]. It is soluble in acetonitrile and in small concentration in water-containing solvent mixtures. Therefore, MY was used as a model component. Due to the low solubility of MY in MeCN:H₂O solvent mixture $2 \times 10^{-5} \text{ mol L}^{-1}$ solution of MY was prepared in MeCN:H₂O (50:50, v/v, pH=3). The solution was contaminated with $2 \times 10^{-5} \text{ mol L}^{-1}$ of anthracene.

On this stage of the experiment, we wanted to confirm that high content of water in the liquid phase can change the mechanism of adsorption and evaluate these changings for commercial and proposed adsorbents. Particularly we expected that lipophilic component of the mixture (MY) will saturate corresponding centers of non-specific adsorption and thus reveal the specific ones in the proposed adsorbents.

In fact, the expectations were implemented only partly. Indeed, in a diluted solution of MY total adsorption capacity of C18 cartridge toward anthracene is reduced about 1.5 times (Figure 104b), and 90% anthracene recovery (C10%) is also reduced in more than 1.5 times (compare Figure 102c and Figure 104c).

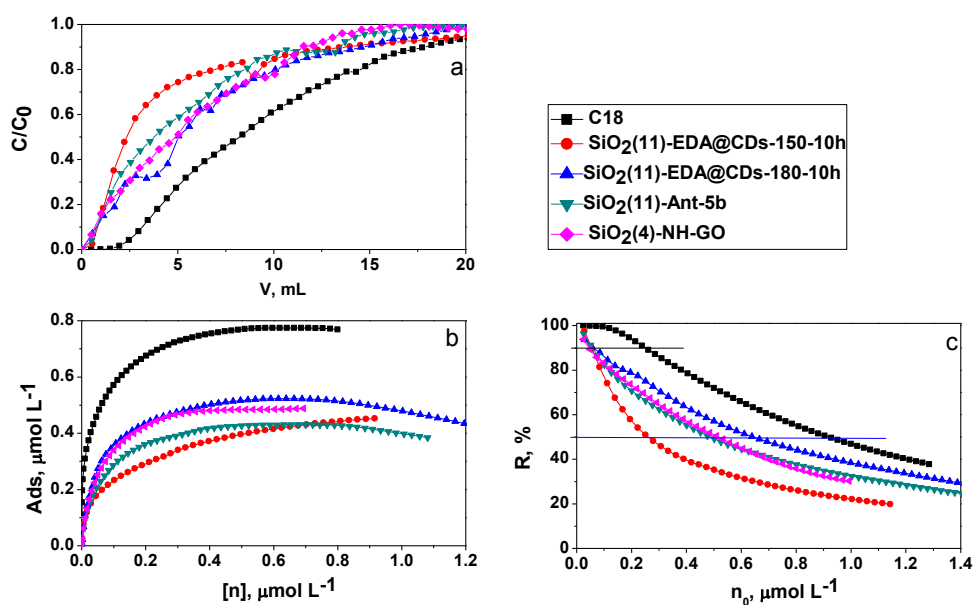


Figure 104 - Dynamic adsorption of anthracene from $2 \cdot 10^{-5} \text{ mol L}^{-1}$ MY solution in $\text{MeCN:H}_2\text{O}=50:50$ with $\text{pH}=3.0$, contaminated with $1 \cdot 10^{-5} \text{ mol L}^{-1}$ of anthracene: a) the breakthrough curves, b) dynamic adsorption capacity of SPE the cartridges, c) adsorption rate (R , %). The adsorbent mass 200 mg, anthracene concentration $1 \cdot 10^{-5} \text{ mol L}^{-1}$.

These results were predicted from the experiment with the individual solution of anthracene (chapter 8.2). But the aim of the current research was to analyze the influence of interfering reagent on capacity and affinity of the adsorbents towards anthracene. This analysis can be made by the comparison of the dynamic adsorption parameters presented in Table 38, for example, C50%. By comparison of Figure 102c and Figure 104c it can be seen that in MY solution C50% for anthracene expectedly reduced for about 20% but for the proposed adsorbents its remained unchanged

(SiO₂(11)-EDA@CDs-180-600) or even increased on 66% (for SiO₂(11)-Ant-5b) and 25% (for SiO₂(11)-EDA@CDs-150-600).

Table 38 - Dynamic adsorption parameters from the breakthrough curves

Adsorbent	V _{10%} , mL	V _{50%} , mL	V _{90%} , mL	C _{10%} , nmol g ⁻¹	C _{50%} , nmol g ⁻¹	C _{90%} , nmol g ⁻¹	K _d , mL g ⁻¹
MeCN:water (50:50), pH=3							
C18	3.2	8.1	18.2	158	400	898	3856
SiO ₂ (11)-EDA@CDs-150-600	0.8	2.3	14.0	39	115	698	3378
SiO ₂ (11)-EDA@CDs-180-600	0.8	5.0	15.0	39	248	744	3512
SiO ₂ (11)-Ant-5b	0.8	3.8	11.6	38	185	564	3061
SiO ₂ (4)-GOQDs	0.8	5.0	12.1	38	241	584	3252

It is well agreed with the conclusion made above about dominating of non-specific hydrophobic interaction for the adsorbents bearing hydrophobic moieties immobilized. Consequently, MY is interfered with active sides of such adsorbents and reduce their capacity and affinity. However, in the case of anthracene-containing adsorbents total loading of anthracene is small and thus overall lipophilicity of the adsorbent is also small. Therefore SiO₂(11)-Ant-5b has modest total capacity toward anthracene

(185 nmol g⁻¹) but higher selectivity. The K_d of anthracene in MY solution even increased from 2923 to 3061 mL g⁻¹, Table 38. Similar conclusions can be made for the adsorbents with immobilized quantum dots. Particularly, SiO₂(11)-EDA@CDs-180-10h is more hydrophobic than SiO₂(11)-EDA@CDs-150-10h (see chapter 8.1) thus it has higher K_d of anthracene (Table 38). But for the same reason in MY solution C_{50%} of anthracene has increased for more hydrophilic adsorbent - SiO₂(11)-EDA@CDs-150-600 with specific active sites for π - π interaction.

Next general conclusion that can be made from the experiment performed above: for selective adsorption of aromatic compounds from lipid-containing objects using water-containing mobile phase it is essential to use the adsorbents with reduced hydrophobicity, having specific sites of π - π interactions.

The second part of the research was devoted to real samples of vegetable oil artificially contaminated with anthracene.

As it is demonstrated in chapter 8.1, to reveal adsorption properties of the proposed adsorbents it is preferably to use water-free solvents for sample preparation. Consequently, based on miscibility properties of solvents with oil, acetone and heptane were used as solvents. Commercial sunflower oil was dissolved in these solvents to prepare 1% (v/v) solution. The solution was spoiled with $1 \cdot 10^{-5} \text{ mol L}^{-1}$ anthracene in the same solvent. Since acetone absorbs UV light, determination of anthracene in this solution was performed at 356 nm.

The results of anthracene adsorption from 1% solution of sunflower oil in acetone is presented in Figure 105.

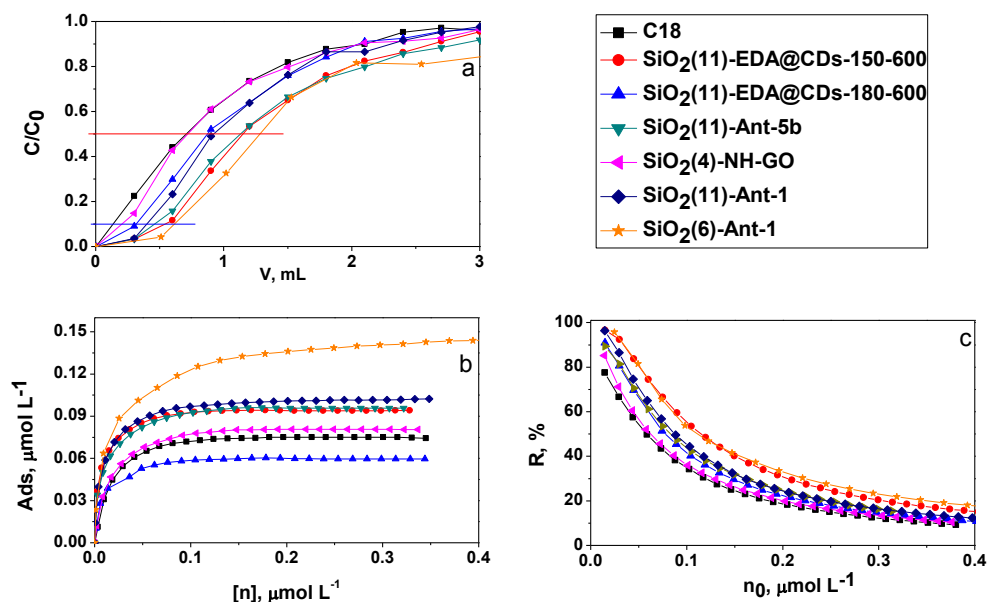


Figure 105 - Dynamic adsorption of anthracene from 1% solution of sunflower oil in acetone, contaminated with $1 \cdot 10^{-5} \text{ mol L}^{-1}$ of anthracene: a) the breakthrough curves, b) dynamic adsorption capacity of SPE the cartridges, c) adsorption rate (R , %). The adsorbent mass 200 mg, anthracene concentration $1 \cdot 10^{-5} \text{ mol L}^{-1}$

The first observation from breakthrough curves presented in Figure 105a that C18 cartridge does not adsorb anthracene from oil solution in acetone. This observation is quite predictable if non-specific adsorption of lipophilic compounds on C18 is considered. Oil matrix saturates active centers of C18 adsorbent and thus anthracene pass the SPE cartridge. Contrary, several from the proposed adsorbents demonstrated much higher than C18 adsorption characteristics such as total adsorption capacity and recovery, Figure 105b-c. For example, $V_{10\%}$ for several proposed adsorbents is 3-6 times higher than for C18 (Table 39).

Table 39 - Dynamic adsorption parameters from the breakthrough curves

Adsorbent	V _{10%} , mL	V _{50%} , mL	V _{90%} , mL	C _{10%} , nmol g ⁻¹	C _{50%} , nmol g ⁻¹	C _{90%} , nmol g ⁻¹	K _d , mL g ⁻¹
Acetone							
C18	0.1	0.7	2.1	6	36	104	1327
SiO ₂ (11)-EDA@CDs-150-600	0.5	1.2	2.6	27	58	131	1600
SiO ₂ (11)-EDA@CDs-180-600	0.3	0.9	2.1	16	43	104	1013
SiO ₂ (11)-Ant-5b	0.5	1.1	2.8	23	56	140	1512
SiO ₂ (4)-GOQDs	0.2	0.7	2.1	10	34	101	1382
SiO ₂ (6)-Ant-1	0.6	1.3	3.7	29	63	178	2733
SiO ₂ (11)-Ant-1	0.4	0.9	2.3	20	46	113	1626
Heptane							
C18	0.1	0.7	2.9	5	35	143	1306
SiO ₂ (11)-Ant-5b	0.9	1.5	4.2	44	74	207	2270
SiO ₂ (6)-Ant-1	1.2	2.8	6.6	57	134	316	3714
SiO ₂ (11)-Ant-2b	0.6	1.8	6	29	88	293	3071

It would seem strange that adsorbents with immobilized anthracene, which demonstrated the worth properties in all previous tests, demonstrate unexpectedly good adsorption properties in the current experiment, Figure 105a. But, would we consider the adsorbent behavior in MY acetonitrile/water solution, it became much clear. In accordance with the results of chemical analysis (Table 24), the SiO₂-Ant adsorbents have 20-40% of immobilized anthracene fragments.

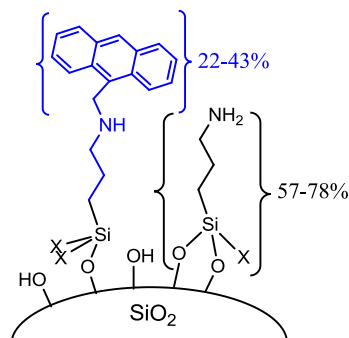


Figure 106 – Composition of the immobilized layer on SiO₂-Ant adsorbents

The rest are polar aminopropyl groups, Figure 106. Therefore, SiO₂-Ant overall hydrophobicity of SiO₂-Ant are very small, and they rather can be attributed to bimodal balanced hydrophobic/hydrophilic adsorbents. In the cases, when adsorption of the aromatics occurs due to non-selective hydrophobic interaction (for example in acetonitrile/water media), SiO₂-Ant demonstrated feeble adsorption properties. Contrary, in low-polar or apolar liquid phases SiO₂-Ant can demonstrate specific adsorption of aromatics due to π - π interaction with the analyte. Hydrophilic surrounding helps to reduce non-specific adsorption of lipid matrix.

Thus anthracene-contained materials can adsorb anthracene more selectively than known SPE cartridges from the oil-containing matrix that makes SiO₂-Ant promising to use in SPE cartridges for determination of PAHs in lipid samples without saponification of them. Maximum dynamic adsorption capacity (C_{90%}) achieved for SiO₂-Ant adsorbents was 101-178 nmol g⁻¹ of anthracene, Table 39.

If our assumption about the mechanism of aromatic adsorption on SiO₂-Ant is actual, these adsorbents shall also uptake PAHs from even less polar solvents than acetone, for example apolar heptane. To verify the proposed adsorption mechanism, 1% solution of commercial sunflower oil was prepared in heptane and spoiled with 1 10⁻⁵ mol L⁻¹ of anthracene. The solution was passed through the SPE cartridges with different SiO₂-Ant adsorbents. The results of the dynamic adsorption of anthracene from the solution are presented in Figure 107.

Indeed, SiO₂-Ant cartridges extract anthracene from heptane solution of oil, while C18 adsorbent is absolutely useless. From Figure 107a it can be seen that SiO₂(6)-Ant-1 and SiO₂(11)-Ant-5b can quantitatively remove anthracene from the solution. The dynamic adsorption capacity of any SiO₂-Ant, as well as adsorption rate,

is higher than that for C18 cartridge (Figure 107b) regardless to the fact that concentration of immobilized groups on C18 phase at least for 2-3 times higher than on SiO₂-Ant. The adsorption results summarized in Table 39 demonstrate that K_d of anthracene in heptane is even higher than in acetone and reached $3.7 \cdot 10^3 \text{ mL g}^{-1}$. This means that SiO₂-Ant can be used for selective pre-concentration of PAHs even from 1% of a solution of oil in heptane, that makes them unique.

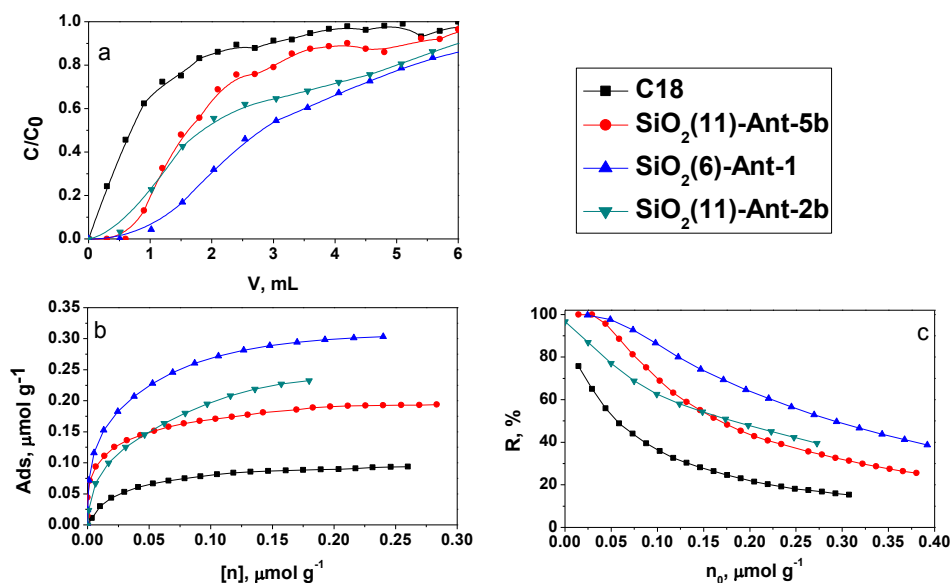


Figure 107 - Dynamic adsorption of anthracene from 1% solution of sunflower oil in heptane, contaminated with $1 \cdot 10^{-5} \text{ mol L}^{-1}$ of anthracene: a) the breakthrough curves, b) dynamic adsorption capacity of SPE the cartridges, c) adsorption rate ($R, \%$). The adsorbent mass 200 mg, anthracene concentration $1 \cdot 10^{-5} \text{ mol L}^{-1}$

The affinity of studied adsorbents to anthracene is decreased in the next order: SiO₂(6)-Ant-1 > SiO₂(11)-Ant-2b > SiO₂(11)-Ant-5b > C18. Values of C50% for heptane solution are in 1.5-2 times higher than for acetone. Therefore, it can be concluded that decreasing of solvent polarity improves the specificity of the adsorbents with π - π mechanism of adsorption.

8.4. Conclusion for Chapter 8

- 1) In MeCN SiO₂-NH₂@CDs and SiO₂(4)-GOQDs showed higher the maximum operating capacity toward anthracene than C18.
- 2) The affinity of CDs-containing adsorbent towards anthracene is increased with the temperature of the particle preparation from SiO₂(4)-NH₂@CDs-150-600 to SiO₂(4)-NH₂@CDs-200-600. The same effect is observed for SiO₂(11)-

EDA@CDs. This effect can be explained by the fact that the higher temperature of the precursor thermal treatment promotes the formation of basal graphene structure in the resulted CDs with less defected sp^2 conjugated aromatic system. Such systems have a higher density of π -electrons, and thus stronger tendency to form π - π stacking complexes.

- 3) With the addition of water to mobile-phase selectivity of the proposed adsorbents toward anthracene is decreased. This was attributed to increasing of non-specific hydrophobic interaction between immobilized groups on the adsorbent surface and the analyte.
- 4) It was demonstrated that π - π stacking interaction with the analyte determine the selectivity of anthracene adsorption on SiO_2 -Ant from acetone and heptane solutions.
- 5) In the presence of the interfering reagent such as MY $C_{50\%}$ of anthracene on C18 cartridge was reduced for about 20%, while the proposed adsorbents demonstrated unchanged or even higher capacity. For example, $C_{50\%}$ for $SiO_2(11)$ -Ant-5b) was increased on 66% and on 25% for $SiO_2(11)$ -EDA@CDs-150-600.
- 6) Several proposed adsorbents demonstrated much higher than C18 adsorption characteristics, such as total adsorption capacity and recovery, in dynamic preconcentration of anthracene from the real sample of sunflower oil.
- 7) The values of K_d for anthracene adsorption on SiO_2 -Ant from heptane solution higher than from acetone, and as high as $3.7 \cdot 10^3$ mL/g. This makes SiO_2 -Ant attractive for selective pre-concentration of PAHs from high lipid content objects, such as vegetable oils.

9. General conclusions

- 1) The concentration of the functional groups on $\text{SiO}_2\text{-NH}_2$ depends on the pore size. The increasing pore size of silica gel from 0 to 11 nm lead to decreasing aminopropyl groups concentration 3.3 to $2.3 \mu\text{mol m}^{-2}$.
- 2) The concentration of grafted functional groups was estimated from CNH, TGA, pH and conductometric titration. According to mean value with a confidence interval, the concentration of aminopropyl groups is lead in range $0.5\text{-}0.96 \text{ mmol g}^{-1}$, while the concentration of mercaptopropyl was found $0.4\text{-}0.62 \text{ mmol g}^{-1}$.
- 3) Kinetics study of surface assembling reaction for $\text{SiO}_2\text{-Ant}$ synthesis by N-alkylation showed that the reaction has finished for 120 min and surface saturation with anthracene fragments reached its maximum. The reaction is good fits the pseudo-second-order model.
- 4) The increasing pore size of silica gel leads to increasing of loading degree of anthracene-derivatives.
- 5) One step immobilization of anthracene-containing organosilane resulted in $\text{SiO}_2\text{-Ant}$ adsorbent with higher loading of the anthracene moieties (up to 33-50%), while surface assembling synthesis of $\text{SiO}_2\text{-Ant}$ resulted in more polar adsorbent with 20-30 % of anthracene fragments.
- 6) Formation of surface excimer complex between two neighbor immobilized anthracene groups can be monitored using solid fluorescence spectroscopy from the intensity of the band at 480 nm related to the presence of anthracene excimer on the silica surface. Excimer on non-porous silica has been formed more quickly than on the porous one.
- 7) It was demonstrated that CDs can be obtained inside of the silica support porous by incomplete pyrolysis of citric acid. This approach can better confine the CDs particle size. Dissolution of the silica support releases the CDs with excitation-independent emission behavior and ensure homogeneous distribution of particles size.
- 8) XPS spectra of silica-embedded CDs suggest the formation of partly decarboxylated carbon nanoparticles. In silica gel with larger pores, a short time (less than 100 min) of $\text{SiO}_2\text{@CA}$ pyrolysis resulted in the formation of the particles,

which exhibit strong blue-shifted PL with a maximum at 420 nm. Increasing of pyrolysis time leads to the formation of luminescent solids with red-shifted (450 nm) PL.

- 9) Excitation-independent PL makes CDs attractive for the development of optical sensors and bioimaging. Increasing the template pore size from 4.9 up to 9.1 nm has no effect on the size of CDs, which remains constant at about 5 nm. The PL emission of CDs obtained from $\text{SiO}_2\text{-NH}_2\text{@CDs-t}$ (for $t > 120$ min) also remains constant regardless of the template pore size. This makes the proposed methodology of CDs preparation very robust.
- 10) CDs eluted from $\text{SiO}_2\text{-EDA@CDs}$ showed enhancing QY up to 90%.
- 11) The CDs-containing adsorbents can be prepared by chemical immobilization of CDs inside of the pores of $\text{SiO}_2\text{-NH}_2$. Summarizing the results of FTIR, XPS TEM and PL spectroscopy it can be concluded that CDs are firmly bound to silica surface due to the formation of a covalent amide bond with immobilized aminosilanes and thus can be used as adsorbents.
- 12) Ultrasonic treatment of GO leads to the introduction of GOQDs on aminosilica gel pores. Silica gel with modified GOQDs demonstrated enlargement in surface area that is important for the analytical application of the resulted material.
- 13) The affinity of CDs-containing adsorbent towards anthracene in the organic medium is increased with the temperature of the particle preparation. It can be explained by the fact that a higher temperature of the thermal treatment promotes the formation of basal graphene structure with less defected sp^2 conjugated aromatic system. Such systems have a higher density of π -electrons and thus a stronger tendency to form π - π stacking complexes. This results in increasing affinity towards PAHs.
- 14) It was proved that selective adsorption of anthracene as a PAHs representative on $\text{SiO}_2\text{-Ant}$ is observed due to π - π interaction of the immobilized molecules. $\text{SiO}_2\text{-Ant}$ can be attributed to bimodal balanced hydrophobic/hydrophilic adsorbents. In low-polar or apolar liquid phases $\text{SiO}_2\text{-Ant}$ can demonstrate specific adsorption of aromatics due to π - π interaction with the analyte. Hydrophilic surrounding helps to reduce non-specific adsorption of lipid matrix.

- 15) SiO_2 -Ant can adsorb PAHs more selectively than known SPE cartridges, particularly from the oil-containing matrix. That makes SiO_2 -Ant promising to use in SPE cartridges for determination of PAHs in lipid samples without saponification of them.
- 16) Silica gel modified with GOQDs was successfully used for the modification of carbon paste electrode. CPE modified with SiO_2 -GOQDs demonstrated enhanced sensitivity towards DES and EST and less profound towards TMP and SMZ. The lowest LOD values were found for EST ($0.009 \mu\text{mol L}^{-1}$). Oxidation peaks for all analytes were shifted to lower potentials for about 100 – 150 mV, demonstrating better interaction between the analytes and active centers of the electrode. This fact was explained by essential π - π stacking interaction between immobilized GOQDs and selected hormones.
- 17) It has been demonstrated that silica gel with immobilized anthracene, GOQDs and CDs moieties can be used as adsorbents for SPE of PAHs from materials with high lipophilic media. The best results can be achieved when the adsorbents applied for extraction of PAHs from apolar solvents such as heptane. Addition of water to the mobile phase can change adsorption mechanism and essentially reduce the adsorbent selectivity.

10. Future work

In this work, three kinds of hybrid materials such as silica gel modified with anthracene groups, graphene oxide quantum dots and carbon dots were synthesized, characterized and evaluated as an adsorbent for solid-phase extraction of anthracene analyte solution in aqueous and oil medium. In addition, CDs with excitation-independent emission and high QY were obtained using a nanoreactor approach. Silica gel modified with graphene oxide quantum dots demonstrates good results for electrochemical determination of antibiotics and hormones as modified carbon paste electrode.

There are several lines of research arising from this work which should be pursued.

- a) Due to enhance adsorption selectivity of silica gel modified with anthracene moieties toward anthracene molecule in oil sample, to develop the methodology of its adsorption from the real sample containing a mixture of PAHs with further detection by chromatographic technique.
- b) Due to the presence of oxidized functional groups onto SiO_2 -GOQDs and SiO_2 - NH_2 @CDs, to examine adsorption efficiency of these SPE cartridges toward other aromatic pollutants such as pesticides.
- c) Based on the possibility to use SiO_2 -GOQDs as carbon paste electrode for detection of biomolecules, Chapter 6.9, to develop a methodology for electrochemical determination of biomolecules in real sample using electrode prepared from SiO_2 -GOQDs and SiO_2 - NH_2 @CDs.
- d) Carbonization process during the synthesis of CDs can lead to the creation of aromatic domains with carboxylic groups and as a result formation complex with metals and aromatic molecules by electron transfer. Because of these features, to investigate using CDs as photoluminescent probes for metals and biomolecules detection.
- e) High QY of prepared CDs can be useful for bioimage application, thus evaluation of the cytotoxicity of CDs is encouraged.

11. References

1. Phillips DH (1999) Polycyclic aromatic hydrocarbons in the diet. 139–147
2. Webster L, Tronczynski J, Korytar P, et al (2010) Determination of parent and alkylated polycyclic aromatic hydrocarbons (PAHs) in biota and sediment. *ICES Tech Mar Environ Sci* No 45 26 pp
3. Tong X, Wei Q, Zhan X, et al (2016) The New Graphene Family Materials: Synthesis and Applications in Oxygen Reduction Reaction. *Catalysts* 7:1. <https://doi.org/10.3390/catal7010001>
4. Menichini E, Bocca A, Merli F, et al (1991) Polycyclic aromatic hydrocarbons in olive oils on the Italian market. *Food Addit Contam* 8:363–369. <https://doi.org/10.1080/02652039109373985>
5. Sanz-Landaluze J, Bartolome L, Zuloaga O, et al (2006) Accelerated extraction for determination of polycyclic aromatic hydrocarbons in marine biota. *Anal Bioanal Chem* 384:1331–1340. <https://doi.org/10.1007/s00216-005-0249-5>
6. Cui Z, Ge N, Zhang A, et al (2015) Comprehensive determination of polycyclic aromatic hydrocarbons in Chinese herbal medicines by solid phase extraction and gas chromatography coupled to tandem mass spectrometry. *Anal Bioanal Chem* 407:1989–97. <https://doi.org/10.1007/s00216-015-8463-2>
7. Zougagh M, Redigolo H, Ríos A, Valcárcel M (2004) Screening and confirmation of PAHs in vegetable oil samples by use of supercritical fluid extraction in conjunction with liquid chromatography and fluorimetric detection. *Anal Chim Acta* 525:265–271. <https://doi.org/10.1016/j.aca.2004.07.072>
8. Kielbasa A, Buszewski B (2017) PAHs in animal tissues-the analytics of PAHs in new reference materials and their homogeneity. *Anal Methods* 9:76–83. <https://doi.org/10.1039/c6ay01858k>
9. Li K, Li H, Liu L, et al (2007) Solid-phase extraction with C30 bonded silica for analysis of polycyclic aromatic hydrocarbons in airborne particulate matters by gas chromatography-mass spectrometry. *J Chromatogr A*. <https://doi.org/10.1016/j.chroma.2007.03.129>
10. González-Mariño I, Quintana JB, Rodríguez I, et al (2009) Comparison of molecularly imprinted, mixed-mode and hydrophilic balance sorbents performance in the solid-phase extraction of amphetamine drugs from wastewater samples for liquid chromatography-tandem mass spectrometry determination. *J Chromatogr A* 1216:8435–8441. <https://doi.org/10.1016/j.chroma.2009.09.069>
11. Maya F, Estela JM, Cerdà V (2010) Interfacing on-line solid phase extraction with monolithic column multisyringe chromatography and chemiluminescence detection: An effective tool for fast, sensitive and selective determination of thiazide diuretics. *Talanta* 80:1333–1340. <https://doi.org/10.1016/j.talanta.2009.09.033>
12. Sychov CS, Ilyin MM, Davankov VA, Sochilina KO (2004) Elucidation of retention mechanisms on hypercrosslinked polystyrene used as column packing material for high-performance liquid chromatography. *J Chromatogr A* 1030:17–24. <https://doi.org/10.1016/j.chroma.2003.10.098>
13. Stankovich S, Dikin DA, Piner RD, et al (2007) Synthesis of graphene-based

- nanosheets via chemical reduction of exfoliated graphite oxide. *Carbon* N Y 45:1558–1565. <https://doi.org/10.1016/j.carbon.2007.02.034>
14. Sitko R, Zawisza B, Malicka E (2013) Graphene as a new sorbent in analytical chemistry. *TrAC - Trends Anal Chem* 51:33–43. <https://doi.org/10.1016/j.trac.2013.05.011>
 15. Lochmüller CH, Colborn AS, Hunnicutt ML, Harris JM (1984) Bound Pyrene Excimer Photophysics and the Organization and Distribution of Reaction Sites on Silica. *J Am Chem Soc* 106:4077–4082. <https://doi.org/10.1021/ja00327a002>
 16. Hicks JC, Dabestani R, Buchanan AC, Jones CW (2006) Spacing and site isolation of amine groups in 3-aminopropyl-grafted silica materials: The role of protecting groups. *Chem Mater* 18:5022–5032. <https://doi.org/10.1021/cm061382w>
 17. Mikhralieva A, Zaitsev V, Xing Y, et al (2020) Excitation-Independent Blue-Emitting Carbon Dots from Mesoporous Aminosilica Nanoreactor for Bioanalytical Application. *ACS Appl Nano Mater* 0: <https://doi.org/10.1021/acsanm.0c00363>
 18. Mikhralieva A, Zaitsev V, Aucélio RQ, et al (2020) Benefit of porous silica nanoreactor in preparation of fluorescence carbon dots from citric acid. *Nano Express*. <https://doi.org/10.1088/2632-959x/ab7e0d>
 19. Zhao Z, Zhang L, Cai Y, Chen Y (2014) Distribution of polycyclic aromatic hydrocarbon (PAH) residues in several tissues of edible fishes from the largest freshwater lake in China, Poyang Lake, and associated human health risk assessment. *Ecotoxicol Environ Saf* 104:323–331. <https://doi.org/10.1016/j.ecoenv.2014.01.037>
 20. EPA HPA.pdf
 21. Marvanová S, Vondráček J, Pěňčíková K, et al (2008) Toxic effects of methylated benz[a]anthracenes in liver cells. *Chem Res Toxicol*. <https://doi.org/10.1021/tx700305x>
 22. Lee B-K (2010) Sources, Distribution and Toxicity of Polyaromatic Hydrocarbons (PAHs) in Particulate Matter. In: *Air Pollution*
 23. Abdel-Shafy HI, Mansour MSM (2016) A review on polycyclic aromatic hydrocarbons: Source, environmental impact, effect on human health and remediation. *Egypt J Pet* 25:107–123. <https://doi.org/10.1016/j.ejpe.2015.03.011>
 24. Vives I, Grimalt JO, Fernández P, Rosseland B (2004) Polycyclic aromatic hydrocarbons in fish from remote and high mountain lakes in Europe and Greenland. *Sci Total Environ* 324:67–77. <https://doi.org/10.1016/j.scitotenv.2003.10.026>
 25. Yebra-Pimentel I, Martínez-Carballo E, Regueiro J, Simal-Gándara J (2013) The potential of solvent-minimized extraction methods in the determination of polycyclic aromatic hydrocarbons in fish oils. *Food Chem* 139:1036–1043. <https://doi.org/10.1016/j.foodchem.2013.02.012>
 26. Janoszka B, Warzecha L, Błaszczuk U, Bodzek D (2004) Organic compounds formed in thermally treated high-protein food. Part II: Azaarenes. *Acta Chromatogr* 129–141
 27. Lund M, Duedahl-Olesen L, Christensen JH (2009) Extraction of polycyclic aromatic hydrocarbons from smoked fish using pressurized liquid extraction

- with integrated fat removal. *Talanta* 79:10–15. <https://doi.org/10.1016/j.talanta.2009.02.048>
28. Speer K, Steeg E, Horstmann P, et al (1990) Determination and distribution of polycyclic aromatic hydrocarbons in native vegetable oils, smoked fish products, mussels and oysters, and bream from the river Elbe. *J High Resolut Chromatogr* 13:104–111. <https://doi.org/10.1002/jhrc.1240130206>
 29. Serpe FP, Esposito M, Gallo P, Serpe L (2010) Optimisation and validation of an HPLC method for determination of polycyclic aromatic hydrocarbons (PAHs) in mussels. *Food Chem* 122:920–925. <https://doi.org/10.1016/j.foodchem.2010.03.062>
 30. EC (European Commission) (2005) COMMISSION REGULATION (EC) No 208/2005 of 4 February 2005 amending Regulation (EC) No 466/2001 as regards polycyclic aromatic hydrocarbons. *Off J Eur Union L* 34:3–5
 31. Johnson LL, Arkoosh MR, Bravo CF, et al (2008) The Effects of Polycyclic Aromatic Hydrocarbons in Fish from Puget Sound, Washington
 32. Howard JW, Teague RT, White RH, Fry BE (1966) Extraction and Estimation of Polycyclic Aromatic Hydrocarbons in Smoked Foods. I. General Method. *J AOAC Int.* <https://doi.org/10.1093/jaoac/49.3.595>
 33. Welling P, Kaandorp B (1986) Determination of polycyclic aromatic hydrocarbons (PAH) in edible vegetable oils by liquid chromatography and programmed fluorescence detection Comparison of caffeine complexation and XAD-2 chromatography sample clean-up. *Z Lebensm Unters Forsch* 183:111–115. <https://doi.org/10.1007/BF01041927>
 34. Buckingham PL, Evans JC (2016) Hazardous Waste Management / M . D . LaGrega ,
 35. Fang G-C, Chang K-F, Lu C, Bai H (2002) Toxic equivalency factors study of polycyclic aromatic hydrocarbons (PAHs) in Taichung City, Taiwan. *Toxicol Ind Health* 18:279–288. <https://doi.org/10.1191/0748233702th151oa>
 36. Law R (2014) Technical Guideline No . 08 – Processing and analysis of water , biota and sediment samples for the determination of hydrocarbon contamination using gas chromatography -mass spectrometry AND IMPACT ASSESSMENT ASSOCIATED WITH SUBSEA
 37. Moret S, Conte LS (2000) Polycyclic aromatic hydrocarbons in edible fats and oils: occurrence and analytical methods. *J Chromatogr A* 882:245–253. [https://doi.org/10.1016/S0021-9673\(00\)00079-0](https://doi.org/10.1016/S0021-9673(00)00079-0)
 38. Head S (1968) Contamination of coconut oil by PAH. 706–712
 39. Flotron V, Houessou J, Bosio A, et al (2003) Rapid determination of polycyclic aromatic hydrocarbons in sewage sludges using microwave-assisted solvent extraction. *J Chromatogr A* 999:175–184. [https://doi.org/10.1016/S0021-9673\(03\)00424-2](https://doi.org/10.1016/S0021-9673(03)00424-2)
 40. Miège C, Dugay J, Hennion M. (2003) Optimization, validation and comparison of various extraction techniques for the trace determination of polycyclic aromatic hydrocarbons in sewage sludges by liquid chromatography coupled to diode-array and fluorescence detection. *J Chromatogr A* 995:87–97. [https://doi.org/10.1016/S0021-9673\(03\)00497-7](https://doi.org/10.1016/S0021-9673(03)00497-7)
 41. Olatunji OS, Fatoki OS, Ximba BJ, Opeolu BO (2014) Polycyclic aromatic hydrocarbons (PAHs) in edible oil: tetmperature effect on recovery from base

- hydrolysis product and health risk factor. *Food Public Heal* 4:23–30. <https://doi.org/10.5923/j.fph.20140402.02>
42. Moret S, Conte LS (2002) A rapid method for polycyclic aromatic hydrocarbon determination in vegetable oils. *J Sep Sci* 25:96–100. [https://doi.org/10.1002/1615-9314\(20020101\)25:1/2<96::AID-JSSC96>3.0.CO;2-5](https://doi.org/10.1002/1615-9314(20020101)25:1/2<96::AID-JSSC96>3.0.CO;2-5)
 43. Fromberg A, Højgård A, Duedahl-Olesen L (2007) Analysis of polycyclic aromatic hydrocarbons in vegetable oils combining gel permeation chromatography with solid-phase extraction clean-up. *Food Addit Contam* 24:758–767. <https://doi.org/10.1080/02652030601150505>
 44. Van Look L, Deschuytere P, Van Peteghem C (1989) Thin-layer chromatographic method for the detection of anabolics in fatty tissues. *J Chromatogr B Biomed Sci Appl* 489:213–218. [https://doi.org/10.1016/S0378-4347\(00\)82898-4](https://doi.org/10.1016/S0378-4347(00)82898-4)
 45. Singh V, Joung D, Zhai L, et al (2011) Graphene based materials: Past, present and future. *Prog Mater Sci* 56:1178–1271. <https://doi.org/10.1016/j.pmatsci.2011.03.003>
 46. Lawrence JF, Weber DF (1984) Determination of Polycyclic Aromatic Hydrocarbons in Some Canadian Commercial Fish, Shellfish, and Meat Products by Liquid Chromatography with Confirmation by Capillary Gas Chromatography-Mass Spectrometry. *J Agric Food Chem.* <https://doi.org/10.1021/jf00124a022>
 47. Purcaro G, Moret S, Conte LS (2013) Overview on polycyclic aromatic hydrocarbons: Occurrence, legislation and innovative determination in foods. *Talanta*
 48. Wijeratne MCP, Samarajeewa U, Rodrigo MCP (1996) Polycyclic aromatic hydrocarbons in coconut kernel products. *J Natl Sci Counc Sri Lanka.* <https://doi.org/10.4038/jnsfsr.v24i4.5561>
 49. D. RE (1998) Analytical Supercritical Fluid Extraction Techniques
 50. Jira W (2004) A GC/MS method for the determination of carcinogenic polycyclic aromatic hydrocarbons (PAH) in smoked meat products and liquid smokes. *Eur Food Res Technol* 218:208–212. <https://doi.org/10.1007/s00217-003-0827-8>
 51. Sychoy S, Davankov VA, Proskurina NA, Mikheeva AJ (2009) The unique selectivity of π -interactions for solid-phase extraction. *LC GC Eur* 22:
 52. Simko P, Gergely S, Karovicova J, et al (1993) Influence of cooking on benzo(a)pyrene content in smoked sausages. *Meat Sci.* [https://doi.org/10.1016/0309-1740\(93\)90079-W](https://doi.org/10.1016/0309-1740(93)90079-W)
 53. Rojo Camargo MC, Antonioli PR, Vicente E, Tfouni S a V (2011) Polycyclic aromatic hydrocarbons in Brazilian commercial soybean oils and dietary exposure. *Food Addit Contam Part B, Surveill* 4:152–9. <https://doi.org/10.1080/19393210.2011.585244>
 54. Andrade-eiroa A, Canle M, Leroy-cancellieri V, Cerdà V (2016) Trends in Analytical Chemistry Solid-phase extraction of organic compounds : A critical review (Part I). *Trends Anal Chem* 80:641–654. <https://doi.org/10.1016/j.trac.2015.08.015>
 55. Gadzała-Kopciuch RM, Kluska M, Welniak M, et al (1999) Aryl Chemically

- Bonded Phases for Determination of Selected Polycyclic Aromatic Hydrocarbons Isolated from Environmental Samples Utilizing SPE/HPLC. *Polish J Environ Stud* 8:383–387
56. Barranco A, Alonso-Salces RM, Bakkali A, et al (2003) Solid-phase clean-up in the liquid chromatographic determination of polycyclic aromatic hydrocarbons in edible oils. *J Chromatogr A* 988:33–40. [https://doi.org/10.1016/S0021-9673\(02\)02059-9](https://doi.org/10.1016/S0021-9673(02)02059-9)
 57. Proskurina N, Davankov V, Ilyin M, et al (2009) Determination of polyaromatic hydrocarbons in fat-containing food using selective solid-phase extraction. *Sorption Chromatogr Process* 167–176
 58. Oh SY, Kim KP, Jung MW, et al (2003) Selective solid-phase extraction of polycyclic aromatic hydrocarbons by the chemically modified polymeric adsorbents with protoporphyrin IX. *Chromatographia* 57:665–670. <https://doi.org/10.1007/BF02491746>
 59. Kibbey CE, Meyerhoff ME (1993) Shape-selective separation of polycyclic aromatic hydrocarbons by reversed-phase liquid chromatography on tetraphenylporphyrin-based stationary phases. *J Chromatogr A* 641:49–55. [https://doi.org/10.1016/0021-9673\(93\)83457-4](https://doi.org/10.1016/0021-9673(93)83457-4)
 60. Chen L, Wang T, Tong J (2011) Application of derivatized magnetic materials to the separation and the preconcentration of pollutants in water samples. *TrAC - Trends Anal Chem* 30:1095–1108. <https://doi.org/10.1016/j.trac.2011.02.013>
 61. Purcaro G, Morrison P, Moret S, et al (2007) Determination of polycyclic aromatic hydrocarbons in vegetable oils using solid-phase microextraction-comprehensive two-dimensional gas chromatography coupled with time-of-flight mass spectrometry. *J Chromatogr A* 1161:284–291. <https://doi.org/10.1016/j.chroma.2007.05.105>
 62. Hu C, Jia L, Liu Q, Zhang S (2010) Development of magnetic octadecylsilane particles as solid-phase extraction adsorbent for the determination of fat-soluble vitamins in fruit juice-milk beverage by capillary liquid chromatography. *J Sep Sci* 33:2145–2152. <https://doi.org/10.1002/jssc.201000074>
 63. Basheer C, Wong W, Makahleh A, et al (2011) Hydrazone-based ligands for micro-solid phase extraction-high performance liquid chromatographic determination of biogenic amines in orange juice. *J Chromatogr A* 1218:4332–4339. <https://doi.org/10.1016/j.chroma.2011.04.073>
 64. Ballesteros-Gómez A, Rubio S (2009) Hemimicelles of alkyl carboxylates chemisorbed onto magnetic nanoparticles: Study and application to the extraction of carcinogenic polycyclic aromatic hydrocarbons in environmental water samples. *Anal Chem* 81:9012–9020. <https://doi.org/10.1021/ac9016264>
 65. Huang Y, Zhou Q, Xie G (2011) Development of micro-solid phase extraction with titanate nanotube array modified by cetyltrimethylammonium bromide for sensitive determination of polycyclic aromatic hydrocarbons from environmental water samples. *J Hazard Mater* 193:82–9. <https://doi.org/10.1016/j.jhazmat.2011.07.025>
 66. Sadowska-Rociek A, Surma M, Cieřlik E (2014) Determination of Polycyclic Aromatic Hydrocarbons in Coffee and Coffee Substitutes using Dispersive SPE and Gas Chromatography-Mass Spectrometry. *Food Anal Methods* 8:109–121. <https://doi.org/10.1007/s12161-014-9876-9>

67. Hunter CA, Sanders JKM (1990) The Nature of π - π Interactions. *J Am Chem Soc.* <https://doi.org/10.1021/ja00170a016>
68. Mano F Bio-Nanomaterials Biomimetic and Bioinspired Nanomaterials Biomimetic , Bioresponsive , and Bioactive Materials Handbook of Biomineralization Biomimetic Organic Synthesis Molecular Assembly of Biomimetic Systems
69. Hoeben FJM, Jonkheijm P, Meijer EW, Schenning APHJ (2005) About supramolecular assemblies of π -conjugated systems. *Chem Rev* 105:1491–1546. <https://doi.org/10.1021/cr030070z>
70. Chen L, Lu Y, Li S, et al (2013) Application of graphene-based solid-phase extraction for ultra-fast determination of malachite green and its metabolite in fish tissues. *Food Chem* 141:1383–1389. <https://doi.org/10.1016/j.foodchem.2013.04.090>
71. Wang WD, Huang YM, Shu WQ, Cao J (2007) Multiwalled carbon nanotubes as adsorbents of solid-phase extraction for determination of polycyclic aromatic hydrocarbons in environmental waters coupled with high-performance liquid chromatography. *J Chromatogr A* 1173:27–36. <https://doi.org/10.1016/j.chroma.2007.10.027>
72. Carr JW, Harris JM (1987) Heterogeneity of Reversed-Phase Chromatographic Surfaces : Quenching of Sorbed Pyrene Fluorescence. 2700
73. Ayadim M, Habib Jiwan JL, De Silva AP, Soumilion JP (1996) Photosensing by a fluorescing probe covalently attached to the silica. *Tetrahedron Lett* 37:7039–7042. [https://doi.org/10.1016/0040-4039\(96\)01543-2](https://doi.org/10.1016/0040-4039(96)01543-2)
74. Lü F, Gao L, Li H, et al (2007) Molecular engineered silica surfaces with an assembled anthracene monolayer as a fluorescent sensor for organic copper(II) salts. *Appl Surf Sci* 253:4123–4131. <https://doi.org/10.1016/j.apsusc.2006.09.038>
75. Boos KS, Grimm CH (1999) High-performance liquid chromatography integrated solid-phase extraction in bioanalysis using restricted access precolumn packings. *TrAC - Trends Anal Chem.* [https://doi.org/10.1016/S0165-9936\(98\)00102-2](https://doi.org/10.1016/S0165-9936(98)00102-2)
76. Vijay D, Sastry GN (2010) The cooperativity of cation- π and π - π interactions. *Chem Phys Lett* 485:235–242. <https://doi.org/10.1016/j.cplett.2009.12.012>
77. Magiera S, Pardylla A, Baranowska I (2015) Ultrasonics Sonochemistry Effects of various factors of ultrasonic treatment on the extraction recovery of drugs from fish tissues. *Ultrason - Sonochemistry* 26:388–398. <https://doi.org/10.1016/j.ultsonch.2015.03.005>
78. Feng C, Lin CS, Fan W, et al (2014) Stacking of polycyclic aromatic hydrocarbons as prototype for graphene multilayers , studied using density functional theory augmented with a dispersion term Stacking of polycyclic aromatic hydrocarbons as prototype for graphene multilayers , studied usin. 194702:. <https://doi.org/10.1063/1.3251785>
79. Li Y, Tu X, Wang H, et al (2015) First-principles investigation on the electronic efficiency and binding energy of the contacts formed by graphene and poly-aromatic hydrocarbon anchoring groups. *J Chem Phys* 142:. <https://doi.org/10.1063/1.4918738>
80. Quiñero D, Garau C, Rotger C, et al (2002) Anion- π interactions: Do they

- exist? *Angew Chemie - Int Ed* 41:3389–3392. [https://doi.org/10.1002/1521-3773\(20020916\)41:18<3389::AID-ANIE3389>3.0.CO;2-S](https://doi.org/10.1002/1521-3773(20020916)41:18<3389::AID-ANIE3389>3.0.CO;2-S)
81. Long RQ, Yang RT (2001) Carbon nanotubes as superior sorbent for dioxin removal [1]. *J. Am. Chem. Soc.*
 82. Cai Y, Jiang G, Liu J, Zhou Q (2003) Multiwalled carbon nanotubes as a solid-phase extraction adsorbent for the determination of bisphenol A, 4-n-nonylphenol, and 4-tert-octylphenol. *Anal Chem.* <https://doi.org/10.1021/ac0263566>
 83. Huang K-J, Liu Y-J, Li J, et al (2014) Ultra-trace determination of polycyclic aromatic hydrocarbons using solid-phase extraction coupled with HPLC based on graphene-functionalized silica gel composites. *Anal Methods* 6:194. <https://doi.org/10.1039/c3ay41588k>
 84. Cai YQ, Jiang G Bin, Liu JF, Zhou QX (2003) Multi-walled carbon nanotubes packed cartridge for the solid-phase extraction of several phthalate esters from water samples and their determination by high performance liquid chromatography. *Anal Chim Acta.* <https://doi.org/10.1016/j.aca.2003.08.006>
 85. Kueseng P, Thammakhet C, Thavarungkul P, Kanatharana P (2010) Multiwalled carbon nanotubes/cryogel composite, a new sorbent for determination of trace polycyclic aromatic hydrocarbons. *Microchem J* 96:317–323. <https://doi.org/10.1016/j.microc.2010.05.002>
 86. Liu Q, Shi J, Sun J, et al (2011) Graphene and Graphene Oxide Sheets Supported on Silica as Versatile and High-Performance Adsorbents for Solid-Phase Extraction. *Angew Chemie Int Ed* 50:5913–5917. <https://doi.org/10.1002/anie.201007138>
 87. Stevenson PG, Kayillo S, Dennis GR, Shalliker RA (2007) Effects of π - π Interactions on the Separation of PAHs on Phenyl-Type Stationary Phases. *J Liq Chromatogr Relat Technol* 31:324–347. <https://doi.org/10.1080/10826070701780607>
 88. Tanaka N, Tokuda Y, Iwaguchi K, Araki M (1982) Effect of stationary phase structure on retention and selectivity in reversed-phase liquid chromatography. *J Chromatogr A.* [https://doi.org/10.1016/S0021-9673\(00\)82036-1](https://doi.org/10.1016/S0021-9673(00)82036-1)
 89. Kroto HW, Heath JR, O'Brien SC, et al (1985) C₆₀: Buckminsterfullerene. *Nature.* <https://doi.org/10.1038/318162a0>
 90. Pyell U, Garrigues P, Felix G (1993) Separation of tetrachloro-p-dioxin isomers by high- performance liquid chromatography with electron- acceptor and electron-donor stationary phases. 634:169–181
 91. Kimata K, Hosoya K, Kuroki H, et al (1997) Selectivity of electron-donor- and electron-acceptor-bonded silica packing materials for hydrophobic environmental contaminants in polar and non-polar eluents. *J Chromatogr A* 786:237–248. [https://doi.org/10.1016/S0021-9673\(97\)00597-9](https://doi.org/10.1016/S0021-9673(97)00597-9)
 92. Ding L, Fang Y (2010) Chemically assembled monolayers of fluorophores as chemical sensing materials. *Chem Soc Rev* 39:4258. <https://doi.org/10.1039/c003028g>
 93. Paul BK, Guchhait N (2011) Morphological transition of the host-structure influences solvent-relaxation: A wavelength-selective fluorescence exploration through environment-sensitive intramolecular charge transfer photophysics. *Spectrochim Acta - Part A Mol Biomol Spectrosc* 81:590–597.

- <https://doi.org/10.1016/j.saa.2011.06.056>
94. Carr J w., Harris JM (1986) Fluorescence Studies of the Stationary-Phase Chemical Environment in Reversed-Phase Liquid Chromatography. *Anal Chem* 58:626–631. <https://doi.org/10.1021/ac00294a031>
 95. Kobayashi T, Nagakura S, Szwarc M (1979) Direct observation of excimer formation in anthracene and 9,9'-bianthryl. *Chem Phys.* [https://doi.org/10.1016/0301-0104\(79\)85080-6](https://doi.org/10.1016/0301-0104(79)85080-6)
 96. The OF (1967) Interaction of Excited Aromatic Hydrocarbons with Aromatic Amines Noboru MATAGA and Kiyoshi EZUMI of Chemistry , Faculty of Engineering Science , Osaka University , Osaka (Received December 2 , 1966). 367:
 97. Letters CF (1978) PHOTOCHEMICALLY INDUCED HYDROGEN ISOTOPE EXCHANGE. 197–200
 98. Thomas JK (2005) Physical aspects of radiation-induced processes on SiO₂, ??-Al₂O₃, zeolites, and clays. *Chem Rev* 105:1683–1734. <https://doi.org/10.1021/cr020378a>
 99. Thomas a, Polarz S, Antonietti M (2003) Influence of spatial restrictions on equilibrium reactions: A case study about the excimer formation of pyrene. *J Phys Chem B* 107:5081–5087. <https://doi.org/10.1021/jp026587g>
 100. Lochmüller CH, Wenzel TJ (1990) Spectroscopic Studies of Pyrene at Silica Interfaces. *J Phys Chem* 94:4230–4235
 101. Lochmuller CH, Colborn AS, Hunnicutt ML (1983) Organization and Distribution of Molecules Chemically Bound to Silica. *Anal Chem* 55:1344–1348. <https://doi.org/10.1021/ac00259a036>
 102. Hara K, De Mayo P, Ware WR, et al (1980) Biphasic photochemistry: time-resolved spectra of adsorbed hydrocarbons. *Chem Phys Lett.* [https://doi.org/10.1016/0009-2614\(80\)80023-6](https://doi.org/10.1016/0009-2614(80)80023-6)
 103. Zhang Z, Zhang J, Chen N, Qu L (2012) Graphene quantum dots: an emerging material for energy-related applications and beyond. *Energy Environ Sci* 5:8869. <https://doi.org/10.1039/c2ee22982j>
 104. Allen MJ, Tung VC, Kaner RB (2009) Honeycomb Carbon : A Review of Graphene
 105. Iijima S (1991) Helical microtubules of graphitic carbon. *Nature.* <https://doi.org/10.1038/354056a0>
 106. Novoselov KS (2012) Electric Field Effect in Atomically Thin Carbon Films. 666:. <https://doi.org/10.1126/science.1102896>
 107. Neto AHC (2009) The electronic properties of graphene. 81:. <https://doi.org/10.1103/RevModPhys.81.109>
 108. Alam S, Nizam B, Maksudul U (2016) Synthesis of graphene. *Int Nano Lett* 6:65–83. <https://doi.org/10.1007/s40089-015-0176-1>
 109. Choi W, Lahiri I, Seelaboyina R, Kang YS (2010) Synthesis of graphene and its applications: A review. *Crit Rev Solid State Mater Sci.* <https://doi.org/10.1080/10408430903505036>
 110. Liu Z, Suenaga K, Harris PJF, Iijima S (2009) Open and closed edges of graphene layers. *Phys Rev Lett* 102:1–4. <https://doi.org/10.1103/PhysRevLett.102.015501>
 111. Liu N, Luo F, Wu H, et al (2008) One-step ionic-liquid-assisted electrochemical

- synthesis of ionic-liquid-functionalized graphene sheets directly from graphite. *Adv Funct Mater* 18:1518–1525. <https://doi.org/10.1002/adfm.200700797>
112. S. RR (2009) Colloidal Suspensions of Highly Reduced Graphene Oxide in a Wide Variety of Organic Solvents. *Nano Lett* 9:1593. <https://doi.org/10.1021/nl803798y>
 113. Dong Y, Shao J, Chen C, et al (2012) Blue luminescent graphene quantum dots and graphene oxide prepared by tuning the carbonization degree of citric acid. *Carbon N Y* 50:4738–4743. <https://doi.org/10.1016/j.carbon.2012.06.002>
 114. Rollings E, Gweon G, Zhou SY, et al (2006) Synthesis and characterization of atomically thin graphite films on a silicon carbide substrate. 67:2172–2177. <https://doi.org/10.1016/j.jpcs.2006.05.010>
 115. Wang X, You H, Liu F, et al (2009) Large-scale synthesis of few-layered graphene using CVD. *Chem Vap Depos.* <https://doi.org/10.1002/cvde.200806737>
 116. Geim AK, Novoselov KS (2007) The rise of graphene. *Nat Mater.* <https://doi.org/10.1038/nmat1849>
 117. SRISUDA S, VIROTE B (2008) Adsorption of formaldehyde vapor by amine-functionalized mesoporous silica materials. *J Environ Sci.* [https://doi.org/10.1016/S1001-0742\(08\)60059-5](https://doi.org/10.1016/S1001-0742(08)60059-5)
 118. Gao W, Ci BL, Song L, et al (2009) Graphene Shape Control by Multistage Cutting and Transfer. 4487–4491. <https://doi.org/10.1002/adma.200900942>
 119. Liang X, Fu Z, Chou SY (2007) Graphene Transistors Fabricated via Transfer-Printing In Device Active-Areas on Large Wafer. 1–5
 120. Zheng Q, Kim J-K (2015) Graphene for Transparent Conductors. <https://doi.org/10.1007/978-1-4939-2769-2>
 121. Brownson DAC, Banks CE (2010) Graphene electrochemistry: An overview of potential applications. *Analyst* 135:2768–2778. <https://doi.org/10.1039/c0an00590h>
 122. Sprinkle M, Siegel D, Hu Y, et al (2009) First direct observation of a nearly ideal graphene band structure. *Phys Rev Lett.* <https://doi.org/10.1103/PhysRevLett.103.226803>
 123. Wu Z, Ren W, Gao L, et al (2008) Synthesis of high-quality graphene with a pre-determined number of layers. *Carbon N Y* 47:493–499. <https://doi.org/10.1016/j.carbon.2008.10.031>
 124. Machac P, Hrebicek T (2016) COMMUNICATIONS SYNTHESIS OF GRAPHENE ON Ni / SiC STRUCTURE. 67:147–149. <https://doi.org/10.1515/jee-2016-0021>
 125. Juang Z, Wu C, Lo C, et al (2009) Synthesis of graphene on silicon carbide substrates at low temperature. *Carbon N Y* 47:2026–2031. <https://doi.org/10.1016/j.carbon.2009.03.051>
 126. Sutter PW, Flege J, Sutter ELIA (2008) Epitaxial graphene on ruthenium. 7:.. <https://doi.org/10.1038/nmat2166>
 127. Li X, Cai W, Colombo L, Ruoff RS (2009) Evolution of Graphene Growth on Ni and Cu by Carbon Isotope Labeling. 12:
 128. Li X, Zhu Y, Cai W, et al (2009) Transfer of large-area graphene films for high-performance transparent conductive electrodes. *Nano Lett.* <https://doi.org/10.1021/nl902623y>

129. Kwon SY, Ciobanu C V., Petrova V, et al (2009) Growth of semiconducting graphene on palladium. *Nano Lett.* <https://doi.org/10.1021/nl902140j>
130. Cano-Márquez AG, Rodríguez-Macías FJ, Campos-Delgado J, et al (2009) Ex-MWNTs: Graphene sheets and ribbons produced by lithium intercalation and exfoliation of carbon nanotubes. *Nano Lett.* <https://doi.org/10.1021/nl803585s>
131. Jiao L, Zhang L, Wang X, et al (2009) Narrow graphene nanoribbons from carbon nanotubes. *Nature* 458:877–880. <https://doi.org/10.1038/nature07919>
132. Kosynkin D V, Higginbotham AL, Sinitskii A, et al (2009) Longitudinal unzipping of carbon nanotubes to form graphene nanoribbons. *Nature* 458:872–876. <https://doi.org/10.1038/nature07872>
133. Shao G, Lu Y, Wu F (2012) Graphene oxide : the mechanisms of oxidation and exfoliation. 4400–4409. <https://doi.org/10.1007/s10853-012-6294-5>
134. Zeng J, Zhang RQ, Treutlein HR (2012) Quantum simulations of materials and biological systems
135. Dimiev AM, Eigler S (2016) Graphene Oxide: Fundamentals and Applications
136. Hummers WS, Offeman RE (1958) Preparation of Graphitic Oxide. *J Am Chem Soc* 80:1339–1339. <https://doi.org/10.1021/ja01539a017>
137. Dreyer DR, Park S, Bielawski CW, Ruoff RS (2010) The chemistry of graphene oxide. *Chem Soc Rev* 39:228–240. <https://doi.org/10.1039/b920539j>
138. Marcano DC, Kosynkin D V., Berlin JM, et al (2010) Improved synthesis of graphene oxide. *ACS Nano* 4:4806–4814. <https://doi.org/10.1021/nn1006368>
139. Wissler M (2006) Graphite and carbon powders for electrochemical applications. *J Power Sources* 156:142–150. <https://doi.org/10.1016/j.jpowsour.2006.02.064>
140. Eda G, Ball J, Mattevi C, et al (2011) Partially oxidized graphene as a precursor to graphene. *J Mater Chem.* <https://doi.org/10.1039/c1jm11266j>
141. Ray SC (2015) Applications of Graphene and Graphene-Oxide based Nanomaterials
142. Weitz RT, Bittner AM, Scolari M, et al (2007) Electronic Transport Properties of Individual Chemically Reduced Graphene Oxide Sheets. 0–4
143. Szabó T, Berkesi O, Forgó P, et al (2006) Evolution of surface functional groups in a series of progressively oxidized graphite oxides. *Chem Mater* 18:2740–2749. <https://doi.org/10.1021/cm060258+>
144. Nakajima T, Matsuo Y (1994) Formation process and structure of graphite oxide. *Carbon N Y* 32:469–475. [https://doi.org/10.1016/0008-6223\(94\)90168-6](https://doi.org/10.1016/0008-6223(94)90168-6)
145. Lerf A, He H, Forster M, Klinowski J (1998) Structure of Graphite Oxide Revisited[†]. *J Phys Chem B* 102:4477–4482. <https://doi.org/10.1021/jp9731821>
146. Bagri A, Grantab R, Medhekar N V., Shenoy VB (2010) Stability and formation mechanisms of carbonyl- and hydroxyl-decorated holes in graphene oxide. *J Phys Chem C.* <https://doi.org/10.1021/jp908801c>
147. Kim MC, Hwang GS, Ruoff RS, et al (2009) Epoxide reduction with hydrazine on graphene : A first principles study Epoxide reduction with hydrazine on graphene : A first principles study. 064704:1–6. <https://doi.org/10.1063/1.3197007>
148. Gao X, Jang J, Nagase S (2010) Hydrazine and Thermal Reduction of Graphene Oxide : Reaction Mechanisms , Product Structures , and Reaction Design. 832–842

149. Yang D, Velamakanni A, Bozoklu G, et al (2009) Chemical analysis of graphene oxide films after heat and chemical treatments by X-ray photoelectron and Micro-Raman spectroscopy. *Carbon* N Y. <https://doi.org/10.1016/j.carbon.2008.09.045>
150. Botas C, Alvarez P, Blanco C, et al (2012) Tailored graphene materials by chemical reduction of graphene oxides of different atomic structure. *Rsc Adv* 2:9643–9650. <https://doi.org/10.1039/c2ra21447d>
151. Gao W, Alemany LB, Ci L, Ajayan PM (2009) New insights into the structure and reduction of graphite oxide. *Nat Chem* 1:403–408. <https://doi.org/10.1038/nchem.281> [doi]
152. Liu Z, Robinson JT, Sun X, Dai H (2008) PEGylated Nano-Graphene Oxide for Delivery of Water Insoluble Cancer Drugs (b). *J Am Chem Soc* 130:10876–10877. <https://doi.org/10.1021/ja803688x>
153. Mohanty N, Berry V (2008) Graphene-based single-bacterium resolution biodevice and DNA transistor: Interfacing graphene derivatives with nanoscale and microscale biocomponents. *Nano Lett* 8:4469–4476. <https://doi.org/10.1021/nl802412n>
154. Zheng W, Shen B, Zhai W World ' s largest Science , Technology & Medicine Open Access book publisher Surface Functionalization of Graphene with Polymers for Enhanced Properties
155. Stankovich S, Piner RD, Nguyen SBT, Ruoff RS (2006) Synthesis and exfoliation of isocyanate-treated graphene oxide nanoplatelets. *Carbon* N Y 44:3342–3347. <https://doi.org/10.1016/j.carbon.2006.06.004>
156. Wang S, Chia PJ, Chua LL, et al (2008) Band-like transport in surface-functionalized highly solution-processable graphene nanosheets. *Adv Mater* 20:3440–3446. <https://doi.org/10.1002/adma.200800279>
157. Yang H, Li F, Shan C, et al (2009) Covalent functionalization of chemically converted graphene sheets via silane and its reinforcement. *J Mater Chem* 19:4632. <https://doi.org/10.1039/b901421g>
158. Hao R, Qian W, Zhang L, Hou Y (2008) Aqueous dispersions of TCNQ-anion-stabilized graphene sheets. *Chem Commun* 6576. <https://doi.org/10.1039/b816971c>
159. Xu Y, Bai H, Lu G, et al (2008) Flexible Graphene Films via the Filtration of Water-Soluble. 5856–5857
160. Gacal BN, Koz B, Gacal B, et al (2009) Pyrene functional poly(vinyl alcohol) by “click” chemistry. *J Polym Sci Part A Polym Chem*. <https://doi.org/10.1002/pola.23240>
161. Liu Z, Sun X, Nakayama-Ratchford N, Dai H (2007) Supramolecular chemistry on water-soluble carbon nanotubes for drug loading and delivery. *ACS Nano* 1:50–56. <https://doi.org/10.1021/nn700040t>
162. Sygula A, Fronczek FR, Sygula R, et al (2007) A double concave hydrocarbon buckycatcher. *J Am Chem Soc* 129:3842–3843. <https://doi.org/10.1021/ja070616p>
163. Liu J, Yang W, Tao L, et al (2010) Thermosensitive graphene nanocomposites formed using pyrene-terminal polymers made by RAFT polymerization. *J Polym Sci Part A Polym Chem*. <https://doi.org/10.1002/pola.23802>
164. Lu CH, Yang HH, Zhu CL, et al (2009) A graphene platform for sensing

- biomolecules. *Angew Chemie - Int Ed* 48:4785–4787. <https://doi.org/10.1002/anie.200901479>
165. Ferrari AC (2007) Raman spectroscopy of graphene and graphite : Disorder , electron – phonon coupling , doping and nonadiabatic effects. 143:47–57. <https://doi.org/10.1016/j.ssc.2007.03.052>
 166. Terrones M, Botello-méndez AR, Campos-delgado J, et al (2010) Graphene and graphite nanoribbons : Morphology , properties , synthesis , defects and applications. <https://doi.org/10.1016/j.nantod.2010.06.010>
 167. Sattler KD (2016) Carbon nanomaterials sourcebook: Graphene, fullerenes, nanotubes, and nanodiamonds
 168. Ni Z, Wang Y, Yu T, Shen Z (2010) Raman spectroscopy and imaging of graphene. *Nano Res* 1:273–291. <https://doi.org/10.1007/s12274-008-8036-1>
 169. Xu X, Ray R, Gu Y, et al (2004) Electrophoretic analysis and purification of fluorescent single-walled carbon nanotube fragments. *J Am Chem Soc* 126:12736–12737. <https://doi.org/10.1021/ja040082h>
 170. Zong J, Zhu Y, Yang X, et al (2011) Synthesis of photoluminescent carbogenic dots using mesoporous silica spheres as nanoreactors. *Chem Commun* 47:764–766. <https://doi.org/10.1039/c0cc03092a>
 171. Gu ZG, Li DJ, Zheng C, et al (2017) MOF-Templated Synthesis of Ultrasmall Photoluminescent Carbon-Nanodot Arrays for Optical Applications. *Angew Chemie - Int Ed* 56:6853–6858. <https://doi.org/10.1002/anie.201702162>
 172. Xu H, Zhou S, Xiao L, et al (2015) Fabrication of a nitrogen-doped graphene quantum dot from MOF-derived porous carbon and its application for highly selective fluorescence detection of Fe ³⁺. *J Mater Chem C* 3:291–297. <https://doi.org/10.1039/C4TC01991A>
 173. Kausar A (2019) Polymer/carbon-based quantum dot nanocomposite: forthcoming materials for technical application. *J Macromol Sci Part A Pure Appl Chem* 56:341–356. <https://doi.org/10.1080/10601325.2019.1578614>
 174. Molaei MJ (2019) A review on nanostructured carbon quantum dots and their applications in biotechnology, sensors, and chemiluminescence. *Talanta* 196:456–478
 175. Yao B, Huang H, Liu Y, Kang Z (2019) Carbon Dots: A Small Conundrum. *Trends Chem* 1:235–246. <https://doi.org/10.1016/j.trechm.2019.02.003>
 176. Liu ML, Chen B Bin, Li CM, Huang CZ (2019) Carbon dots: synthesis, formation mechanism, fluorescence origin and sensing applications. *Green Chem* 21:449–471. <https://doi.org/10.1039/C8GC02736F>
 177. Yuan T, Meng T, He P, et al (2019) Carbon quantum dots: an emerging material for optoelectronic applications. *J Mater Chem C* 7:6820–6835. <https://doi.org/10.1039/C9TC01730E>
 178. Mintz KJ, Zhou Y, Leblanc RM (2019) Recent development of carbon quantum dots regarding their optical properties, photoluminescence mechanism, and core structure. *Nanoscale* 11:4634–4652. <https://doi.org/10.1039/C8NR10059D>
 179. Anwar S, Ding H, Xu M, et al (2019) Recent Advances in Synthesis, Optical Properties, and Biomedical Applications of Carbon Dots. *ACS Appl Bio Mater* 2:2317–2338. <https://doi.org/10.1021/acsabm.9b00112>
 180. Hinterberger V, Damm C, Haines P, et al (2019) Purification and structural elucidation of carbon dots by column chromatography. *Nanoscale* 11:8464–

8474. <https://doi.org/10.1039/C9NR01029G>
181. Hu C, Li M, Qiu J, Sun Y-P (2019) Design and fabrication of carbon dots for energy conversion and storage. *Chem Soc Rev* 48:2315–2337. <https://doi.org/10.1039/C8CS00750K>
 182. Zhang X, Wang S, Zhu C, et al (2013) Carbon-dots derived from nanodiamond: Photoluminescence tunable nanoparticles for cell imaging. *J Colloid Interface Sci* 397:39–44. <https://doi.org/10.1016/j.jcis.2013.01.063>
 183. Bao L, Zhang Z-L, Tian Z-Q, et al (2011) Electrochemical Tuning of Luminescent Carbon Nanodots: From Preparation to Luminescence Mechanism. *Adv Mater* 23:5801–5806. <https://doi.org/10.1002/adma.201102866>
 184. Wang Q, Zheng H, Long Y, et al (2011) Microwave-hydrothermal synthesis of fluorescent carbon dots from graphite oxide. *Carbon N Y* 49:3134–3140. <https://doi.org/10.1016/j.carbon.2011.03.041>
 185. Li X, Wang H, Shimizu Y, et al (2011) Preparation of carbon quantum dots with tunable photoluminescence by rapid laser passivation in ordinary organic solvents. *Chem Commun* 47:932–934. <https://doi.org/10.1039/c0cc03552a>
 186. Yuan F, Ding L, Li Y, et al (2015) Multicolor fluorescent graphene quantum dots colorimetrically responsive to all-pH and a wide temperature range. *Nanoscale* 7:11727–11733. <https://doi.org/10.1039/c5nr02007g>
 187. Naik JP, Sutradhar P, Saha M (2017) Molecular scale rapid synthesis of graphene quantum dots (GQDs). *J Nanostructure Chem* 7:85–89. <https://doi.org/10.1007/s40097-017-0222-9>
 188. Campuzano S, Yáñez-Sedeño P, Pingarrón JM (2019) Carbon dots and graphene quantum dots in electrochemical biosensing. *Nanomaterials* 9:. <https://doi.org/10.3390/nano9040634>
 189. Zhu S, Song Y, Zhao X, et al (2015) The photoluminescence mechanism in carbon dots (graphene quantum dots, carbon nanodots, and polymer dots): current state and future perspective. *Nano Res* 8:355–381. <https://doi.org/10.1007/s12274-014-0644-3>
 190. Dai Q, Zhao H, Fan Z, et al (2018) In Situ Nanoreactors: Controllable Photoluminescent Carbon-Rich Polymer Nanodots Derived from Fatty Acid under Photoirradiation. *Macromol Rapid Commun* 39:1800152. <https://doi.org/10.1002/marc.201800152>
 191. Chu K-W, Lee SL, Chang C-J, Liu L (2019) Recent progress of carbon dot precursors and photocatalysis applications. *Polymers (Basel)* 11:. <https://doi.org/10.3390/polym11040689>
 192. Kurdyukov DA, Eurov DA, Rabchinskii MK, et al (2018) Controllable spherical aggregation of monodisperse carbon nanodots. *Nanoscale* 10:13223–13235. <https://doi.org/10.1039/c8nr01900b>
 193. Deeney C, Wang S, Belhout SA, et al (2018) Templated microwave synthesis of luminescent carbon nanofibers. *RSC Adv* 8:12907–12917. <https://doi.org/10.1039/C7RA13383A>
 194. Liu X, Li HB, Shi L, et al (2017) Structure and photoluminescence evolution of nanodots during pyrolysis of citric acid: From molecular nanoclusters to carbogenic nanoparticles. *J Mater Chem C* 5:10302–10312. <https://doi.org/10.1039/c7tc03429f>
 195. Liu R, Wu D, Liu S, et al (2009) An Aqueous Route to Multicolor

- Photoluminescent Carbon Dots Using Silica Spheres as Carriers. *Angew Chemie Int Ed* 48:4598–4601. <https://doi.org/10.1002/anie.200900652>
196. Zhu Y, Wang G, Jiang H, et al (2014) One-step ultrasonic synthesis of graphene quantum dots with high quantum yield and their application in sensing alkaline phosphatase. *Chem Commun (Camb)* 51:948–51. <https://doi.org/10.1039/c4cc07449a>
 197. Deng J, Lu Q, Mi N, et al (2014) Electrochemical synthesis of carbon nanodots directly from alcohols. *Chem - A Eur J*. <https://doi.org/10.1002/chem.201304869>
 198. Hu SL, Niu KY, Sun J, et al (2009) One-step synthesis of fluorescent carbon nanoparticles by laser irradiation. *J Mater Chem*. <https://doi.org/10.1039/b812943f>
 199. Zhai X, Zhang P, Liu C, et al (2012) Highly luminescent carbon nanodots by microwave-assisted pyrolysis. *Chem Commun*. <https://doi.org/10.1039/c2cc33869f>
 200. Bhunia SK, Saha A, Maity AR, et al (2013) Carbon nanoparticle-based fluorescent bioimaging probes. *Sci Rep*. <https://doi.org/10.1038/srep01473>
 201. Bourlinos AB, Stassinopoulos A, Anglos D, et al (2008) Surface Functionalized Carbogenic Quantum Dots. *Small* 4:455–458. <https://doi.org/10.1002/sml.200700578>
 202. Wang C, Xu Z, Lin H, et al (2015) Large Scale Synthesis of Highly Stable Fluorescent Carbon Dots Using Silica Spheres as Carriers for Targeted Bioimaging of Cancer Cells. *Part Part Syst Charact* 32:944–951. <https://doi.org/10.1002/ppsc.201500062>
 203. Roa R, Kim WK, Kanduč M, et al (2017) Catalyzed Bimolecular Reactions in Responsive Nanoreactors. *ACS Catal* 7:5604–5611. <https://doi.org/10.1021/acscatal.7b01701>
 204. Kwon W, Rhee S-W (2012) Facile synthesis of graphitic carbon quantum dots with size tunability and uniformity using reverse micelles. *Chem Commun* 48:5256. <https://doi.org/10.1039/c2cc31687k>
 205. Cui C, Lei J, Yang L, et al (2018) Carbon-dot-encapsulated molecularly imprinted mesoporous organosilica for fluorescent sensing of rhodamine 6G. *Res Chem Intermed* 1–8. <https://doi.org/10.1007/s11164-018-3279-2>
 206. Kurdyukov DA, Eurov DA, Stovpiaga EY, et al (2016) Template synthesis of monodisperse carbon nanodots. *Phys Solid State* 58:2545–2549. <https://doi.org/10.1134/S1063783416120167>
 207. Nelson DK, Razbirin BS, Starukhin AN, et al (2016) Photoluminescence of carbon dots from mesoporous silica. *Opt Mater (Amst)* 59:28–33. <https://doi.org/10.1016/j.optmat.2016.03.051>
 208. Wang F, Xie Z, Zhang H, et al (2011) Highly Luminescent Organosilane-Functionalized Carbon Dots. *Adv Funct Mater* 21:1027–1031. <https://doi.org/10.1002/adfm.201002279>
 209. Vriezema DM, Comellas Aragonès M, Elemans JAAW, et al (2005) Self-Assembled Nanoreactors. *Chem Rev* 105:1445–1490. <https://doi.org/10.1021/cr0300688>
 210. Oliinyk B V., Korytko D, Lysenko V, Alekseev S (2019) Are fluorescent silicon nanoparticles formed in a one-pot aqueous synthesis? *Chem Mater*

- acs.chemmater.9b01067. <https://doi.org/10.1021/acs.chemmater.9b01067>
211. Baldovi HG, Valencia S, Alvaro M, et al (2015) Highly fluorescent C-dots obtained by pyrolysis of quaternary ammonium ions trapped in all-silica ITQ-29 zeolite. *Nanoscale* 7:1744–1752. <https://doi.org/10.1039/c4nr05295a>
 212. Liu J, Zhang H, Wang N, et al (2019) Template-Modulated Afterglow of Carbon Dots in Zeolites: Room-Temperature Phosphorescence and Thermally Activated Delayed Fluorescence. *ACS Mater Lett* 58–63. <https://doi.org/10.1021/acsmaterialslett.9b00073>
 213. Xu H, Zhou S, Liu J, Wei Y (2018) Nanospace-confined preparation of uniform nitrogen-doped graphene quantum dots for highly selective fluorescence dual-function determination of Fe 3+ and ascorbic acid. *RSC Adv* 8:5500–5508. <https://doi.org/10.1039/C7RA13001E>
 214. Wang Y, Li Y, Yan Y, et al (2013) Luminescent carbon dots in a new magnesium aluminophosphate zeolite. *Chem Commun* 49:9006–9008. <https://doi.org/10.1039/c3cc43375g>
 215. Xu X, Chen J, Shi W, et al (2019) Synthesis of carbon nanodots in zeolite SAPO-46 channels for Q-switched fiber laser generation. *J Alloys Compd.* <https://doi.org/10.1016/j.jallcom.2018.12.181>
 216. Xu H, Zhou S, Xiao L, et al (2015) Nanoreactor-confined synthesis and separation of yellow-luminescent graphene quantum dots with a recyclable SBA-15 template and their application for Fe(III) sensing. *Carbon N Y* 87:215–225. <https://doi.org/10.1016/j.carbon.2015.02.036>
 217. Bourlinos AB, Stassinopoulos A, Anglos D, et al (2008) Photoluminescent Carbogenic Dots. *Chem Mater* 20:4539–4541. <https://doi.org/10.1021/cm800506r>
 218. Ortega-Liebana MC, Chung NX, Limpens R, et al (2017) Uniform luminescent carbon nanodots prepared by rapid pyrolysis of organic precursors confined within nanoporous templating structures. *Carbon N. Y.* 117:437–446
 219. Mitchell S, Michels N-L, Kunze K, Pérez-Ramírez J (2012) Visualization of hierarchically structured zeolite bodies from macro to nano length scales. *Nat Chem* 4:825–831. <https://doi.org/10.1038/nchem.1403>
 220. Vostrikova A V., Prikhozhenko ES, Mayorova OA, et al (2018) Thermal carbonization in nanoscale reactors: Controlled formation of carbon nanodots inside porous CaCO₃ microparticles. *Sci Rep* 8:1–7. <https://doi.org/10.1038/s41598-018-27488-w>
 221. Rezaei B, Hassani Z, Shahshahanipour M, et al (2018) Application of modified mesoporous boehmite (γ -AlOOH) with green synthesis carbon quantum dots for a fabrication biosensor to determine trace amounts of doxorubicin. *Luminescence* 33:1377–1386. <https://doi.org/10.1002/bio.3558>
 222. He Y, He J, Zhang H, et al (2017) Luminescent properties and energy transfer of luminescent carbon dots assembled mesoporous Al₂O₃: Eu³⁺ co-doped materials for temperature sensing. *J Colloid Interface Sci.* <https://doi.org/10.1016/j.jcis.2017.02.013>
 223. Liu J, Ren X, Yan Y, et al (2018) A new two-dimensional layered germanate with: In situ embedded carbon dots for optical temperature sensing. *Inorg Chem Front* 5:139–144. <https://doi.org/10.1039/c7qi00602k>
 224. Hayashi K, Ogawa S, Watanabe H, et al (2019) Pyrolytic production of

- fluorescent pyrone derivatives produced in the confined space of super-microporous silicas. *Bull Chem Soc Jpn* 92:1170–1174. <https://doi.org/10.1246/bcsj.20190060>
225. Lu Y, Wang J, Yuan H, Xiao D (2014) Separation of carbon quantum dots on a C18 column by binary gradient elution via HPLC. *Anal Methods* 6:8124–8128. <https://doi.org/10.1039/C4AY01052C>
 226. Tian X, Yin X (2019) Carbon Dots, Unconventional Preparation Strategies, and Applications Beyond Photoluminescence. *Small* 15:1901803. <https://doi.org/10.1002/sml.201901803>
 227. Benítez-Martínez S, Valcárcel M (2015) Graphene quantum dots in analytical science. *TrAC - Trends Anal. Chem.* 72:93–113
 228. Devi P, Rajput P, Thakur A, et al (2019) Recent advances in carbon quantum dot-based sensing of heavy metals in water. *TrAC Trends Anal Chem* 114:171–195. <https://doi.org/10.1016/j.trac.2019.03.003>
 229. Zhu S, Meng Q, Wang L, et al (2013) Highly photoluminescent carbon dots for multicolor patterning, sensors, and bioimaging. *Angew Chemie - Int Ed* 52:3953–3957. <https://doi.org/10.1002/anie.201300519>
 230. Zhang B, Liu CY, Liu Y (2010) A novel one-step approach to synthesize fluorescent carbon nanoparticles. *Eur J Inorg Chem* 4411–4414. <https://doi.org/10.1002/ejic.201000622>
 231. Rahimi M, Mahani M, Hassani Z (2019) Carbon quantum dots fluorescence quenching for potassium optode construction. *Luminescence* 34:402–406. <https://doi.org/10.1002/bio.3634>
 232. Ding H, Yu S-B, Wei J-S, Xiong H-M (2016) Full-Color Light-Emitting Carbon Dots with a Surface-State-Controlled Luminescence Mechanism. *ACS Nano* 10:484–491. <https://doi.org/10.1021/acsnano.5b05406>
 233. Lu Y, Zhang L, Lin H (2014) The use of a microreactor for rapid screening of the reaction conditions and investigation of the photoluminescence mechanism of carbon dots. *Chem - A Eur J* 20:4246–4250. <https://doi.org/10.1002/chem.201304358>
 234. Qu D, Sun Z (2020) The formation mechanism and fluorophores of carbon dots synthesized: Via a bottom-up route. *Mater Chem Front* 4:400–420. <https://doi.org/10.1039/c9qm00552h>
 235. Deeney C, Wang S, Belhout SA, et al (2018) Templated microwave synthesis of luminescent carbon nanofibers. *RSC Adv* 8:12907–12917. <https://doi.org/10.1039/c7ra13383a>
 236. Kurdyukov DA, Eurov DA, Rabchinskii MK, et al (2018) Controllable spherical aggregation of monodisperse carbon nanodots. *Nanoscale* 10:13223–13235. <https://doi.org/10.1039/c8nr01900b>
 237. Nelson DK, Razbirin BS, Starukhin AN, et al (2016) Photoluminescence of carbon dots from mesoporous silica. *Opt Mater (Amst)* 59:28–33. <https://doi.org/10.1016/j.optmat.2016.03.051>
 238. Dong Y, Shao J, Chen C, et al (2012) Blue luminescent graphene quantum dots and graphene oxide prepared by tuning the carbonization degree of citric acid. *Carbon N Y* 50:4738–4743. <https://doi.org/10.1016/j.carbon.2012.06.002>
 239. Zong J, Zhu Y, Yang X, et al (2011) Synthesis of photoluminescent carbogenic dots using mesoporous silica spheres as nanoreactorsw. *Chem Commun* 47:764–

766. <https://doi.org/10.1039/c0cc03092a>
240. Schneider J, Reckmeier CJ, Xiong Y, et al (2017) Molecular fluorescence in citric acid-based carbon dots. *J Phys Chem C*. <https://doi.org/10.1021/acs.jpcc.6b12519>
 241. Yang ZC, Wang M, Yong AM, et al (2011) Intrinsically fluorescent carbon dots with tunable emission derived from hydrothermal treatment of glucose in the presence of monopotassium phosphate. *Chem Commun*. <https://doi.org/10.1039/c1cc14860e>
 242. Huang H, Lv JJ, Zhou DL, et al (2013) One-pot green synthesis of nitrogen-doped carbon nanoparticles as fluorescent probes for mercury ions. *RSC Adv*. <https://doi.org/10.1039/c3ra43452d>
 243. Mehta VN, Jha S, Kailasa SK (2014) One-pot green synthesis of carbon dots by using *Saccharum officinarum* juice for fluorescent imaging of bacteria (*Escherichia coli*) and yeast (*Saccharomyces cerevisiae*) cells. *Mater Sci Eng C*. <https://doi.org/10.1016/j.msec.2014.01.038>
 244. Sahu S, Behera B, Maiti TK, Mohapatra S (2012) Simple one-step synthesis of highly luminescent carbon dots from orange juice: Application as excellent bio-imaging agents. *Chem Commun*. <https://doi.org/10.1039/c2cc33796g>
 245. Yang Y, Cui J, Zheng M, et al (2012) One-step synthesis of amino-functionalized fluorescent carbon nanoparticles by hydrothermal carbonization of chitosan. *Chem Commun*. <https://doi.org/10.1039/c1cc15678k>
 246. Krysmann MJ, Kellarakis A, Dallas P, Giannelis EP (2012) Formation mechanism of carbogenic nanoparticles with dual photoluminescence emission. *J Am Chem Soc*. <https://doi.org/10.1021/ja204661r>
 247. Shi L, Yang JH, Zeng HB, et al (2016) Carbon dots with high fluorescence quantum yield: The fluorescence originates from organic fluorophores. *Nanoscale*. <https://doi.org/10.1039/c6nr00451b>
 248. Miao X, Qu D, Yang D, et al (2018) Synthesis of Carbon Dots with Multiple Color Emission by Controlled Graphitization and Surface Functionalization. *Adv Mater*. <https://doi.org/10.1002/adma.201704740>
 249. Jiang K, Sun S, Zhang L, et al (2015) Red, green, and blue luminescence by carbon dots: Full-color emission tuning and multicolor cellular imaging. *Angew Chemie - Int Ed*. <https://doi.org/10.1002/anie.201501193>
 250. Liu ML, Yang L, Li RS, et al (2017) Large-scale simultaneous synthesis of highly photoluminescent green amorphous carbon nanodots and yellow crystalline graphene quantum dots at room temperature. *Green Chem*. <https://doi.org/10.1039/c7gc01236e>
 251. Kim S, Hwang SW, Kim MK, et al (2012) Anomalous behaviors of visible luminescence from graphene quantum dots: Interplay between size and shape. *ACS Nano*. <https://doi.org/10.1021/nn302878r>
 252. Bao L, Liu C, Zhang Z-L, Pang D-W (2015) Photoluminescence-Tunable Carbon Nanodots: Surface-State Energy-Gap Tuning. *Adv Mater*. <https://doi.org/10.1002/adma.201405070>
 253. Liu ML, Chen B Bin, Li CM, Huang CZ (2019) Carbon dots: Synthesis, formation mechanism, fluorescence origin and sensing applications. *Green Chem* 21:449–471. <https://doi.org/10.1039/c8gc02736f>
 254. Gedda G, Lee CY, Lin YC, Wu HF (2016) Green synthesis of carbon dots from

- prawn shells for highly selective and sensitive detection of copper ions. *Sensors Actuators, B Chem* 224:396–403. <https://doi.org/10.1016/j.snb.2015.09.065>
255. Rao L, Tang Y, Li Z, et al (2017) Efficient synthesis of highly fluorescent carbon dots by microreactor method and their application in Fe³⁺ ion detection. *Mater Sci Eng C* 81:213–223. <https://doi.org/10.1016/j.msec.2017.07.046>
 256. Yuan YH, Liu ZX, Li RS, et al (2016) Synthesis of nitrogen-doping carbon dots with different photoluminescence properties by controlling the surface states. *Nanoscale*. <https://doi.org/10.1039/c6nr00402d>
 257. Liu S, Cui J, Huang J, et al (2019) Facile one-pot synthesis of highly fluorescent nitrogen-doped carbon dots by mild hydrothermal method and their applications in detection of Cr(VI) ions. *Spectrochim Acta - Part A Mol Biomol Spectrosc* 206:65–71. <https://doi.org/10.1016/j.saa.2018.07.082>
 258. Liao J, Cheng Z, Zhou L (2016) Nitrogen-Doping Enhanced Fluorescent Carbon Dots: Green Synthesis and Their Applications for Bioimaging and Label-Free Detection of Au³⁺ Ions. *ACS Sustain Chem Eng*. <https://doi.org/10.1021/acssuschemeng.6b00018>
 259. Liu ML, Chen B Bin, Li CM, Huang CZ (2019) Carbon dots: Synthesis, formation mechanism, fluorescence origin and sensing applications. *Green Chem*.
 260. Kang X, Wang S, Zhu M (2018) Observation of a new type of aggregation-induced emission in nanoclusters. *Chem Sci*. <https://doi.org/10.1039/c7sc05317g>
 261. Song W, Duan W, Liu Y, et al (2017) Ratiometric Detection of Intracellular Lysine and pH with One-Pot Synthesized Dual Emissive Carbon Dots. *Anal Chem*. <https://doi.org/10.1021/acs.analchem.7b04211>
 262. Buiculescu R, Stefanakis D, Androulidaki M, et al (2016) Controlling carbon nanodot fluorescence for optical biosensing. *Analyst*. <https://doi.org/10.1039/c6an00783j>
 263. Chen B Bin, Liu ZX, Deng WC, et al (2016) A large-scale synthesis of photoluminescent carbon quantum dots: A self-exothermic reaction driving the formation of the nanocrystalline core at room temperature. *Green Chem*. <https://doi.org/10.1039/c6gc01820c>
 264. Lin M, Zou HY, Yang T, et al (2016) An inner filter effect based sensor of tetracycline hydrochloride as developed by loading photoluminescent carbon nanodots in the electrospun nanofibers. *Nanoscale*. <https://doi.org/10.1039/c5nr08177g>
 265. Li Z, Wang Y, Ni Y, Kokot S (2015) A sensor based on blue luminescent graphene quantum dots for analysis of a common explosive substance and an industrial intermediate, 2,4,6-trinitrophenol. *Spectrochim Acta - Part A Mol Biomol Spectrosc* 137:1213–1221. <https://doi.org/10.1016/j.saa.2014.09.009>
 266. Zhang Y, Wang Y, Guan Y, Feng L (2015) Uncovering the pK_a dependent fluorescence quenching of carbon dots induced by chlorophenols. *Nanoscale*. <https://doi.org/10.1039/c5nr00490j>
 267. Wang L, Cheng C, Tapas S, et al (2015) Carbon dots modified mesoporous organosilica as an adsorbent for the removal of 2,4-dichlorophenol and heavy metal ions. *J Mater Chem A*. <https://doi.org/10.1039/c5ta01652e>
 268. Li YK, Yang T, Chen ML, Wang JH (2018) Supported carbon dots serve as

- high-performance adsorbent for the retention of trace cadmium. *Talanta*. <https://doi.org/10.1016/j.talanta.2017.12.020>
269. Mehdinia A, Mashkani M, Jabbari A, et al (2020) Extraction of trace amounts of cadmium in fish and mollusk by Fe₃O₄@N-carbon quantum dots as adsorbent. *J Food Meas Charact*. <https://doi.org/10.1007/s11694-019-00319-w>
 270. Guo Z, Li Q, Li Z, et al (2020) Fabrication of efficient alginate composite beads embedded with N-doped carbon dots and their application for enhanced rare earth elements adsorption from aqueous solutions. *J Colloid Interface Sci*. <https://doi.org/10.1016/j.jcis.2019.12.030>
 271. Shi W, Guo F, Wang H, et al (2018) Carbon dots decorated magnetic ZnFe₂O₄ nanoparticles with enhanced adsorption capacity for the removal of dye from aqueous solution. *Appl Surf Sci*. <https://doi.org/10.1016/j.apsusc.2017.10.099>
 272. Zhang H, Qiao X, Cai T, et al (2017) Preparation and characterization of carbon dot-decorated silica stationary phase in deep eutectic solvents for hydrophilic interaction chromatography. *Anal Bioanal Chem* 409:2401–2410. <https://doi.org/10.1007/s00216-017-0187-z>
 273. Yang D, Tammina SK, Li X, Yang Y (2019) Enhanced removal and detection of benzo[a]pyrene in environmental water samples using carbon dots-modified magnetic nanocomposites. *Ecotoxicol Environ Saf* 170:383–390. <https://doi.org/10.1016/j.ecoenv.2018.11.138>
 274. Deng Y, Ok YS, Mohan D, et al (2019) Carbamazepine removal from water by carbon dot-modified magnetic carbon nanotubes. *Environ Res*. <https://doi.org/10.1016/j.envres.2018.11.035>
 275. Vladimir N. Zaitsev (1997) Complexing silicas: preparation, structure of bonded layer, surface chemistry. 240. <https://doi.org/10.13140/RG.2.1.3014.9848>
 276. Marcano DC, Kosynkin D V, Berlin JM, et al (2010) Improved synthesis of graphene oxide. *ACS Nano* 4:4806–4814
 277. Shi R, Yan L, Xu T, et al (2015) Graphene oxide bound silica for solid-phase extraction of 14 polycyclic aromatic hydrocarbons in mainstream cigarette smoke. *J Chromatogr A* 1375:1–7. <https://doi.org/10.1016/j.chroma.2014.11.057>
 278. Dmytri Konyaev, Sergiy Myerniy YK CLINP 2.1. In: V.N. Karazin Kharkiv Natl. Univ.
 279. Tkachenko O, Rahim A, Baraban A, et al (2013) Hybrid silica-organic material with immobilized amino groups: surface probing and use for electrochemical determination of nitrite ions. *J Sol-Gel Sci Technol* 67:145–154. <https://doi.org/10.1007/s10971-013-3060-3>
 280. Tkachenko O, Panteleimonov A, Padalko I, et al (2014) Silica functionalized with 1-propyl-3-methylimidazolium chloride as an efficient adsorbent for the removal of Eosin Yellow and Reactive Blue 4. *Chem Eng J* 254:324–332. <https://doi.org/10.1016/j.cej.2014.05.117>
 281. Zaitsev VN, Khalaf VA, Zaitseva GN (2008) Organosilica composite for preconcentration of phenolic compounds from aqueous solutions. 1335–1342. <https://doi.org/10.1007/s00216-008-1934-y>
 282. Ferrari AC (2007) Raman spectroscopy of graphene and graphite: Disorder, electron-phonon coupling, doping and nonadiabatic effects. *Solid State*

- Commun 143:47–57. <https://doi.org/10.1016/j.ssc.2007.03.052>
283. Eigler S, Dotzer C, Hirsch A (2012) Visualization of defect densities in reduced graphene oxide. *Carbon* N Y 50:3666–3673. <https://doi.org/10.1016/j.carbon.2012.03.039>
 284. Grimm S, Schweiger M, Eigler S, Zaumseil J (2016) High-Quality Reduced Graphene Oxide by CVD-Assisted Annealing. *J Phys Chem C* 120:3036–3041. <https://doi.org/10.1021/acs.jpcc.5b11598>
 285. Uddin MT, Rahman MA, Rukanuzzaman M, Islam MA (2017) A potential low cost adsorbent for the removal of cationic dyes from aqueous solutions. *Appl Water Sci* 7:2831–2842. <https://doi.org/10.1007/s13201-017-0542-4>
 286. Liu R, Wu D, Liu S, et al (2009) An aqueous route to multicolor photoluminescent carbon dots using silica spheres as carriers. *Angew Chemie - Int Ed* 48:4598–4601. <https://doi.org/10.1002/anie.200900652>
 287. Miha J, Szegedi A, Popova M, et al (2012) Journal of Solid State Chemistry Controlled drug release on amine functionalized spherical MCM-41. 194:257–263. <https://doi.org/10.1016/j.jssc.2012.05.030>
 288. Daigle H (2014) Microporosity development in shallow marine sediments from the Nankai Trough Site C0018. *Mar Geol* 357:293–303. <https://doi.org/10.1016/j.margeo.2014.09.041>
 289. Tadros T (2013) Encyclopedia of Colloid and Interface Science
 290. Gushikem Y, Benvenutti E V, Kholin Y V (2014) Synthesis and applications of functionalized silsesquioxane polymers attached to organic and inorganic matrices *. <https://doi.org/10.1351/pac200880071593>
 291. Zaitsev VN (2015) Preparation , structure and thermal stability of onium- and amino-functionalized silicas for the use as catalysts supports. <https://doi.org/10.1016/j.jcis.2006.06.003>
 292. Барабан АЮ, Кравченко ВВ, Сухов РВ, et al (2012) Поверхностные явления. 21:287–296
 293. Kostenko LS, Alekseev SA, Zaitsev VN, et al (2015) Thermochemical Methods for the Characterization Organosilicas with Immobilized Aminophosphonic Acid of the Термохимические методы изучения состава органокремнеземов с иммобилизованными аминокислотами. 10:45–52
 294. Fadeev AY, Lisichkin G V. (1996) Structure and molecular organization of bonded layers of chemically modified silica. *Adsorpt New Modif Inorg Sorbents* 99:191–212
 295. Zaitsev VN (2008) Organosilica composite for preconcentration of phenolic compounds from aqueous solutions Organosilica composite for preconcentration of phenolic compounds from aqueous solutions. <https://doi.org/10.1007/s00216-008-1934-y>
 296. Walcarius A, Etienne M, Ecole C, Supe N (2003) Rate of Access to the Binding Sites in Organically Modified Silicates . 2 . Ordered Mesoporous Silicas Grafted with Amine or Thiol Groups. 2161–2173
 297. Zaitseva N V, Kobylinska NG, Walcarius A, Zaitsev VN (2012) Speciation of partly oxidized thiol-organosilica surface
 298. S. RMN (1936) The Nitroprusside Reaction as a Test for Reduced Glutathione. *Nature* 138:75–76
 299. Farhana S, Raof A, Mohamad S, Abas MR (2013) Synthesis and Evaluation of

- Molecularly Imprinted Silica Gel for 2-Hydroxybenzoic Acid in Aqueous Solution. 5952–5965. <https://doi.org/10.3390/ijms14035952>
300. Viet D, Eun J, Kim J, et al (2013) A gentle method to graft thiol-functional groups onto silica gel for adsorption of silver ions and immobilization of silver nanoparticles. *Powder Technol* 235:221–227. <https://doi.org/10.1016/j.powtec.2012.10.015>
 301. Arakaki LNH, Fonseca MG, Edson C, et al (2006) Extraction of Pb (II), Cd (II), and Hg (II) from aqueous solution by nitrogen and thiol functionality grafted to silica gel measured by calorimetry. 450:12–15. <https://doi.org/10.1016/j.tca.2006.06.012>
 302. Walcarius A, Delac^ C (2005) Mercury (II) binding to thiol-functionalized mesoporous silicas : critical effect of pH and sorbent properties on capacity and selectivity. 547:3–13. <https://doi.org/10.1016/j.aca.2004.11.047>
 303. Zaitsev VN, Kobylinskaya NG, Kostenko LS, Gerda VI (2008) Conductometric determination of the concentration of acid centers on functionalized materials. *J Anal Chem*. <https://doi.org/10.1134/s1061934808080121>
 304. Atkins P, De Paula J, Ronald F (2009) *Quanta, Matter and Change. A molecular approach to physiscal chemistry*, Oxford Uni
 305. Ivaldi C, Miletto I, Paul G, et al (2019) Influence of silicodactyly in the preparation of hybrid materials. *Molecules*. <https://doi.org/10.3390/molecules24050848>
 306. Descalzo AB, Marcos MD, Amoro P (2005) Anthrylmethylamine functionalised mesoporous silica-based materials as hybrid fluorescent chemosensors for ATP. 2721–2731. <https://doi.org/10.1039/b501609f>
 307. Trifluo- D Selective Enolate Formation. 6–9
 308. Velde MVN Van De (1985) Anthracene Silica Gel , a New Polycyclic-Aromatic-Bonded Stationary Phase for HPLC. 281:239–241
 309. Calero P, Soto J (2008) Synthesis , Characterisation and Optical Properties of Silica Nanoparticles Coated with Anthracene Fluorophore and Thiourea Hydrogen-Bonding. 5649–5658. <https://doi.org/10.1002/ejic.200800721>
 310. Shahid M, Srivastava P, Razi SS, et al (2013) Detection of Zn²⁺ ion on a reusable fluorescent mesoporous silica beads in aqueous medium. *J Incl Phenom Macrocycl Chem* 77:241–248. <https://doi.org/10.1007/s10847-012-0238-1>
 311. Hicks JC, Dabestani R, Buchanan AC, Jones CW (2006) Spacing and site isolation of amine groups in 3-aminopropyl-grafted silica materials: The role of protecting groups. *Chem Mater* 18:5022–5032. <https://doi.org/10.1021/cm061382w>
 312. Deoliveira E, Torres JD, Silva CC, et al (2006) Tetramethylguanidine Covalently Bonded onto Silica Gel as Catalyst for the Addition of Nitromethane to Cyclopentenone. 17:994–999
 313. Chem P, Wang J, Masui Y, Onaka M (2012) Polymer Chemistry Facile synthesis of novel poly (a -aminonitrile) networks through one-pot Strecker reactions †. 865–867. <https://doi.org/10.1039/c2py00002d>
 314. Permatasari FA, Hasdi A, Iskandar F, Ogi T (2016) Role of C – N Configurations in the Photoluminescence of Graphene Quantum Dots Synthesized by a Hydrothermal Route. 1–8. <https://doi.org/10.1038/srep21042>
 315. Sobol PE, Chastain J *Handbook of X-ray Photoelectron Spectroscopy* Edited by

316. Zhang L, Liu J, Yang J, et al (2008) Direct synthesis of highly ordered amine-functionalized mesoporous ethane-silicas. 109:172–183. <https://doi.org/10.1016/j.micromeso.2007.04.050>
317. Dugas V, Chevalier Y (2003) Surface hydroxylation and silane grafting on fumed and thermal silica. 264:354–361. [https://doi.org/10.1016/S0021-9797\(03\)00552-6](https://doi.org/10.1016/S0021-9797(03)00552-6)
318. de Monredon S, Pottier A, Maquet J, et al (2006) Characterisation of the grafting of (3-aminoethyl)aminopropyltrimethoxy silane on precipitated silica. *New J Chem* 30:797. <https://doi.org/10.1039/b517934c>
319. Vrancken KC, Van Der Voort P, Possemiers K, Vansant EF (1995) Surface and Structural Properties of Silica Gel in the Modification with γ -Aminopropyltriethoxysilane. *J Colloid Interface Sci* 174:86–91. <https://doi.org/10.1006/JCIS.1995.1367>
320. Wilkinson F, Worrall DR, Williams SL (1995) Primary Photochemical Processes of Anthracene Adsorbed on Silica-Gel. *J Phys Chem* 99:6689–6696. <https://doi.org/10.1021/j100017a061>
321. Spectrum F (2018) Investigation of Ageing in Bitumen Using Fluorescence Spectrum. 1–11. <https://doi.org/10.3390/ma11081325>
322. Freek J. M. Hoeben, Pascal Jonkheijm, E. W. Meijer and APHJS (2014) About Supramolecular Assemblies of π -Conjugated Systems. *Angew Chem Int Ed Engl* 53:12537–41. <https://doi.org/10.1002/anie.201408279>
323. Choi S-H (2017) Unique properties of graphene quantum dots and their applications in photonic/electronic devices. *J Phys D Appl Phys* 50:103002. <https://doi.org/10.1088/1361-6463/aa5244>
324. Alvand M, Shemirani F (2017) A Fe₃O₄@SiO₂@graphene quantum dot core-shell structured nanomaterial as a fluorescent probe and for magnetic removal of mercury(II) ion. *Microchim Acta* 184:1621–1629. <https://doi.org/10.1007/s00604-017-2134-2>
325. Lu L, Zhou L, Chen J, et al (2018) Nanochannel-Confined Graphene Quantum Dots for Ultrasensitive Electrochemical Analysis of Complex Samples. *ACS Nano* 12:12673–12681. <https://doi.org/10.1021/acsnano.8b07564>
326. Baruah U, Chowdhury D (2016) Ethylene diamine mediated cobalt nanoparticle studded graphene oxide quantum dots with tunable photoluminescence properties. *RSC Adv* 6:67102–67112. <https://doi.org/10.1039/C6RA12686C>
327. Wang L, Wang Y, Xu T, et al (2014) Gram-scale synthesis of single-crystalline graphene quantum dots with superior optical properties. *Nat Commun* 5:5357. <https://doi.org/10.1038/ncomms6357>
328. Nodeh HR, Wan A, Kamboh A (2015) Dispersive graphene-based silica coated magnetic nanoparticles as a new adsorbent for preconcentration of chlorinated pesticides from environmental water. *RSC Adv* 5:76424–76434. <https://doi.org/10.1039/C5RA13450A>
329. Wu Q, Sun Y, Gao J, et al (2018) Ionic liquid-functionalized graphene quantum dot-bonded silica as multi-mode HPLC stationary phase with enhanced selectivity for acid compounds. *New J Chem* 42:. <https://doi.org/10.1039/c7nj05200f>
330. Gómez-Urbano JL, Gómez-Cámer JL, Botas C, et al (2018) Hydrothermally reduced graphene oxide for the effective wrapping of sulfur particles showing

- long term stability as electrodes for Li-S batteries. Carbon N Y. <https://doi.org/10.1016/j.carbon.2018.06.053>
331. Das TK, Banerjee S, Pandey M, et al (2017) Effect of surface functional groups on hydrogen adsorption properties of Pd dispersed reduced graphene oxide. *Int J Hydrogen Energy*. <https://doi.org/10.1016/j.ijhydene.2016.12.024>
 332. Li Y, Chen H, Voo LY, et al (2012) Synthesis of partially hydrogenated graphene and brominated graphene. *J Mater Chem* 22:15021. <https://doi.org/10.1039/c2jm32307a>
 333. Qu J, Gao F, Zhou Q, et al (2013) Highly atom-economic synthesis of graphene/Mn₃O₄ hybrid composites for electrochemical supercapacitors. *Nanoscale* 5:2999–3005. <https://doi.org/10.1039/c3nr33700f>
 334. Sitko R, Zawisza B, Talik E, et al (2014) Spherical silica particles decorated with graphene oxide nanosheets as a new sorbent in inorganic trace analysis. *Anal Chim Acta* 834:22–9. <https://doi.org/10.1016/j.aca.2014.05.014>
 335. Zhao Y, Yuan F, Quan X, et al (2015) An electrochemical sensor for selective determination of sulfamethoxazole in surface water using a molecularly imprinted polymer modified BDD electrode. *Anal Methods* 7:2693–2698. <https://doi.org/10.1039/c4ay03055a>
 336. Berlin A., Dean J., Draper M.H., Smith E.M.B. SF (1987) Immunotoxicology
 337. Giusti RM, Iwamoto K, Hatch EE (1995) Diethylstilbestrol revisited: A review of the long-term health effects. *Ann Intern Med* 122:778–788. <https://doi.org/10.7326/0003-4819-122-10-199505150-00008>
 338. Bridges JW, Bridges O (2013) Hormones as growth promoters: The precautionary principle or a political risk assessment? *Precautionary Princ 20th Century Late Lessons from Early Warn* 161–169
 339. Tang J, Xiang L, Zhao F, et al (2015) Development of an Up-Conversion Homogenous Immunoassay for the Determination of Diethylstilbestrol in Water. *Anal Lett* 48:796–808. <https://doi.org/10.1080/00032719.2014.961605>
 340. Yin K, Yu F, Liu D, et al (2016) Cyanine-based colorimetric and fluorescent probe for the selective detection of diethylstilbestrol in seawater, shrimp and fish samples. *Sensors Actuators, B Chem* 223:799–805. <https://doi.org/10.1016/j.snb.2015.10.014>
 341. Yang Y, Chen J, Shi YP (2012) Determination of diethylstilbestrol in milk using carbon nanotube-reinforced hollow fiber solid-phase microextraction combined with high-performance liquid chromatography. *Talanta* 97:222–228. <https://doi.org/10.1016/j.talanta.2012.04.021>
 342. Wang J, Chen Z, Li Z, Yang Y (2016) Magnetic nanoparticles based dispersive micro-solid-phase extraction as a novel technique for the determination of estrogens in pork samples. *Food Chem* 204:135–140. <https://doi.org/10.1016/j.foodchem.2016.02.016>
 343. de Souza L V., da Rosa DS, Tkachenko OS, et al (2019) The role silica pore structure plays in the performance of modified carbon paste electrodes. *Ionics (Kiel)* 25:3259–3268. <https://doi.org/10.1007/s11581-019-02882-0>
 344. Porada R, Fendrych K, Baś B (2020) The Mn-zeolite/Graphite Modified Glassy Carbon Electrode: Fabrication, Characterization and Analytical Applications. *Electroanalysis*. <https://doi.org/10.1002/elan.201900744>
 345. Mintz KJ, Zhou Y, Leblanc RM (2019) Recent development of carbon quantum

- dots regarding their optical properties, photoluminescence mechanism, and core structure. *Nanoscale* 11:4634–4652. <https://doi.org/10.1039/c8nr10059d>
346. Mohd Yazid SNA, Chin SF, Pang SC, Ng SM (2013) Detection of Sn(II) ions via quenching of the fluorescence of carbon nanodots. *Microchim Acta* 180:137–143. <https://doi.org/10.1007/s00604-012-0908-0>
 347. Kumawat MK, Thakur M, Gurung RB, Srivastava R (2017) Graphene Quantum Dots for Cell Proliferation, Nucleus Imaging, and Photoluminescent Sensing Applications. *Sci Rep* 7:1–16. <https://doi.org/10.1038/s41598-017-16025-w>
 348. Liu L, Mi Z, Hu Q, et al (2018) One-step synthesis of fluorescent carbon dots for sensitive and selective detection of hyperin. *Talanta* 186:315–321. <https://doi.org/10.1016/j.talanta.2018.04.065>
 349. Chen W, Hu C, Yang Y, et al (2016) Rapid Synthesis of Carbon Dots by Hydrothermal Treatment of Lignin. <https://doi.org/10.3390/ma9030184>
 350. Bernard S, Beyssac O (2010) XANES, Raman and XRD study of anthracene-based cokes and saccharose-based chars submitted to high-temperature pyrolysis. *Carbon N Y* 1–11. <https://doi.org/10.1016/j.carbon.2010.03.024>
 351. Song H, Liu X, Wang B, et al (2019) High production-yield solid-state carbon dots with tunable photoluminescence for white/multi-color light-emitting diodes. *Sci Bull* 64:1788–1794. <https://doi.org/10.1016/j.scib.2019.10.006>
 352. Li X, Zhang S, Kulinich SA, et al (2014) Engineering surface states of carbon dots to achieve controllable luminescence for solid-luminescent composites and sensitive Be²⁺ detection. *Sci Rep* 4:1–8. <https://doi.org/10.1038/srep04976>
 353. Zhang Y-N, Niu Q, Gu X, et al (2019) Recent progress on carbon nanomaterials for the electrochemical detection and removal of environmental pollutants. *Nanoscale* 11:11992–12014. <https://doi.org/10.1039/c9nr02935d>
 354. Patra AS, Gogoi G, Qureshi M (2018) Ordered–Disordered BaZrO₃– δ Hollow Nanosphere/Carbon Dot Hybrid Nanocomposite: A New Visible-Light-Driven Efficient Composite Photocatalyst for Hydrogen Production and Dye Degradation. *ACS Omega* 3:10980–10991. <https://doi.org/10.1021/acsomega.8b01577>
 355. Callura JC, Perkins KM, Noack CW, et al (2018) Selective adsorption of rare earth elements onto functionalized silica particles. *Green Chem* 20:1515–1526. <https://doi.org/10.1039/C8GC00051D>
 356. Guner T, Yuce H, Tascioglu D, et al (2019) Optimization and performance of nitrogen-doped carbon dots as a color conversion layer for white-LED applications. 2004–2013. <https://doi.org/10.3762/bjnano.10.197>
 357. Chowdhury ZZ, Abd Hamid SB, Zain SM (2015) Evaluating design parameters for breakthrough curve analysis and kinetics of fixed bed columns for Cu(II) cations using lignocellulosic wastes. *BioResources*. <https://doi.org/10.15376/biores.10.1.732-749>
 358. Zock PL, De Vries JHM, Katan MB (1994) Impact of myristic acid versus palmitic acid on serum lipid and lipoprotein levels in healthy women and men. *Arterioscler Thromb Vasc Biol* 14:567–575. <https://doi.org/10.1161/01.ATV.14.4.567>

12. Attachment

A Published papers

1. Mikhraliieva A, Zaitsev V, Xing Y, et al (2020) Excitation-Independent Blue-Emitting Carbon Dots from Mesoporous Aminosilica Nanoreactor for Bioanalytical Application. ACS Appl Nano Mater 0: <https://doi.org/10.1021/acsanm.0c00363>

ACS **APPLIED**
NANO MATERIALS

www.acsanm.org

Article

Excitation-Independent Blue-Emitting Carbon Dots from Mesoporous Aminosilica Nanoreactor for Bioanalytical Application

Albina Mikhraliieva, Vladimir Zaitsev,* Yutao Xing, Horácio Coelho-Júnior, and Rubem Luis Sommer

 Cite This: ACS Appl. Nano Mater. 2020, 3, 3652–3664

 Read Online

ACCESS |

 Metrics & More

 Article Recommendations

 Supporting Information

ABSTRACT: Here we present the first example of excitation-independent blue-emitting carbon dots (iC-dots) obtained by pyrolysis of citric acid (CA) without post-treatment chromatographic separation. To confine the growth and shape of carbon nanoparticles, silica gel with immobilized aminopropyl groups ($\text{SiO}_2\text{-NH}_2$) was used as a nanoreactor. It was demonstrated that the carbonization of $\text{SiO}_2\text{-NH}_2$ with embedded CA resulted in the formation of unbound wC-dots and immobilized iC-dots. Because of their firm attachment to the surface, iC-dots can be easily separated from low-molecular impurities and wC-dots by simply rinsing the nanocomposite with water. From atomic force and transmission electron microscopies iC-dots can be represented as flattened spheroids with 2–4 nm of height and 5 nm in lateral size. The size distribution profile for wC-dots is very wide with about 95% the particles within the 2.5–5.5 nm size range. Increasing the template pore size from 4.9 up to 9.1 nm has no effect on the size of the iC-dots. From Fourier transform infrared analysis and X-ray photoelectron spectroscopy data it was assumed that iC-dots belong to N-doped C-nanoparticles with 9:1 carbon to nitrogen atomic ratio. As-prepared iC-dots demonstrate excitation-independent photoluminescence at 445 nm with quantum yields up to 16.8%, which makes them attractive for bioanalytical application.

KEYWORDS: carbon dots, nanoreactor, aminosilica, citric acid, photoluminescence

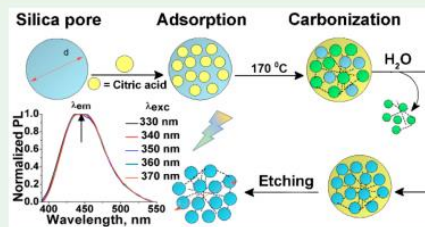



Figure A 1 - Published paper in ACS Applied Nano Materials. Materials for Chapter 7.2

2. Mikhraliieva A, Zaitsev V, Aucélio RQ, et al (2020) Benefit of porous silica nanoreactor in preparation of fluorescence carbon dots from citric acid. Nano Express. <https://doi.org/10.1088/2632-959x/ab7e0d>

IOP Publishing Nano Express 1 (2020) 010011 <https://doi.org/10.1088/2632-959x/ab7e0d>

NANO EXPRESS

 CrossMark

PAPER

Benefit of porous silica nanoreactor in preparation of fluorescence carbon dots from citric acid

OPEN ACCESS


RECEIVED
21 February 2020




REVISED
4 March 2020

ACCEPTED FOR PUBLICATION
9 March 2020

PUBLISHED
30 March 2020

Original content from this work may be used under the terms of the [Creative Commons Attribution 4.0 licence](#).
Any further distribution of this work must maintain attribution to the author(s) and the title of the work, journal citation and DOI.



Albina Mikhraliieva , **Vladimir Zaitsev** , **Ricardo Q Aucélio**, **Henrique B da Motta** and **Michael Nazarkovsky** 

Department of Chemistry, Pontifical Catholic University of Rio de Janeiro Marques de São Vicente, 225, 22451-900, Rio de Janeiro, Brasil
E-mail: vnzaitsev@puc-rio.br

Keywords: carbon dots, nanoreactor, citric acid, photoluminescence
Supplementary material for this article is available [online](#)

Abstract
A facile and robust synthesis of carbon dots (CDs) emitting blue-light in water without activation and stabilization has been developed by pyrolysis of citric acid (CA) adsorbed in silica gel (SiO₂) pores. Effect of the host pore size on luminescent properties of SiO₂@CDs nanocomposite as well as water suspension of CDs has been studied. The synthesis conditions such as concentration of the precursor, duration of synthesis also have been investigated. It has been demonstrated that upon the thermal treatment of silica gels saturated with CA (60% of maximum loading) at 170 °C for 5–600 min, luminescent CDs are shaped inside the nanoreactor pores. These SiO₂@CDs emit photoluminescence centered at 450 nm. Silica-immobilized CDs can be separated from the source molecules and side-products by centrifugation, which allows avoiding the dialysis of the resulted mixture and so improve the scaling of the synthesis. The CDs can be easily released from SiO₂@CDs by washing it with water. Water-eluted CDs demonstrate photoluminescence at 447 nm. The smaller pore size of the host and longer time of thermal treatment promote the formation of the CDs with better photoluminescent peak symmetry and higher quantum yield up to 10.1%.

Figure A 2 - Published paper in Nano Express. Materials. Materials for Chapter 7.2

B Participation in Congress

Oral presentation

Síntese, caracterização e propriedades de fluorescência superficial de materiais à base de sílica gel com fragmentos de antraceno. XVII Encontro Regional da Sociedade Brasileira de Química - Regional Rio de Janeiro (XVIIERSBQ-Rio), Rio de Janeiro, Brazil, 2019 (awarded work).

Preparação de nanopontos de carbono fluorescentes utilizando aminosilica como nanoreator, II Jornada de Pós-Graduação e Pesquisa – DQ PUC-Rio, Rio de Janeiro, Brazil, 2018.

Adsorvente seletivo a base de sílica-antraceno para remoção de compostos aromáticos. **I Jornada de Pós-Graduação e Pesquisa – DQ PUC-Rio,** Rio de Janeiro, Brazil, 2017 (awarded work).

Poster presentation

Scanning Electron Microscopy – Assistant Technique In The Preparation Of Fluorescence Carbon Dots On Silica Gel. 27º CONGRESSO DA SOCIEDADE BRASILEIRA DE MICROSCOPIA E MICROANÁLISE, Rio de Janeiro, Brazil, 2019.

Quantum Confinement of Strongly Fluorescent Carbon Dots in Silica-Based Nanoreactors. **III Jornada de Pós-Graduação e Pesquisa dos Programas de Pós-graduação em Química da PUC-Rio e do Instituto Militar de Engenharia (IME),** Rio de Janeiro, Brazil, 2019.

Síntese, caracterização e propriedades de fluorescência superficial de materiais à base de sílica gel com fragmentos de antraceno. XVII Encontro Regional da Sociedade Brasileira de Química - Regional Rio de Janeiro (XVIIERSBQ-Rio), Rio de Janeiro, Brazil, 2019.

Effect of functionalization of porous silica as nanoreactor for preparation of fluorescent carbon dots. Chemistry & Water American Chemical Society Fall 2019 National Meeting & Expo, San Diego, USA, 2019.

Blue-emitting carbon dots from aminosilica nanoreactor. **17th Annual Meeting of the Brazilian Materials Research Society**, Natal, Brazil, 2018.

Effect of functionalization of porous silica as nanoreactor for preparation of fluorescent Carbon Dots. **41^a Reunião Anual da Sociedade Brasileira de Química**, Foz do Iguaçu, Brazil, 2018.

Influence of thermal-resistant template on size and fluorescence properties of Carbon Dots. **The World Conference on Carbon**, Madrid, Spain, 2018.

Graphene@silica for removal of polyaromatic compounds. **XVI Brazilian MRS meeting**, Gramado, Brazil, 2017.

Um método simplificado para a síntese de Nanopontos de Carbono com distribuição do tamanho de partículas estreita. **XVI Encontro Regional da Sociedade Brasileira de Química**. Rio de Janeiro, Brazil, 2017.